Optically active quantum dots in bottom-up nanowires

THÈSE N^{O} 6812 (2015)

PRÉSENTÉE LE 13 NOVEMBRE 2015

À LA FACULTÉ DES SCIENCES ET TECHNIQUES DE L'INGÉNIEUR

LABORATOIRE DES MATÉRIAUX SEMICONDUCTEURS

PROGRAMME DOCTORAL EN SCIENCE ET GÉNIE DES MATÉRIAUX

ÉCOLE POLYTECHNIQUE FÉDÉRALE DE LAUSANNE

POUR L'OBTENTION DU GRADE DE DOCTEUR ÈS SCIENCES

PAR

Yannik FONTANA

acceptée sur proposition du jury:

Prof. N. Marzari, président du jury
Prof. A. Fontcuberta i Morral, directrice de thèse
Prof. P. Plochocka, rapporteuse
Prof. V. Zwiller, rapporteur
Prof. E. Kapon, rapporteur

ÉCOLE POLYTECHNIQUE
FÉDÉRALE DE LAUSANNE

Suisse
2015

Abstract

This thesis is dedicated to the discovery and progressive study of quantum emitters embedded in the shell of coaxial gallium arsenide/ aluminum-gallium arsenide nanowires. The bottom-up core/shell nanowires were grown in a molecular beam epitaxy machine. During the shell growth, diffusion-driven phenomena lead to segregation effects. Gallium-rich regions are formed on the nanoscopic scale. The observation has been made that the reduced dimensionality of these regions provides true tridimensional confinement for the carriers. The recombination spectra of the electrons with the holes in what was coined "shell quantum dots" thus appear as a set of narrow, intense peaks.

The formation of shell quantum dots is taking place on a large range of growth temperatures and nominal alloy fractions, giving freedom to engineer the growth process. The shell thickness plays an important role in the quantum dot density and total ensemble spectrum. In addition, the adjunction of an aluminum arsenide predeposition layer increases the local curvature and has been seen to foster the formation of the quantum dots.

Single emitter spectroscopy reveals the few-particles electronic structure of quantum dots, with systematic signatures for the different degrees of occupation of the quantum dot. The shape anisotropy of the quantum dots leads to observable spin-spin interactions which lift the exciton level (one hole and one electron) degeneracy. Undesirable in most cases, this effect allows in this case to find that the orientation of the quantum dots in the wire is not hard-wired to the growth direction or to the nanowire long axis.

The latter observation is confirmed by magneto-photoluminescence experiments. The energetic splitting and shifts of the spin sublevels when an external magnetic field is applied also confirms the small size of the quantum dots. It is found that for GaAs in the strong confinement regime, the Landé coefficients of the electron and hole take opposite signs and are dependent on the angle at which the field is applied. These effects allow the tuning of the exciton composite Landé coefficient and could be used to reduce the splitting between the exciton spin sublevels or create optically degenerate coupled Λ systems.

Finally, the sub-nanosecond dynamics happening in the quantum dots are probed with time-correlated photon counting. It is shown that the carriers in the shell are quickly captured by the quantum dots. In addition, it is proposed that the electron population is reduced due to diffusion-assisted trapping in the nanowire core or through electron-acceptor recombination.

Keywords: Nanowires • Semiconductors • Quantum dots • Material science Solid-state physics • Nano-science • Spectroscopy • Optics • Single-photon emitters

Résumé

Cette thèse est dédiée à la découverte et l'étude progressive d'émetteurs quantiques incorporés dans la couche extérieure de nanofils composé d'un assemblage coaxial d'arséniure de gallium et d'arséniure d'aluminium-gallium. Les nanofils coeur/coquille sont des nano-structures auto-assemblées fabriquées par épitaxie à jets moléculaires. Durant la croissance de la coquille, des phénomènes de diffusion mènent à des effets de ségrégation. Des régions riches en gallium se forment à l'échelle nanoscopique. Cette réduction dimensionnelle conduit à l'établissement d'un confinement tridimensionnel pour les électrons et les trous. Les spectres de recombinaison des électrons et des trous dans ce qui à été nommé "boite quantique de coquille" ("shell quantum dots") apparaissent ainsi comme des séries de pics intenses et fins.

La formation de boites quantique de coquille s'effectue sur une large plage de température de croissance ainsi que pour une gamme étendue d'alliages, permettant une certaine liberté dans l'optimisation du procédé de croissance. L'épaisseur de la coquille joue un rôle important pour la densité de boite quantiques ainsi que pour la plage spectrale totale. De plus, l'addition d'une couche d'arséniure d'aluminium dîte "de prédeposition" accroît la courbure locale de la structure. Il a été observé que cet accroissement conduit à une facilitation de la formation de boite quantique.

Une étude spectroscopique réalisée sur des émetteurs uniques révèle la structures énergétique des boites quantiques contenant un nombre fini de charges, avec une signature systématique suivant le degré d'occupation de la boite. L'anisotropie géométrique des boites amènent à l'observation d'interactions spin-spin brisants la dégénérescence de l'état de l'exciton (un électron lié à un trou). Si cet effet est en général indésirable, il permet dans ce cas de réaliser que l'orientation des boites quantiques dans le nanofil n'est pas liée à la direction de croissance de la coquille ou à l'axe principal du nanofil.

Cette observation est confirmée par des expériences de photoluminescence réalisées en champs magnétiques. La séparation et le décalage des sous-niveaux énergétique liés à différentes orientations des spins confirme la taille réduite des boites quantiques. Il est montré que pour de l'arséniure de gallium dans le régime de confinement fort, les coefficients de Landé de l'électron et du trou prennent des

signes opposés et dépendent de l'orientation du champ magnétique. Ces effets permettent d'ajuster le coefficient de Landé global de l'exciton, et peuvent être mis en oeuvre de manière à réduire la séparation entre les sous-niveau de spin de l'exciton ou pour créer des systèmes Λ couplés et optiquement dégénérés.

Finalement, la dynamiques des porteurs de charges dans les boites quantiques est testée à l'échelle de la picoseconde grâce à une technique de comptage de photons corrélés en temps. Ces mesures démontrent la rapidité des phénomènes de captures des porteurs par les boites quantiques. De plus, un modèle est proposé pour lequel la population d'électrons est réduite à la suite du piégeage desdits électrons dans le coeur du nanofil, une conséquence directe de leur diffusion dans le semiconducteur. Une alternative possible est la recombinaison unipolaire des électron au travers d'une transition électron-accepteur.

Mots-Clefs: Nanofils • Semiconducteurs • Boites quantiques • Science des Matériaux • Physique des solides • Nano-science • Spectroscopie • Optique Émetteurs de photons isolés

Zusammenfassung

Diese Arbeit beschäftigt sich mit der Entdeckung und Untersuchung von Quanten-Emittern, die im äusseren Mantel von koaxialen Gallium-Arsenid / Aluminium-Gallium-Arsenid Nanodrähten eingebettet sind. Die Kern-Mantel Nanodrähte wurden in einer Molekularstrahlepitaxie Anlage nach dem Bottom-Up Verfahren gewachsen. Während des Mantel-Wachstums führen Diffusions-gesteuerte Phänomene zu Ausscheidungseffekten, so dass sich Gallium-reiche Bereiche nanoskopischer Grösse formieren. Es wurde beobachtet, dass die verminderte Dimensionalität dieser Bereiche zu dreidimensionalen Confinement der Ladungsträger führt. Das Rekombinationsspektrum der Elektronen mit Löchern in den Bereichen, die Mantel-Quantenpunkten genannt werden, setzt sich somit aus einer Reihe dünner, intensiver Peaks zusammen. Die Mantel-Quantenpunkte bilden sich über einen grossen Bereich von Wachstumstemperatur und nomineller Legierungsanteile, wodurch der Wachstumsprozess gezielt eingestellt werden kann. Die Manteldicke hat einen wesentlichen Einfluss auf die Quantenpunkt-Dichte und das Spektrum des Gesamtensembles. Zusätzlich wurde festgestellt, dass das Hinzufügen einer Aluminium-Arsenid Prädespoitionslage, welche die lokale Krümmung erhöht, die Formierung von Quantenpunkten begünstigt. Mittels Einzel-Emitter Spektroskopie wurde die für Wenig-Teilchen-Systeme typische elektronische Struktur, mit den charakteristische Signaturen der verschiedenen Besetzungslevel des Quantenpunkts, offenbart. Die Formanisotropie der Quantenpunkte führt zu einer messbaren Spin-Spin Wechselwirkung, welche die Entartung der exzitonischen Levels (ein Elektron und ein Loch) aufhebt. Obwohl dies im Allgemeinen nicht von Vorteil ist, hilft dieser Effekt in diesem Fall, festzustellen, dass die Quantenpunkt-Orientierung weder durch die Wachstumsrichtung noch durch die Längsachse des Nanodrahtes vorgegeben ist. Diese Beobachtung wird durch Magneto-Photolumineszenz Experimente bestätigt. Die Aufspaltung und die Verschiebung der Spin Energieniveaus in einem magnetischen Feld zeigen ausserdem die geringe Grösse der Quantenpunkte. Es wurde beobachtet, dass die Landé Koeffizienten der Elektronen und Löcher im Regime des starken Confinement entgegengesetzte Vorzeichen haben und vom

Winkeln des angelegten Feldes abhängen. Durch diese Effekte lässt sich der exzitonische Landé Koeffizient einstellen und es könnte somit die Aufspaltung der exzitonischen Subniveaus minimiert oder optisch entartete, gekoppelte Lambda Systeme erzeugt werden. Schliesslich wurde die Sub-Nanosekunden-Dynamik in den Quantenpunkt mit Zeit-korreliertem Photonenzählen untersucht. Es wurde gezeigt, dass die Ladungsträger des Mantels in kurzer Zeit von den Quantenpunkten eingefangen werden. Zusätzlich, wird nahegelegt, dass die Elekronen-Population durch Diffusions-unterstütztes Einfangen im Nanodraht-Kern oder durch Elektron-Akzeptor Rekombination reduziert wird.

Riassunto

Questa tesi è dedicata alla scoperta e al progressivo studio di emettitori quantici incorporati nella shell di nanofili coassiali GaAs-AlGaAs core-shell. I nanofili sono stati cresciuti tramite epitassia da fasci molecolari. Durante la crescita della shell, fenomeni di diffusione portano ad effetti di segregazione, per cui regioni con un accumulo di gallio vengono a formarsi a livello nanoscopico. La ridotta dimensione di queste regioni porta a un effettivo confinemento quantico tridimensionale dei portatori di carica. L emissione spettrale della ricombinazione degli elettroni con le buche di quello che stato chiamato "shell quantum do" appare come una serie di stretti, intensi picchi. La formazione dei "shell quantum dots" avviene su un largo intervallo di temperature e contenuto nominale relativo di alluminio, rendendo possibile la modulazione del processo di crescita. Lo spessore della shell gioca un ruolo importante nella densità dei quantum dots e, di conseguenza, nello spettro totale. Inoltre, l aggiunta di uno strato predepositato di AlAs aumenta la curvatura locale, la quale favorisce la formazione di quantum dots. Lo studio spettroscopico di un singolo emettitore ne rivela la struttura elettronica, mostrando sistematicamente i differenti livelli occupazionali. La forma anisotropa dei quantum dots porta all osservazione dell interazione spin-spin che rimuove la degenerazione del livello eccitonico (una buca e un elettrone). Generalmente non voluto, questo effetto porta qui a trovare che l orientazione dei quantum dots nei nanofili non è lungo la direzione di crescita o l asse principale dei nanofili. L ultima osservazione è stata confermata dagli esperimenti di magneto-fotoluminescenza. La divisione e lo spostamento dei sublivelli energetici di spin dovuta all applicazione di un campo magnetico esterno confermano le ridotte dimensioni dei quantum dots. È stato trovato che per GaAs in regime di forte confinamento, i coefficienti di Landé per l elettrone e per la buca hanno segni opposti e dipendono dall angolo a cui il campo viene applicato. Questi effetti permettono di regolare il coefficiente eccitonico di Landé e possono essere usati per ridurre la divisione tra i sublivelli eccitonici di spin o creare sistemi ? accoppiati otticamente degeneri. Infine, le dinamiche dei portatori di carica che avvengono su scale dei picosecondi nei quantum dots sono misurate tramite un sistema "Time Correlated Single Phonon Counting". Grazie a questa

tecnica, stato dimostrato che i portatori di carica nella shell sono velocemente catturati dai quantum dots. Inoltre, viene spiegato come la popolazione di elettroni può diminuire a causa della cattura nel core grazie alla diffusione o attraverso la ricombinazione di un elettrone con un accettore.

Contents

List of Figures

List of Tables

Introduction 1

The current period, starting from the second half of the XXth century, is often referred to as the *Silicon Age*. The invention of the transistor marked its beginning[1]. However, reducing the progress in electronics solely to silicon transistors would be belittling. Other components have come to play an important role in today's life. These include light emitting diodes (LEDs), solar cells, solid-state lasers, power electronics devices and so on. In most cases, silicon is a convenient yet limited choice, dictated by price and, maybe more importantly, the accurate tuning of the material properties.

The emergence of nanotechnology brought a new perspective to electronics. It placed within reach the possibility of actively controlling and design the quantum properties of matter. Every material property arises from quantum mechanical effects, as quantum mechanics determines the interactions and bonds between atoms. Altering the structure of materials at the nanoscale allows to move away from the tridimensional, quasi-infinite crystal constrain. For semiconductors, several breakthrough have been made. Heterostructured quantum wells (QW),[1] wires and dots (QD)[2] have been realized using different types of semiconductors as matrix and active materials. New electronic features follow from the quantum confinement of carriers. Notably, the changes in density of electronic states (DOS) significantly impact several important properties such as conductivity or light emission.[3–5] The figure 1.1 illustrates the reshaping of the DOS of an arbitrary semiconductor (in cyan) confined in different geometries by a matrix material acting as a barrier for the carriers (light grey). From the bulk, extended 3D material down to the isolated "0D" islands, the DOS changes, losing its typical character until it can be related to the energy spectrum of an atom. Given the span of these new opportunities, it is not surprising that a significant effort has been made to explore other types of nanostructures, not necessarily monolithic and planar.

[1]Interesting fact, the first version of a (point-contact) transistor was made out of germanium, a material abandoned later in favor of silicon. IBM and Samsung announced in 2015 transistors with 7 nm channels, which, in order to work properly, needed to be made of a silicon-germanium alloy, potentially marking the return of germanium in the electronic industry

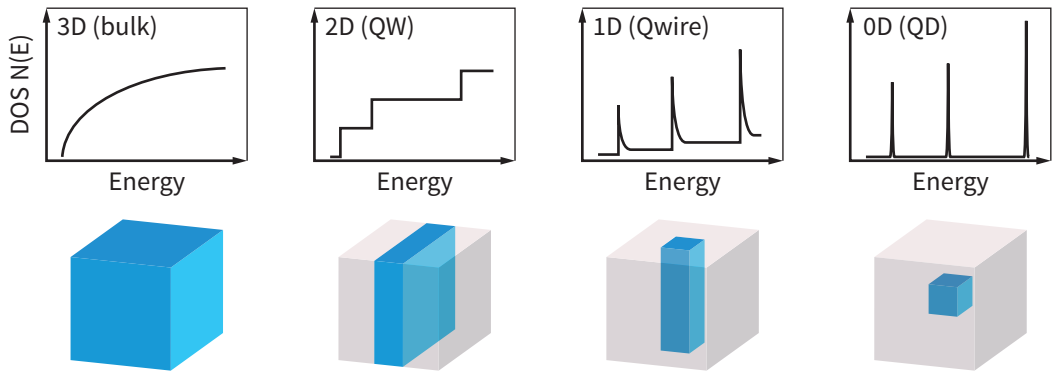

Figure 1.1 • Confinement effects on the density of electronic states in nanostructured materials. The DOS for (from left to right) bulk, quantum well, quantum wire and quantum dot heterostructures is shown. The carriers are confined in the cyan material by the barrier material (in grey). The bottom row represents the confinement directions.

In their seminal work, R.S. Wagner and W.S. Ellis demonstrated that it was possible to grow single crystalline semiconductor structures with an extreme aspect ratio using a new protocol, coined vapor-liquid-solid (VLS) where the precursor material in a gaseous phase (vapor) is incorporated into a metal catalyst droplet (liquid) until supersaturation and precipitation of the solid material below the droplet (solid).[6] The resulting structures were named whiskers, now called nanowires (NW) since the diameter of these filamentary single crystals dropped below the micrometer scale. Nanowires did not attract attention right after their discovery, and have been often considered as "parasitic" material happening during planar growth (in particular of wide-gap semiconductors). The revival of the nanowire field was fostered by another discovery: Carbon nanotubes (CNTs), which were identified in 1991 and quickly raised a massive interest for quasi-1D, free-standing nanostructures.[7]

NWs are related to CNTs by their shape: several microns in length, with a diameter in the nanometer range. However the diversity of CNTs is limited to the different arrangement of carbon atoms along the tubes, while NWs can be made from many different materials: Si, ZnO, GaN, VO_2, GaAs and so on. On the crystallographic side, polymorphism in NWs is commonly observed.[8–10] The wurtzite (hexagonal) phase of several materials (*e.g.* III-Vs) is only observed in nanowires, where it becomes a stable phase. Starting from there, polymorphic structures (homostructures) can be imagined.[11–13]

Other complex structures can also be built with nanowires. Similar to planar growth, heterostructures can be realized. Thanks to free lateral surfaces, NWs allow for the relaxation of the stress induced by an axial heterojunction.[14] The next obvious step was to try to master both polymorphism and heterostructures.[15,16] Technically, silicon and high-performance III-V materials could be combined to overcome the cost barriers of high-performance III-V's and the low performance (low carrier

mobility, indirect bandgap) of Si. In addition, NWs of few tens of nanometers interact strongly with light. This interaction, tunable to a wide extent, gives a particular advantage to NWs regarding photonic properties.[17,18]

In the meantime, a significant amount of work has been done on solid-state self-assembled planar QDs made of III-V, particularly for $In_xGa_{1-x}As$ grown following the Stranski-Krastanov protocol (SKQD). As previously described, QDs possess discrete electronic levels, to the point that they are often referred to as *artificial atoms*. They hold the advantage to be in a solid-state form, with tunable electronic levels *via* composition and size. This analogy led to the observations of several phenomena invoking the quantum nature of dots.[19–25] In particular quantum dots are promising as gain material in QDs-based lasers, active medium in LEDs and solar cells, up-and down-converters for light harvesting and ultimately as single and entangled photon sources to be used as key elements for quantum information and quantum computing technologies.[26] Embedding QDs in NWs allows one to overcome a major inconvenience of planar structures, namely the poor light extraction efficiency.

The goal of this thesis is to provide information on a new kind of QDs self-assembled *via* diffusion in the shell of radially heterostructured GaAs/AlGaAs NWs. From now on, the dissertation will cover first the basics behind the growth of bottom-up NWs, their general optical properties as well as the optical properties of epitaxial QDs. An overview of the main experimental techniques used during the research project will then be presented. The results chapters start with a description of the QDs, coined shell-QDs, followed by a study of the growth conditions and geometries leading to the observation of shell-QDs and their impact on the QDs population. Results focusing on the optical properties of single QDs, showing their characteristics as single-photon emitters and discussing the different states of single shell-QDs in NWs, is then presented. The influence of an external magnetic field on the QDs spectrum is then examined, and several key characteristics of GaAs-based QDs are unveiled. Finally, a short discussion on the reasons leading to the observation of various excitonic complexes and in particular the positively charged trion conclude the results part.

Nanowires and quantum dots

2

This chapter aims to provide the reader with an introduction and overview of the fields of NWs, QDs and QDs in NWs. In order to do so, a brief description of both systems, NWs and QDs shall be given. Emphasis will be put on their optical properties, as they are of prime interest for this thesis. Colloidal NWs and QDs will not be discussed and the following section will solely consider epitaxial nanostructures.

2.1 Semiconductor nanowires

Bottom-up semiconductor NWs can be considered as a "re-emerging field". Indeed, the basic principle used to grow NWs was found in the 60's when Si whiskers were created from the seeding by gold droplets. Similarly, several materials, when grown in planar layers, have the tendency to materialize in the form of NWs. First, most scientists either paid no attention to these structures, or tried to minimize their growth as they would be dertimental to the planar growth. The total effort on the topic remained small until the 90's. Nanowiskers were then "rebranded" nanowires. At this point and since then, the potential of NWs for nanoelectronics, photonics and sensing triggered a world-wide, intensive research on these particular nanostructures. The research effort covered and is still going on for a wide range of semiconductor materials: Si, III-Vs, nitrides, oxydes and so on. The initial research on the growth mechanism was soon complemented by experiment in the framework of electronic transport, mechanics and optics.[27–30] An important step has been the discovery that materials with strongly mismatched lattice parameters could be combined thanks to the facilitated strain relaxation in NWs. This trump card made NWs very popular as they could be used to overcome limitations linked with strain-related defects in planar structures. In addition, the fact that many materials could be produced in crystalline phases not stable in bulk spurred the research: NWs gave access to new materials, impossible to obtain with planar epitaxy. Finally, NWs have exceptional properties with regards to their interaction with light as they support a wide variety of optical

modes. This makes semiconductor NWs extremely attractive for photonics application. Relatively simple geometries allows for resonant interaction or out-coupling of the light very efficiently. This is in direct opposition to planar emitters, for which the flat material-vacuum interface present a severe obstacle for photon transmission. The outcome of NWs is the possibility to engineer structures with tailored electronic structures, able to function as cavities and light trapping medium or conversely able to in- and out-couple the light with a high efficiency, making them perfect to boost the emission efficiency of, *e.g.* single-photon emitters or to capture light for solar-cell applications.

2.1.1 Nanowire growth

Semiconductor NWs growth relies heavily on technologies initially developed for "2D" or "planar" growth of semiconductor materials.[31,32] Two techniques are mainly used to grow high quality III-V NWs. The first is chemical vapour deposition (CVD) and particularly the metal-organic CVD (MOCVD) variant. The second is molecular beam epitaxy (MBE), and is the one used to grow the NWs investigated in this thesis. The top row of figure 2.1 shows the main reactants for the deposition of GaAs with (a) MO-CVD and (b) MBE. The panels (c) and (d) show a schematic of respectively a MO-CVD reactor and an MBE chamber. The two approaches are briefly described hereafter:

MOCVD The principle of MOCVD relies on injecting in a low pressure (between 10 and 10^2 Torr) chamber gaseous compounds of the elementary species of the targeted semiconductor. For III-V semiconductor, the group III element is often injected in the form of a metalo-organic complex (*e.g.* : trimethylindium $In(CH_3)_3$ for indium) while the group V element is an hydride gas (*e.g.* : phosphine PH_3 for phosphorus). The cracking reaction of the gas at the sample surface allows for the incorporation of the elements, with a stoichiometry that can be controlled by the V/III ratio. CVD-based techniques are at the core of most of the modern semiconductor industries.

MBE MBE is a technologically more stringent method, as it involve working in a ultra-high vacuum environment (typically 10^{-10} to 10^{-9} Torr). For MBE growth, the precursors are the bare components or molecule of these components (*e.g.* : Ga and molecular arsenic (As_4) for GaAs). Heated in effusion cells, the materials form extremely low density jets (molecular beams) directed toward a heated growth substrate. The beam flux are controlled by shutters and the temperature of the effusion cells. The low beam fluxes result in very low growth rate, opening the possibilities for the creation of close-to-perfect interfaces and extreme-purity materials. This is required for example for the making of QWs of accurate thickness used in solid-state lasers or two-dimensional electron gas (2DEG).

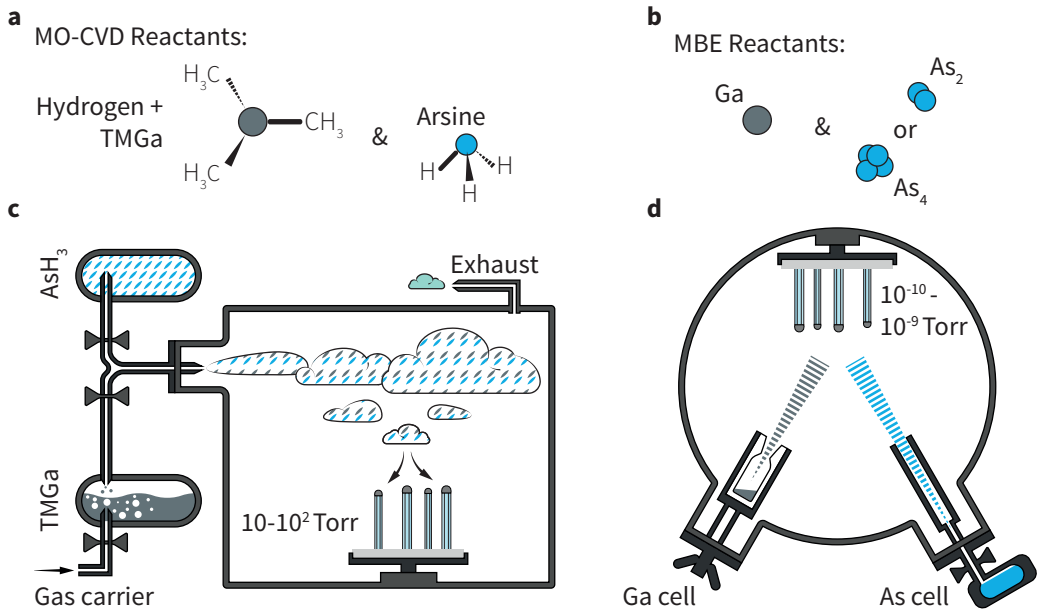

Figure 2.1 • **a.** Usual reagents used to deposit GaAs by metalorganic chemical vapor deposition: trimethylGallium (TMGa) and arsine ASH_3. **b.** Molecular beam epitaxy uses directly gallium atoms and arsenic tetramers or dimers to deposit the material. **c.** Schematic of a MO-CVD growth chamber. TMGa is first loaded in a gas carrier (often hydrogen) before being injected. **d.** MBE growth chamber. The components are send in the form of very low pressure jets toward the growth target.

Nanowires can be grown with MOCVD and MBE following two main routes: selective area epitaxy (SAE), for which a mask with openings is used to allow the growth on selected part of the growth substrate, and vapor-liquid-solid (VLS) growth. The latter is the mechanism used in this work. The basic principle of VLS rely on the mechanism proposed by Wagner and Ellis in 1964 already.[6] They reported about the creation of silicon microwires, for which the growth was catalyzed by gold particles. The three main steps of VLS growth are the following:

1. Catalyst droplets are formed on the growth substrate.

2. The precursors of the growth materials come in contact with the catalyst, and are incorporated in the droplet in solution.

3. When the growth elements reach the supersaturation threshold in the catalyst droplet, precipitation occurs, creating a seed crystal. The NW growth is then sustained by a constant feeding of the materials through the catalyst, but also through diffusion on the substrate and side facets for certain species.

A workflow of a typical VLS growth process (self-catalysed, see below) on silicon wafer is shown in figure 2.2(a). The bottom panel (b) represents the epitaxial growth

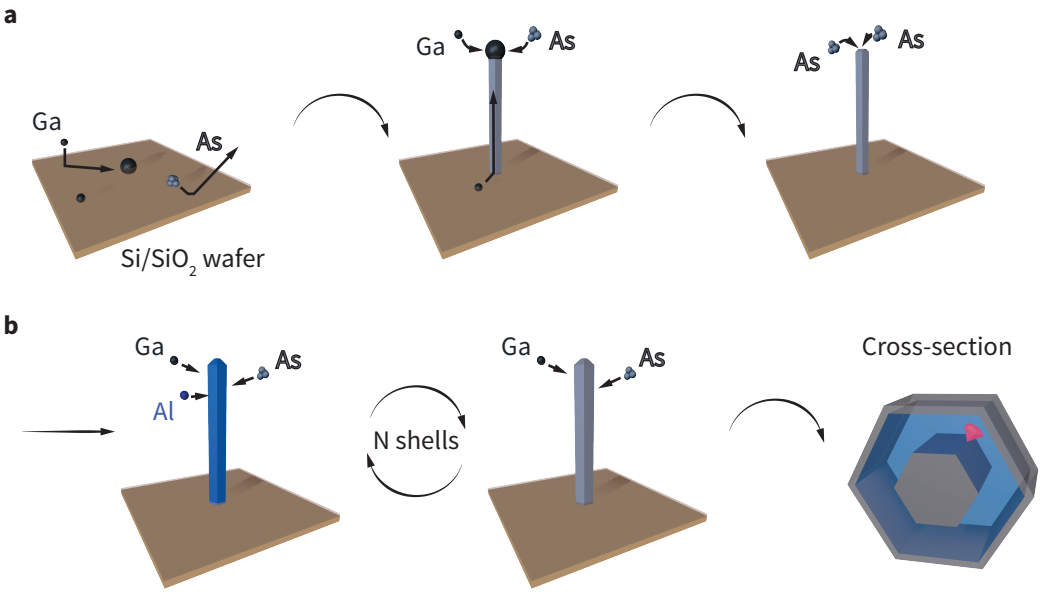

Figure 2.2 • a. MBE VLS growth process of a NW. The first step shows the droplet formation, followed by the actual NW growth and the termination. **b.** Growth process of a radial (multi) shell heterostructure. Epitaxial layers are deposited directly on NW grown following the process in (a).

of, in this case, an aluminum gallium arsenide ($Al_xGa_{1-x}As$, with the shorthand notation AlGaAs) shell. The looping arrows illustrate the fact that several shells can be iteratively grown around the same NW core, typically obtain by VLS during the initial stage of the growth process.

Eventually, gold has become the main catalyst used in NW growth for many compounds and many substrate. Colloidal nanoparticles, thermal dewetting of a thin gold layer or electron-beam patterning of gold nanostructures are as many ways to produce liquid gold droplets, the first step of the VLS process. As convenient as it is, gold can be detrimental if it comes to be incorporated in the semiconductor, either during growth or afterward by diffusion. Since gold atoms act as deep traps, scattering and non-radiative recombination centers for the electronic carriers in certain semiconductors, gold is usually banned from the growth process if the goals are either high carrier mobilities and/or high luminescence yield.

For GaAs NWs, an alternative approach to prevent the inclusion of gold is to use directly gallium as a droplet collector (other metals have also been investigated for GaAs and InAs[33–35]). The method is then devised as follows: the growth wafer is covered by a SiO_2 layer, on which As atoms cannot stick. On the opposite, Ga atoms are trapped on the substrate and start diffusing. Ga adatoms subsequently gather together to form nanodroplets. When the droplets reach a certain size, arsenic starts to be incorporated. For a certain amount of arsenic in solution, GaAs precipitates under the droplet and the nanowires grow.[36] The solubility of As can be evaluated from the

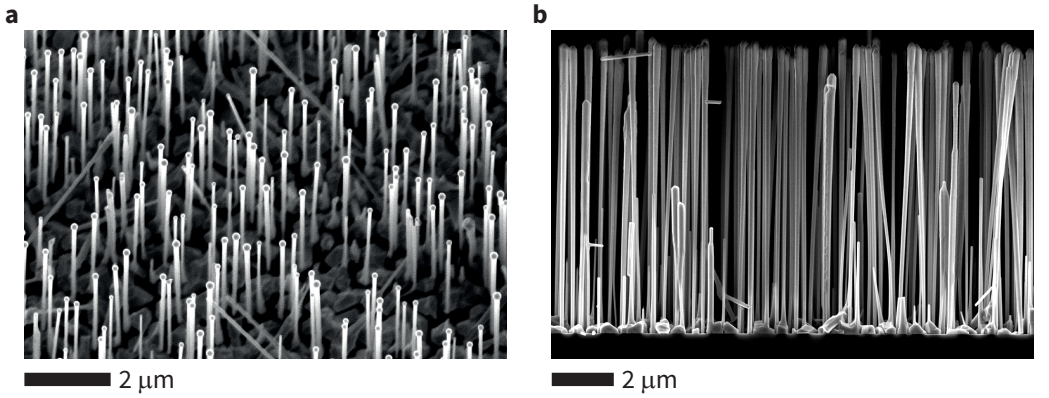

Figure 2.3 • SEM images of NWs grown by gallium-assisted VLS on Si substrates. The growth was done in a MBE system. **a.** GaAs NWs, with their Ga droplet clearly visible at the tip. **b.** GaAs-AlGaAs radial-heterostructure NWs. A clear reverse-tapering is can be noticed. The reverse-tapering is due to a high NW density on the substrate, leading to shadowing effects during the growth.

Ga-As phase diagram for a given temperature, however this evaluation is not strictly correct, as the growth is a non-equilibrium process. This approach, called self-catalysed, catalyst-free or sometimes Ga-assisted growth is more complicated to master compared to Au-catalyzed growth. The use of ready-made colloids or the patterning of a substrate with the catalyst material is not possible, and the catalyst droplet will be affected by a change in the group II flux. Recently, self-catalyzed NWs growth on silicon substrate was successfully realized and Russo *et al.* demonstrated the growth NWs fields with a yield of verticality near unity.[37,38] Another powerful option when growing NWs is the ability to grow radial shells, switching from axial to "2D-equivalent" growth. The shell material can be either the same as for the core or different. For self-catalyzed NWs grown by MBE, the temperature is usually reduced from around 600-700 C to 400-500 C, and the As-flux has to be increased.

The figure 2.3 includes two scanning electron microscope images showing the results of a Ga-assisted growth on Si. In figure 2.3(a), the NWs are regular GaAs wires, and the process was stopped after the growth of the core, without consuming the droplet (corresponding to stopping at the second step in the figure 2.2(a)). The droplets can be clearly distinguished, at the tip of each NW. The right image (b) show a grown sample with GaAs NWs capped with a radial AlGaAs shell. Two main differences in morphology can be observed between the image in (a) and (b) : (i) The droplet at the tip of the NWs is absent for the NWs with a shell, as it was consumed to terminate the axial growth and (ii) the NWs exhibit a noticeable reverse-tapering. The reverse-tapering is a consequence from the high NWs density on the substrate. Since the effusion cells are tilted with respect to the growth substrate, if the NWs are tall and closely-packed they will shadow each other. This results in an increased amount of material deposited around the top part of the wires, while the bases receive

a lower amount than expected if the deposition thickness was uniform.

The possibility to grow epitaxial shells extends further the potential to combine materials and proves to be useful to realize engineered nano-structures.[39–42] These radial junctions can be either shells of different materials (or material compositions), can be made of the same material with different doping, or a combination of both. Hence, this technique allows the obtention of a wide range of structures including p-i-n junctions, "sandwich" quantum wells or remotely δ-doped interface quantum wells for the generation of two-dimensional gas of carriers.

2.1.2 Optical properties of nanowires

Photonic origins

The optical properties of NWs are mainly determined by the properties of the bulk material *e.g.* GaAs in cubic, zincblende (ZB) crystalline arrangement. Quantum confinement is expected to play an important role for GaAs NWs emission only for extremely small diameter. The diameter of NWs grown with self-catalyzed VLS is usually comprised between 30 and 100 nm. This value is much larger than the exciton Bohr radius (around 12 nm) and radial confinement effects can be safely neglected. Deviations from the bulk ZB emission arise from the fact that (i) GaAs can be stable in the hexagonal, wurtzite (WZ) phase and (ii) defects along the NW can form during the growth process, e.g. stacking faults.

For pure ZB GaAs NWs the only deviation from bulk properties is then originating from the strong anisotropy of the nanostructure, few tens of nanometers wide for a length of several microns. This impacts strongly on the interaction of NWs with light fields in the cases where light is absorbed, scattered or emitted. Making the simplification that the NWs are illuminated with a planar wave, and that the light's k-vector is perpendicular to the NW long axis, two main regimes can be differentiated. For NWs with a diameter significantly smaller than the wavelength of excitation , the interaction is said to be in the *quasi-static* regime. In this case, the light field can be considered to be constant inside the NW. If the light is polarized parallel to the NW's long axis, the electric field will not be significantly reduced.[43] However, if the polarization is perpendicular to the NW's axis, the electric field is modified as follows:

$$E_{NW} = \frac{2\epsilon_0}{(\epsilon_{NW} + \epsilon_0)} E_0 \tag{2.1}$$

Where E_{NW} is the electric field inside the NW, ϵ_{NW} is the value of the dielectric function of the NW's material for a given wavelength, ϵ_0 is the dielectric constant of the surrounding medium (usually air or vacuum) and E_0 is the electric field amplitude of the impinging light. From equ. 2.1, it is clear that a strong dielectric contrast between the nanowire and the surrounding medium will lead to a strongly polarized response of the nanowire, with almost no in-coupling for light polarized perpendicular to the wire's axis. In other words, the local density of optical states (LDOS) for perpendicularly

polarized light is strongly reduced. Thus, the coupling strength for transition dipoles radiating light perpendicular to the wire is also dramatically reduced. For this reason, thin wires barely absorb or emit light polarized perpendicularly (the case for WZ is different).

When the value of the wavelength and the NW's diameter becomes comparable, resonant phenomena leads to oscillations in the optical response commonly named *Mie resonances*, *leaky mode resonances* or *whispering-gallery resonances*. The last name is very illustrative and in direct analogy with sound waves bouncing on the walls and looping back in a gallery of whispers. These resonances can be described intuitively as light "bouncing" against the NW's wall because of partial internal reflection. If the wavelength is such that the incoming light can interfere constructively in the NW, the conditions are resonant and the optical cross-section is strongly modulated.[44–48] As the diameter of the NW increases, higher order modes can oscillate in the structure for a given wavelength.

The figure 2.4 presents the optical response of an infinitely long GaAs nanowire in vacuum illuminated by a plane wave incoming perpendicularly to the wire's axis. The color plots show the relative optical cross-sections for scattering (top row) and absorption (bottom row) phenomena in function of the wavelength and wire diameter for light polarized parallel (left) and perpendicular (middle column). The right column shows the optical anisotropy P_a defined as

$$P_a^\lambda = \frac{I_{||}^\lambda - I_\perp^\lambda}{I_{||}^\lambda + I_\perp^\lambda} \tag{2.2}$$

Where $I_{||}$ ($I_\perp$) are the intensities parallel (perpendicular) to the NW and directly proportional to the cross-sections. The superscript λ emphasizes the dependence on the wavelength.

For small wire diameters, the Mie model converges toward the quasi-static results, with a strong anisotropy along the wire. For larger wires, the response oscillates, and in particular, the anisotropy can be balanced or even reversed. The oscillations are stronger above 850 nm for the scattering cross-section, while they are absent for the absorption. This is of course linked to the 870 nm (1.42 eV) room temperature bandgap of GaAs (indicated by dashed white lines in figure 2.4). The wire cannot absorb light above 870 nm (at least by creation of electron-hole pairs) and for scattering, the light absorption at lower level strongly damps the optical oscillation, reducing the contrast between resonant and non-resonant conditions.

In any case, the shape anisotropy usually gives rise to an optical polarization anisotropy, also in emission (photoluminescence experiments), generally called *antenna effect*. This effect can be noticeable and must be accounted for, as can be seen in chapter 6. For light emitted from within the NW, the problem is more complex as the exact position and dipole orientation of the emitter will also influence the measurement.

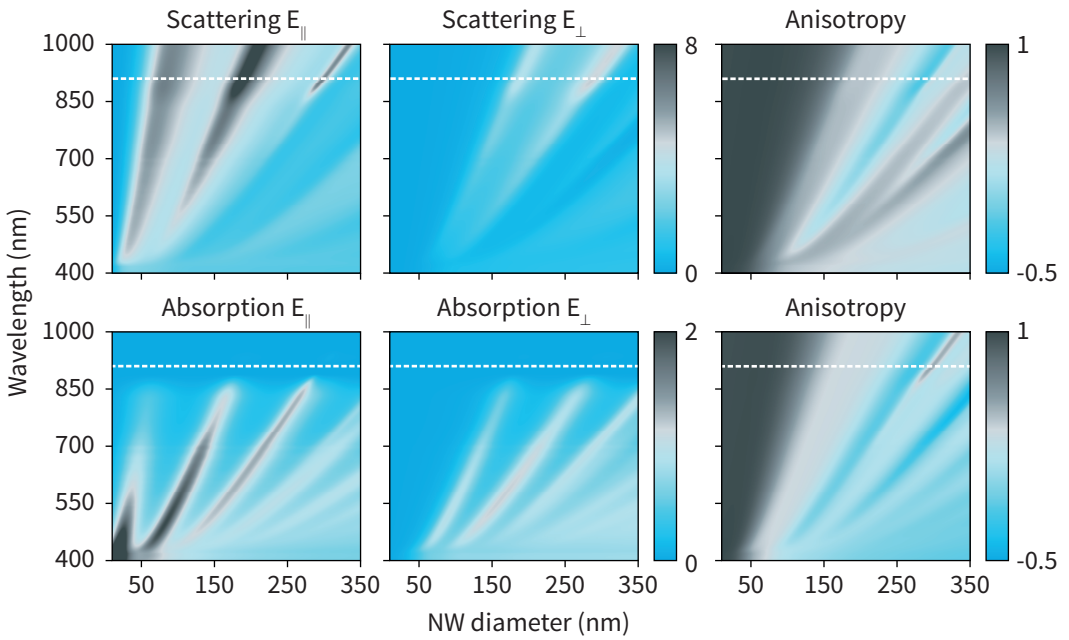

Figure 2.4 • Calculated scattering (top) and absorption (bottom row) cross-section of an infinitely long, cylindrical NW in vacuum illuminated by a monochromatic plane wave at normal incidence. The right column shows the optical anisotropy in the two cases. For small wire diameters (long wavelength), the quasi-static approximations hold. For comparable wavelengths and diameters, a serie of resonant modes modify the optical response.

Another important particularity of NWs emitting or excited at optical wavelengths is the ability to act as waveguides. Light coupled to a guided mode of a NW will travel along the axis. Depending on their diameters, NWs can host multiple modes, classified using the waveguide terminology (transverse electric or magnetic TE and TM, hybrid HE or EH). If the ratio of the diameter and the wavelength is high enough (generally for NW diameters above 100 nm), high order modes with different modal structures can be guided.[49,50] Regardless of the diameter, the fundamental guided mode HE_{11} will always be present since there is no cutoff frequency for this mode. The inset (a) of figure 2.5 represent the transverse electric field distribution within a cylindrical wire for the fundamental HE_{11} mode and the higher-order, HE_{21} mode. Notice that the fundamental mode naturally possess a gaussian profile, and is linearly polarized, which in turn makes it ideal to use for most of the photonics applications. Two cases are making guided modes in NWs particularly interesting:

Reflection at the NW end facets If the end facets are flat and smooth, guided light can be reflected back and forth along the nanowire. This corresponds to the typical case of a Fabry-Perot resonator, with the two end-facets acting as two mirrors. Such a behavior is likely to be observed mainly for light with an energy

below or close to the bandgap. Indeed, for light at higher energy the probability of absorption, already high, increases with every round-trip. The peak spacing is representative of the length of the nanowire, and the spacing non-linearity can be attributed to the dispersion of light in the material. This type of resonance is particularly interesting for NW-based nano-lasers, as already demonstrated with several materials.[30,51,52]

Out-coupling from a guided mode In this case, the light is radiated from the end facet of the NW. If the facet is flat, a portion of the light will be reflected (see above), and the escaping light will be scattered in spherical waves. If the NW is engineered in such a way that the wave is said to be *adiabatically out-coupled*, the mode will be smoothly expanded while it propagates toward the wire's end, and will be released without significant scattering or back-reflection.[53,54] As depicted in figure2.5(b), this behavior can be obtained by shaping the wire either as a tapered waveguide (with a needle shape) or in a reverse-tapered way (trumpet shape).[55–57] The main difference between the needle and trumpet shape is which medium the mode is expanded in. For needles, the mode develops mainly out of the NWs, while for the trumpet it is expanded in the material, and an additional anti-reflection coating is then a requisite to prevent back-reflection. NWs with these geometries demonstrated excellent out-coupling properties, transmitting to free-space a significant fraction of the emitted light. In addition, the shape of the mode is preserved and if the wire is made asymmetric, the degeneracy of the orthogonally polarized HE_{11} modes can be lifted.[58,59] Non-degenerate modes are useful in order to produce streams of photons with a strong linear polarization.

The pencil/trumpet geometry proves to be notably useful when any high out-coupling efficiency is required. For most planar substrates, total-internal

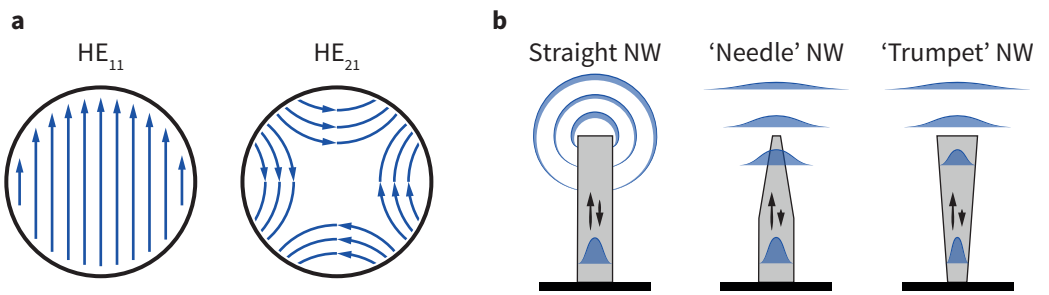

Figure 2.5 • a. Electric field-lines in the cross-section of a cylindrical waveguide. The fundamental (left) and a higher order mode (left) are represented. **b.** Different geometries for light out-coupling with NWs. The tapered (needle) and reverse-tapered (trumpet) geometries are particularly efficient as light scattering at the top of the wire is greatly reduced, resulting in very directional emission with a gaussian profile.

reflection strongly reduces the transmission of light from the substrate to free-space, hindering a high detection efficiency. This ads up to inherent losses in optical detection systems. For a general purpose experimental setup, one can reasonably expect a transmission coefficient of around 0.25 between a perfect emitter, with unity out-coupling efficiency and the obtention of a (single-mode) photon stream. Taking into account imperfect yet realistic detectors and a realistic emitter in a planar sample, the detection efficiency usually get reduced to around 10^{-2} - 10^{-3}. If these low values are usually acceptable for time-integrated measurements and large samples, they become problematic if either the timing is shortened or the signal intensity is reduced. When dealing with single emitter, such as a color center, a molecule or a quantum dot, the signal is inherently reduced compared to bulk samples. If the goal is to trigger single photons on demand, the fidelity of the system is directly connected to the transmission to the detector. Triggering the emission of single photons can be used *e.g.* to entangle photons coming from different sources. In such a scheme, the two emitters are excited simultaneously, and the two resulting photons are to be entangled on a beamsplitter. Considering low value of transmission, the probability to get an entanglement event is the joint probability to get one photon from each emitter after a pulse and can easily get as low as 10^{-6}. For a MHz repetition rate excitation laser, this means one successful operation per second, already in the noise of the best detectors. Considering that the probability scales with the power of the number of emitters, it quickly becomes vanishingly small.

In order to mitigate this problem, significant efforts have been made to increase to out-coupling efficiency of emitters, either by reducing the dielectric contrast at the sample surface, using solid-immersion lenses (similar technology than for commercial LEDs) or designing optical micro- and nano-cavities.[60–65] Cavities allow to (i) modulate strongly the lifetime of light emitters, in such a way that more photons/second can be radiated, and (ii) funnel the light emission into the resonant mode(s) of the cavity. The reduction of the lifetime offers not only the benefits of a faster source, but also of an improved photon indistinguishability.[66] The lifetime reduction is a direct cause of a modification of the LDOS and is linked to the cavity mode-volume V and quality factor Q through the Purcell effect, with a rate enhancement F_p :

$$F_p = \frac{3}{4\pi^2}\left(\frac{\lambda}{n}\right)^3 \frac{Q}{V} \tag{2.3}$$

With λ the wavelength of the emitter, n the refraction index of the material. Modern micro-cavities like micropillars and microdisk boast Q-factors above 10^5 and 10^6 respectively, for modal volumes around 10^{-1} and and 10^{-2} $(\lambda/n)^3$.[67] Nano-cavities like defects in photonic crystals show Q-factor in the order of 10^4 - 10^5 and modal volume around 10^{-2} $(\lambda/n)^3$.[68,69] Tighter confinement can be obtained with plasmonic based cavities, at the expense of a decrease in the quality factor due to ohmic losses.

If the cavity is properly designed, funneling photons through one well defined mode also allows to significantly improve the out-coupling efficiency. However the design of cavities is a complicated and delicate task. In addition, it often relies on chance to obtain a single emitters positioned at the cavity field maximum even if some techniques have been developed to deterministically design the cavity around a predefined emitter.[70,71] Furthermore, the generalized use of etching techniques for fabrication tends to damage the semiconductor material hosting the emitters, with adverse effects on the temporal stability of the emission. Finally, resonant cavities with very high Q-factors do not allow to efficiently out-couple different optical transitions, like the excitonic and biexcitonic transitions from a QD, hindering their use for schemes based on the biexciton-exciton cascade, and possibly locking the QD in the biexcitonic configuration for long times.

For these reasons, using directly NWs as mediators between an electronic excitation and photons is specially interesting: the photons can be efficiently coupled to a guided mode, with a moderate and wavelength non-selective Purcell enhancement.[72] The light can then be easily propagated in free space. In addition, bottom-up assembly of NWs allows for smooth side facets and eventually defect-free crystals, reducing surface effects. Alternatively, a NW lattice can be used to form photonic crystals, thus acting collectively as a resonator.[73–75]

Electronic origins

Another particularity of NWs optical properties lies in their band structure. As briefly said at the beginning of the chapter, the diameter of NWs grown following the catalyst-free VLS route is usually too large to give rise to radial quantum confinement. Still, other (quantum) effects tightly linked to the nanowire dimensions can be observed.

The first one pertains to the crystalline phase of GaAs (and happens with many other III-Vs semiconductors). The bulk phase, stable at all dimension is ZB, with a bandgap energy of 1.51 eV at 10K. The second phase, found in NWs, is WZ. The bandgap at low temperature has been the subject of a controversy for several year.[9,33,76–78] Resonant Raman spectroscopy yield an energy comparable to ZB, however, the excitonic energy for the two phases might differ slightly.[79,80] The two different phases are represented as projection on the (110) axis, corresponding to the crystalline family of the NWs facet in figure 2.6(a), where the Ga atoms are represented by closed grey symbols while the As atoms are represented by closed blue circles. Because the difference is limited to a change in the stacking sequence, a NW can change phase during growth. The resulting polytypism give birth to homojunctions with a type-II band alignment. The panel (b) of figure 2.6 shows on the upper row a drawing of a NW starting in the WZ phase, then changing to the ZB phase and alternating in short sequences. The last orange dash represents a stacking fault, i.e. a single layer with a different stacking configuration. In this case, the phase does not change, but stacking faults can still introduce defects in the bandgap, responsible for the scattering of carriers in transport experiments, and for redshifted peaks in the photoluminescence spectra. The bottom row of figure 2.6 shows the

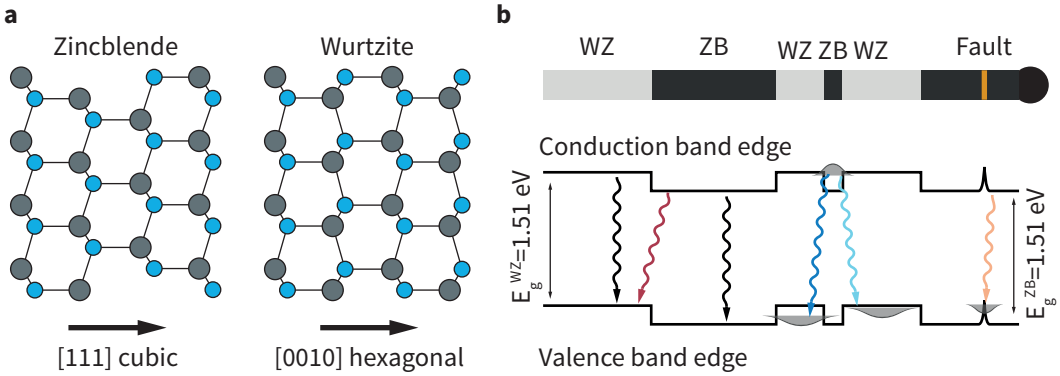

Figure 2.6 • a. Projection along [110] of the two stable structures of GaAs: zincblende (left) and wurzite (right). For both structures, Ga (As) atoms are represented in grey (blue). **b.** Schematic representation of homojunctions and different confinement effects for a wire composed of both WZ (light grey) and ZB (anthracite) segments and their effect on the luminescence. Additionally, a defect, *e.g.* composed of a single stacking fault, can also locally modify the luminescence signal (here in orange). For short segments, quantum confinement creates sublevels, here pictured as grey wavefunctions, which can be populated by electrons (holes) in ZB (WZ)

band-edge diagram associated with the nanowire drawn above. The type-II band alignment leads to red-shifted photon emission. If the segment are short enough, carrier confinement in the segment can take place for either electrons (in ZB) or holes (in WZ). Electronic sublevels are formed and can be populated. This translates to the emission of photons with variating energies depending on the length of the segment.[11,81] The complementary carriers will be weakly bound to the confined carriers because of band bending and Coulomb attraction, but like simple homojunctions, they will be spatially separated (spatially indirect excitons).

Moreover, the different conduction band symmetries for ZB and WZ lead to a difference in the allowed transition dipole orientations. Because of its symmetry, the cubic ZB phase allows for an equally strong recombination for dipoles in the plane perpendicular to the wire axis and along the NW axis. On the opposite,the Γ-point symmetry of the WZ phase forbid the recombination of dipoles oriented along the NW axis. Thus, optical anisotropy of electronic origin in both absorption (at least close to the band-edge) and emission is absent for ZB, but strong for WZ.

The band symmetry anisotropy combines with the previously described photonic antenna effect and strongly reduces the optical excitation and detection for thin WZ NWs.

2.2 Quantum dots

QDs are stemming from the efforts made in the last decades to create artificial, engineered, heterostructures and aiming to control electrons and holes at the

nanoscale. The complexity of heterostructures evolved from bulk heterojunctions to quantum wells (QWs) and quantum wires (Qwires). The underlying idea was to be able to modify at will the band-structure of materials and thus toaloow the discovery of new functionalities. The possibility to engineer and harness quantum states for technological purposes opens new doors in computing, light emission and energy harvesting. This technological goal has to be greatly accounted for the progress made in this field.[82] QDs represent heterostructures with the lowest achievable dimensionality, as the carrier wavefunctions are confined in three dimensions. The particular properties of QDs come directly from the major modifications in the density of electronic states due to tridimensional confinement, as described in the chapter 1 and illustrated in figure 1.1. The discreteness of the electronic levels and the sharp optical transitions stemming from QDs earned them the name of *artificial atoms*. Yet, this description can be misleading as many differences exists between atoms and QDs. By definition epitaxial QDs are embedded in a crystalline matrix and several effects emerge from the interaction between the quantized states and the continuum.

QDs are by far not exclusively based on the confinement of electrons *and* holes in a material, or within the bulk of a matrix. A very active field is using electrostatically-defined QDs created by the depletion of a 2DEG by metallic gates. Another type of QDs, colloidal QDs, are synthesized by chemical means and are now widely used in biology (labeling), and regarded as a competitive technology for next generation displays and light-emitting devices. The discussion hereafter focuses only on epitaxial QDs, defined as optically active 0D heterostructure, of predominantly of type-I, in a bulk matrix.

2.2.1 Fabrication of optically active epitaxial quantum dots

The fabrication techniques are relying on similar deposition processes used for NWs. The main difference is the paramount use of MBE over CVD techniques. This usually results in structures with extremely high quality and well controlled dimensions. Arguably, the most developed QDs systems are three, chronologically:

Interface fluctuation The QDs consist of a very localized fluctuation in the number of layers composing a QW. The local decrease in the confinement potential strength allows the confinement of excitons. Both are strongly confined in the growth direction, but weakly confined in the plane of the QW. Only the center of motion of the exciton participate to the lateral quantization effect. For this reason, interface fluctuation QDs are said to be in the *weak confinement* regime.[22,83,84]

Stranski-Krastanov The main type of QDs grown epitaxially, Stranski-Krastanov (SKQDs) rely on lattice mismatch to form small islands of, *e.g.* $In_xGa_{(1-x)}As$ in a GaAs (sometimes $Al_xGa_{(1-x)}As$) matrix.[85,86] Usually, the growth begin with sequences of GaAs buffer layers to isolate the SKQDs from the growth

substrate. Following that, InAs is deposited, and, at a certain thickness (few monolayers) will lead to the formation of dome or pyramid-shaped InAs islands. The thin primitive InAs layer will stay and form the *wetting layer*, behaving like a narrow QW directly below the QDs. Strain is providing the driving force for the QDs nucleation and the formation of In(Ga)As pyramids or domes. The structure is then capped with GaAs. The residual strain fields existing few nanometers on top of the capped QDs can be used as stressors to guide the alignment of other layers of SKQDs, allowing the formation of QD-molecules. As a result of the growth mechanism, SKQDs are highly strained structures, which in turn affects the electronic structure. Growth variants, including 2DEG below and GaAs-AlGaAs superlattices above the SKQD layer allows to embed the QDs in a Schottky diode structure. Another important tweak is the implementation below and above the QD layer of GaAs/AlGaAs stacks acting as Bragg reflectors. Those structures effectively embed the QDs in a planar Fabry-Perot cavity, hence modifying their radiative properties.

Droplet epitaxy Because strain is the driving force for Stranski-Krastanov processes, SKQDs cannot be grown with the almost completely lattice matched GaAs-AlGaAs system. To overcome that, a recent technique, droplet epitaxy, can be used.[87–89] This technique, very similar to the initial phase of NWs growth, relies on the formation of Ga droplets AlGaAs epilayer. The droplets are then solidified with arsenic, leading to the formation of GaAs crystallites. Subsequently, the GaAs crystallites are capped with AlGaAs. This technique marks the comeback of the GaAs-AlGaAs tandem for QDs. Unlike interface fluctuations QDs, droplet epitaxy QDs are operating mainly in the strong confinement regime, and can be fabricated with or within wetting layer, which can prove to be beneficial in certain cases.[90,91]

These three main type of QDs can be seen in figure 2.7. The panel (a) shows potential interface fluctuation QDs in a narrow GaAs QW, imaged with a scanning tunneling microscope (STM) during the QW growth.[22] The contrast in the image comes from atomic steps at the interface. The panel (b) shows a cross-section of SKQDs (dark half-domes) layers grown on top of each other, self-aligned by the residual strain field after the capping of QDs in GaAs. The wetting layer can be seen as a basal darker stripe, in particular under the first QD layers. The imaging was done using transmission electron microscopy (TEM).[92] The third kind of epitaxial QDs described above can be seen in figure 2.7(c). It shows an atomic force image of a droplet epitaxy GaAs QD grown on a [111]B GaAs substrate (yellow dome). The image was realized on a uncapped sample, and the height of the quantum dot is recorder during the AFM scan.[93] As it can be seen, droplet epitaxy growth on a substrate with a highly symmetric orientation allows to obtain QDs that possess, in turn, a very high symmetry. This is an

important, long sought result as it allows to enhance the characteristic of the quantum states confined within the QD (as it will be discussed in 2.2.2). A comparison of these three examples of epitaxial QDs gives the opportunity to realize the difference in size (in particular, lateral size) of the structure and confining potential. While the lateral dimensions of SK and droplet epitaxy QDs fall below 40nm, the interface fluctuations imaged in figure 2.7(a) can reach dimensions in the 100 nm range. This visually explains why interface fluctuation QDs do not usually operate in the strong confinement regime: the exciton, while strongly confined in the growth direction (normal to the image), can spread significantly in the plane of the QW.

Apart from these three methods, many other techniques and derivatives can be used to grow QDs: either strain-driven *via* underlying stressors, local etching and filling of an AlGaAs substrate or pre-patterning and segregation-assisted methods.[94–96] Different materials can also be used, either III-V or wider gap II-VI and nitride-based materials. Finally, the pre-patterning of growth substrates in order to obtained position-controlled QDs is also yielding highly interesting results. As an example, the optical quality of QDs grown on reverse-pyramid as improved.[97–99] Furthermore, a reverse-pyramid QDs design allows to use either lattice-matched (GaAs/AlGaAs) or mismatched (InGaAs-GaAs) couples.The benefits of having deterministically positioned QDs is inestimable, as it allows to think about making on-chip photonics interconnects between the (coupled) QDs and ultimately scale-up quantum systems to a size hardly achievable in the present conditions.

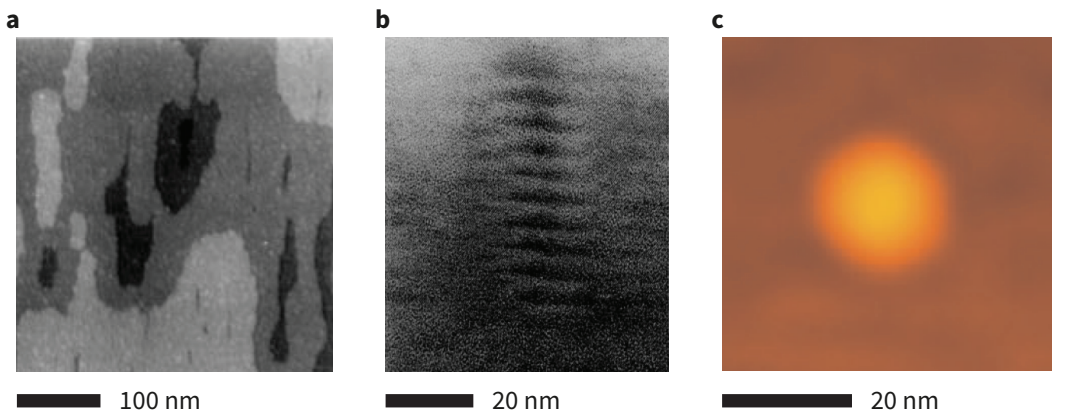

Figure 2.7 • a. STM image of a QW interface, showing monolayer steps, locally leading to a relaxation of the QW potential (adapted from ref. 22). **b.** TEM micrograph of SKQDs. Several layers are grown sequentially, and the sample is imaged as a cross-section (adapted from ref. 92). **c.** AFM scan of an uncapped GaAs QD grown by modified droplet epitaxy. The QD symmetry can be seen to be very high. (Adapted from ref. 93)

2.2.2 General properties of quantum dots

Confined states in quantum dots

The optical properties of semiconductor QDs are governed by the electronic level structure of the QDs. Calculating exactly the electronic levels of QDs is generally a very challenging task, given the intermediate size of the heterostructure and the multiple factors influencing the energy of these levels (such as many-body effects, strain, piezoelectric field etc). In order to picture the level structure, the discussion will be based on the typical idealized QD: a flat cylinder of narrower-bandgap material embedded in a wider-bandgap matrix. This geometry describes relatively well generic epitaxial QDs and axial QDs in NWs, as they tend to be flattened in the growth direction. The figure 2.8(a) shows this sample geometry, with the QD (dark grey) in a wider bandgap matrix (light grey). The band-edge diagrams along the strong confinement axis and perpendicular to it are drawn as cuts.

In this case, the confinement in the z direction is strong, and for both electrons and holes, only the first level can be confined within the QD. This level is split in a manifold of sublevels because of the (weaker) lateral confinement. These sublevels can be labeled with quantum numbers (in the very same way as atomic or molecular physics). The eigenstates energy associated with these sublevels scales with increasing quantum numbers, essentially similarly to atomic system.

n The radial quantum number, with values {0, 1, 2, 3 ...}

l The (orbital) angular momentum quantum number, with values {0, ±1, ±2, ±3 ...}

The lowest level, with quantum numbers (0,0), is commonly called the *s-shell*, because its symmetry is analogous to s-shell electrons in atomic systems. The two states with quantum numbers (0,±1) are degenerate in energy (due to symmetry), and form the *p-shell*. Further, the *d-shell* is composed of the triply-degenerate (1,0) and (0,±2) states. For very small QDs with moderate barrier height (the case of few-nanometers GaAs QDs in AlGaAs for example), the p-shell and, *a fortiori*, the d-shell states eigenenergies are more important than the barrier height and these states are delocalized in the matrix continuum.

As said previously, these sublevels exist theoretically for each band in the semiconductor. The sublevel structure of a strongly confined QD is represented in the panel (b) of figure 2.8. The QD potential is represented as being a "hard-wall" potential, but the arguments hold for different potential landscapes. The drawing represent the electron ground and the triply degenerate first excited state (labeled as s-shell (e) and p-shell (e)). Heavy hole states are similarly represented. For light holes, only the ground state is drawn (dashed line).

In the following part, the focus is set on the couple GaAs and AlGaAs with 42% of aluminum if not specified otherwise (corresponding to the direct-indirect crossover

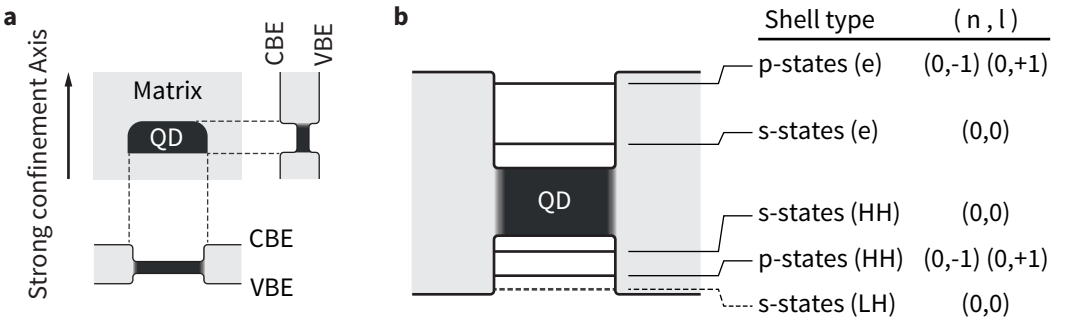

Figure 2.8 • a. Generic QD (dark grey) in a matrix (light grey), forming a type-I 0D heterostructure. Cuts along and perpendicular to the growth axis show the shape of the potential for electrons (CBE) and holes (VBE). **b.** Scheme of a QD representing the different confined levels for electrons (e), heavy holes (HH) and light holes (LH). The radial and angular momentum quantum numbers of the single particles are represented for the different states.

concentration as well as the energy maximum of the conduction band edge). For direct band-gap material like GaAs, the main bands at the high-symmetry Γ point are the electron conduction band and the heavy, light and split-off hole valence bands. In the bulk, the heavy and light hole (HH and LH) bands are degenerate at the Γ point, while the split-off is shifted down by several hundreds of meV (340 meV at room temperature) due to spin-orbit and crystal-field interaction. For this reason, optical transitions between the conduction and split-off band is extremely weak, even in the bulk. For a GaAs QDs in an AlGaAs matrix, the maximal energetic barrier for holes is around 100 meV. Thus, split-off holes cannot be confined and exist as delocalized states.

In addition, the energy of the sublevels associated with a particular band will vary with the effective mass of the carrier: $E^c_{band} \propto \frac{1}{m^{band}_{eff}}$. For a given confinement potential, the confinement energy will then vary for carriers belonging to different bands. The effective mass ratio between the heavy and the light hole in GaAs is $\frac{m^{HH}_{eff}}{m^{LH}_{eff}} = \frac{0.51}{0.082} \approx 6$. As a result, HH-LH degeneracy is lifted and the LH states are down-shifted, with an energy splitting ΔE_{HH-LH} generally in the order of 100 meV. This energetic splitting allows to neglect the LH states most of the time, and consider the simplification where the hole ground-state is purely of heavy-type. This simplification is not always justified: strongly elongated or asymmetric structures and certain strain states can induce a significant mixing of the LH and HH characters. Strain is a particularly complicated case as it can lead to mixing, or if engineered so restore the pure character.[100,101] For sake of simplicity and because most of the physics is captured, the quantum states in a QD are usually described based only on electron and HH.

A missing ingredient in the discussion developed above is the spin of the carriers.

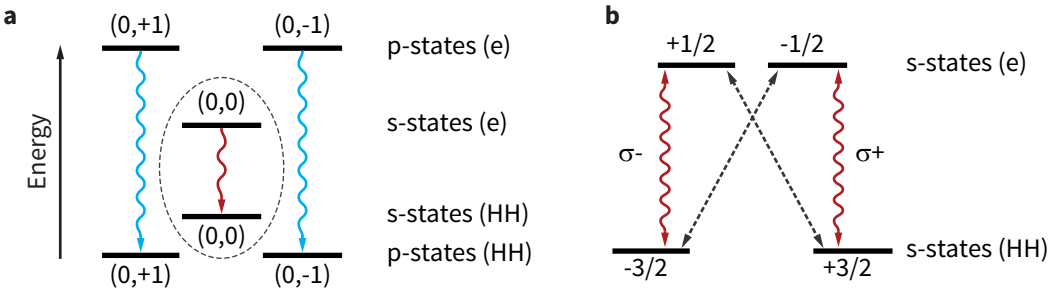

Figure 2.9 • a. Summary of the allowed shell-shell optical transitions (wavy arrows represent allowed transitions. Transitions are only allowed between shells of the same type. **b.** Selection rules including spins for the s-shell transition (circled states in (a)). The red, wavy arrows stand for allowed transitions, while dashed-anthracite arrows represents forbidden ("dark") transitions.

Electrons and holes, being fermions, possess a half-integer spin, with spin-projection $s = \pm\frac{1}{2}$. Thus, for each state previously described, two configurations are possible: spin-up or spin-down. Because of Pauli's exclusion principle, two particles with the same spin cannot occupy the same electronic level. Hence, each state corresponding to a set of (n,l) can be occupied by maximally two carriers with opposite spins.

Selection rules

Optical transitions are not allowed between all the electron and hole sublevels. Additionally, the role of the carriers spin is also critical. Photons do not have spins, so the difference in spin-projection between an electron and a hole recombining should be null. Similarly, circularly polarized light has an angular momentum of $\pm\hbar$ (per photon). Thus difference in total angular momentum (j_z) between an electron and a hole should match in order to radiatively recombine. The rules are summarized as:

$$\begin{aligned} \Delta s^{e-h} &= 0 \\ \Delta j_z^{e-h} &= \pm 1 \end{aligned} \tag{2.4}$$

The total angular momentum depends on several momenta associated with (i) the internal angular momentum of the band considered, (ii) the orbital angular momentum of the particle (l) and (iii) of its spin angular momentum. Taking that into account, the electron total angular projections are $\pm\frac{1}{2}$ while the HH total angular projection j_z can be either equal to $\frac{3}{2}$ or $-\frac{3}{2}$. For the LH, $j_z = \pm\frac{1}{2}$. Keeping this in mind, we can figure out the dipole-allowed optical transitions between the electron and hole states of a QD. It is important to notice that these optical selection rules hold completely for symmetrical QDs. In the case of asymmetry, forbidden transitions can become at least partially allowed due to state mixing. The possible optical transitions in the ideal case are described in figure 2.9. In figure 2.9(a), the possible optical transitions between the shells are marked with wavy arrows. Direct radiative recombination is only

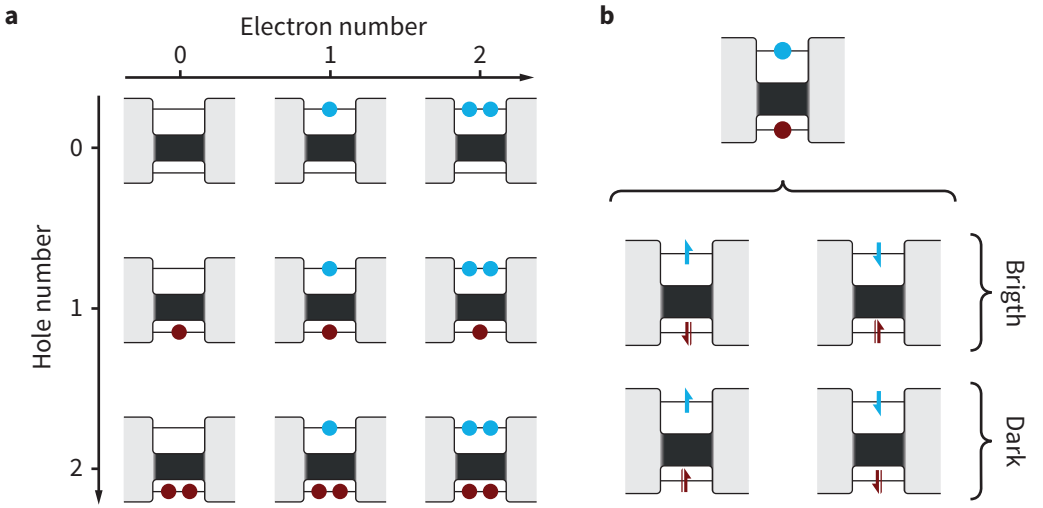

Figure 2.10 • a. Schematic of the occupation configurations for a 2-level QD , from a empty (up, left) to a fully occupied QD (down, right). In this case, the spin degree of freedom is not taken into account. **b.** Example of different spin configurations for a QD confining one electron-hole pair (exciton). The orientation of the arrows represent the spin projection. Single (double) arrows stands for electrons (holes). The bright and dark excitons (see figure 2.9(b)) are indicated by the right parenthesis.

possible between electron and hole shells of the same type (same quantum number), *e.g.* p(electron)-p(hole). Otherwise, the orbital angular momentum is not conserved and the transition is forbidden, as for *e.g.* p(electron-s(hole). In a photoluminescence spectrum, this will translate in a group of peak corresponding to transitions between s-shell states. If p (d) -shell states can be confined for both electrons and holes, a second (third) group of peaks will appear for high excitation intensities, blue-shifted of several tens of meV with respect to the s-shell transitions.

The relaxation of the carriers between excited states (d, p etc.) and the ground state of the single-particle (s) is usually a fast process, mediated by low-energy acoustic phonons. Hence, in order to record an optical signal from the p-shell, the s-shell has to be filled. This explains why higher shell emission is mainly observed at high excitation power. Even in the case of the generation of optically polarized carriers (for example all the electrons with spin-up, done with circularly polarized light), the interaction with the solid will induce spin-flip processes and at thermal equilibrium will allow the single-particle ground states to be fully occupied.

Charge states of a two-level quantum dot

The multiplicity of different electronic configurations in a QD can give rise to a rich emission spectrum, in particular if excited levels are considered. The identification of the exact states emitting light is further complicated by different aspects witch will

influence the exact energy of recombination. The first one is the material forming the QD, which can be a ternary or quaternary alloys with changing material parameters. The second is the exact size and shape of the QD. Finally, the presence of strain or built-in electric fields can lead to a reorganization in the electronic hierarchy.

Even focusing exclusively on a two-level QD, *i.e.* the ground electron and HH s-shell levels, several configurations can be expected depending on the number of carriers inside the QD. A set composed of a single electron and hole confined in a dot will interact, primarily *via* the Coulomb attraction (see subsection 2.2.2), and will form a bound electron-hole pair: an exciton (X). In this elementary case, possible configurations for each single-particle states are either spin-up or -down. So the four possible X configurations are (see also figure 2.10(b)):

$$\begin{aligned} &|\uparrow\Downarrow\rangle \\ &|\downarrow\Uparrow\rangle \\ &|\uparrow\Uparrow\rangle \\ &|\downarrow\Downarrow\rangle \end{aligned} \tag{2.5}$$

Neglecting the spin orentiations, a two-levels QD can be in nine different carrier configurations (figure 2.10(a)). If the spin of lone electrons/holes is taken into account, 16 different configurations can be counted. The trivial case is if no carriers are present in the QD. In this case, the QD is said to be empty, or in its ground state [1]. Following that, a two-level QD can be loaded with a maximum two electrons and 2 holes, independently. This is represented in figure 2.10(a). The panel (b) of the same figure represent the different spin configurations in the case of a QD loaded with only one electron and one hole. The spin degree of freedom is, in this case, maximal since both electron and hole can be spin-up or -down. In figure 2.10(b), the four cases written in the list 2.5 are grouped by two: the bright and dark excitons. This is exactly what was discussed in the section on selection rules and can be seen in the figure 2.9(b).

In order to be able to recombine radiatively, the QD must be in configuration including at least one electron and one hole with antiparallel spin orientation. Thus four out of the nine possible configurations can radiate light:

Exciton (X) one electron + one hole with anti-parallel spins, transferring the QD into its GS after a photon emission.

[1] *caveat*: The QD ground state (GS) should not be mistaken for the single-particle ground states. In the first case, the GS refers to the lowest energy state of the complete QD system, *i.e.* the lowest-energy state for all the possible configurations or the QD. In the single-particle picture, the GS represents the lowest-energy state of a confined electron (or hole). To summarize, if both an electron and a hole occupy their respective GS, the QD is in an excited state (first excited state).

Biexciton (XX) two electrons + two holes, transferring the QD into the X state after photon emission.

Positively charged exciton (X^+) one electron + two holes, also called positive trion, transferring the QD into the 1-hole state after photon emission.

Negatively charged exciton (X^-) two electron + one holes, also called negative trion, transferring the QD into the 1-electron state after photon emission.

With the sole consideration of the single-particle energies, all these optical transitions would radiate photons at the same energy. The next subsection will discuss the effects that lift this degeneracy.

Coulomb interactions in quantum dots

In the simple, single-particle description, all the radiative transitions should occur at the same energy. This is generally not the case and for an optical spectrum showing the four transitions, a discrete energy shift (meV range) between the X and the other complexes will be noticed. This shift is normally called "binding energy", and measured with respect to the X transition energy. The shift results from the different carriers-carriers interactions for different QD filling. These interactions can be separated in three categories: direct Coulomb interactions, the exchange and the correlation energies. All are much weaker than the confinement energies for small quantum dots. Considering that the exchange and correlation energies are rather weak and complex to describe compared to the direct Coulomb interactions, only the latter are described hereafter.

The Coulomb effect is based on the simple picture that two particles (i and j) of opposite or same charges will attract each other, or conversely repulse each other and thus lower or rise the energy of the system. If in a coarse approach the Coulomb terms for the electron-hole, electron-electron and hole-hole energies are considered to be V_{eh}, V_{ee} and V_{hh}, the energies for the different states involved in optical transitions (exception made of the QD GS) can be expressed as the product of a matrix of interaction coefficients and the vector of the different energies:

$$\begin{pmatrix} E_{1e} \\ E_{1h} \\ E_{1e1h} \\ E_{2e1h} \\ E_{1e2h} \\ E_{2e2h} \end{pmatrix} = \begin{pmatrix} 0 & 1 & 0 & 0 & 0 & 0 \\ 0 & 0 & 1 & 0 & 0 & 0 \\ 1 & 1 & 1 & 1 & 0 & 0 \\ 1 & 2 & 1 & 2 & 1 & 0 \\ 1 & 1 & 2 & 2 & 0 & 1 \\ 2 & 2 & 2 & 4 & 1 & 1 \end{pmatrix} \cdot \begin{pmatrix} E_{gap} \\ E_e^{sp} \\ E_h^{sp} \\ V_{eh} \\ V_{ee} \\ V_{hh} \end{pmatrix} \tag{2.6}$$

With the subscript describing the charges in the QD. From there, the optical transition energies can be calculated:

$$\begin{pmatrix} E_X \\ E_{X^-} \\ E_{X^+} \\ E_{XX} \end{pmatrix} = \begin{pmatrix} E_{1e1h} \\ E_{2e1h} \\ E_{1e2h} \\ E_{2e2h} \end{pmatrix} - \begin{pmatrix} 0 \\ E_{1e} \\ E_{1h} \\ E_{1e1h} \end{pmatrix} \tag{2.7}$$

The binding energy for an exciton complex is usually described as the difference between the energy of the transition of this complex and the X energy: $\Delta E_{*-X} = E_* - E_X$. A schematic representation of the energy levels for different QD charge configurations can be seen in figure 2.11(a), plotted in function of the total number of carriers in the QD. In this case, the bandgap energy (corresponding to the first column in the coefficient matrix in equ. 2.2.2) has been omitted. The light blue levels correspond to negatively charged configurations, black one to neutral, and red to positively charged configurations. This diagram shows that despite emitting photons relatively close in energy, a significant difference in energetic shelving exist between the radiative states. The energy levels were estimated with a simplified model, based on two ingredients: the calculation of the single-particle GSs in a cubic (10 nm side) GaAs QD in $Al_{0.4}Ga_{0.6}As$ and the binding energies typically measured for the different excitonic complexes (see figure 6.5 in chapter 6). In this estimation, the values for respectively V_{eh}, V_{ee} and V_{hh} are ≈ -33, ≈ 28 and ≈ 32 meV. The small differences between the absolute value of the three terms can be understood if one imagines that both the electron and hole wavefunctions are tightly confined within the QD. For a thigh confinement, it is harder for two carriers of the same kind to rearrange in order to minimize their interaction. Realistic carrier-carrier interactions are not straightforward to calculate as it requires an excellent knowledge of the QD potential. The shape, size and composition of the QD will play an important role to determine the energetic ordering and binding energies of the excitonic complexes. In addition, electric and strain fields can complicate the picture significantly. As an illustrative example, the figure 2.11(b) shows the calculated emission spectrum of a QD with the parameter described above (upper, dark grey spectrum). The energy was shifted so that the X energy serves as a reference. The energy shifts are all negative and reproduce the spectra usually measured in photoluminescence experiments. The light grey spectrum underneath is calculated with a slightly decreased V_{eh} of -30 meV. A decrease in V_{eh} could be due to the effect of *e.g.* an electric field: the wavefunctions of the electrons and holes will be slightly pulled apart, and as a result their overlap would decrease. Despite this moderate, 10% difference, the changes in the calculated spectrum are striking. Only the X^- remains with a negative energy. The XX and X^+ are now anti-binding, with an energy superior to the X. This scenario has already been seen for QDs with similar shapes but different sizes, and was thought to be due to a variation in the piezo-electric field created by the lattice mismatch between the dots and the matrix.[102] The removal of the XX binding energy was also already achieved by external means, using either electric field, strain field or a

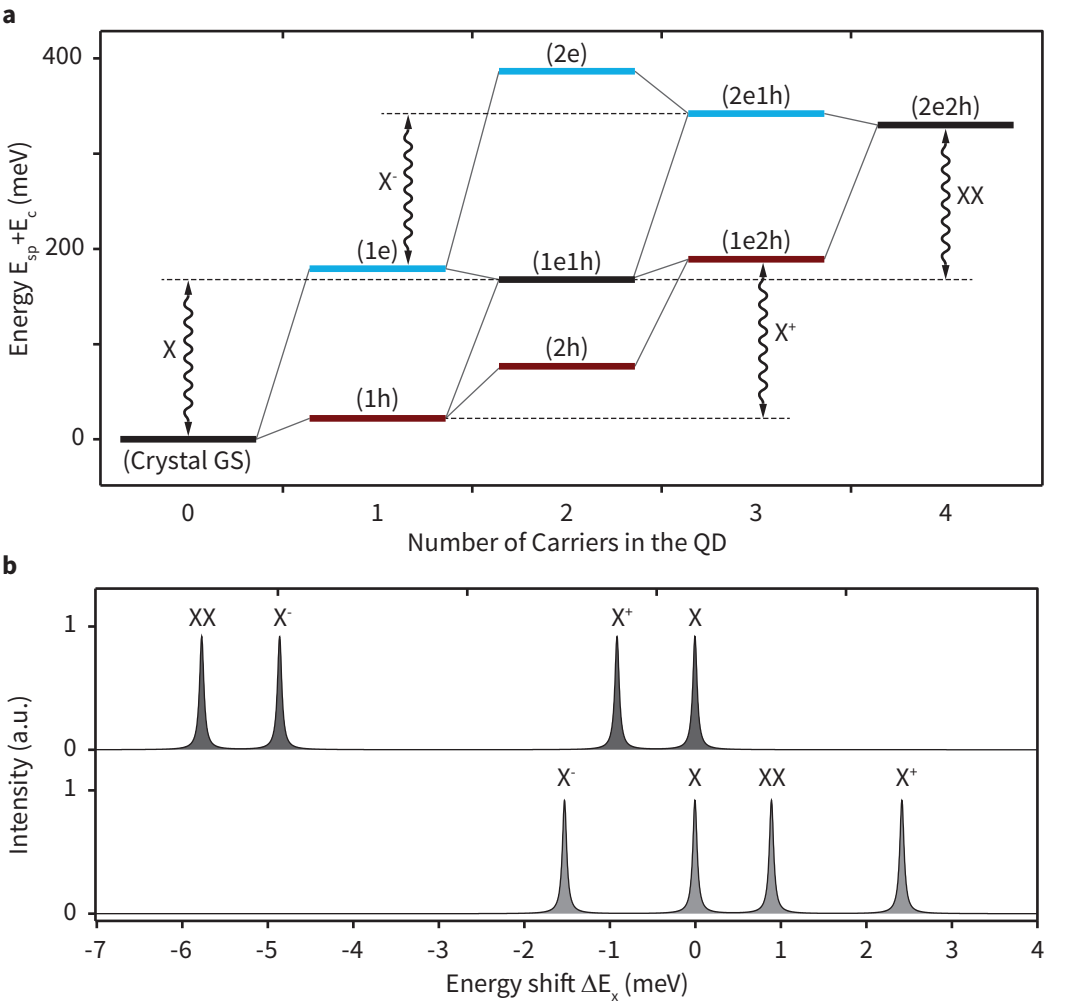

Figure 2.11 • **a.** Energy scaling of the QD charge configurations, calculated based on the SP states of a cubic GaAs QD (10nm side) in the effective mass approximation. The Coulomb interaction terms are adjusted to reproduce the binding energies commonly seen in experiments. The bandgap energy is omitted: only the energy of the single-particle eigenstates E_{SP} and the Coulomb interaction energies E_c are taken into account. The black levels represent electrically neutral states, the light blue (red) levels stand for negatively (positively) charged states. Wavy arrows represent the four different optical transitions. **b.** Dark grey: Made-up spectrum representing the emission of the four optically active transitions shown in (a). The emission energies are rigidly shifted (neutral exciton (X) recombination corresponding to 0), allowing to realize the *binding* or *antibinding* character of the other excitonic complexes. Light grey: similar made-up spectrum, but for a value of V_{eh} reduced by 10% in order to illustrate the effect of a modification of the Coulomb terms on the optical spectrum. For both spectra, all the peaks are represented with am equal broadening of 100 μeV and intensities set to 1, arbitrarily.

combination of both to tune the different Coulomb terms.[103]

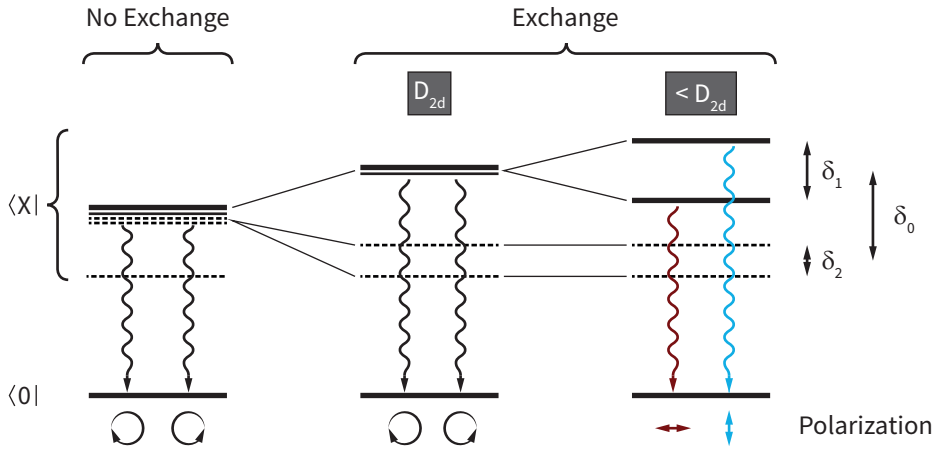

Figure 2.12 • Diagram of the evolution of the states for the exciton. Left: without exchange interaction, the exciton states are 4-fold degenerate. Right: The exchange interaction split the bright (solid lines) from the dark (dashed lines) states. The dark states are split by an energy δ_2. For QDs with high symmetry, the bright excitons are 2-fold degenerate and emit circularly polarized photons. For lower symmetries, the bright excitons are split by an energy δ_1 and radiates linear, cross-polarized photons.

Exchange interactions and fine-structure splitting

Because of the extra degree of freedom given by the spins orientation, certain electronic states like the X are actually multiplets. Without further interactions, each excitonic spin state can be represented by its total angular momentum, and is a "pure" eigenstate of the system. Yet, the exchange interaction couples the electron and hole spins and perturbs the system. The spin states previously described and shown in the list 2.5 are not eigenstates of the X anymore, and depending on the symmetry, the degeneracy of the four spin states can be partially or totally lifted.

The Hamiltonian corresponding to this interaction can be expressed in its matrix form as follows:[104,105]

$$\mathcal{H}_{exchange} = \frac{1}{2}\begin{pmatrix} \delta_0 & \delta_1 & 0 & 0 \\ \delta_1 & \delta_0 & 0 & 0 \\ 0 & 0 & -\delta_0 & \delta_2 \\ 0 & 0 & \delta_2 & -\delta_0 \end{pmatrix} \tag{2.8}$$

And act on a basis made of the "pure" states $\{|\uparrow\Downarrow\rangle, |\downarrow\Uparrow\rangle, |\uparrow\Uparrow\rangle, |\downarrow\Downarrow\rangle\}$.

The result is that for non-trivial values of the hamiltonian, the states will hybridize. The value δ_0 gives the magnitude of the splitting between the bright states and the dark states. A non-zero δ_1 will result in an hybridization of the bright states, with a splitting energy often called the fine-structure splitting (FSS) or the anisotropic exchange energy, as it depends on the anisotropy of the system and can be canceled for QDs with a high-enough symmetry (C_{2v} or higher). The last parameter δ_2, called the isotropic exchange

energy, is always positive and thus will mix the dark states regardless of the symmetry of the system. Finally, for asymmetric dots, the eigenstates of the system are modified as:

$$\begin{pmatrix} |\uparrow\Downarrow\rangle \\ |\downarrow\Uparrow\rangle \\ |\uparrow\Uparrow\rangle \\ |\downarrow\Downarrow\rangle \end{pmatrix} \xrightarrow{exchange} \begin{pmatrix} \frac{1}{\sqrt{2}}(|\uparrow\Downarrow\rangle + |\downarrow\Uparrow\rangle) \\ \frac{1}{\sqrt{2}}(|\uparrow\Downarrow\rangle - |\downarrow\Uparrow\rangle) \\ \frac{1}{\sqrt{2}}(|\uparrow\Uparrow\rangle + |\downarrow\Downarrow\rangle) \\ \frac{1}{\sqrt{2}}(|\uparrow\Uparrow\rangle - |\downarrow\Downarrow\rangle) \end{pmatrix} \tag{2.9}$$

Hence, the new states are linear combination of the "pure" states. This has a profound influence on the polarization of the emitted photons. If the state is now a linear combination of up and down spins, the emitted light will be as well a linear combination of circularly polarized photons, *i.e.* the emitted photons will be linearly polarized. Further, their polarization will be orthogonal, reflecting the orthogonality of the hybridized states. The figure 2.12 summarize the exchange interaction, and show the evolution of the exciton states, on the left without considering the interaction of spins, then with the exchange term but a zero FSS and finally for an asymmetric QD with a FSS. The polarization of the emitted photon is represented at the bottom.

The situation is easier for the charged excitons. The X^+ and X^- are composed of two particle of the same kind with anti-parallel spins neutralizing each other and canceling any effect related to the exchange interaction. The same reasoning applies to the XX. Two electrons and two holes populate simultaneously the QDs and both the electrons and holes are spin-paired. Yet, the measured emission peak of the XX show a FSS as well, and the photons emitted during the XX decay are linearly polarized. The reason for this splitting is the arrival state of a XX decay being the X state. Hence the emission spectrum of the XX is the perfect mirror of the one arising from the X recombination. The FSS has prevented the use of the biexciton-exciton cascade to generate entangled photon pairs, as the energy difference between the two X states is reflected in the energy of the photons from the X and XX decay. This difference in energy provides a which-path information and consequently affects the entanglement. For this reason, a significant amount of work has been undertaken to reduce the FSS. Different strategies to reduce the FSS can be applied. One method rely on the use of an external perturbation to reduce the energy splitting, in particular with electric, strain or magnetic fields.[106–110] A carefully designed growth process and annealing can also produce QDs with a small to vanishing FSS.[111,112] Finally, filtering the spectrum of the X and XX peaks in order to select only photons within a small overlapping energy window, or temporal filtering techniques, also proved to be effective. Without strictly speaking acting on the FSS, these techniques allowed to erase the which-path information encoded in the photons energy and obtain photon pairs violating Bell's inequalities.[25]

Single photon emission

Finally, this last subsection is dedicated to one of the most outstanding properties of QDs: single-photon emission. This property is shared by other atom-like systems such as single atoms themselves, single molecules and dyes or atomic defects in crystal ("frozen atoms"). The first measurement of light anti-bunching was realized by Kimble *et al.* using a diluted beam of sodium atoms.[113] Note that singe photons can be generated by non-linear optical processes like parametric down-conversion. For QDs, single-photon emission is somewhat expected considering the description of the energetic levels made above. If the light coming from the recombination of single electron-hole pairs can be isolated, the emission must be reduced to a stream of single-photon, with photon-photon spacing initially depending on the system dynamics (how long the electron-hole pair stays excited before recombination). The light is then said to be antibunched.

Anti-bunching and single-photon emission can be confirmed by measuring the *second-order correlation* function of an emitter. In term of light intensity, the normalized second-order correlation function can be written as:

$$g^2(\tau) = \frac{\langle I(t)I(t+\tau)\rangle}{\langle I(t)\rangle\langle I(t+\tau)\rangle} \tag{2.10}$$

Where t and τ are the time and time-delay and $I(t)$ is the time-dependent intensity of the source. The braquets $\langle\rangle$ represent the time-average value. Since the intensity is directly proportional to the number of photons in a mode, they can be interchanged as follows:

$$g^2(\tau) = \frac{\langle n(t)n(t+\tau)\rangle}{\langle n(t)\rangle\langle n(t+\tau)\rangle} \tag{2.11}$$

Practically, it is more convenient to measure the arrival of photons (instead of intensities). In most of the setups, two detectors are used in parallel to measure $g^2(\tau)$ down to $g^2(0)$(see section 3.2.2). The criterion for single-photon emission, *i.e.* the classical/quantum limit is

$$g^2(0) < 0.5 \tag{2.12}$$

Indeed, a pair of uncorrelated single-photon emitters would produce a value $g^2(0) = 0.5$, as well as specially prepared state of classical light (amplitude squeezed state). The 0.5 threshold is then marking the boundary between the classical and the quantum limit.

The single-photon emission characteristic of QDs can be harnessed to produce single photons on demand, *i.e.* triggered photon emission. The easiest implementation of such a scheme consist in exciting the QD with sharp pulses of light at a defined rate. If the optical pulse is much shorter than the excitonic lifetime, single photons will be emitted, at a rate defined by the pulse train. Single-photon emission is an extremely

important feature and is a milestone in the realization of quantum schemes like photon pair, photon-spin, distant n-objects entanglement etc.

2.3 Quantum dots in nanowires

Finally, the last section of this chapter is devoted to a review of quantum dots in nanowires (generically abbreviated NWQDs). While the QDs which form the subject of this thesis are of a very different nature than the QDs described hereafter, an overview of the other possibilities offered using NWs is relevant and allows to situate this research in a broader context. NWQDs are an interesting system in the sense that they provide a new way to create QDs. They also offer the benefit of having an easy way to access a single QD electrically.[114,115] As previously said, the NWs structure can be further used as a photonic component and can be incorporated in a larger system.[116] Furthermore, the possibility to obtain QDs deterministically positioned is directly linked with the control of the NWs positioning. For NWs grown using the Au-Catalyzed approach, this is now commonly achieved. Considering the present context, where the scaling-up of quantum system is becoming a main goal, controlling the emitters position is a tremendous advantage.

2.3.1 Axially defined nanowire quantum dots

As for now, NWQDs are still mainly based on the paradigm of axial QDs proposed by Borgstrom *et al.*[14] During the wire growth, the composition of the alloy is changed *e.g.* by the introduction of another group III or V material in order to obtain a segment with a different bandgap. If the segment is made of a smaller bandgap material presenting a type-I band alignment and if the segment is short enough both electron and holes will experience quantum confinement. The figure 2.13 describes the growth process of an axial QD in a NW. Starting with a gold catalyst, an initial stem of wide bandgap matrix material is grown (in this case InP). Consecutively, the composition of the material is changed following the introduction of a different group V (in this case) or group III material. The segment is usually made of a ternary alloy. The reasons are multiple, but the time required to deplete the catalyst droplet is usually too long to replace completely one species by the other. Following the growth of the segment, the growth is resumed in the initial conditions, with the components of the wide bandgap material. An extra shell can be added after the axial growth is stopped. The method implies that the geometry of the QD is strictly fixed laterally by the NW core diameter. The QD height depends on the growth rate, growth time and elemental ratio. However with VLS, the transition can hardly be atomically sharp and QDs with homogeneous composition and very small height are hard to obtain, because of the intrinsic inertia of the VLS mechanism. Furthermore most of the NWQDs grown following this route are made of lattice mismatched alloys, which can lead to complicated effects in the QD electronic

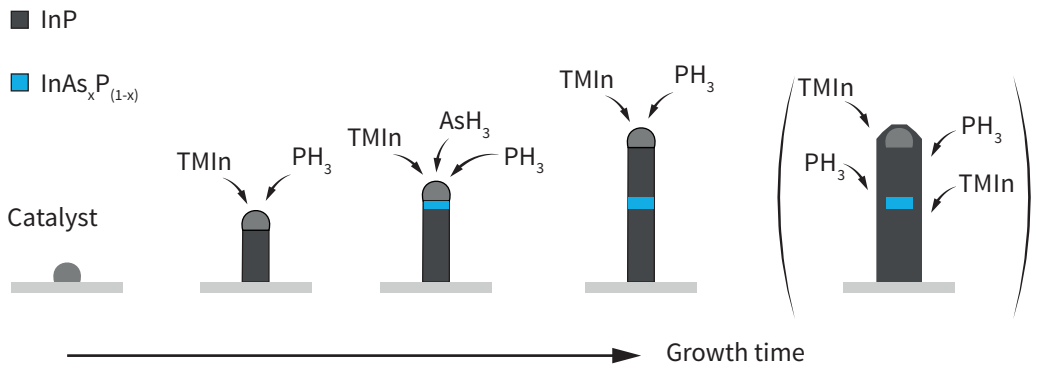

Figure 2.13 • Growth process of an axial $InAs_xP_{1-x}$ QD in an InP NW by MO-CVD using Au-assisted VLS growth. The arsenic flux is turned on during the growth in order to create a thin segment of lower bandgap material forming the QD. Additionally, a last step can be added to the growth process, during which the NW is capped with an extra layer of InP.

structure. On the other hand, VLS is a good method to achieve defect-free structures and implement controlled doping profile in the NW core. SAE can also be used to define QD in NWs. Using this method, it is possible to create sharp interfaces but the control on the phase of the host material is weakened, yielding a non-optimal electronic configuration along the wire. Regardless of the method, axial QDs offer two main advantages. The first one regarding the electronic structure: the symmetry of the QD is tightly linked with the one of the NW, and for this geometry, the FSS is expected to vanish.[117] The second one regarding the coupling to the fundamental guided mode: the centered position of the QD perfectly overlaps with the mode maximum. Axial NWQDs made of a large variety of materials have already been successfully demonstrated. If InAs/InAsP is likely to be the most spread alloy system, other III-V systems, II-VI or nitride materials have also been used.[118–121] The use of wide-gap materials is particularly interesting as the binding energies are usually very high. As a result, optical activity can easily be maintained at room temperature, and single photon emission has been reported in the same conditions.[120,121] An example, adapted from ref. 120, is presented in the panel (a) of figure 2.14. In this case, single photon emission was measured in pulsed-mode and a raw value of $g^2(0)$ equal to 0.33 was found at room temperature, against 0.26 at 3.9 K. The linewidth of the QD increased from 1.45 meV to 36 meV.

As discussed at the beginning of this chapter, another particularity of NWs is polytypism. If a large part of work on polytypism actually aimed to avoid it (obtaining NWs with either pure WZ or pure ZB phase), efforts have been made to insert segments of secondary phase in a primary phase NW (the "host" phase being either WZ or ZB). For materials like GaAs or InP, WZ/ZB homojunctions form a type-II band alignment. In this case, the most striking characteristic is the increased exciton

lifetime due to the spatially indirect transition. In order to confine both electrons and holes in a space small enough so that their wavefunctions overlap, having a single WZ segment in ZB (or vice-versa) is often not sufficient. The best sequence consist of small segments of the secondary phase close to each other. In this way, both electrons and holes can be trapped, preventing the spilling of one of the two species along the wire (see figure 2.6(b)). If the segments are short enough, and the diameter of the wire allows it, single electrons and holes can be confined, resulting in single photon emission. This case was shown to be realistic and the signature of single-photon emission from crystal phase QDs was measured by Akopian *et al.*. Yet, this work still did not show unambiguously the presence of single QDs. From the value of the antibunching measurement, the authors estimated that the captured emission was originating from very few (4) isolated crystal-phase QDs.[12] Other reports on crystal-phase QDs are scarce, since creating clean segments of secondary phase, with a spatial speparation between segments sufficient to investigate them individually with optical method is complicated. In addition, the diameter of the NW should be small enough to also provide lateral confinement. On the other end, the trapping of electrons or hole in WZ/ZB segments confining the carriers only along the growth axis (quantum disks) is relatively well studied and provides interesting informations on the two phases.[11,80,122] The ultimate limit to this approach would be to reduce the segment to a single stacking fault. Optical emission from a single, isolated, defect as just been reported and hold promises for the understanding of the effect of planar defects in NWs.[123]

2.3.2 Alternative approaches to axial heterostructures

Research on alternative form of bottom-up NWQDs has been limited so far. However, reports on the growth of SK-like InAs QDs on the side facets of GaAs NWs has been reported by at least two groups.[124,125] In ref. 124, the QDs are reported to grow astride of the corner defined by two facets and are formed only if an AlAs layer is previously deposited on the GaAs core. The moderate optical qualities of these QDs can be related to their extreme vicinity with the surface. In ref. 125, the InAs QDs grow directly on the GaAs side facets and closely resemble SKQD with pyramidal shape. In addition, these QDs were able to emit single-photons in a relatively narrow linewidth.

Another type of NWQDs, based on a combination of top-down and bottom-up approach consist in growing standard SKQDs or interface fluctuation QDs and then etch the substrate to obtain NWs. This technique theoretically allows to obtain QDs with the excellent characteristics of planar structure, while gaining the advantages of the NW geometry. An optimization of the etching parameters allows to obtain NWs in the shape of needles or trumpets.[56] In this approach, a good surface passivation method has to be used, as the surfaces seems to impact the properties of the QDs. In particular, long-term spectral drift was reported by Yeo *et al.*[126] In this case, the position of the X

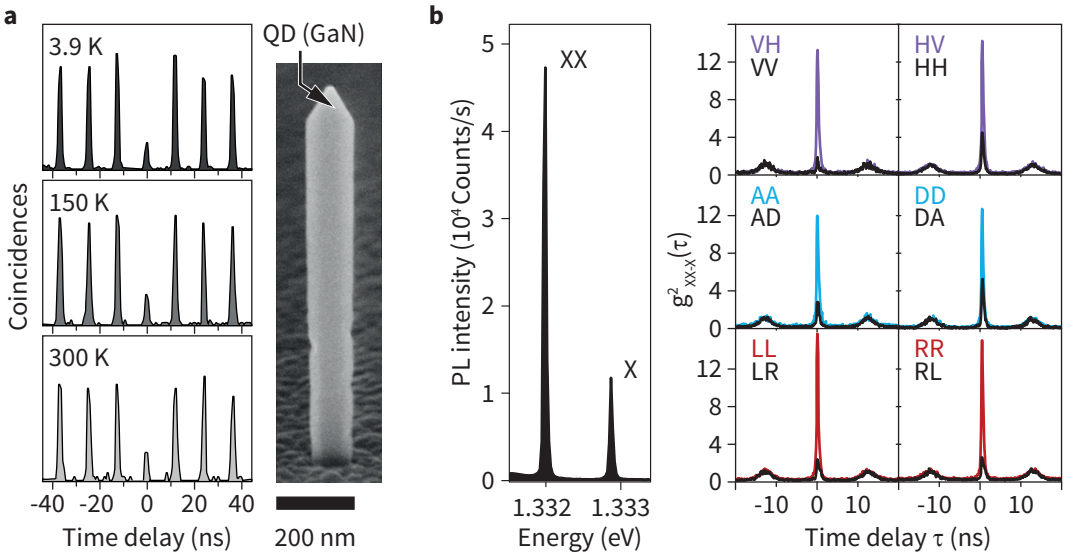

Figure 2.14 • a. Single photon emission up to room temperature, using a GaN QD in an AlGaN NW. The emission is in the UV (4.25-4.35 eV). The SEM image on the right shows the NW, and the arrow indicates the position of the QD, at the tip. Adapted from ref. 120. **b.** Emission spectrum of an optimized axial InAsP QD in an InP NW. The X and XX in the spectrum are used for the measurements on the right. The coincidence histograms show the entanglement of the XX and X photons in the rectilinear (H and V), diagonal (A and D) and circular (R and L) basis. Adapted from ref. 132.

emission peak drifted on a time period of several hours. For top-down defined NWs, the position of the QD is not necessarily on the axis of the wire. This is a disadvantage if the aim is to couple the light emission to a photonic mode comporting a main anti-node at the center of the wire, as it is the case for the fundamental mode found in cylindrical waveguides (HE_{11}). However QDs located off-axis also bring interesting features. One is the ability to couple efficiently to air-modes of NW-photonic crystals or to high order Mie resonances.[49,73,74] In particular the vicinity to the NW surface could allow for an efficient coupling to a neighboring metal-dielectric interface with the evanescent field of the emitter.[127] Off-axis QDs can also be used to monitor strain and the motion of a clamped NW.[128,129] This configuration is proposed for cooling a mechanical oscillator to its vibrational quantum ground state, using the phonon sidebands of the QD to damp the motion of the NW.[130]

Finally, in the spirit of the NW geometry, single-photon emitters based on single NV^- centers were successfully isolated in diamond NWs.[131] In this case, an implanted and annealed diamond substrate was etched down to form arrays of NWs. The realization of diamond-based NWs is a particularly challenging task considering the difficulties to process diamond.

2.3.3 Optical qualities of state-of-the-art structures

Initially the optical quality of QDNWs were relatively low when compared to planar QDs. In particular, the emission peak linewidths were large, often of the order of the meV. The situation significantly evolved in the last years. Similar to planar QDs, the linewidth generally improves if the QD is buried in an overgrown shell (see the step in parenthesis in figure 2.13). In this case, the semiconductor surface, prone to host various carrier traps and adsorb ambient molecules, is located further away from the QD. As a result, the perturbations due to localization of the carriers on surface defects or to variation in the chemical species adsorbed are weakened, and linewidth down to 30 μeV were measured.[133] Improvements in the NW growth mechanism also contributed a lot to the reduction of the linewidth. The phase purification potentially prevents the localization of carriers within the wire. These localization phenomena are considered to be at the origin of charge noise in the optical spectrum of NWQDs. As the carriers get captured and escape from various trapping sites, the electrostatic environment of the QD changes, creating a time-dependent Stark shift which broadens the linewidth. Removing the stacking faults in the NW core and saturating the trapping sites with an appropriate excitation power allowed to measure linewidths down to around 3 μeV (at 300 mK).[134] Some groups also reported the growth of axial GaAs QDs in AlGaAs NWs. The reported values for the linewidth were between 2 meV and 90 μeV.[135] However, the latter report showed a single photon purity at the very threshold between classical and quantum domains.[136] The strong linewidth broadening in axial AlGaAs/GaAs NWQDs is very probably due to a bad control of the interface as GaAs is known to be a challenging material with respect to free-surfaces defects.

Finally, the values for the FSS in state-of-the-art NWQDs are also reaching levels for which the XX-X cascade could be used to generate entangled photon pairs without the need of cumbersome spectral or temporal filtering schemes. Interestingly, the measurement of entanglement could not be realized in a straightforward way. The culprit is the asymmetry of the hexagonal NW, slightly elongated. Since the NW used for this measurements were of the pencil-waveguide type, the emitted photon traveled along the NW before being released into free-space. The birefringence induced by the wire asymmetry was then sufficient to change the photons polarization. As a result, the measurement basis has to be adapted to the new polarization state. Once the new measurement basis set correctly, the entanglement fidelity can be measured and has been reported by two groups simultaneously.[132,137] An example of coincidence measurements of the XX-X cascade, adapted from ref. 132, can be found in the figure 2.14(b). The spectrum of the measured InAsP QD is shown on the left. In addition to the X and XX, the authors found other emission lines arising from the same QD (not shown). However, entanglement could not be measured with these other transitions and the cascade correlation with the XX emission was weak. The right graph represent a part of the correlation analysis, done by projecting the

photons on three different polarization basis: rectilinear, diagonal and circular. Polarization entanglement could be demonstrated (see the details of ref. 132) even if the strong bunching happened for opposite projections than usually measured with planar structures due to the birefringence.

As a final word on the optical properties of NWQDs, it can be said that if the linewidths of NW-embedded emitters are in average still larger than the best SKQDs, tremendous progress have been made. In around ten years, the field enveloped rapidly, and the common broadening of around 1-2 meV can now be reduced by almost three order of magnitudes. The coherence times observed in the best NWQDs are also getting close to the results obtained with planar structures. Hence state-of-the-art NWQDs can now be considered a competitive platform offering in addition enhanced light out-coupling performances and the possibility to position precisely the emitters.

Experimental techniques 3

The main experimental techniques used during this thesis are described in this chapter. The principal methods revolve around photoluminescence spectroscopy, but the exact experimental setup can be adapted depending on what is measured. In addition, a brief overview of cathodoluminescence will be given, as this technique, even though less used, brought valuable insights on the shell-QDs investigated in this thesis.

3.1 Photoluminescence

3.1.1 Principle

When light interacts with matter, a myriad of processes happen with different probabilities. This processes can involve elastic (*e.g.* coherent backscattering) or inelastic (*e.g.* Raman) scattering, emission of one or several photons and can be coherent (*e.g.* stimulated emission) or incoherent. Photoluminescence (PL) arises from the incoherent, spontaneous inter-band recombination of electrons and holes in a semiconductor material, *i.e.* spontaneous emission. For this reason it principally depends on the crystal bandstructure. The bandgap type (direct or indirect), energy, the exciton binding strength and possible defects in the crystal will contribute to the principal feature of a PL spectrum. For indirect gap semiconductor, the PL is usually extremely hard to observe. Because electron-hole pairs recombination will in this case be phonon-assisted (to compensate for the momentum), the radiative recombination probability is low. The lattice phonons will match the difference in momentum, regardless of their energy. Thus, the contribution of phonons with different energies will be reflected in the broadening of the luminescence spectrum. In contrast, PL signals of direct bandgap semiconductors like GaAs or InP can be very intense and can be use to detect the properties of the material. The excitation of the electrons and holes in a bulk semiconductor is usually done using a "pump" laser with an energy above the bandgap energy. Interactions of the "hot" carriers with the crystal will lead to their thermalization *via* the emission of phonons. This process is shown in figure 3.1(a) for the Γ valley of a direct semiconductor (in the momentum space). The pump

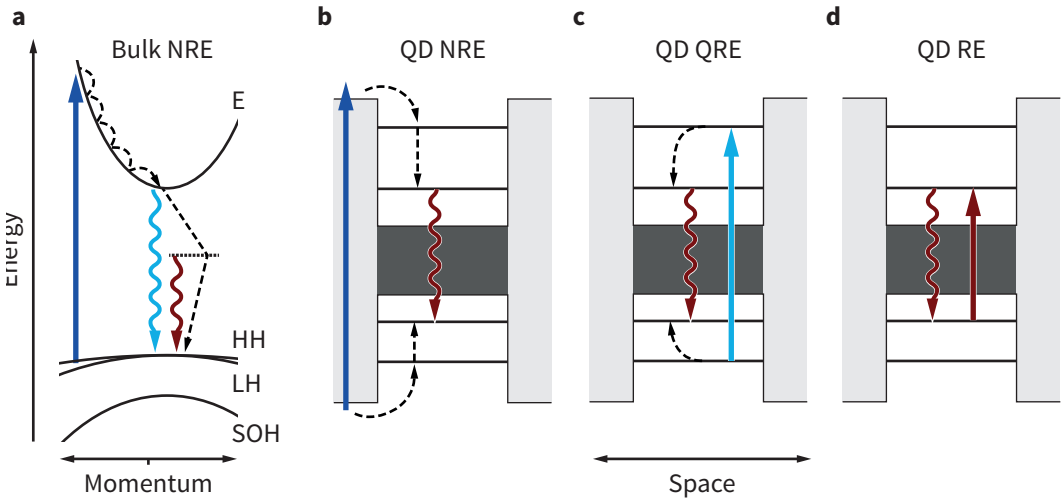

Figure 3.1 • **a.** Non-resonnant excitation (NRE) of carriers and PL process for a bulk semiconductor. **b.** NRE for a QD. Dashed arrows stand for non-radiative,phonon-assisted processes. **c.** Quasi-resonant (QRE) excitation mechanism. QRE is only possible for QDs with p-shell levels. **d.** Resonant excitation (RE) and resonance fluorescence.

laser correspond to the dark blue arrow and the thermalization process associated with phonon emission is represented by black dashed arrows. Band-gap emission is shown in light blue. The case of excitonic emission (an electron and hole bound by their mutual Coulomb attraction) is not represented, but would happen from slightly below the band edge, because of the energy reduction due to Coulomb binding. The other case, represented by a dark red arrow, describe the emission of lower-energy photons arising if an electron (or hole) populate an intra-gap level and recombine from there. The principle of photoluminescence spectroscopy consists in capturing the light emitted by the semiconductor and to analyze it spectrally, *i.e.* its intensity as a function of its color (wavelength).

The figure 3.1(b-d) focuses on the different excitation mechanisms for QDs. On the left, the most common one is essentially identical to the bulk case, and makes use of the bulk matrix around the QD. For moderate laser power, pump photons will generate electrons and holes first in the 3D continuum around the QD. Some carriers will non-radiatively thermalize in the QD, ultimately reaching their respective electron and hole GS. The middle panel shows the case were the QD has bound p-shell states. In this case, a laser resonant with the p-shell interband transition will excite electrons directly within the QD. The interaction with the matrix is greatly reduced and often the carriers maintain the information of the light field, in particular angular momentum. Finally, figure 3.1(d) shows the case of pure resonant excitation (RE). In this case, the pump field is directly tuned to match the X energy. This experimental scheme allows to avoid any interactions with the matrix or dephasing processes due to

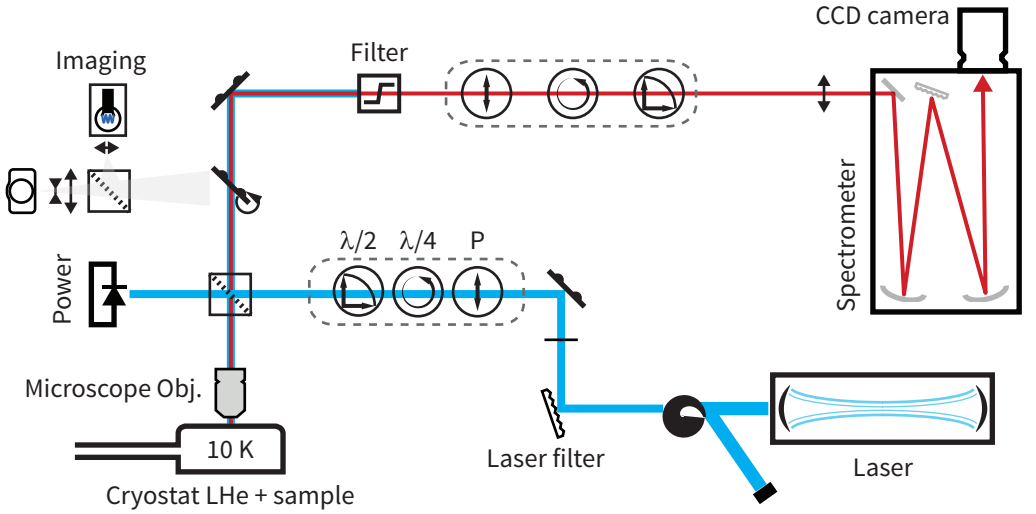

Figure 3.2 • Simplified blueprint of a PL setup. The blue (red) lines represent the laser beam (PL signal). The labels $\lambda/2$, $\lambda/4$, and P stand for waveplates (half-waveplate, quarter-waveplate) and polarizer .

thermalization of carriers. In addition, it usually addresses a single QD in its simplest form: a two-level system. Usually, the linewidth measured with RE will be smaller than with NRE/QRE. If the laser light can be efficiently suppressed, the purity of single-photon emission can also increase significantly in RE or QRE as the background luminescence from the matrix is essentially canceled. Importantly the temporal coherence of the exciton can be improved, up to a level comparable to the driving laser light.[138,139] Finally resonant excitation leads to interesting physical phenomena, based on the interaction of the light field directly with the two-level system.[140–143] The major problem in this case resides in being able to discriminate between the direct laser photons and the ones which interacted with the QD. For this reason, RE (in particular in CW operation) is for now limited to geometries presenting extremely small scattering probabilities, essentially flat substrates or micropillars, and its implementation with NWs is extremely challenging.

3.1.2 Photoluminescence optical setup

During the course of this thesis, several slightly different setups were used. Despite differences in arrangement and exact configuration, they all share the same basic components. These are represented in the figure 3.2. The blue lines represent laser light, using to optically excite (*pump*) the semiconductor material. The laser light can be attenuated with filters in front of the laser output. Usually, the laser light is also filtered spectrally. In the schematic of the setup, this filtering is represented by a grating. Grating filtering has the advantage of being tunable, *i.e.* the filtered

wavelength can be adjusted. This is ideal if several light sources are available or if the laser can be adjusted to different wavelengths. The grating filter is rotated until the light of the correct color passes through a pinhole. The latter ensures that only the selected color is transmitted further to the sample. Alternatively, if only a few sources are used, a narrow bandpass filter can replace the grating filter (laserline filter comes for common laser wavelength). The use of a filter is not always necessary, but it often improves the results. The reason for filtering laser light is that a laser very rarely emits only at the lasing wavelength. For gas lasers, residual plasma light is also emitted, and other modes can also be weakly active. For solid state lasers the background of the gain medium is often strong enough to spoil the measurement, in particular if the measured signal has a low intensity and a wavelength close to the lasing medium light emission. The laser light can then be manipulated with various optical devices. Among the most useful are polarizers, which assure that the transmitted light is linearly polarized and $\lambda/2$, half-waveplate or polarization rotator: they allow to rotate the polarization of the light. Quarter-waveplates ($\lambda/4$) can also be used to generate circularly polarized light, either left or right, starting from a linearly polarized beam. Similarly, these elements can be used in the detection line to analyze the emitted light.

The laser light is then partially reflected on a beamsplitter with a splitting ratio depending on the application. The transmitted light can be monitored by a power-meter (essentially a diode) and allows to know the power sent on the sample. The reflected light is focused by an objective, usually with high magnification and high numerical aperture (NA). The numerical aperture is an important feature and maximizing it is often beneficial for two reasons: (i) the size of the focus depends strongly on the objective aperture, and can be estimated from the Rayleigh criterion $d = 0.61\frac{\lambda_0}{n \cdot NA}$ with λ_0 the light wavelength in vacuum and n the refractive index of the medium. For relatively high NA such as 0.85, the resolution of the system is approximately 2/3 of the wavelength, and the spot size roughly twice as big. (ii) With higher NA comes higher capture solid angle. Thus the signal intensity is strongly linked with the NA of the objective. The sample is usually placed inside a liquid helium (LHe) cryostat. Details on the different types of cryostats used can be found in subsection 3.3.

The light emitted by the sample is then redirected toward a grating spectrometer to disperse the signal. Usually, 500mm focal length spectrometers are used, with different grating periods, typically 300, 600 and 1200 l/mm. Shorter grating periods increase the resolution, but at the cost of signal bandwidth (not all the signal is captured by the detector) and often intensity. The detector is usually a silicon charge-coupled device (CCD) cooled either with a Peltier element of with liquid nitrogen. Alternatively, the spectrum can be analyzed with Fabry-Pérot or Michelson interferometers and detected by single-channel detectors like avalanche diodes.

Most of the time, the lasers used to excite the material can be classified in two categories:

Continuous-Wave operation (CW) For CW lasers, the light output power is constant in time. Divergence from the average is involuntary and due to various noise sources, such as noise from the power supply, and is at best limited by shot noise. These lasers are relatively simple, they allow for a continuous excitation of the material. The instantaneous power is equal to the time-averaged power.

Pulsed operation Pulsed lasers emit pulses of light of various duration at a regular frequency (the repetition rate). Usually, both should be specified (the pulse duration can be defined by its FWHM). The two main operation modes are Q-switching and Mode-locking. Common Q-switched laser diodes as used in this thesis can generate pulses with temporal FWHM between 120 to 50 ps. It is important to realize that most of the Q-switched diodes will exhibit a non-secant temporal profile: the FWHM is not necessarily representative of the pulse broadening. Mode-locked oscillators like Ti:sapphire laser can go down to below 100 fs routinely, but are both more costly and complicated. The repetition rates are commonly scaling between a 100 of MHz down to few Hz for extreme powerful lasers. The instantaneous power is not equal to the time-average power anymore, and is scaling up anti-proportionally to the repetition rate and the pulse duration.

3.1.3 Cryostats

The principal type of the cryostats used for the experiments were cold-finger cryostats. In this case, a sample stage is cooled down by direct contact with liquid Helium (LHe) or Helium vapour. The sample is then cooled by conduction. In figure 3.3, two different types of cold-finger cryostats available for experiments are represented. The panel (a) shows the simplified schematics of a closed-loop, also called cryogen-free cryostat, while (b) represents a classical open circuit or open-loop cold-finger cryostat. The latter should be permanently supplied with liquid helium from an external dewar. Aside from this already important disadvantage, the open-circuit cryostat system used for certain measurements is not designed to incorporate a microscope objective within the refrigerated enclosure. As relative motion between the sample and the objective is likely to occur. As any relative motion between the objective and the sample is directly translated (1:1) to image or laser spot movement, this configuration is much more sensitive to vibration and drift. The minimal temperature which can be reached with cold-finger cryostats can vary depending on the exact design and sample load. The cold-finger cryostats used in this thesis were reaching temperatures down to 3.75 K (closed-loop) and 7-10 K (open-loop).

A second type of cryostat used for this thesis is of the bath-type. This case, represented in figure 3.4(a) consists in an insulated tank of LHe. In our case, a 10 T superconducting magnet is also mounted in the cryostat. The LHe allows to cool the

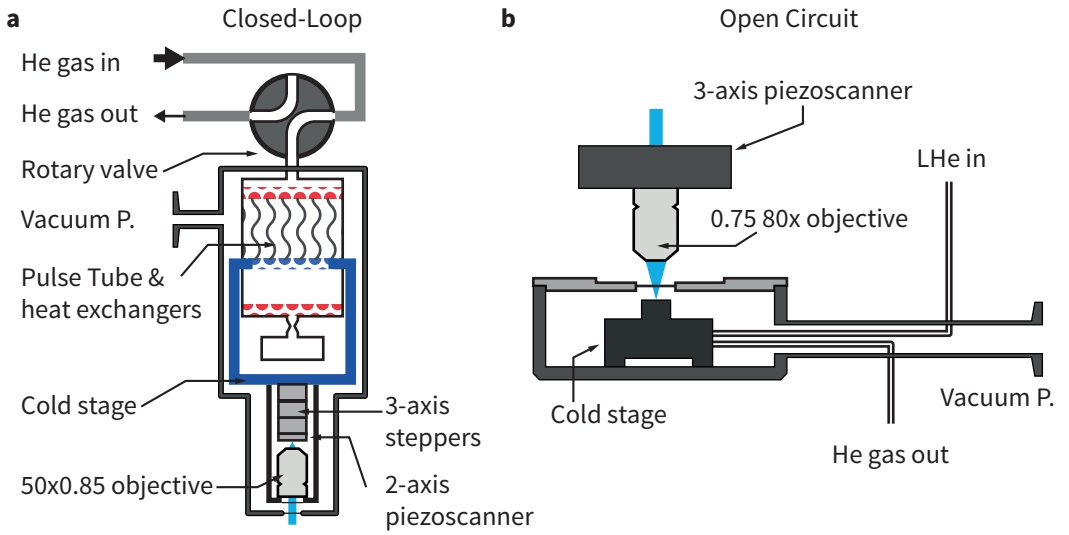

Figure 3.3 • **a.** cryogen-free cryostat based on the pulse-tube design, with an integrated objective and piezo stack.**b.** Classical window-access open-circuit cryostat. The objective is outside and mounted on piezo scanners. This design inherently increase the spatial drift and vibration level.

magnet below the critical temperature and superconductivity ensures quasi-null Ohmic losses and heat generation. The solenoid configuration generates a magnetic field with a fixed direction, in axis with the cryostat. The sample is located in an insert tube. A low pressure of He gas is used to cool the sample by convection down to 4.7 K. In addition, a boat in which the sample is mounted can be rotated in the bore of the magnet. The configuration is drawn in figure 3.4(b). The boat consists in a monolithic assembly of the piezo-actuator stack with the sample and the objective directly coupled to a single-mode (SM) optical fiber. The fiber permits to freely rotate the boat in the magnetic field without affecting the light transmission in and out of the cryostat. The rotation is done mechanically, through cogs and a drive shaft. the shaft can be rotated from outside the cryostat to adjust the tilt of the boat. Hence, in the sample reference frame, only the magnetic field is rotating, while the optical axis stays immobile.[144]

In this setup, because the light is directly coupled to a single-mode (SM) fiber, the microscope is inherently confocal. The limited (around 4 μm) modal area of the fiber act as a pinhole and reject the light emitted out-of axis as well as out of the focal plane of the objective.

3.2 Time-correlated single photon counting

Time-correlated single-photon counting (TCSPC) and related techniques rely on the accurate temporal detection of single-photon. These techniques do not imply

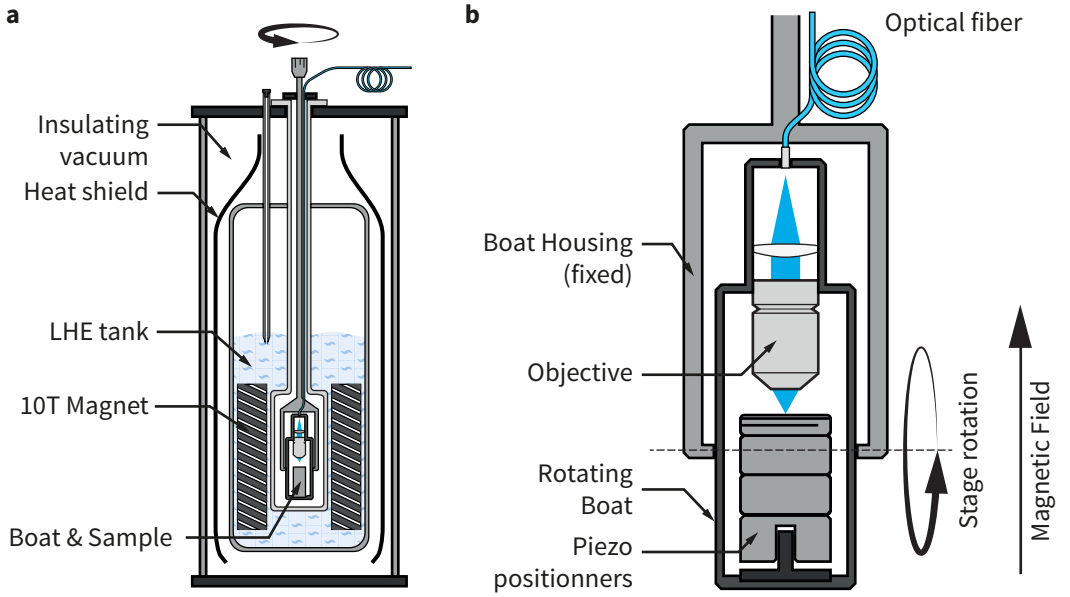

Figure 3.4 • a. LHe bath cryostat including a superconducting solenoid magnet. The sample is cooled by convection in a low-pressure He atmosphere. **b.** Schematic of the rotating boat used for angle-dependent magneto-PL. The objective is directly coupled to a fiber and is mounted in a boat together with the piezo stage supporting the sample. The full boat can be rotated (see arrow) in the magnet bore. The transduction is mechanical, using cogs. Actuation is done from outside the cryostat (see revolving arrow in panel (a))

samples emitting single-photon, but rather the detection of single photon events. The detection of photons is done by either photomultiplier tubes, micro-channel plates or silicon avalanche diodes operated in reverse-bias above the breakdown voltage (SPAD). Recently, superconducting NWs have also been developed and now hold records for detection speed, accuracy and efficiency.[145–147] The timing determination is done in a timing-correlation card. Modern timing cards are based on the fast conversion of analog electrical pulses generated by the detector (NIM, Nuclear Instrumentation Module standard pulse). The conversion is made by a fully digital circuit called a time-to-digital converter (TDC). Each channel (two or more) has its own TDC. The card can calculate the time difference between to successive events between two channels, a start and a stop channel and cast them in bins of predefined size between 4 and 512 ps (time-binning mode). Another operation mode consists in recording independently each individual photon arrival event for each channel (time-tagging mode). The weakness of the latter method is the large amount of data generated. The storage, and even more the treatment of such dataset a posteriori quickly becomes an extremely heavy task for long recording times.

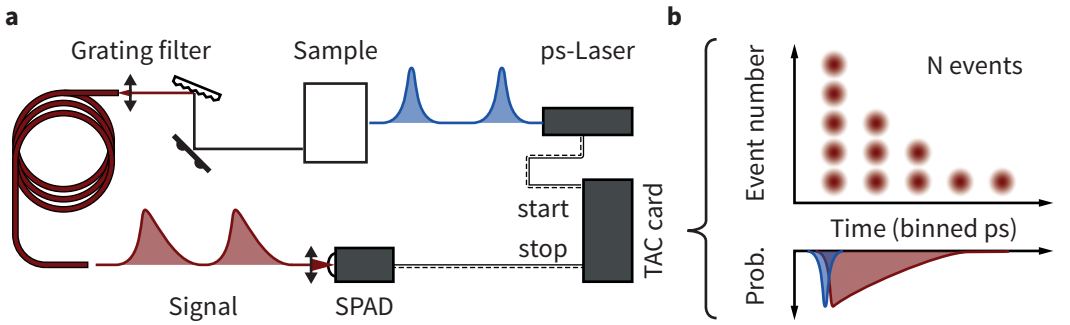

Figure 3.5 • a. Setup for TCSPC-base lifetime measurement. Pump pulses at a defined repetition rate excite the sample. Each pulse starts the TDC. The time-dependent PL is spectrally filtered by a (home-made) monochromator and injected in a SM fiber. Finally the fiber is coupled to a SPAD and a detected photon event is translated into a TDC-stop NIM pulse. **b.** The different arrival time are bin-casted and a histogram can be built (upper graph). The total number of counts in the histogram corresponds to the number of detection events. It is the discrete analog to the intensity (or probability for single-photons) distribution (lower graph).

3.2.1 Lifetime measurement

As seen previously, excited electrons and holes will recombine with a certain yield. However, if the saturation intensity can give an idea of how fast optical transitions can happen for a given system, it is still a very indirect measurement of the carrier recombination dynamics. A dedicated measurement can be done using TCSPC. The working principle consists in very quickly populate the excited levels, and let the system evolve while monitoring the emitted intensity as a function of time. Yet, this can usually not be done in a single-shot, as neither the detection efficiency nor the timing accuracy of detectors is perfect. Instead, the measurement is repeated many time and only one timing event is measured for each shot. This leads to a statistical sampling corresponding to the time-evolution of the system.

The implementation is done using as a pump a fast, pulsed laser. Ideally, the excitation pulse should be Dirac-like, however it is limited by the optical pulse length. The laser signals the emission of an optical pulse sending a synchronized electronic pulse. The latter triggers the start-channel of the timing card. The stop event happens when the detector converts a detected photon to an electrical NIM pulse and send it to the timing card stop-channel. For lifetime measurement, the retrieved time-difference between the start and stop is bin-casted and stored in the card's memory.

In our case, the excitation source is a Q-switched diode laser operating at 475 nm, with a pulse FWHM between 70 to 100 ps (subject to power broadening). The detection is done with SPADs with a timing jitter between 30 and 40 ps. The basic setup can be seen in figure 3.5(a). In general, the emission from the sample is filtered by a home-made grating filter based on a 600l/mm ruled reflection grating and projected on a fiber

end. The fiber small core diameter acts as a spectrometer slit, limiting the bandwidth. The other end of the fiber is relayed to a SPAD. The panel (b) of figure 3.5 is showing the binning result after a number of "stop-event" N. The histogram essentially reproduces the time-dependent intensity (in general), or the photon probability distribution (for single-photon emitters). To avoid artifacts, the intensity of the pump laser is kept low enough, so that the detection frequency on the SPAD (event/s) is at most 1% of the number of pulses per second. From this, one can imagine the interest of having high-repetition rate lasers. In our case, the repetition rate is adjustable between 2.5-40 MHz.

From the histogram, a decay model can be fitted to the decay trace in order to retrieve the lifetime(s) of the optical transition(s). In case of a single radiative decay channel, the evolution of the number of excited electron-hole pair (N) can be written as:

$$\frac{dN}{dt} = -\gamma N \Rightarrow N(t) = N_0 e^{-\gamma t} = N_0 e^{-\frac{t}{\tau}} \tag{3.1}$$

And by direct equivalence between the number of excited electron-hole pairs and the PL intensity (I):

$$I(t) = I_0 e^{-\frac{t}{\tau}} \tag{3.2}$$

Where the subscript 0 points to either the number or intensity at time 0, γ is the recombination rate (similar to the Einstein coefficient for spontaneous emission) and τ is the lifetime. Ultimately, the timing resolution depends on the total instrument response function (see section3.4), and is often close to the value of the slowest element (either the laser or the diodes).

3.2.2 Second-order correlation and photon antibunching

Using the same key elements as in the previous subsection (timing card and SPADs), TCSPC can be harnessed to prove single-photon emission and the generation of non-classical light (sub-poissonian photon distribution). As seen in chapter 2, a single QD theoretically emits only one photon at the time. One can measure this important effect in a photon antibunching experiment. The setup used for this measurement is a Hanbury Brown and Twiss interferometer (HBT).[148] A HBT is based on splitting a photons stream in two at a 50:50 splitting ratio beamsplitter and redirecting the signals on two SPAD detectors. In such a way, each photon can be detected only in one arm. If the source emits single photons, the two detectors cannot be triggered simultaneously and a dip will appear for a time-delay value between the detectors around zero. If the light field is classical, such as a coherent laser beam, the photon spacing is random, and thus the probability of coincidental counts is equal for any delay time. If the photons are "bunched" and tend to be emitted in bursts (*e.g.* thermal light), a coincidence peak will appear for a vanishing time-delay. The interferometer is based on the interference of the measured intensities, which is very different from interference of the light wave amplitudes

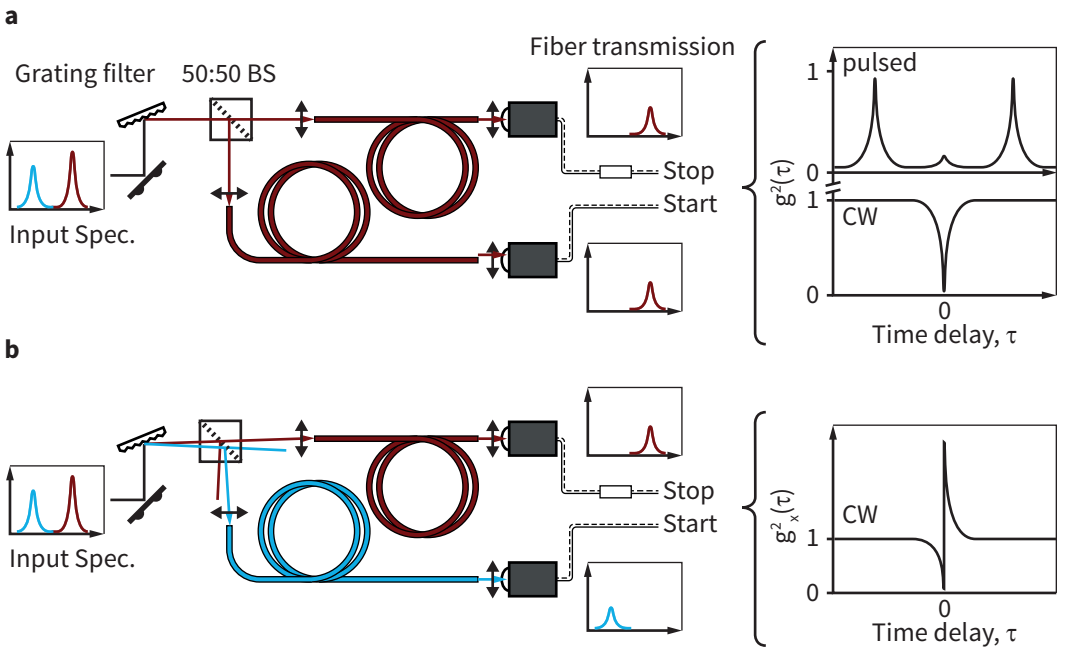

Figure 3.6 • a. Hanburry-Brown and Twiss (HBT) setup for $g^2(\tau)$ autocorrelation measurements. **b.** HBT setup adjusted for a cross-correlation measurement (in this case a XX-X cascade). The color of the optical fibers represent the captured wavelength. The square box on one of the two signal lines from the diodes stands for the electrical delay. The right side of the figures show the expected signal.

(*e.g.* measured with a Michelson interferometer). The former allows to measure $g^2(\tau)$ (see chapter 6.1), the degree of second-order coherence, while the latter actually measures $g^1(\tau)$, the degree of first-order coherence.

Antibunching measurements can be performed either using a continuous-wave (CW) or a pulsed excitation source. CW measurements have the advantage of showing the continuous probability of photon re-emission as a function of time, but can suffer from detector and/or counting card time-jitter. Oppositely, a pulsed g^2 measurement will be robust to time-jitter in the detection setup, but a low repetition rate will cut away some informations for $\tau \neq 0$, while at high repetition rate, the next-neighbor peaks can coalesce.

The setup implementation of an HBT can be found in figure 3.6, the panel (a) shows a $g^2(\tau)$ autocorrelation configuration. In this case, the incoming light (Input Spec.) consists of two different emission peaks (in blue and red). The spectrum is filtered by a custom monochromator (same as for the lifetime determination). The dispersed light is then separated on a beamsplitter and projected on two different SM fibers. The key point is that the small aperture of the SM fiber captures light in a narrow spectral range (around 1.6 meV at 680 nm, with a gaussian transmission profile). Both fibers are adjusted to pick up the red peak (say, the X peak) and connected to SPADs. In turn,

the SPADs are connected to the timing card. In order to be able to measure negative delay times, the signal from the "stop" SPAD is electrically delayed, meaning that if two photons hit the two SPADs simultaneously, their absolute time difference $\tau_{simult.}$ will be positive. Thus, an event pair (consisting in both start and stop triggering) where a photon triggers the stop detector before the start detector recorded a photon arrival can still be measured, but in this case the time delay between the two $\tau_{stop-start} < \tau_{simult.}$. The absolute timescale can be renormalized to obtain the relative time-delay commonly used $\tau = \tau_{absolute} - \tau_{simult.}$.

The right part of the figure illustrates photon antibunching in pulsed-mode (top) and CW-mode (bottom). Usually, the coincidence counts are renormalized to 1 for $\tau \to \infty$. Both modes show a strong reduction of $g^2(0)$. The residual counts can come from unfiltered background emission and dark counts (both modes), timing jitter of the detector and card (mainly CW) and optical repumping (pulsed).

The panel (b) of figure 3.6 shows a different ability of this configuration: in this case the fiber connected to the start detector (now in blue) is readjusted in order to capture the light in a spectral window corresponding to the blue peak. The setup is now in *cross-correlation* mode, it measure the correlation $g_x^2(\tau)$ between two different peaks photon fluxes. On the right, the coincidence histogram show a negative dip at negative time-delay as in the autocorrelation histogram. However, a very strong correlation happens for positive time-delays. This would allow us to identify unambiguously the red and blue peak as being the X and XX emission peaks from a single QD: the strong antibunching for $g_x^2(\tau \leq 0)$ shows that the photons in the two peaks are stemming from the same QD. The strong bunching for $g_x^2(\tau \geq 0)$ means that a blue photon emission is very likely to be shortly followed by the emission of a red photon. This is typically the case in a biexciton-exciton cascade process $|XX\rangle \to |X\rangle \to |0\rangle$.

Hence, this HBT setup allows to measure both intensity auto- and cross-correlation, making it particularly flexible. As previously said, the correlations are usually done using the time-binning mode of the timing-card. The time-tagging mode can also be used and the correlation rebuilt in post processing. While being more flexible and allowing to calculate the real correlation function (time-binning allows only for first-neighbor correlation), this mode is rarely used because of the storage size and processing time.

3.3 Cathodoluminescence

Another technique which might be used to analyze and map light emission from semiconductor materials is cathodoluminescence (CL). In this case, the excitation of electrons in the conduction band is done through the energy transfer between an electron probe beam and the carriers in the material.[149] CL systems are often used to make luminescence mapping of sample, as the spatial resolution is maximized by the few-nanometer probe size (and mitigated by the interaction volume and the diffusion of carriers). A map is acquired by recording the light emission during the raster

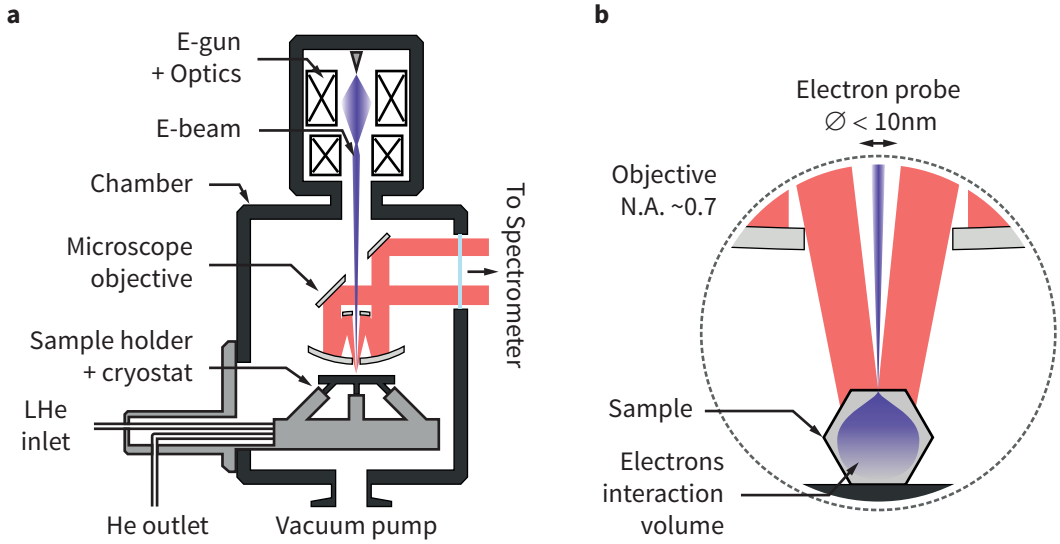

Figure 3.7 • a. Cathodoluminescence setup as it was used for this work. The proprietary design revolves around a Cassegrain objective. The excited luminescence (in light red) is captured and redirected toward a spectrometer and CCD camera. **b.** Close-up of the electron beam interaction (purple) with a sample. The electron probe size is smaller than 10 nm, yet a significant zone of the sample can be excited by electrons scattering in the sample (interaction volume). The electron interaction volume is strongly dependent on the beam characteristic and the sample geometry.

scanning of the electron beam on the sample. If the signal strength allows it, a full spectrum can be acquired for each pixel, resulting in a data cube which can be analyzed afterward.

CL can be implemented either in scanning or transmission electron microscope (CLSEM / CLTEM). In the case of SEM, the electron beam characteristic is typical of these systems, with acceleration voltages usually between 1 and 30 kV and electron beam fluency ranging from pico- to nano amperes. Most of the conventional CL setups consist of a regular SEM microscope equipped with an add-on CL package. In this case, the CL signal is collected and redirected by a parabolic mirror located above the sample. A small hole in the mirror let the electron beam pass and excite the sample. If the results can be excellent on optimized systems, the proper alignment of the mirror is often tedious and requires a skilled operator. In addition, aberrations linked to out-of-axis optical imaging with a parabolic mirror, the field of view of this kind of system is limited to few microns.

The results presented in this thesis were obtained using a dedicated instrument, built around an optical microscope head and designed to maximize the CL signal gathering. The design is presented in figure 3.7. The reflective Cassegrain-type objective (right above the sample holder) makes the alignment easier and more accurate, while maintaining a high collection efficiency. The absence of refractive

elements ensures minimal chromatic aberrations. In addition, a LHe cryostat can be used to cool down the sample to a minimal temperature of 7 K. Using a cryostat in an electron microscope make the vibration management extremely important, in particular at high magnification. In this case, the cryostat, when stabilized at low temperature, allows to measure without significant drift or vibrations even at magnification of 40000x.

A close-up of the interaction between the electron beam and the sample is drawn in figure 3.7(b). With a proper beam alignment, the electron probe can be reduced to less than 10nm. However the beam interacts with the sample and generates the so-called *interaction volume*, in which electrons cascade and are able to excite the material. In addition, excited electrons and holes can diffuse in the material and recombine away from their excitation locus. Considering that the luminescence signal is collected from the whole field of view of the objective, the limiting factor for spatial resolution is not so much linked with the probe size than with the combination of the interaction volume and diffusion effects. Both effects are harder to evaluate for nanostructured materials like NWs than for planar structure. If the interaction volume is around 1 μm (in lateral dimensions and depth, depending on the beam characteristics) for flat substrate, it is likely to be strongly modified in nanostructures as electrons escaping the material will not be likely to be scattered in again. For thin samples, higher beam acceleration voltage can lead to a decrease of the interaction volume in the probed sample, as it will mainly develop in the substrate underneath. Similarly, the vicinity of both the surface and the lower bandgap GaAs core impinge on the carrier diffusion length in GaAs-AlGaAs core-shell NWs.

Altogether, the crux of CL is that it usually allows to improve significantly the spatial resolution, despite the interaction volume and diffusion length.

3.4 About resolution and response functions

In every measurement protocol, an inherent broadening is induced by the measurement apparatus. This effect can be treated in terms of the interplay between the signal and the instrument total response function (IRF). This is true for spatial, spectral and temporal signals. The effect of the apparatus on the measurement become more pronounced when the measured length approach or is smaller than the instrument resolution. In this case, taking the IRF into account is important.

For example, a spectrometer is characterized by a certain resolution. The measurement of an emission peak with a full-width at half maximum (FWHM) approaching this resolution limit will produce a result (the measured FWHM) strongly influenced by the spectrometer. The finite resolution of an apparatus can be taken into account if its response function is know, as the measured intensity profile (and thus the FWHM) can be described as the signal convoluted with the IRF spectrum:

$$I_{meas}(\xi) = I(\xi) \otimes IRF(\xi) \tag{3.3}$$

With ξ being the measurement variable. Measuring the IRF necessitates either a well-know reference signal or a "perfect signal", *i.e.* Dirac-like. For a 500 mm spectrometer with its slit closed at the minimum and a 1340 pixels camera, a stabilized Helium-Neon laser produces a measured spectrum with a FWHM of ar. 118 μeV. Considering that for this laser, the linewidth is around 2 MHz, *i.e.* 0.0083 μeV, the excitation can be considered as being Dirac-like. Hence, the spectrum of the helium-neon laser measures the IRF.

The same applies for temporal like lifetime measurements. In this case, the total IRF can arise from multiple sources. In particular: from the pulse duration of the laser, finite detection jitter of the SPAD(s) and finally the time-jitter of the timing-card. In this case, the total FWHM of the IRF reads:

$$FWHM_{tot} = \sqrt{FWHM_{laser}^2 + FWHM_{SPAD}^2 + FWHM_{Card}^2} \tag{3.4}$$

With the FWHM of the temporal response function for each instrument. Considering an IRF FWHM of 80 ps for the laser, 34 ps for the SPAD and 4 ps for the timing-card, the total IRF FWHM would be $\sim$ 77 ps, and is largely dominated by the response of the laser. The IRF during CW $g^2(t)$ measurement is also fairly important, as it contributes to reduce the dip contrast, and thus reduces the measured $g^2(0)$ value. For this reason, the raw data need to be corrected a posteriori.

Signature of AlGaAs Shell quantum dots in GaAs/AlGaAs nanowires

4

In this chapter, the initial measurements that revealed the presence of segregation phenomena within the shell of GaAs-AlGaAs NWs are presented. These phenomena induce "plane-like" Al-rich regions consistently observed in core-shell structures. In addition, punctual, minute Ga-rich islands are also observed and accounted for the particular optical spectra recorded in photoluminescence experiments: These segregated islands lead to localized modifications in the alloy bandstructure where electrons and holes can be localized and recombine radiatively with a high efficiency. Several techniques were harnessed in order to observe these segregated islands, in particular transmission electron microscopy (TEM) based techniques. In turn, the strong localization of the emitters is illustrated thanks to an increase in spatial resolution brought by CL-SEM. The latter technique is used to show that the emitters are indeed localized in the shell. Photoluminescence measurements show that the emission from the shell is composed of narrow, intense peaks associated with excitonic recombination in the Ga-rich islands acting as QDs.

4.1 Samples

The samples used for this thesis were grown in a high-mobility grade Molecular Beam Epitaxy machine (MBE), described in the section 5 of chapter 2 and illustrated in the figure 2.1(b). The samples consist of GaAs NWs (core), grown with the self-catalysed VLS mechanism on silicon substrates. The growth protocol is outlined below:

1. The substrate is coated with a thin silicon oxide layer. In the first step, arsenic (in As_4 form) does not stick on the substrate while gallium diffuses on the surface, eventually forming droplets. When the droplets are large enough (tens of nm), arsenic can get incorporated until saturation, at which GaAs is formed.

2. The growth temperature for the cores is set to 640°C with an elemental V/III ratio of 60. A careful control on the oxide chemistry and thickness combined with the appropriate V/III flux ratio allows to yield high values of vertical NWs, in certain cases close to unity. The cores are grown until reaching the desired length, usually between 10 and 20 μm. One hour growth usually yields 10 μm long NWs. The axial growth is quenched and the catalyst droplet crystallized by closing the Ga-flux while maintaining the As-flux constant for 20 minutes.

3. For the shell growth, the As-flux is increased (in order to prevent desorption from the side-facets) in order to reach a V/III ratio of 100. This is usually reached for As partial pressure of $1.3{\cdot}10^{-5}$ Torr and Ga equivalent growth rate of 0.3 Å/s. The temperature is set to the planar growth value of 460°C (for all the samples if not mentioned otherwise). This temperature has been chosen as it gives the best quality of material when growing quantum wells on NWs. Subsequently, an $Al_xGa_{(1-x)}As$ shell is grown around the NWs (typically 50 nm). The nominal Al fraction depends on the sample, but is usually set to either 33% or 51%. For multiple-shell (MS) NWs, layers of $Al_xGa_{(1-x)}As$ with different compositions are successively stacked on top of each others.

4. The growth is terminated with the deposition of a thin, 5 nm GaAs capping layer. The purpose of this last step is to prevent an oxydation of the AlGaAs shell when the NWs are in contact with air and airborne moisture. It must be emphasized that this capping layer usually oxidized and should be seen more as $(GaAs)_x/(Ga_2O_3)_{(1-x)}$ than pure GaAs. For this reason, the last capping shell is not expected to play any role regarding carrier confinement or any functionality.

4.2 Core-Shell NWs morphology

4.2.1 GaAs core

The growth conditions described above for the GaAs core leads to the formation of zincblende (ZB) GaAs NWs. Deviation from the perfect crystal arise from single defects along the NW axis. Bright and dark-field TEM measurements revealed a significant density of stacking faults/twins, but the formation of wurtzite segments was rarely observed. The ZB crystal phase is automatically transferred to the shell thanks to direct epitaxy during the stage 3 of the growth, and so the GaAs and AlGaAs can be thought as being pure ZB. The same structure transfer happens for WZ cores (at least up to several 100 nm of material).[42]

4.2.2 AlGaAs shell

Representative cross-sections for two types of samples are shown in figure 4.1. The micrographs are obtained using annular dark-field (ADF) imaging in a transmission

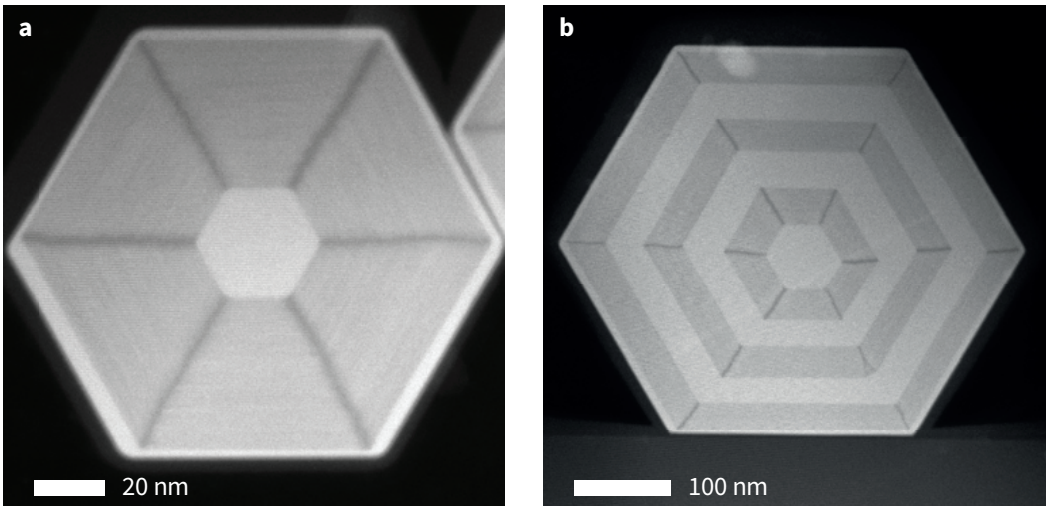

Figure 4.1 • a. Representative ADF-STEM micrograph of the cross section of a single-shell GaAs-$Al_{51}Ga_{49}As$ NW. **b.** Cross-section image of a multi-shell GaAs-$Al_{33}Ga_{67}As$ NW. The heavier Ga-rich regions appear in lighter grey. The Al-rich segregation planes at each corner of the hexagon are easily seen in both case (a) and (b).

electron microscope working in scanning mode (STEM). The sample in the panel (a) is a single-shell GaAs-$Al_{51}Ga_{49}As$ NW, while (b) represents a multi-shell (in this case 3) GaAs-$Al_{33}Ga_{67}As$ NW. The contrast between pure GaAs (light grey) and AlGaAs (darker) regions is clear and show sharp interfaces between the two. Interestingly, in both cases the AlGaAs shells present darker stripes at every hexagon's corner. These stripes correspond to Al-rich planes, few nanometer wide, running along the NW and located at each corner.

They appear as a consequences of segregation processes taking place at specific locations. Their origin is to be found in a difference in adatoms mobility for the two group-III species of the alloy (in this case Ga and Al). Such segregated planes have already been reported in either lithography defined V-groove structures and more recently in other types of III-V core-shell semiconductor NWs.[150–154]

In a first approach, for which the alloy is considered as an ideal solution, the chemical potential μ of alloy species i on a surface can be described (along one dimension) as follow:

$$\mu_i = \mu_i^0 + \frac{V_0}{2E}\sigma_\tau^2 + V_0\big(\gamma(\theta) + \gamma''(\theta)\big)\kappa + k_B T ln(x_i) \tag{4.1}$$

With V_0 the atomic volume, k_B the Boltzmann constant, T the temperature at which the process takes place and x_i the mole fraction of the species. The first term is the nominal chemical potential. The second describes the effect of a tangential stress σ_τ for a material with young modulus E. The third term depends on γ, the surface

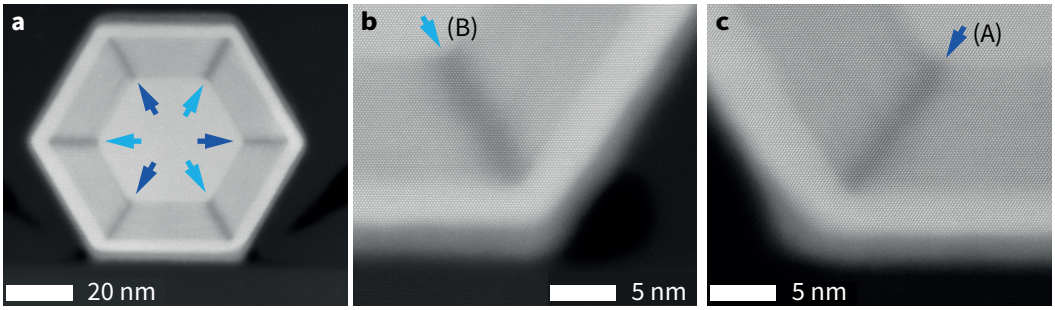

Figure 4.2 • a. ADF-STEM images of a GaAs-AlGaAs core-shell NW showing the Al-segregation planes at each of the corner. The difference in stripe thickness is in this case clear and illustrates the effect of polarity on capillary effects during the growth. **b.** Close-up on a thick stripe, connected with the (B) polarity. **c.** Close-up of a thinner stripe stemming from a (B) polarity subfacet.

free energy which is a function of θ, the surface (or facet) orientation. The last term represent the contribution coming from the enthropy of mixing and depends on the molar fraction.

In general, it is reasonable to consider the GaAs-AlGaAs binary system as being perfectly lattice-matched. The mismatch at room temperature is $\frac{a_0(Al_xGa_{(1-x)}As)-a_0(GaAs)}{a_0(GaAs)} = 0.0014x$, less than one per mil for fraction of Al smaller than 0.7.[155] The lattice mismatch further reduces with temperature, and at 450°C is about half its value at room temperature. For this reason, the crystal-strain driven growth process in GaAs-AlGaAs system are usually dismissed.

The main term in equ. 4.1 relates to curvature and surface orientation. It can be seen as describing "capillary" effects, *i.e.* mass transport arising from a gradient in surface energy. It is expected to play crucial role in the case of NWs. Indeed at the boundary between two facets, the crystal curvature is high. Furthermore, small {112} family subfacets tends to develop in-between the main 110 type facets. Thus both curvature and orientation are expected to cause a change in the chemical potential of Al and Ga adatoms. The effect can easily be seen in the appearance of the Al-rich stripes mentioned above and particularly clearly revealed in figure 4.2. If the surface of two adjacent {110}-family facets is not varying, the process is said to be "self-limited". This means that the thickness of the stripe will converge during growth toward a certain value and then remain stable. However, the area of the NW side facets does increase during growth. For relatively thin shells (typically 20-50 nm or 20 nm as shown in figure 4.1 4.2), no widening or narrowing can be seen, but the trajectory of the stripes seems wavy, as if the energy equilibrium does not present a deep minimum, allowing some deviations.

An additional specificity arises from the very nature of {112} subfacets. In this case the crystal polarity is out of the growth plane: the facets can be seen as either group-III or group-V terminated, coined A-polar or B-polar. The polarity is also likely

to influence the chemical potential and the growth rate. The latter might happen via a modification of the incoming adatoms sticking coefficients. The role of polarity has been reported first in case of MO-CVD growth.[156] For MBE growth, figure 4.2 shows that similar effects can take place. The thick and thin stripes associated with (B) and (A) polarity are clearly visible in panel (a) and close-up panels (b) and (c). The polarity breaks the symmetry of the observed structure from 6-fold down to intertwined 3-fold. The chemical composition of the Al-rich segregated planes was measured by TEM-implemented electron energy loss spectroscopy (EELS) and energy dispersive X-ray spectroscopy (EDX) and shown to reach Al fraction up to 0.5-0.6 for a nominal Al fraction of 0.33.

In addition, one may notice in figure 4.1(a) a stripe pattern in the shell of the structure, perpendicular to the <110> growth directions. The sample preparation (PIPS and ion milling) can hardly be responsible for these stripes and an imaging artifact is also unlikely to produce such a regular pattern, changing for all six facets. Considering that, a possible explanation could be connected with spontaneous short-period, long-range ordering of the Ga and Al atoms in the AlGaAs lattice. Clearly observed and explained for other compounds (chalcopyrite like $CuGaSe_2$ or $ZnGeAs_2$), this effect relies on different principles for AlGaAs and has not been often reported, its observation proving to be elusive.[157,158]

4.2.3 Punctual segregations in AlGaAs shells

In certain cases, deviations from the nominal composition can happen in the form of Ga-rich regions. The rest of this dissertation will focus on these Ga-rich segregation and it will be shown that they can behave as QDs with all the characteristics associated with such 0-D structures. An example of a punctual Ga-rich segregation is provided in figure 4.3. The panel (a) shows one of the stripe discussed previously separating the two side-facets of a multi-shell NW. However, instead of keeping a steady width and composition, the stripe seems to split open. This can be seen in the close-up displayed in panel (b) of the same figure. The stripe diverge in two branches, both Al-rich, while the central part present a contrast indicating a depletion in Al. The orientation of the side of the strip and of the fork are labeled in white. In this specific case, it can be seen that right before the next GaAs shell, the Al concentration increase again, to form a barrier with (121) orientation. This is seen in a clearer way in the panels (c), (d) and (e). In this case the elemental mapping based on EELS data are shown for respectively Al and Ga. The last panel shows the Ga/Al ratio, varying from around the nominal fraction of 0.7 down to 0.4 for the Al-rich regions.

For the case shown in figure 4.3, the Ga-rich island is located at the external part of the AlGaAs shell and is encompassed by Al-rich barriers. The shape seems to be a fairly well delimited triangle. However, some NW cross-section TEM analysis also illustrated variations of this nanostructure geometry. This is typically shown in figure 4.4. The structures observed in TEM are not necessarily optically active or able to

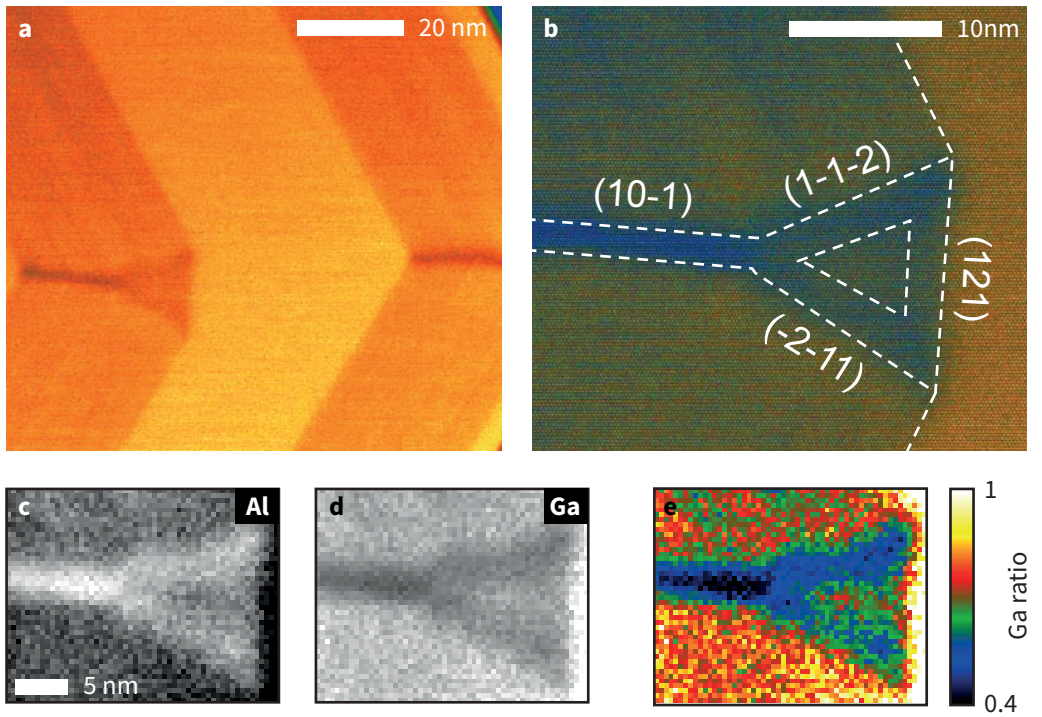

Figure 4.3 • **a.** ADF-STEM false-color cross-section image of a multi-shell GaAs-$Al_{33}Ga_{67}As$. One of the stripe presents a noticeable deviation in its shape, diverging toward a fork-like structure encompassing an island with different composition. **b.** Close-up of the fork, revealing a 5-6 nm wide region surrounded by the fork ''barriers''. **c.** and **d.** show the elemental EELS mapping for Al and Ga, with darker shade standing for lower elemental signal. **e.** Ga/Al ratio in the region of the Ga-rich island. The scale for (c)-(e) is the same.

confine carriers, but they are useful in the goal of illustrating the possible segregation effects taking place in the AlGaAs shell of NWs.

4.3 Shell luminescence: shell-QDs

4.3.1 Photoluminescence spectroscopy

Upon excitation by laser light and provided that the excitation energy is large enough, electrons from the AlGaAs valence band can be promoted to the conduction band (see section 3.1 and figure 3.1(a)). The setup used for PL experiments was already presented in section 3.1.2.

If the Ga-rich islands seen in TEM are able to trap excitons and act like QDs, narrow peaks are expected to appear in the emission spectrum of a NW, resulting from the non-resonant excitation of the AlGaAs matrix.

A typical spectrum can be seen in figure 4.5(a), where the full emission range of

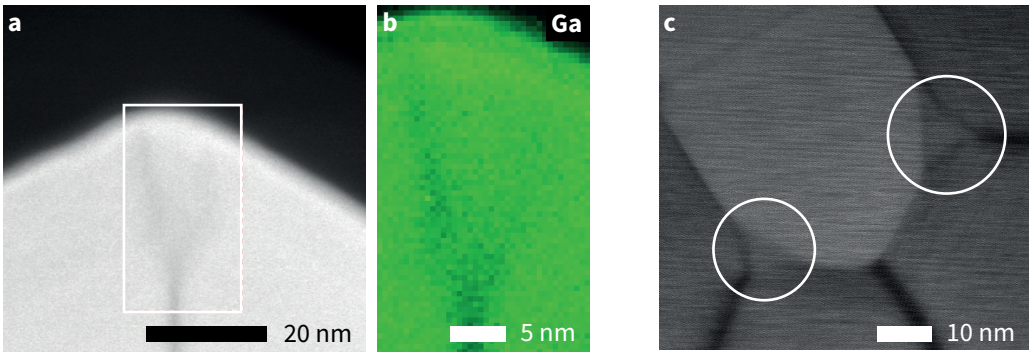

Figure 4.4 • a. ADF-STEM of a NW shell presenting a faint elongated "fork-like" structure. **b.** Elemental Ga EELS map of the zone delimited in (a). In this case the two Al-rich branches are well seen, but do not merge again after splitting. **c.** Example of segregations (outlined with white circles) occurring right after the core. The apparent elongation of the core is due to an oblique cut of the NW during the sample preparation.

a GaAs/$Al_{33}Ga_{67}As$ single shell NW is plotted as a function of the wavelength. The spectrum can be readily split in two main ranges.

1. The low energy (long wavelengths) range, between 800 and 850 nm (1.44-1.55 eV). In this region, the emission is coming from the GaAs core.

2. The high energy (short wavelengths) range, between 620 and 780 nm (1.59-2 eV). For these energies, the emission cannot come from the core. It is thus stemming from the AlGaAs shell.

The bulk ZB GaAs spectrum can be complicated by different factors. In particular, the presence of defects in the core's crystal phase, such as WZ segments (if any) or plane defects (rotational twins, stacking faults etc.) will affect the luminescence, as already explained and illustrated in figure 2.6. In figure 4.5(a), the pure phase and crystal defects-related ranges are indicated by arrows. The latter forms a low-energy tail to the ZB GaAs peak. The red-shift of the GaAs peak has also been attributed to band-bending and spatially indirect transition induced by the presence of the AlGaAs shell.[159,160]

In the high-energy range of the figure 4.5(a), it is straightforward to realize that the shape of the PL is very different from the emission of bulk material. The spectrum is composed of sharp and intense peaks, incompatible with bulk AlGaAs. Different spectra taken in the high-energy region for NWs with different shell compositions is represented in figure 4.5(b). Similar sharp peaks are recorded. A control experiment with a pure AlAs shell showed no PL at high energy.

The panel (c) shows a schematic of a NW cross-section, and the associated simplified bandedge diagram with the possible optical transition. Panel (d) shows the

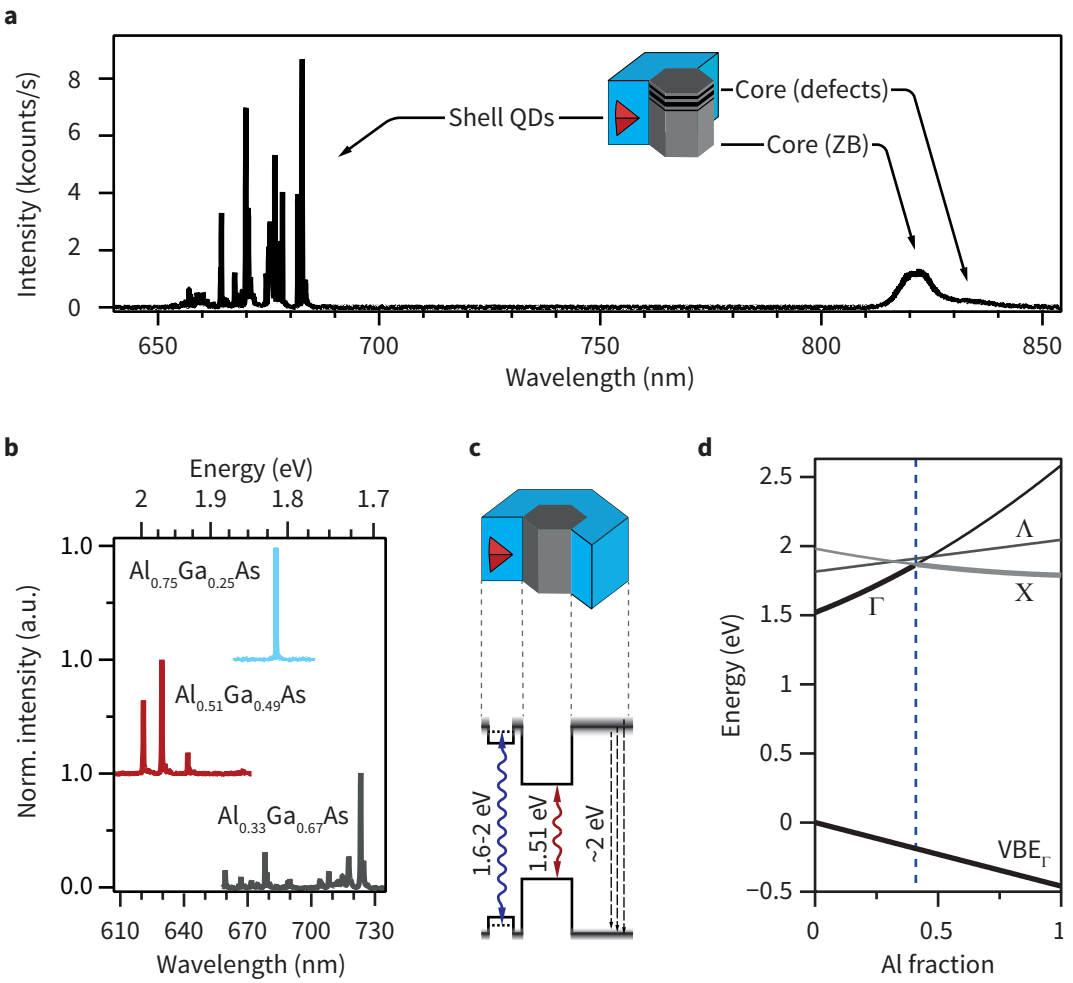

Figure 4.5 • **a.** Typical PL wide-range spectrum of a GaAs-AlGaAs core-shell single NW at 3.85 K. The luminescence from the core and the associated defects (twins, crystalline changes) is recorded above 820 nm. The shell bulk emission is absent (indirect band transition for Al fraction above 0.44) but luminescence below the AlGaAs bandgap is recorded and associated with segregated shell-QDs. **b.** Example of spectra for three shell compositions (33, 51 and 75 Al fraction) at 10 K. **c.** Schematic of a NW and its associated the band-edge diagram with the low bandgap core (grey), the mainly indirect wide gap shell (cyan) and a shell-QD (red). **d.** Band edges for a random AlGaAs alloy. The valence band maximum and the three conduction band minima are drawn. The global conduction band minimum is outlined in bold, with the cross-over point (Γ-X) at around 0.4 Al fraction marked with a dashed line.

energy dependance of the valence band maximum and conduction band minima at high-symmetry points of the Brillouin zone (Γ, Λ and X) as a function of the Al fraction in a random AlGaAs alloy at 5 K. A crossing point between momentum-space direct and indirect transition can be seen for fractions around 0.4. For this reason, the luminescence of AlGaAs (even at lower, 0.33 Al fractions) is negligible. This explains the lack of an AlGaAs-related peak in the spectra. The same reason leads to the conclusion that the sharp peaks seen in 4.5(a-b) can be attributed to the Ga-rich islands seen in TEM experiments. These islands are thus playing the role of quantum-confining nanostructures (shell-QDs). Alternative explanations have been given by Rudolph *et al.* in ref. 161, where the sharp peaks in the NWs spectra originates from point defects in the AlGaAs lattice, probably As-antisite defects. Several indicators and arguments against this interpretation will be given by later results. For now, the first counter-argument is the spread of the high energy emission range, down to 1.7 eV (figure 4.5(b), grey spectrum). Point defect in AlGaAs are spectrally located closer to the AlGaAs bandgap. Also, the intensity of the sharp peaks is considerable and poorly explained by bound excitons in a quasi-indirect crystal.

4.3.2 Cathodoluminescence imaging

If PL can provide detailed spectra, the imaging of where the emission is taking place in the NW is limited by the optical resolution. This is particularly true in the case of highly scattering structures like NW, where the resolution given by the point-spread function of the optical system is not necessarily reached.

A method to overcome this limitation is to use CL to excite the NWs at different points, and record the emitted light. The following measurements were realized at 10K in a setup described in section 3.3 and figure 3.7. The acceleration voltage is typically between 2 and 5 keV. The fluence of the beam is controlled by apertures of different sizes, and typically can be set at a minimum of few tens of pA up to hundreds of nA.

First, a low magnification image of single shell NWs is shown in figure 4.6. Panel (a) shows the CL signal from the core (GaAs) of three NWs, with the following color-code: blue stands for the bulk ZB GaAs spectral region while red is used for the lower energy, defect-related tail (see bottom inset). The emission from the core can be seen to be continuous along all the NWs. In this particular sample, the last microns of the tip of the NW appear to be particularly defective.

Panel (b) shows the full core emission (bulk ZB + defects) in blue, while the high energy emission corresponding spectrally to the sharp peaks seen in figure 4.5 is encoded in red (see bottom inset). It can be seen that several red luminescence centers can be localized along each NW. From this mapping, it does not seem that the defects resulting in red-shifted core emission are correlated with the presence or absence of optically active shell-QDs

In each CL maps, the white asterisk mark the position corresponding to the (upper,

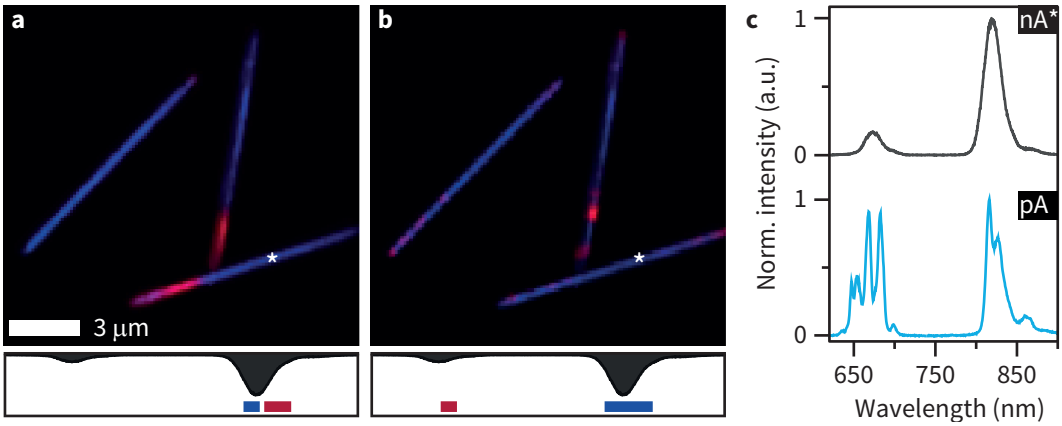

Figure 4.6 • a. CL mapping of the core emission of GaAs/AlGaAs NWs. The blue regions represent emission from pure ZB GaAs. The red color outlines regions emitting light related to crystalline defcts. **b.** CL mapping of the same NWs. The full core emission is shown in blue. The red color corresponds to emission in the high energy range (shell-QDs). Localized emitters can be seen along the NWs. The bottom insets in (a-b) graphically represents the spectral regions for the color-coding. **c.** top, black line: CL spectrum extracted for the position marked with a white star in (a) and (b). The electron beam fluence (nA) is shown in the inset legend. Bottom, blue line: spectrum from a different NW, showing a spectrum for a much reduced fluence (pA). The broad peak corresponding to shell-QD emission decomposes in a set of much sharper emission lines.

black line) spectrum shown in figure 4.6(c). In this spectrum, one can clearly distinguish the GaAs peak and a vanishing defect-related tail. In addition, the set of sharp peaks present in PL at high energy left place to a broad, lower intensity peak. It has to be notted that in this case, the electron beam fluence was relatively large, in the nA range. The lower, blue-line spectrum shows the result of an excitation at much lower fluence, in the tens of pA (different NW). The decrease in beam fluence translates into a clear increase of the shell-QD/GaAs emission ratio. In addition, the features of the spectra become much sharper, with the re-appearance of individual peaks instead of the broad single gaussian-like feature seen for nA fluences.

Thus, it appears that the shell-QD emission is very sensitive to the electron beam fluence. A high fluence broadens the spectra, but also reduces the emission intensity of the exposed QDs. This is the results of a total saturation of the QDs and the opening of non-radiative decay channels (*e.g.* through Auger processes). It should be noted that this broadening and intensity reduction are not permanent. None of the shell-QDs observed so far seemed to be permanently bleached by the electron beam exposition. The deposition of carbon residues on the NWs during observation with SEM might induce changes in the emission spectrum, but in this case, the linewidth broadening due to the high excitation linked with an electron beam hinders the observation of small shifts of the emission peaks.

Figure 4.7 shows iso-color (spectral window around 3 nm) high-magnification CL

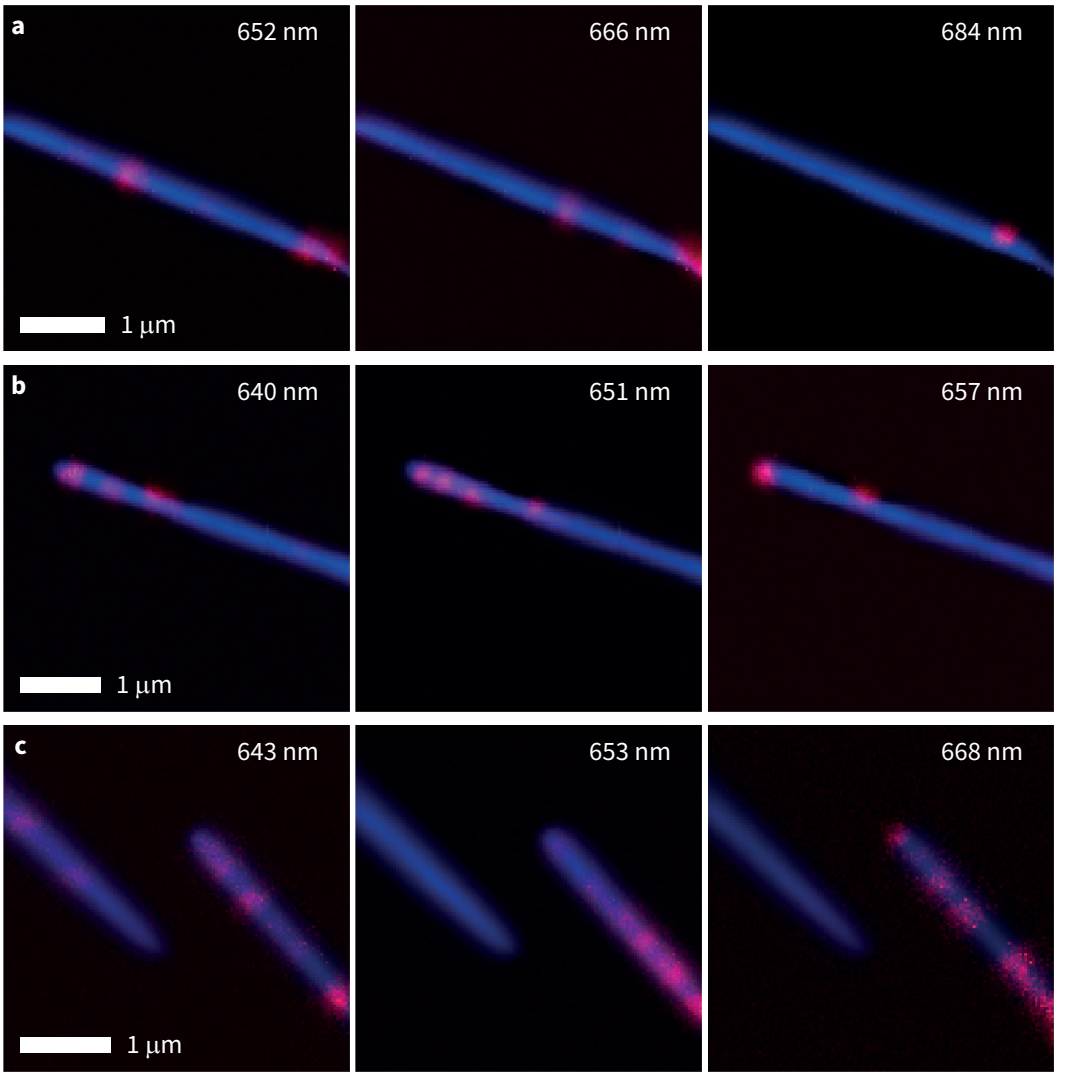

Figure 4.7 • a. High magnification CL mapping of a NW at three different emission wavelength (inset). The blue shade is systematically representing the GaAs core emission while the red color is used to mark the location of shell-QDs at the designated wavelength. **b.** Same as (a), for a different NW. **c.** CL mapping of twor NWs tips close to each other.

mappings of shell-QDs in different NWs ((a-c), top to bottom) and at different emission wavelength (from left to right). The NWs core CL signal is shown in blue (spectral window of 10-20 nm centered at 830 nm). The position of the shell-QDs spectral window is indicated for each mapping in the top-right corner.

The three panels clearly show the different emitters located at different position within the wires. They also reveal that the emission is coming from extremely localized regions. Mappings like the 684 nm cut of panel (a) or the 657 nm cut of panel (b) illustrate particularly well the location of the emitters in the shell of the wire. In these

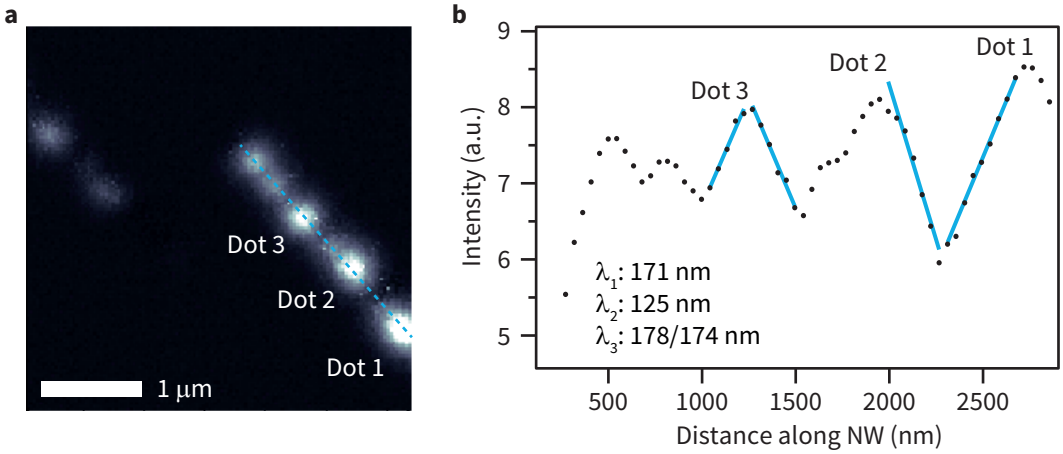

Figure 4.8 • a. Panchromatic CL mapping of the three frames in figure 4.7(c). Three bright and isolated shell-QDs are indicated (Dot 1, 2 and 3). **b.** Intensity of the CL signal along the NW in (a), marked by the dashed blue line. The solid blue lines indicate the fits to retrieve the carrier diffusion length λ. The latter are indicated in the graph for the shell-QDs 1, 2 and 3. Two values are provided for Dot 3, as the two sides left and right of the maxima were possible to fit.

two mappings, the luminescence is clearly coming from a location shifted with respect to the NW axis. Interestingly, it seems that optically active shell-QDs often tend to be "clustered" on hot-spots, and even the improved resolution of CL over PL (in our case around 10 times better, but highly dependent on the setups and samples) is not sufficient to resolve close-by emitters.

This clustering effects can be intuitively understood if one considers the formation of Ga-rich islands. It is expected that a particular "topographic" environment (curvature and chemical potential gradients) is required for the segregation process to take place. Hence it seems probable that these regions present favorable conditions to give rise to several Ga-rich islands, close to each other.

The overall resolution of CL mappings is a combination of various factors. The incoming beam diameter, around 5-10 nm, plays a negligible role in the resolution. Instead, the interaction volume of the electron beam with the semiconductor and the diffusion of the generated electron-hole pairs are the main factors limiting the resolution.

Both factors are greatly complicated by the specific NW geometry. The interaction volume in a NW will differ from the one in the case of a planar structure for similar electron parameters as the primary or generated electrons can "leak" out of the structure by the side facets. In our case, the diffusion of electron-hole pairs in the shell is expected to be reduced compared to bulk values for two main resons: (i) the presence of interfaces with vacuum on the external side of the shell, inducing surface recombination and (ii) the presence of the low bandgap GaAs core, acting as a sink for electron and holes in the shell.

An estimate of the resolution and of the shell-QDs "carrier capture area", representing the joint diffusion length of electron and holes, is provided in figure 4.8. Panel (a) shows a high-energy panchromatic mapping of the region shown in figure 4.7(c). Several shell-QDs can be seen, amongst which three particularly bright and isolated (marked Dot 1, Dot 2 and Dot 3). The intensity linescan corresponding to the dashed blue line is shown in figure 4.8(b). The decrease in intensity is fitted by an exponential decay model, and the related decay length λ can be extracted. They are shown for each dot as an inset. The measurement could be realized on both side of Dot 3 and yield very similar values. Altogether, the extracted values are closely-grouped around 150 nm.

These values are in stark contrast with the expected diffusion length in a quasi-indirect semiconductor, for which diffusion values up to few microns are commonly measured. The GaAs/AlGaAs type-I band alignment between the core and the shell creates a strong radial gradient in the (electronic) chemical potential. As a consequence, the spread of carrier in the shell is strongly decreased. In addition, even if the electron beam interaction volume is reduced by the NW geometry, it is expected that it reaches an effective radius in this range of a hundred of nanometers.

It should be noted that an advantage of CL is the absence of strong scattering phenomena destroying the shape of an optical pump beam. Instead, even if the interaction volume broaden the excitation area, the shape remains mainly gaussian. Thus, provided that good beam setting can be found (in term of acceleration voltage and beam fluence), the interaction volume could remain limited while the number of electron-hole pair is also kept low. In turn, the "primary" spatial resolution could be maintained while spectra with sharp features are restored. The contrast in particularly striking in figure 4.6(c). Once individual emission peaks can be resolved and isolated in a iso-color image, a gaussian profile can fitted for each emitter and the limitation on the localization accuracy is given mainly by the number of photon collected. This strategy, somewhat analogous to "superresolution" microscopy techniques based on stochastic reconstruction, would allow to build particularly high-resolution images of the localized emitters.

4.4 Measurement-based calculations of energy states

A possibility to link images of structures obtained by TEM and optically active QDs measured in PL or CL experiments relies on simulation of the electronic structure based on the micrographs. Two complementary sophisticated types of simulations have been realized for the structures shown above. These methods allow to get insight in the quantum confinement phenomena happening in these nanostructures.

The first one is based on the well-developed method of empirical pseudopotentials. The computational setup consist in a half-a-million atoms cell. A 9nm tall square -based pyramidal region of Ga-rich material (90%) is enclosed in Al-rich barriers (2.5 nm in

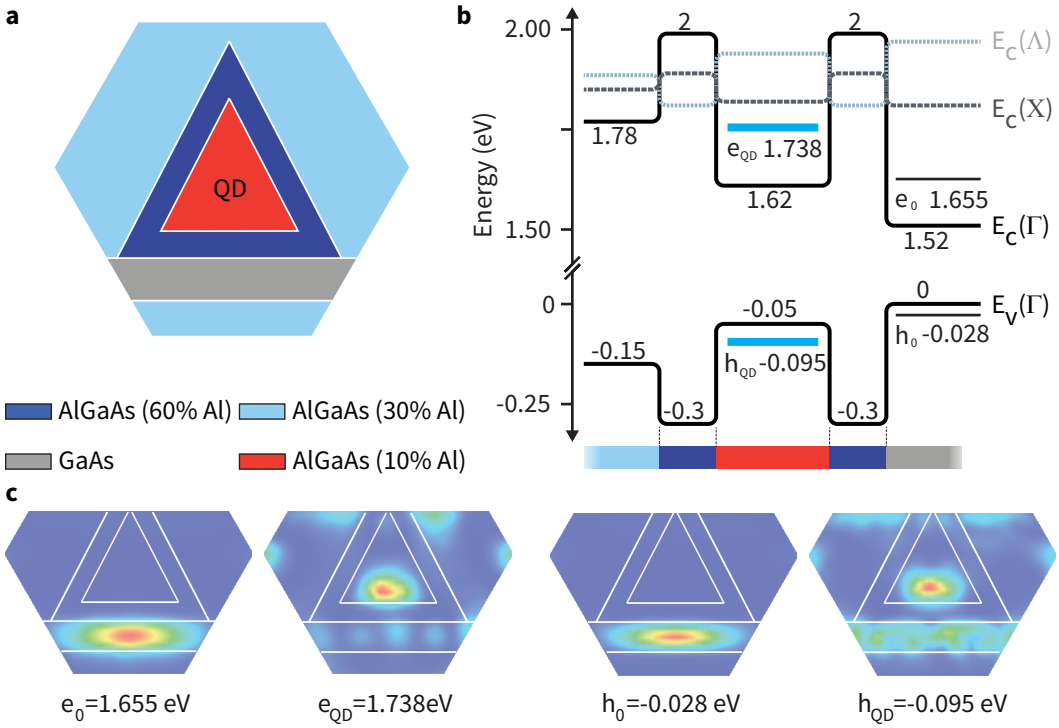

Figure 4.9 • **a.** 2D representation of the computational cell. The Al-depleted region is surrounded by Al-enriched barriers. The pyramidal structure is in direct contact with a $Al_{0.3}Ga_{0.7}As$ matrix, and pure GaAs on its bottom facets [121]. **b.** Drawing of the band-edge structure corresponding to 3D empirical pseudopotential calculations based on TEM images of a segregated island. **c.** Probability functions for the lowest electron (e_0) and hole (h_0) energy and for e_{QD} (h_{QD}), the lowest-energy states localized in the segregated island.

thickness, 60% Al). The pyramid is surrounded by an AlGaAs matrix (30 % Al) on four facets and by a pure GaAs layer on the base (representing the GaAs core or alternatively the next GaAs shell). A 2D representation of the computational cell is shown in figure 4.9(a). The atomic Schrödinger equation is solved using the superposition of the atomic pseudopotential of Ga, As and Al as global potential. Random alloying is assumed to position the Al atoms on the lattice sites.

The results are visible in figure 4.9. In panel (b), the valence and conduction band-edge(s) are shown. The conduction bands minima at high symmetry points Γ, X and Λ are drawn in different colors. The different computed states for electrons and holes are represented in their respective locations with black levels. Panel (c) shows the squared modulus of the wavefunctions for electron and holes corresponding to two kind of situation: the lowest-energy states computed (e_0 and h_0) and lowest-energy states located mainly in the segregated island (e_{QD} and h_{QD}).

The results for the lowest energy states (for both electron and holes) are expected: the carriers reside exclusively in the low-bandgap GaAs region. The confinement en-

ergy is in this case related to quantum confinement introduced artificially by the computational cell design, as the GaAs region small thickness acts as a quantum well.

On the other hand, higher energy levels are found to be confined mainly in the Ga-rich pyramid, despite the very small thickness of the Al-rich barrier and the direct contact with GaAs. For larger spacing between the Ga-rich regions and low bandgap GaAs, the wavefunction leakage in the GaAs continuum is expected to be ultimately zero. The calculation predicts transitions energies in the order of 1.8 eV (evidently strongly dependent on the size). In addition, the electron and hole wavefunctions are found to overlap to a great extent, in real- and momentum-space. Thus a high oscillator strength is expected, translated in short lifetimes and high brightness. Both predictions will be confirmed by PL measurement described in the next section and chapters.

The second method used to explore the possibility of quantum confinement of the carriers in the segregated islands seen in TEM rely on a different, less scalable approach, namely Local Density Approximation Density Functional Theory (LDA-DFT). This *ab-initio* strategy does not allow to simulate a real-size 3D problem, but in counterpart interesting effects can be taken into account, *i.e.* the polarity of the crystal and the resulting internal electric fields. The computational cell for LDA-DFT calculations consists in a 5000 atoms 2D diamond supercell, repeated periodically in the three axis. In the plane, a Ga-rich triangle standing for the segregated island is defined, surrounded by Al-rich barrier, one of which being polar. Out of plane, the periodic boundary condition extends the geometry to infinity. For this reason, the calculated problem is reduced to finding the solutions for a quantum wire instead of a quantum dot. Initially, two sets of calculations were run. The first consists in a matrix material made of randomly alloyed AlGaAs on two sides of the triangle and of GaAs on the third side, where the polar barrier is defined. In the second set, the matrix is completely made of AlGaAs.

The results of the first calculation set are shown in figure 4.10(a), and in 4.10(b) for the second set. For the valence (hole) states, the results are similar for the two sets. The hole wavefunction is confined by the AlGaAs barriers inside the Ga-rich island. The geometry (triangular) more than the polarity seems to play a role in the fact that the wavefunction penetrates slightly less in the polar barrier than in the non-polar ones.

The situation is different for the conduction (electron) states. In both cases the wavefunction, while being mainly localized in the Ga-rich triangular area, also has a significant fraction spilling out of it. The effect is more pronounced for the set with adjacent GaAs, as expected. As for the valence states, the effect of the barrier polarity is not noticeable.

Finally, a third set of LDA-DFT calculation was made for a scaled-up case, closer to the realistic dimensions. The computational cell was similar as the one of the first set, but the number of atoms was increase to above 12000. Because of the high computational cost of this arrangement, the problem was solved for conduction states only. The result of this calculation is shown in figure 4.10(c). For this larger structure,

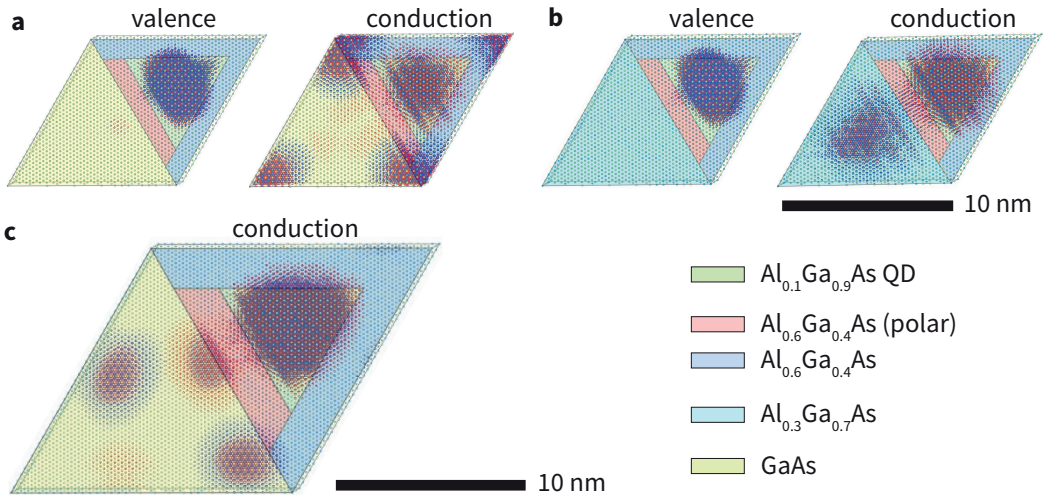

Figure 4.10 • LDA-DFT calculations for valence and conduction states, based on TEM measurements. The calculation include internal electric fields (polar facets). **a.** Segregated Ga regions shielded by Al-rich barriers from a pure GaAs matrix. **b.** Same as (a) but for a $Al_{0.3}Ga_{0.7}As$ matrix. Both (a) and (b) are 5000-atoms calculations. **c.** 12000 atoms model analog to (a). The confinement is much more pronounced since the Ga-segregated island is larger. Due to 2D nature of the calculations, the simulations actually represent a quantum wire.

the conduction state wavefunction is clearly localized in the Ga-rich triangle. The non-zero probability in the GaAs are at least partially due to computation artifacts and it can be seen that the confined wavefunction does not physically spill out of the barriers. It should be noted that in this case, the Al-rich barrier are also thicker, and thus helps the confinement within the Ga-rich region.

It should be added that for LDA-DFT calculation, the calculated energy splitting between the confined valence and conduction states is also approximatively 1.85 eV. However, the fact that this energy difference fits what is commonly observed in PL spectra should be mitigated and is likely to be fortuitous, given the usual inaccuracy of DFT-based method to predict correct valence-conduction bands separation.

In general, the two methods agree in the sense that both predict confinement of both electrons and holes in the segregated islands seen in TEM measurements. The large-scale empirical pseudopotential calculations ensure that this is the case even for 3D confined structures. In addition they predict reliable optical transition energies in range with what is commonly observed. The LDA-DFT calculations allow to confirm these results and rule out a significant effect of the facets polarity in the confinement of the electron and hole wavefunctions.

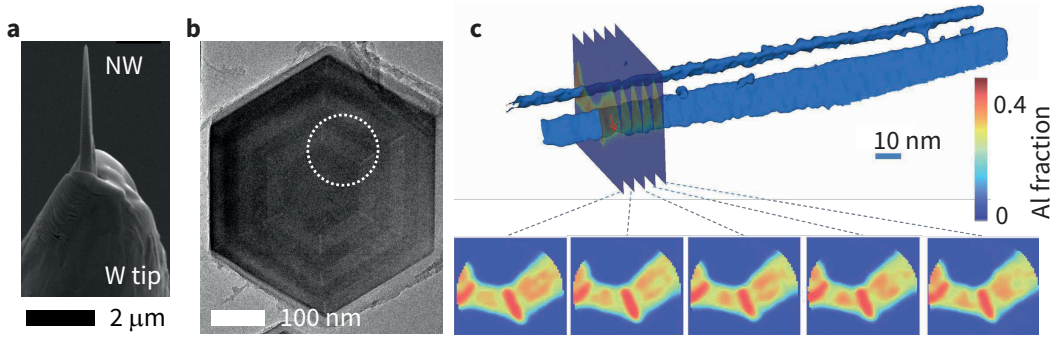

Figure 4.11 • a. SEM image of a tungsten (W) tip fitted with a NW ready for analysis, the NW has been (FIB) sharpened in a needle shape. **b.** Cross-section TEM of a specimen used for APT analysis. The dashed circle represents the area observed by APT. **c.** In blue (up), 3D reconstruction of the isosurface corresponding to an Al fraction of 0.4. The cuts (down) show the cross-sections of the sample. The Al-rich planes can be well identified, as well as minor inhomogeneities in between them.

4.5 3D mapping with atom-probe tomography

Another important insight in the morphology of Ga-rich segregated islands in the shell of GaAs-AlGaAs NWs has been provided by atom-probe tomography (APT). As reported recently by Mancini *et al.* (see ref. 162), core-shell NWs composition can be measured with high spatial and elemental resolution in a small region of interest by APT.

Briefly, the technique consists in applying a high electric field between the NW tip, and an electrode. The ionization of atoms is then triggered and the atoms are detected on a distant multi-channels 2D detector. The nature of the detected atoms is determined with a time-of-flight (TOF) method. The triggering is provided by a punctual excitation of the atoms at the tip of the sample with a short laser pulse. The pulses provide the necessary energy for the atoms to get ionized at a regular rate. Because only the atoms at the surface of the tip get ionized, the z-position of the atoms is intrinsically bound to the corresponding laser pulse. More details can be found in refs. 162, 163.

The analysis was made on GaAs-$Al_{33}Ga_{67}As$ multi-shell NWs. Since the as-grown NWs diameter is too large to obtain a good field at the tip, focused ion beam (FIB) was used to sharpen the NWs into suitable pencil shapes. The image of a sample ready for APT analysis is visible in figure 4.11(a). The sharpened NW can be seen mounted on a tungsten tip (marked W) serving as a holder. The approximate field-of-view resulting from the sharpening is outlined in dashed white in a TEM image of the corresponding sample (figure 4.11(b)). In the same figure, the upper part of panel (c) shows the alloy composition boundaries (isosurfaces) for Al-rich regions. Thus the two Al-segregated planes become plainly visible and are seen running continuously along the wire. The lower part shows five successive cuts in the dataset corresponding to cross-sections

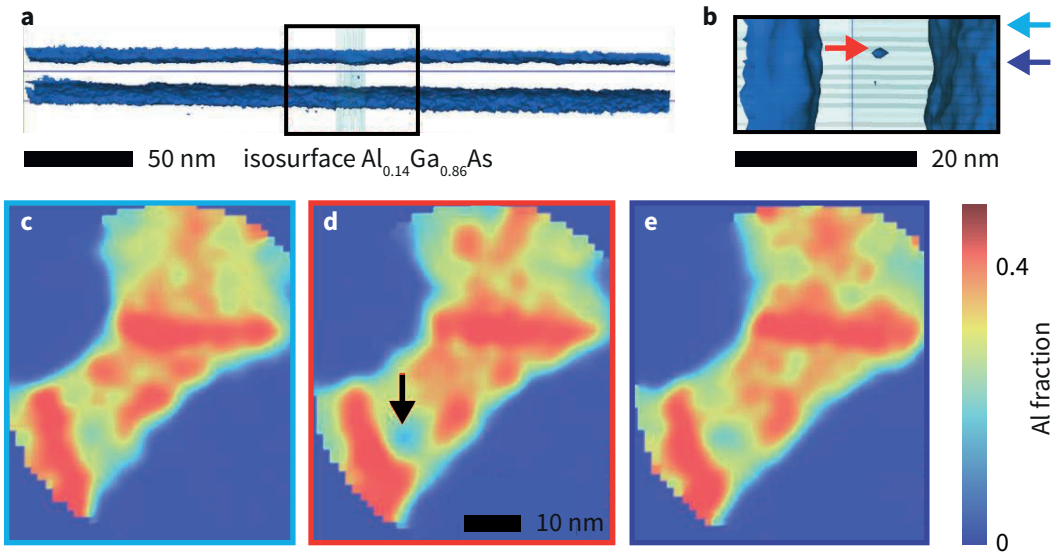

Figure 4.12 • **a.** APT reconstruction of the $Al_0.14$ isosurfaces along the NW. The isosurfaces mark the limits of Ga-rich regions. **b.** close up of the black delimitation in panel (a). The core/first shell (GaAs/AlGaAs) and first/second shells (AlGaAs/GaAs) boundaries can be seen, as well as a clear isolated Ga-rich island in the AlGaAs shell. **c.**-**e.** Cross-section representations at the arrows drawn in (b). The Ga-rich island is clearly isolated in the middle of the matrix. Panel (d) shows a gradual decrease in Al fraction down to less than 0.07.

along the analyzed NW. Again, the Al-rich stripes can be easily recognized, as well as the boundaries between the AlGaAs shell and the GaAs core and shell respectively. The composition in between the stripes is not completely homogeneous. Local Al-rich "patches" are observed but in this case, no well-defined Ga-rich region could be identified.

It could be noticed that the cross-sections look distorted from the planar facets as they can be seen in TEM. In particular, the Al stripes seems to protrude slightly outward. This phenomenon, known as local magnification effect, is an artifact of the measurement and is not related to a local change in morphology in this particular NW.

Finally, the figure 4.12 shows an APT analysis along a different NW, along around 300 nm. The panel (a) shows the isosurfaces corresponding to an Al fraction of 0.14, *i.e.* they mark the transition between AlGaAs and Ga-rich regions. As expected, the inner border between the GaAs core and the AlGaAs shell is represented by one of these isosurfaces, as well as the outer border between the AlGaAs shell and the next GaAs shell.

This time, a clear feature can be seen in the middle of the analysed segment. It corresponds to an isolated Ga-rich island in the middle of the shell (outlined with a black box). The panel (b) of figure 4.12 shows a close-up of this region (image rotated by 90 degrees). It is clear that the isosurface for this alloy composition can be seen as an

ellipsoid of few nanometers in diameter. The arrows indicates the various heights for which cross-sections are displayed in panels (c) to (e). The punctual Al depletion can be seen clearly in these three cuts, in particular for the cross-section shown in (d). The Ga-rich region is slightly below 10 nm in diameter, and the alloy composition varies relatively smoothly until reaching the minimum, at an Al fraction less than 0.07. The upper and lower cuts show that the Ga-rich island is finite in 3D.

In this case, a noticeable difference compared to TEM images is that the Ga-rich structure does not seems to be encompassed within a divergent Al-stripe like it can be seen *e.g.* in figure 4.3. However, it is still located just next to one of this stripe, and is flanked by another Al-rich region. Thus in both cases, the creation of an Al-depleted region is likely to come from the formation of a neighboring Al-rich region. The segregated stripes at the hexagon corners are likely to serve as "hot-spots" for the formation of nearby Ga-rich pockets, localized in 3D and which can act as QDs provided that their size and the Ga fraction is high enough.

4.6 Conclusions

In this chapter a new type of NW-based optically active QDs, called shell-QDs, were introduced. The QDs optical signal consists of sharp emission peaks (FWHM systematically below 1 meV, often in the 100μeV range) in the red region of the visible spectrum. According to the high-resolution (S)TEM cross-section measurements, the shell-QDs consists in nanometer-size Ga-rich islands nested in the AlGaAs shell of the NWs. Self-assembly of these islands is thought to be driven by segregation process associated with curvature-dependent chemical potential as well as orientation-dependent sticking coefficient of the Al and Ga atoms during growth. As for now, the control over the creation of shell-QDs is still limited (see next chapter), in particular, the location of the QDs along the NWs cannot be predetermined. A better understanding of the interplay between the core morphology and the detection of shell-QDs is key in order to deterministically grow and position shell-QDs along their NW hosts.

Low-temperature CL was leveraged to overcome the limited spatial resolution of PL. CL mappings revealed that the sharp peaks seen in low-temperature PL measurements stem from localized emitters clearly located in the AlGaAs shell of GaAs/AlGaAs NWs. Shell-QDs located less than 250 nm apart could be resolved.

Further, two different calculation methods, based on the (S)TEM measurements, were harnessed in order to provide a link between the Ga-rich islands in TEM micrography and the measured luminescence spectra from NWs in both CL and PL experiments. Despite the difference between empirical pseudopotential and LDA-DFT methods, both confirm that the features spotted by TEM analysis can act as optically active QDs. Both also predict a strong confinement, limited to the ground states of electron and holes.

Finally, APT proved to be a powerful method to investigate the NWs composition in 3D. The APT measurements match the TEM results and an example was provided showing clearly a Ga-rich island, located near an Al-rich stripe and completely surrounded by the AlGaAs matrix.

Publications • The results presented in this chapter can be found partially in the following peer-reviewed publications:

> "Self-assembled quantum dots in a nanowire system for quantum photonics", M. Heiss, Y. Fontana, A. Gustafsson, G. Wüst, C. Magen, D.D. O'Regan, J.W. Luo, B. Ketterer, S. Conesa-Boj, A.V. Kuhlmann, J. Houel, E. Russo-Averchi, J.R. Morante, M. Cantoni, N. Marzari, J. Arbiol, A. Zunger, R.J. Warburton and A. Fontcuberta i Morral, *Nature Mater.*, **12**, 439-444, 2013.
>
> "Three-dimensional nanoscale study of Al segregation and quantum dot formation in GaAs/AlGaAs core-shell nanowires", L. Mancini, Y. Fontana, S. Conesa-Boj, I. Blum, F. Vurpillot, L. Francaviglia, E. Russo-Averchi, M. Heiss, J. Arbiol, A. Fontcuberta i Morral and L. Rigutti, *Appl. Phys Lett.*, **105**, 243106, 2014.

Contributions • E. Russo-Averchi, M. Heiss and A. Fontcuberta i Morral grew the NW samples. J. Arbiol, C. Magen and S. Conesa-Boj performed the (S)TEM measurements and the preparation of the (S)TEM samples. L. Mancini, I. Blum, F. Vurpillot and L. Rigutti prepared and measured the NWs in the APT experiments. J.W. Luo and A. Zunger realized the empirical pseudo-potential calculations. D.D. O'Regan and N. Marzari realized the LDA-DFT calculations. The results were thoroughly discussed and analyzed by YF, AFiM and each respective third-party collaborators.

Acknowledgements • S. Sonderegger, J. Berney, O. Gougeon and D. Gachet of Attolight^{TM} are warmly thanked for the access to a Attolight^{TM} Rosa CL tool, and for the precious councils pertaining to CL measurements. G. Jacopin and M. Shahmohammadi, J-D Gagniére and B. Deveaud are also thanked for the access to fs-time resolved and CL apparatus and for the precious ideas, particularly on CL.

Effects of Growth Conditions 5

This chapter focuses on the effect of growth conditions on the generation of optically active QDs in the shell of GaAs/AlGaAs NWs. As with a multitude of other epitaxial systems, the conditions such as temperature or nominal alloying can influence the resulting structures. Most of the time, the expected functionalities can be improved and optimized for a given set of growth conditions.

In a first step, it will be shown that the formation of optically active shell-QDs in NWs occurs for broad range of alloys. Following, the effect of temperature on the QDs density and emission energy will be presented. Finally, as the growth of self-assembled segregated QDs is inherently time-dependent and thus tied to the shell thickness, results as a function of the shell thickness will be discussed. In addition, it will be shown that the insertion of a thin AlAs "predeposition" layer can strongly influence the observation of shell-QDs in the NWs with thin shells.

5.1 Methods for large scale photoluminescence study

In order to produce volumes of data large enough to extract statistically meaningful results, a slight variant of typical micro-PL measurement is used. The measurement on as grown NW ensemble leads to the observation of inhomogeneously broadened spectra, for which the contribution from individual QDs can barely be isolated. On the other hand, confocal PL measurement on single NWs can yield a low number of peaks per spectrum, in particular for sample for which shell-QDs are scarce. These limitations are overcome by depositing NWs on silicon substrate coated with gold (acting as a back-mirror) in such a way that the NW density is high. The focal spot of the laser beam on the sample is slightly enlarged (defocusing) in order to illuminate a broader area, where the luminescence is collected.

This principle is pictured in figure 5.1(a) were the black circle represents the full field-of-view (FOV) and the laser spot (purple) is shown to illuminate several QDs at the same time. Within this spot, the luminescence of several QDs is recorded (blue spots). The laser power is kept low. The low excitation power ensures that QD carrier filling

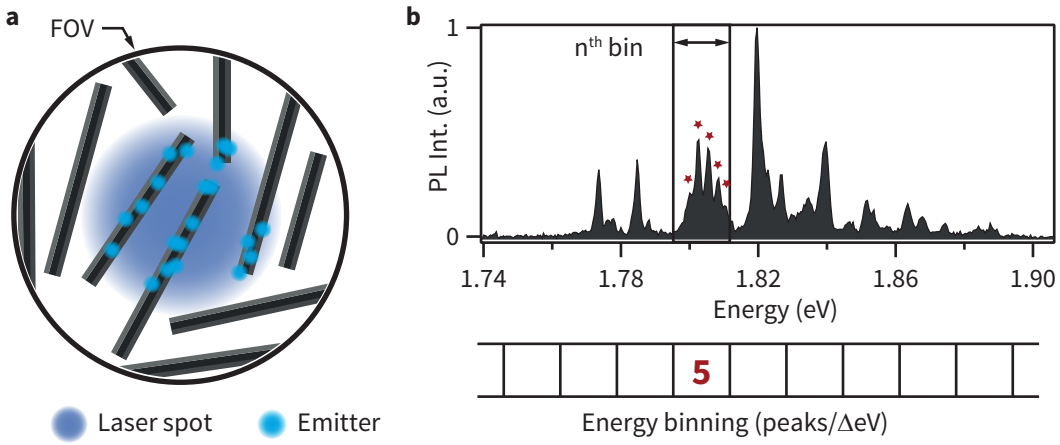

Figure 5.1 • a. Field-of-View (FOV) of a high-density sample. The laser spots (purple spot) illuminates several QDs/NWs which in turn emit the recorded signal (blue spots). **b.** Representative spectrum of a measurement. Individual peaks are tagged (red stars) before being casted in bins of defined energy span (bins below the spectrum). In this case, this spectrum contributes to five peaks in the nth bin.

and multiexcitonic produce multiple peaks for a single shell-QD. The spectra acquired following this method consist of a multitude of peaks. A representative example is shown in figure 5.1(b). The main strategy consist of relying on an automated routine to find individual peaks in the spectra, tag them and cast them in occurrence histogram. The procedure is shown in figure 5.1(b) with the red stars, marking individual peaks, subsequently casted in a bin. Iteration over several dozens of spectra allows to build histograms with a high number of occurrences per bin. The bin size is chosen in order that the total number of bins is approximately equal to the square root of the number of tagged peaks. However, the same bin size is always used for histograms pertaining to the same measurement series. The advantage over PL on large ensembles is that the measurement is mostly decoupled from intensity effects. In other words, the statistic will not be biased if (for arbitrary reasons) QDs in a certain spectral range emit more strongly than others.

The experiments were performed in an open-loop cold finger cryostat, at 10 K similar to the one described in figure 3.3(right). The laser used to excite the NWs is an Ar-Kr ion laser operating at 488 nm. The laser power was typically 1 μW before the objective. The signal was analyzed with a 500 mm spectrometer and a 300 l/mm grating (Al fraction and temperature measurements) or a 600 l/mm grating (shell thickness measurements) and recorded on a Peltier cooled silicon CCD camera.

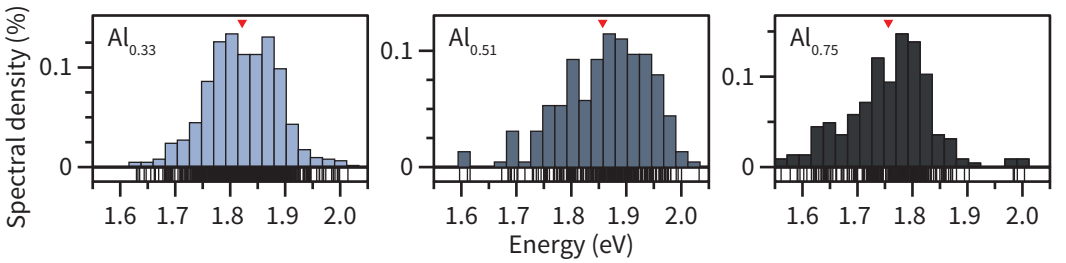

Figure 5.2 • Histogram of the spectral density for three different shell compositions, 0.33, 0.51 and 0.75 Al fraction, as shown in the graphs insets. The bar-code graph of the individual peaks making up the histogram is shown below 0 ordinate.

5.2 Effect of the Aluminum content in the shells

The figure 5.2 shows the spectral density histograms, *i.e.* the number of peaks per energy bin. The spectral density is normalized to an integrated value of 1 (sum over the complete histogram). Samples with three different shell Al fractions (0.33, in light gray, 0.51, medium gray, and 0.75, dark gray) were tested. The red arrows above the histogram represents the mean value of the distribution. The energy of each tagged peak is reported in a bar-code graph below the 0 ordinate.

At first sight, the distributions shown in figure 5.2 are roughly similar. However, a first differentiation can be made based on the bar-code graphs. The number of optically active QDs per spectra decreases with the increase in Al fraction (each histogram is built on the same number of spectra, 30 ± 1). Second, the mean of the distribution peaks slightly above 1.85 eV for the 0.51 Al fraction shells. Both 0.33 and 0.75 Al fraction have lower mean value, as well as lower energy cut-off.

These results can be explained by considering shell-QDs nucleating in the different shells. The higher the Al content, the harder it is for a QDs to reach a minimum Ga/Al ratio allowing the confinement of both electron and holes. Similarly, owing to the segregation-driven formation process, it is possible that smaller QDs are also endowed with a lower Ga/Al ratio. In this view, the lower mean emission value for the 0.33 Al fraction sample with respect to the 0.51 Al fraction sample is due to the nominally "high" Ga/Al ratio. It allows a significant fraction of the emitter to reach high Ga concentration, even for small QD size (higher density of optically active shell-QDs). The reduced number of emitters above 1.95 eV can be imputed to the height of the conduction band barrier mainly, not high enough to confine the electrons.

Following the same argument, the number of optically active QDs is the lowest for the 0.75 Al fraction sample, as can be seen in the bar-code graph. For this shell composition, the recess in the mean emission value and energy cut-off (below 1.9 eV) is also pronounced compared to the 0.51 Al fraction sample. For a composition of 0.75 Al, the shell is now clearly in the indirect conduction band minimum regime. The band minimum has now a X character. The particularity is that the X minimum

decreases in energy for higher Al fraction. Thus, the electron barrier height decreases as well for high, 0.75 Al fraction of the matrix. An electron confined in a small Ga-rich region can delocalize in the AlGaAs matrix, provided that a zone-edge scattering mechanism compensates the change in crystal momentum. The inter-valley scattering can be strongly assisted by alloy broadening and follow a Fowler-Nordheim process.[164] This mechanism is usually fast in for the GaAs-AlAs couple, in particular compared to the ns-timescale of radiative processes.[165,166] Hence, the situation is the same for shells with Al nominal composition of 0.75 and 0.33 : the material forming the shell provides lower confinement barriers for the electrons than an 0.51 Al fraction shell.

5.3 Dependance on growth temperature

The sample used in the following experiments consist in GaAs core with $Al_{0.33}Ga_{0.67}As$ shells. The shells were grown at different temperature for each sample. The reference is grown at the usual growth temperature of 460°C (T_0). This temperature is the default growth temperature for AlGaAs shells. The reason for this choice is that GaAs QW grown between AlGaAs shells at this temperature show the narrowest linewidth, and this has been related to the smooth and regular growth of the AlGaAs layers.

The resulting histograms of the spectral density of QDs emission for each sample is represented in figure 5.3. The histogram from panels (a) to (g) corresponds to growth temperature offset of {+60, +40, +20, 0, 20, 40, 60} °C respectively. For each histogram, the mean value is indicated by a red triangle, while the bar-code graph below the 0-ordinate shows the spectral position of each peak recorded by the automated peak finding routine.

There is a clear evolution in the histograms of the spectral density. The histograms corresponding to lower growth temperature show a dramatic narrowing in the distribution as well as an increased blue shift of the mean emission energy. In general, all the distributions show one clear maximum, with a distribution looking roughly log-normal, with the highest energy side being the steeper. The steeper cut-off can be explained once again by the limit in energy sets by the AlGaAs matrix barrier height, in particular for the electrons. Thus, the smaller segregated islands cannot confine electrons and are not optically active. These remarks are true for the distributions shown in panels (b) to (g). The histogram of the highest temperature sample (520°C , +60°C) diverges from the general description as a second maximum starts to develop around 1.62 eV.

In order to compare the different measurements in a simplified way, the median of the emission energy associated with all the peaks of each samples is plotted in figure 5.4(a). The first and third quartile of the distribution are indicated as the lower and upper bars associated with each data point. They can be seen as a measure of the

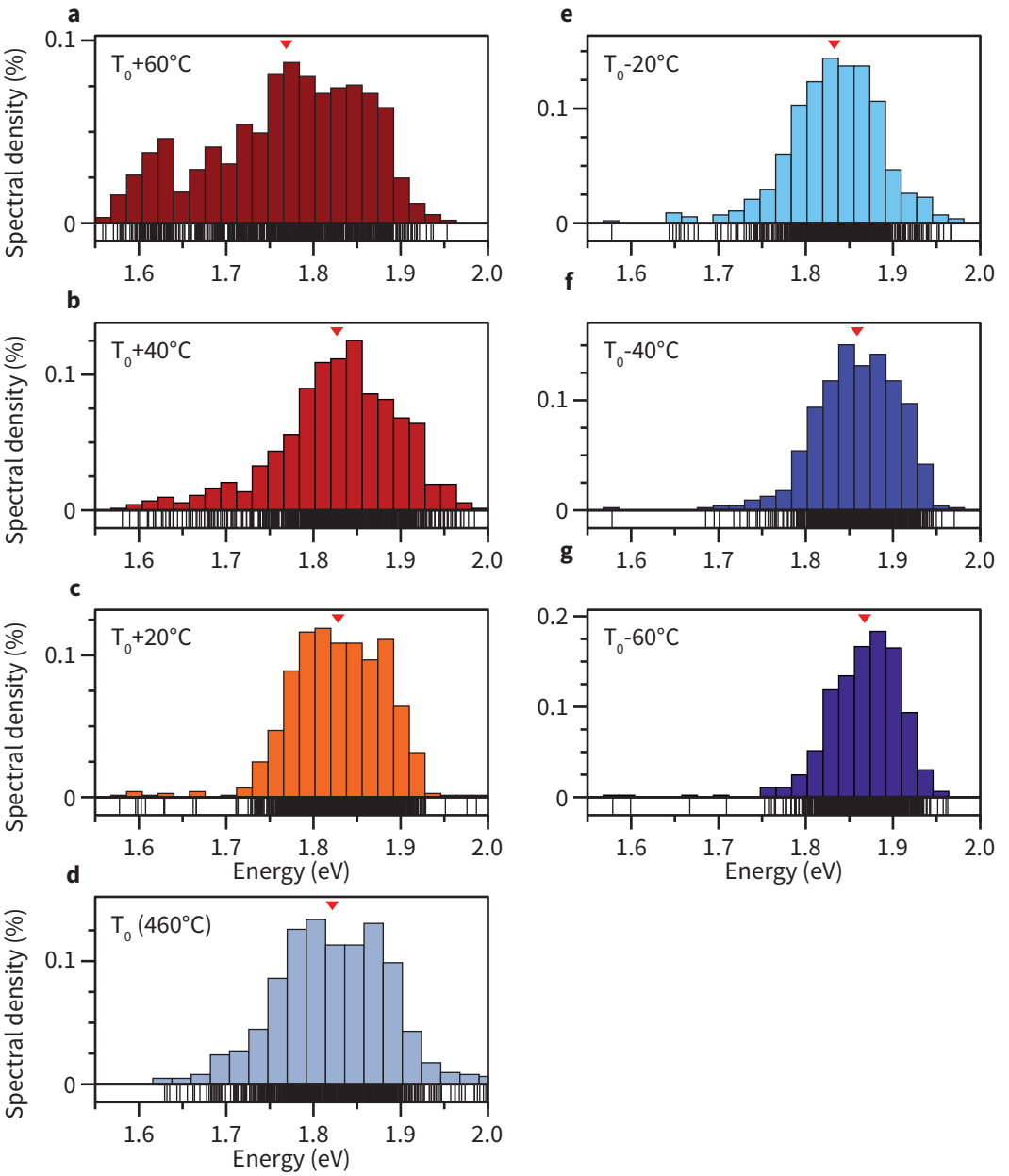

Figure 5.3 • a.-g. Spectral density histograms for shells grown at 7 steps of growth temperatures in the range +60 to -60 around $T_0 = 460°C$ (grey histogram, panel (d)). The red triangles mark the mean value of energy. Each tagged peak is represented in the bar-code graph below the 0-ordinate.

spread of each distribution. This representation show clearly the red-shift associated with an increase in the growth temperature of the shell. At the same time, the spread of the distribution increases dramatically. A significant drop appear for the highest temperature, as it can be seen in the related histogram in figure 5.3(a). Actually, the

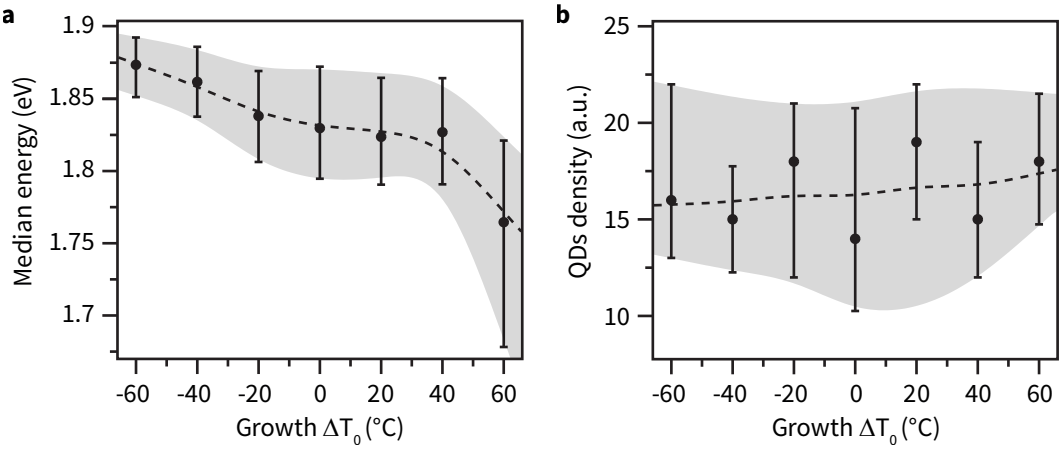

Figure 5.4 • a. Median energy of the histograms in figure 5.3 as a function of the growth temperature offset ΔT compared to T_0 equal to 460°C . The lower and upper bars indicate the value of the first and third quartile of the distribution. **b.** QDs density per spectra versus the growth temperature offset. The lower and upper bounds again represent the first and third quartile of the distribution. The shaded areas and the dashed line are in both case smoothing splines used to guide the eye.

decrease in median and mean emission energy for the highest growth temperature sample, as well as the much larger distribution spread are due to the same particularity. As already noticed before, the histogram in figure 5.3(a) shows a second smaller maximum at around 1.62 eV. This second low-energy maximum pulls the median, mean and first quartile toward significantly lower energies. However, the splitting between the median and third quartile is similar than for other distribution. Hence, the brutal decrease in global emission energy is mainly due to the apparition of this second maximum.

The panel (b) of figure 5.4 shows the median of the QDs density per spectrum as a function of the growth temperature offset. Again, the first and third quartile of the distribution form the lower and upper boundaries. The dashed guide to the eyes hints for a small increase of the QDs density with the temperature. However, given the bounds formed by the first and third quartile and the general spread of the distribution, such a progression is hardly relevant. In general, it can be said that the QDs density is mainly independent of the temperature, in stark contrast with the emission energy distribution. This yields an important information: it seems that the growth temperature has only a marginal impact on the nucleation of Ga-rich islands. Otherwise, considering that the higher temperatures tend to favor the growth/ Ga-enrichment of the segregated shell-QDs, it would be expected that high-temperature samples also present a higher density of optically active shell-QDs.

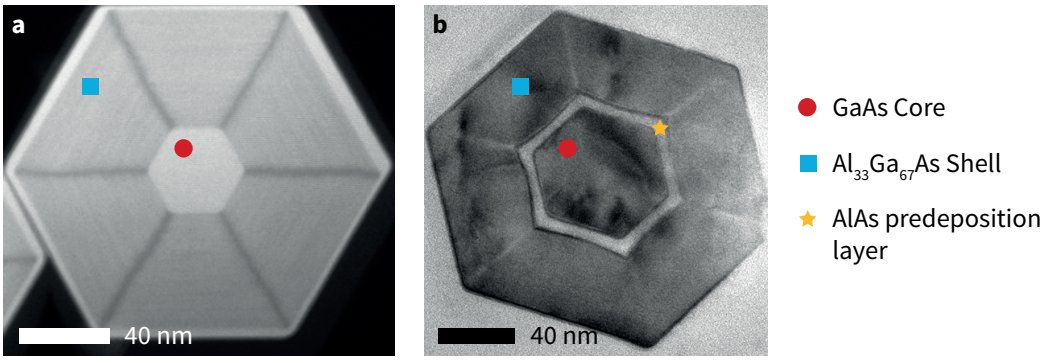

Figure 5.5 • **a.** Dark-field TEM cross-section micrograph of a NW from the core-shell set. **b.** Bright-field cross-section micrograph of a NW from the second set, showing the different core-predeposition layer-shell sequence. Notice the meniscus shape of the AlAs facets in panel (b).

5.4 Impact of shell thickness and AlAs predeposition

Next, the focus is set on the effect of the shell thickness on the occurrence and energetic distribution of shell-QDs. For this purpose, two sets of samples were grown, each with different shell thickness. They share the same parameters in term of alloy compositions (0.33 Al) and shell growth temperature (460°C), but differ in the shell sequence. The first set consists of a single AlGaAs shell grown on a GaAs core, with shell thickness of {15, 30, 50, 65, 8, 100} nm, while the second set consists of first an AlAs predeposition layer of 5 nm deposited around the GaAs core and followed by an AlGaAs shell with thickness of {10, 15, 25, 30, 50} nm respectively. The goal of these two different sets is to evaluate the effect of an intermediate layer (the predeposition layer) and in particular the impact of the modification of the surface prior to the AlGaAs shell deposition.

Representative TEM cross-sections for the two sets are shown in figure 5.5. The panel (a) shows a dark-field cross section of a specimen of the simple core/shell set, while panel (b) shows a bright-field cross-section of a specimen from the second sets, with a core-predeposition layer-shell sequence. The nominally thin AlAs layer exhibits divergence from the expected flat facets. Instead, each facets takes a meniscus shape modifying significantly the curvature profile around the NW.

The treated data for these two experimental sets are shown in the form of spectral density histograms in figure 5.6. The panel (a) and (b) consist in the histogram for the various shell thickness for respectively the set without and with AlAs predeposition layers. The spectral density histograms for the set without AlAs show a progressive behavior, from very few emission peaks exclusively at high energy for the 15 nm shell, the histograms evolve toward broad distributions, presenting several maxima with a growing density of peaks emitting in the lower energy part of the energy range. If the evolution of the median or mean emission energy is not straightforward to capture, in

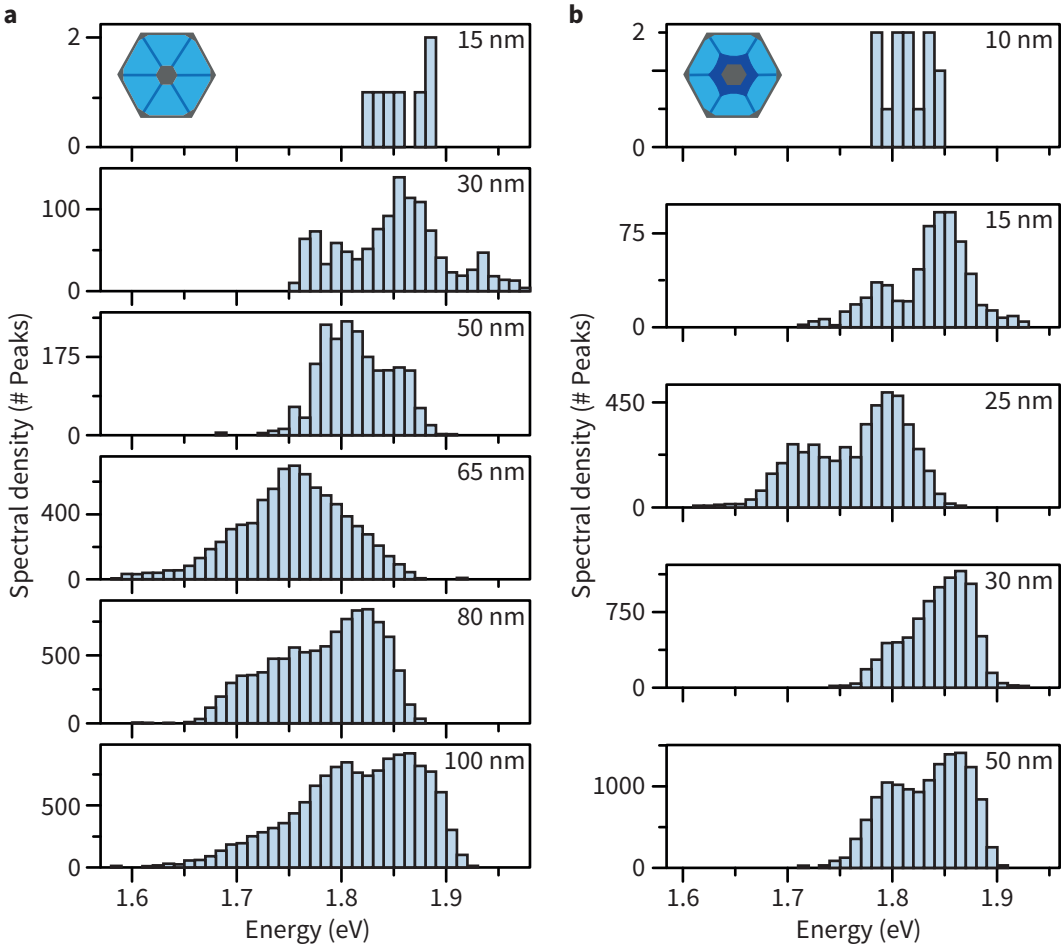

Figure 5.6 • a. Histogram of the spectral density (in number of peaks) versus the emission energy for the set without AlAs predeposition layer. **b.** Same as (a), but for samples with an AlAs predeposition layer. The shell thickness is indicated for each histogram in the upper right corner.

particular due to the obvious multimodal distributions, the red tail of the distributions consistently progress toward lower energies.

The results for the samples with an AlAs layer are far less clear than when the AlAs is absent, but they also cover a smaller range of shell thickness. The high energy cut-off is similar to the single-shell case but globally the progression toward low energy is not more pronounced than for the single-shell set.

In both cases, even the thickest sample shows a pronounced number of peaks emitting in the high energy region. This can be understood if one consider that larger shells only provide the opportunity for larger QDs to develop, but do not necessarily lead to the disappearance of small sized Ga-rich islands. Instead, the probability to form islands of any size uniformly increases with an increase in shell thickness, as the nucleation process not only take place directly after the shell growth. Similarly and

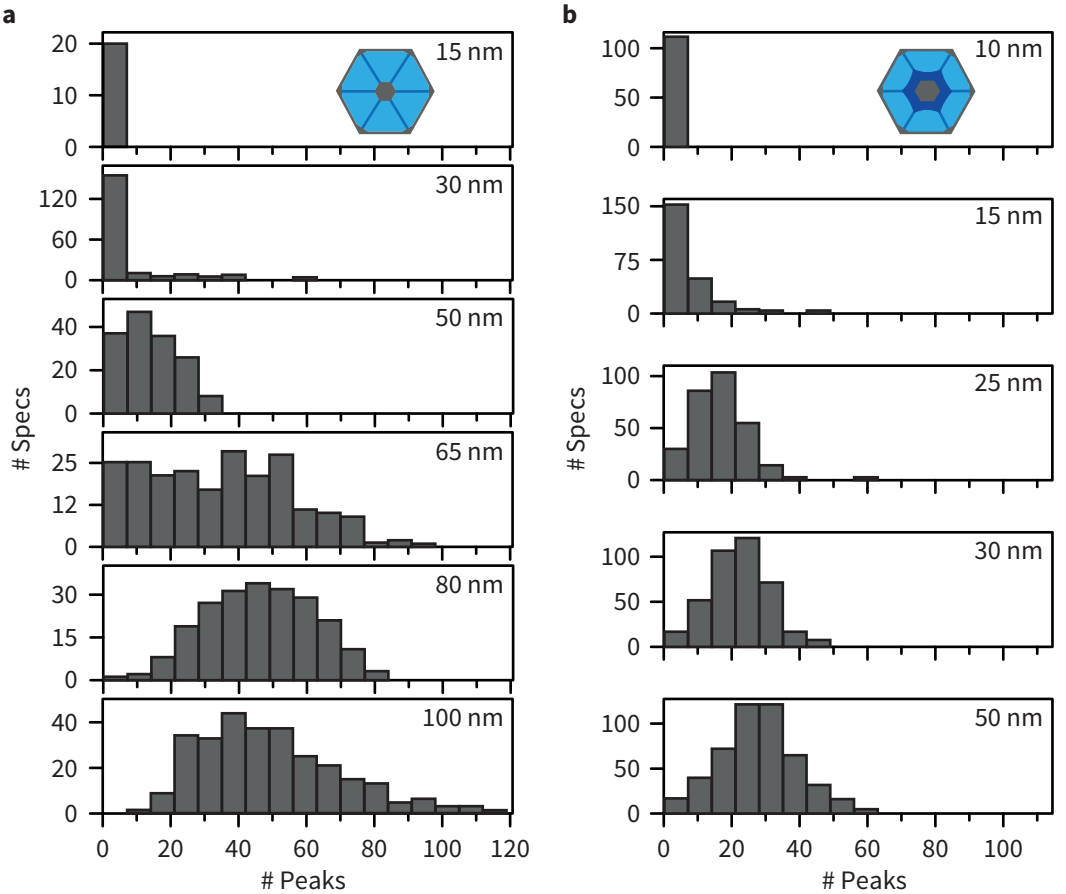

Figure 5.7 • a. Histograms of QDs peak number for the set without predeposition layer. **b.** Histograms of QDs peak number for the set of sample with the AlAs predeposition layer. The AlGaAs shell thickness is indicated in the upper right corner. The histograms shown the number of spectrum (# Specs) showing a certain number of peaks (# Peaks), directly proportional to the (optically active) QDs density.

leading to the same outcome, the "closure" of QDs may happen at any time of the shell growth, and is even a requirement in order to observe any optical activity.

The data for the two sets of measurements can also be treated in order to visualize the density of optically active QDs as a function of the shell thickness. Again, the sets with and without AlAs predeposition layer are compared in figure 5.7. The panel (a) shows the number of spectra recorded which presented a certain amount of emission peaks in the case of the sample without AlAs. It is clear that the thinnest shells at 15 nm show only rare emission peaks, with only 20 spectra showing emission, systematically seven peaks or less. The sample with a 30 nm shell contains slightly more optically active QDs, but the density stays moderate. The situation then rapidly evolves and for the thicker shells, more and more peaks can be tagged per spectrum.

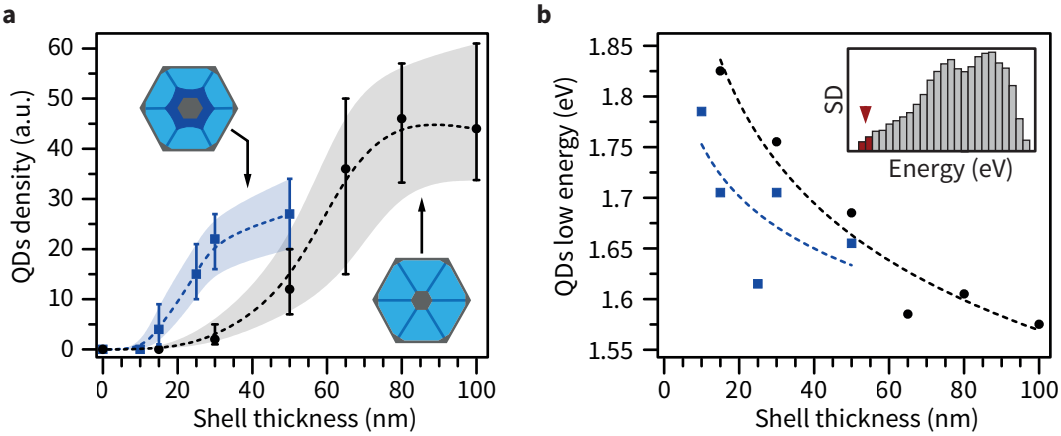

Figure 5.8 • a. Comparison of the QDs density (per spectrum) for the different shell thickness. The lower and upper bounds represent the first and third quartile of the distributions. The shaded areas and dashed lines are guides for the eye. **b.** Energy of the lower non-nul bins of the spectral distributions shown in figure 5.6. The inset shows the plotted value for the histogram corresponding to the 100 nm shell sample. For both graphs, the black dots (blue squares) stand for the set without (with) an AlAs predeposition layer. The dashed lines are guides for the eye.

Compared to this, the QDs density of samples with an AlAs predeposistion layer presents a similar behavior, but with noticeable emission starting for thinner shell and a quicker evolution. It can be noted that the spread in distribution is also staying more symmetric even for thicker shells.

The figure 5.8 summarizes the results of the shell thickness series. The panel (a) shows the evolution of the QDs density per spectrum for samples with increasing shell thickness. The black circles represent the data obtained for the single shell samples, while the blue squares relate to the samples with an AlAs predeposition layer. For the two curves, the density evolution shows a clear onset value followed by a steep increase in density. The onset happens at different values for the two samples sets. In the sample with a simple AlGaAs shell almost no QDs could be measured for shell thicknesses smaller than 30 nm. If an AlAs predeposition layer is grown first, the onset starts for shells as thin as 15 nm.

The threshold thickness for the onset of the QD observation can be understood considering that for thin shells, the potential QDs have fewer chances to develop during the growth process. Thus if the nucleation process does not take place right after the beginning of the shell growth, most of the segregated islands will be small and less Ga-rich (as the island growth is diffusion driven). This leads to shallow changes in the potential for which the confinement of charges is impossible. The scenario of a deactivation of the QDs for thin shells because of the proximity of the interface with vacuum, analogous to the luminescence quenching in thin NWs can be ruled out. Otherwise, the same effect would preclude the observation of active shell-QDs in thin

samples of the AlAs set as well.

Given the difference between the set without and with AlAs predeposition layer, it is clear that the modification of the surface by the thin AlAs layer plays an important role in the QD nucleation. Considering the difference in shape seen in figure 5.5, it is likely that the changes induced in local curvatures (in particular at the facets intersection) and thus in local chemical potential gradients for the adatoms species enhance strongly the segregation processes. Another explanation, probably complementary, is the roughening of the growth interface at the atomic scale. This roughening is likely to occur given the difficulty to grow atomically flat pure AlAs layers on (110) and has been observed in the raman spectrum of superlattices grown on misangled surfaces.[167]

The saturation in QDs density (for both experimental sets) is not straightforward to explain, but two remarks can be made. First considering the measurement technique, for high QDs density, the emission peaks used to obtain a counts of the optically active QDs start to densify, leading to an underestimation of the real number of peaks by the routine. Second, as can be seen in high-resolutions CL-SEM images (*e.g.* see figure 4.7(b)) and in the APT measurements (see figure 4.12), several potential or already optically active QDs are often close together. Thus for larger shell thickness with an increased density of segregated islands, the probability of having two (or more) Al-depleted regions merging is becoming increasingly high. This effect tends to reduce the number of QDs observed (the saturation).

The figure 5.8(b) summarizes the evolution of the energetic tail of the distributions for the set without (black circles) and with AlAs (blue squares). The points are representing the values of the lowest energy bins with non-zero numbers of QDs. As the most red-shifted optically active QDs are probably the larger and most Al-depleted ones, they make for a good benchmark of the QDs (maximal) size in function of the shell thickness. The steady red-shift seen for the dataset without AlAs predeposition confirms that for larger shells, the probability to have large and/or Ga-rich shell-QDs increases. For the set with an AlAs predeposition layer, the trend is far less significative, even if a decrease in energy can be noticed comparing the thinner and larger shell thicknesses. The strong increase in QD density compared to single-shell NWs in conjunction with the absence of a marked trend regarding the QD emission energy leads to think that the effect of the AlAs layer could be to create an higher number of favorable spots for the nucleation of shell-QDs instead of increasing the probability of early nucleation on already existing favorable spots.

Finally, the figure 5.9 presents results similar to the analysis already done on the density and energy of optically active shell-QDs. The major difference is that these results are based on measurements along a single wire, along which several spectra were taken and analyzed individually. As it can be seen in the insets of figure 5.9 , the wire is significantly tapered. Despite being grown with a designed shell thickness set at 100 nm, shadowing effects in dense NWs sample leads to an increased deposition

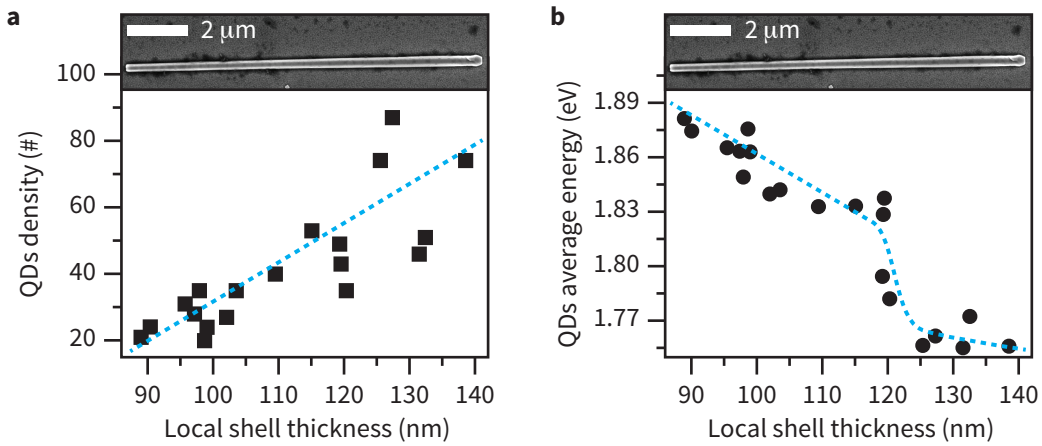

Figure 5.9 • a. Evolution of the QDs peak density along a single NW with nominal shell thickness of 100 nm. **b.** Same as in (a), but for the QDs mean emission energy. The top insets show a SEM picture of the NW. Shading effects create a tapering of the shell, modulating the NW's diameter. The dashed blue lines are guides for the eye.

of material near the top of the wires at the expense of the base. As a result, the shell thickness continuously changes from 90 to 140 nm. In the panel (a), the QDs density can be seen to increase as the the shell becomes thicker. This is in agreement with the measurements performed on several NWs with different nominal shell thicknesses. Interestingly, the scatter between adjacent points slowly increases, also following a trend comparable with the previous measurements.

Similarly, the QDs average energy shown in figure 5.9(b) shows a gradual decrease as the shell becomes thicker. A sudden drop of the average energy happens for shell thickness higher than 120 nm. Again the energy decrease reproduces the trend stated in figure 5.8.

5.5 General discussion

Despite the difficulty to understand the formation mechanism of shell-QDs, the analysis based on the statistical measurements of the density and energies of optically active shell-QDs allows to draw some general lines:

QDs density Concerning the density of optically active shell-QDs, it is clear from the results that the temperature does not seems to play an important role. Amazingly, the median number of peak per spectrum is seen to be rather constant of more than 100°C changes in the shell growth temperature. This seems to indicate that in order to nucleate shell-QDs, some favourable features (such as kinks and atomic steps) should be already present when the growth is initiated. This perspective is supported by the difference in QD density for

samples with and without the deposition of an AlAs layer. This layer is expected to enhance the curvature on particular points such as the (110) facets apex, enhancing the formation of rounded (112) sub-facets as well as the creation and accumulation of atomic steps. Indeed, samples consisting of a core-AlAs-AlGaAs sequence showed a significant increase in QDs density, in particular for thin shell. Thus the surface preparation prior to the function AlGaAs layer growth is the dominant parameter to tune the QDs density. Finally, the effect of the alloy composition is rather small. If the effect of the Al-fraction is hard to understand in term of metallurgy, and argument can be raised considering the diffusion process leading to the shell-QDs formation: shells with smaller Al-fractions will have the tendency to reach very low Al-content for smaller QDs than shell with high nominal Al-fraction, leading to more optically active shell-QDs.

QDs energy It can be seen that both the growth temperature and shell thickness play a role. The effect of the temperature is particularly clear. The distribution evolves smoothly from narrow, high energy distribution at low temperatures to broad distribution, centered at lower energies at high temperature. Thus the temperature, if it does not affect the nucleation of shell-QDs, does play a significant role in their further development. The mechanism seems to include a "frozen" regime at low temperature, for which the mobilities and relative mobilities of the Al and Ga adatoms are small. As the temperature is increased, the mobilities are expected to increase as well. However, the relative mobilities might exhibit increasing differences, leading to more efficient segregation processes. It should be noted that for this range of temperatures, the diffusion processes are exclusively limited to the surfaces, as bulk diffusion only takes place at even higher temperatures. The shell thickness does play a role in the sense that for thicker shell, there is a finite and increasing probability for large segregated islands to form. This is intuitive: It is rather unlikely to obtain the formation of 10-15 nm segregated islands, fully surrounded by the AlGaAs matrix, in a 15 nm thick AlGaAs shell. Finally, in this case again, the exact role of the alloy considering the growth process is nebulous. However, the bandstructure in function of the composition and in particular the conduction band minimum energy makes it clear that QDs showing the highest confinement energy can be created in a matrix with a nominal Al composition maximizing the potential barriers, *i.e.* around 0.44 Al-fraction. For lower fraction, both the valence and conduction (Γ character) barrier energy decreases. For higher fraction, the valence barrier increases, but the conduction acquires an indirect X character and decreases again in energy.

5.6 Conclusions and outlooks

To conclude, it has been shown that the density, average or median emission energy and the full energetic distribution can be tuned up to a certain extent modifying the growth conditions. While the temperature can be used to either "freeze" the energy of optically active QDs into narrower distributions or to create QDs emitting at low-energy, the thickness of the NWs shell can be set in order to obtain a large number of emitters. As a side-effect, the energy distribution will also be broadened. This limitation can be circumvented by the deposition of an intermediate AlAs layer. In this case, the number of shell-QDs can be strongly increased, while maintaining thin shells and thus narrower energy distributions.

Finally, the overall datasets indicate that the emitters are indeed consistent with segregation phenomena, and cannot be conveniently explained by atom-like, "size-less" defects. Interestingly, emitters sharing similar characteristics with the shell-QDs were located in AlGaAs layers grown on Si and Ge.[168,169] The origin of the emitted radiation was in kthe latter case attributed to extrinsic defects in the ternary alloy. However, in light of the effect of roughness and strain on the relative mobilities of Ga and Al, segregation mechanisms could well be at the origin of the observed luminescence in epilayers grown on group-IV substrates.

The control of QD density in NWs is important in several aspects. The first one is the ability to produce samples with the desired density in order to be able to clearly study single shell-QDs. Reducing the number of QDs simplifies greatly the interpretation of optical spectra in various experiments. On the other hand, a good control on the energy distribution together with the density leads to a convenient way to fabricate NW-embedded light sources to be used as nano-LEDs, for intermediate-band solar cells, or as a controllable gain medium for small-scale lasers.

Publications • The results presented in this chapter concerning the shell thickness are currently under reviewing process:

> "Quantum dots in the GaAs/$Al_xGa_{(1-x)}As$ core-shell nanowires: statistical occurrence as a function of the shell thickness", L. Francaviglia, Y. Fontana, S. Conesa-Boj, G. Tütünçuoglu, L. Duchêne, M.B. Tanasescu, F. Matteini and A. Fontcuberta i Morral, in review, 2015.

Contributions • G. Tütünçuoglu and F. Matteini grew the samples. S. Conesa-Boj, L. Duchêne and M.B. Tanasescu prepared the TEM cross-sections and S. Conesa-Boj performed the TEM imaging. K. Rolle participated to the measurements of the temperature serie. L. Francaviglia measured the shell thickness serie and proposed the QD density analysis under the supervision of YF and Anna Fontcuberta i Morral. YF devised the peak counting methodology used throughout the chapter. The global analysis was discussed by YF, LF and AFiM.

Acknowledgements • G. Tütünçuoglu and F. Matteini are thanked for the inspiring discussions on frozen/kinetic regime and for the growth insight.

Optical spectroscopy on single shell quantum dots

6

Chapter 4 introduced shell-QDs and provided evidence that the nanometer-sized Ga-rich islands seen in TEM and APT analysis can trap electron and hole pairs, thus making the islands optically active. Chapter 5 used the emission from the shell-QDs embedded in the NWs to provide feedback about the effects of growth conditions. To do so, a measurement technique at the cross-over between macro and micro-PL was leveraged. This chapter and the following will set a particular emphasis on measurements done on single emitters. The content of this chapter will provide informations on the electronic levels and few-particles effects taking place in shell-QDs, starting with the confirmation that shell-QDs are single photon emitters. The direct outcomes of the various measurements also imply that the alternative model of "deep-level" emission is erroneous.[161]

6.1 Experimental details

Various samples and technical implementations of micro-PL were used to obtain the results presented below. The samples were generally GaAs/$Al_{0.51}Ga_{0.49}As$ core/shell NWs, apart in the sections 6.3.2, 6.4.3 and 6.6, where GaAs/$Al_{0.33}Ga_{0.67}As$ core/shell NWs were used. For the results presented in section 6.4.1, core/multishell NWs with compositions GaAs/$Al_{0.33}Ga_{0.67}As$ were measured, with three shells of AlGaAs.

The samples were all investigated at cryogenic temperature, at 4.7 K in a bath cryostat for measurements shown in section 6.2, at 10 K in a continuous-flow cold-finger cryostat for the measurements in section 6.4.1 (apart for results in figure 6.8), 6.4.2 and 6.12. The other measurements were done in a closed-loop cold-finger cryostat at 3.85 K.

The samples were usually excited with the 632.8 nm line of an HeNe laser. If not indicated otherwise, the laser light was linearly polarized. For the results in sections

6.4.1 and 6.5, the 488 nm line of an Ar^+Kr^+ laser was used as the excitation source.

The pulsed g^2 and lifetime measurements in figure 6.1 have been collected using a Q-switched diode laser emitting at 635 nm. In the same figure, the SPADs (Single Photon counting Avalanche Diode) have an efficiency around 60% at 650, for an individual response time around 300 ps. The other time-resolved measurements are done using a Q-switched diode laser emitting at 470 nm, with a pulse duration of 70-120 ps depending on the power and SPADs with a 50% efficiency at 650 nm and an individual response time of around 40 ps.

The array detectors are all Si-CCD, either Peltier or LN_2 cooled. The spectrometers are all 500 mm single stage spectrometers with a resolution of around 100 μeV, aside for the measurement in figure 6.8, where a triple-stage spectrometer with a total resolution of 20 μeV was used.

6.2 Single photon emission

The previous measurements revealed that the shell of core/shell GaAs/AlGaAs NWs can embed Ga-rich islands. The sharp luminescence peaks at energies between 1.6-1.9 eV have been attributed to the recombination of confined electrons and holes in these nanoscale regions. CL mappings clearly showed that the luminescence centers were tightly localized along the NWs, making the link between the feature observed by TEM and the luminescence spectra. However, in order to confirm that the luminescence is stemming from truly 0-D quantum confined structures (*i.e.* QDs), the photon flux must be analyzed on the basis of the temporal spacing between successive photons. As the ground state of a QDs is only spin-degenerate, it can only be populated by a maximum of two electron-hole pairs. Due to Coulomb interaction, an electron-hole pair will recombine at a different energy if another pair (or single charge) is present in the QD at the same time. This allows to spectrally filter the PL corresponding to the recombination of an electron-hole pair, and since only one pair can recombine at a given time, the QD should act as a photon turnstile, emitting a stream of single photons.

To confirm the quantum light emitting properties of shell-QDs, an HBT intensity interferometer (see section 3.2.2) was used to analyze the light emitted by shell-QDs in single core/shell NWs with a shell Al fraction of 0.51.

The results can be seen in figure 6.1. The spectrum of the measured emission peak is shown in panel (a). Since the linewidth of the peak corresponded to the spectrometer maximal spectral resolution (around 100 μeV), the deconvoluted peak is also shown (overlapped filled blue Lorentzian). The panel (b) shows the lifetime of the peak, *i.e.* the decay in luminescence intensity after a laser excitation pulse. The corresponding lifetime is found to be around 500 ps after deconvolution of the laser pulse and detectors temporal responses (blue fitting line).

Finally, the panel (c) and (d) present the antibunching results for respectively CW

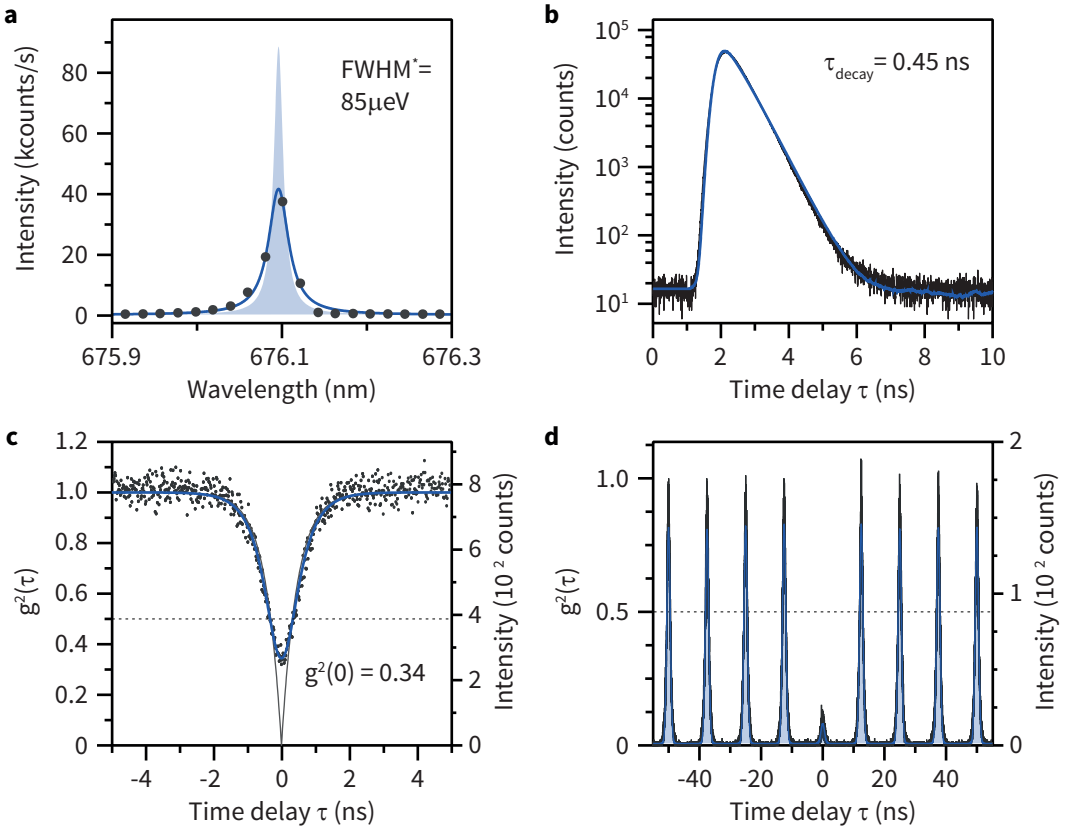

Figure 6.1 • **a.** Spectrum of a single shell-QDs at low excitation power. The solid blue line is a fit taking in consideration the spectral broadening of the spectrometer. The deconvoluted Lorentzian peak is shown in filled light blue. The extracted linewidth is indicated in inset. **b.** Time-resolved PL from the peak shown in (a). The solid blue line is a single-exponential fit accounting for the finite time response of the detector and the broadening of the laser pulse. **c.** CW measurement of $g^2(\tau)$ for the peak in (a). The raw value of $g^2(0)$ is indicated in inset. The classical-quantum threshold is indicated with a dashed black line. The solid blue (thin black) lines are convoluted (deconvoluted) fits to the data for which the radiation decay rate used is the one measured in (b). **d.** Pulsed-excitation analog to (c). The $\tau = 0$ peak is strongly suppressed resulting in a relative peak area of around 0.1. Adapted from ref. 170

and pulsed excitation. The dip in figure 6.1(c) goes well below the 0.5 threshold (dashed black line) marking the delimitation between classical and quantum light states. The remnant counts at zero time delay are increased by the finite time jitter of the detectors, in this case around 300 ps. A fit to the results, taking this time response in consideration, is represented by the solid blue line. The fitted function is of the form

$$I(\tau) = IRF \star (1 - Ae^{-\frac{\tau}{\tau_{decay}}}) \tag{6.1}$$

Where IRF is the instrument response function and the star operator denotes the convolution product. The lifetime τ_{decay} used in the fit is the one extracted from the

measurement shown in figure 6.1(b). The factor A in equation 6.1 accounts for a dip with a residual amount of coincidence counts at zero time delay. The deconvoluted fit is shown as a thin solid black line and can be seen to dive to almost zero, confirming that in this case the time jitter of the detectors strongly contributed to the dip reduction.

The pulsed measurement in panel (d) essentially confirms the CW results. The zero time delay peak is strongly reduced to around 10% of the finite delay peaks. In this case, the jitter of the detectors does not set a limit to the measurements as they only produce a broadening of the temporal distribution of the photon-capture events. The residual counts at zero time delay can be the result of either a slight luminescence background (uncorrelated light from the matrix or from a nearby QD). A second explanation can be found in the relatively broad pulse of the laser. The pulse being around 100 ps long at its FWHM, the chances to excite a QD with a lifetime of 450 ps a second time after the first triggered photon event is not completely zero. The optical cross-talk between SPADs (emission of photons from one SPAD after a detection event detected in turn by the second SPAD) is suppressed by pinholes in the optical path of the two detectors. However, both results converge to prove that the PL peaks seen in the spectra of core/shell NWs are emitted by isolated single photon emitters.

6.3 Few-particles effects and excitonic complexes

6.3.1 Signature of exciton complexes in power-dependent spectra

As discussed in section 2.2.2, a QD with at least one bound state for electrons and for holes can have several charge configurations. This is a direct consequence of the spin-degeneracy of the levels and of the fermionic nature of electrons and holes. The excitonic complex corresponding to four particles (*i.e.* the biexciton XX) is expected to appear at higher excitation rate, as it requires the presence of an X to build onto. The three-particles complexes, namely the positively and negatively charged trions ($X^{+/-}$) are not necessarily expected since the total balance in carrier numbers is maintained during optical excitation.

The figure 6.2(a) presents a wide range spectrum of an isolated shell-QDs in a NW. The GaAs core emission can be seen at an energy of around 1.51 eV, far below in energy compared to the shell-QD emission. The QD emission spectrum is split into a group of emission lines, separated by few meVs. Interestingly, the shell-QD luminescence is in this case competing in intensity with the bulk GaAs core, pointing out the excellent radiative properties of the QD (and its combination with the NW geometry). The panel (b) of the same figure represents a close-up of the spectrum, centered at the emission energy of the shell-QD. The different emission peaks are well distinct and labeled according to their excitonic origin as either X, XX, X^+ and X^-. The exact and complete reasons for the peak attribution will be given along the chapter, but a good hint can already be provided by power-dependent measurements, as the evolution of

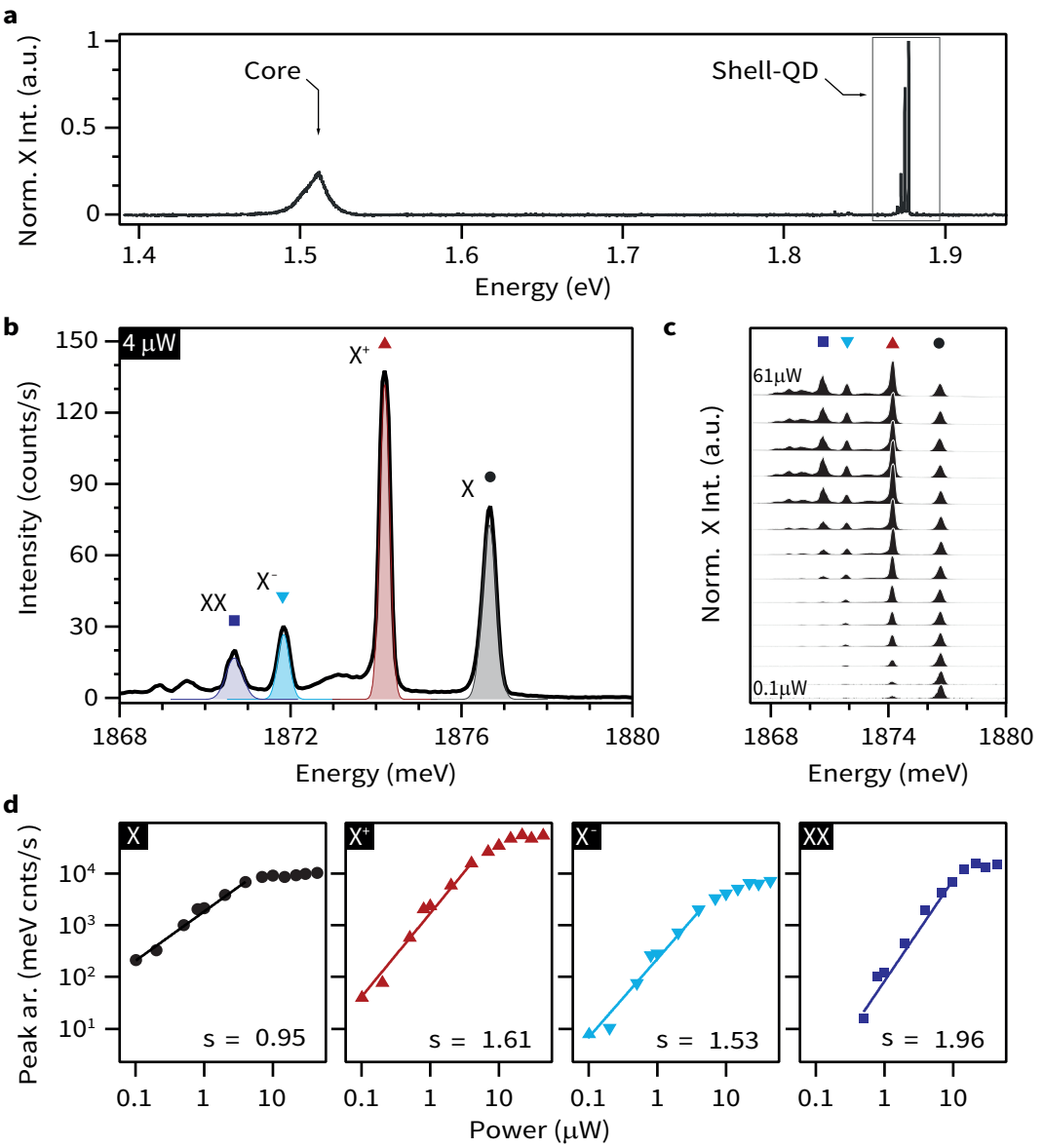

Figure 6.2 • a. Wide-range PL spectrum showing the emission energy of the NW core and an isolated shell-QD. **b.** High-resolution spectrum of the shell-QD spectral region outlined in black in (a). The peaks are labeled according to their charge configurations. **c.** Power dependent spectra, renormalized to the X emission peak (shifted for visibility). The peaks are indicated by their respective symbols (X -black circles-, $X^{+/-}$ -red upward / cyan downward triangles- and XX -purple squares-). **d.** Integrated signal (total peak area) as a function of the excitation power for the four optical transitions shown in (b) and (c). The slope of the fits (solid lines) is indicated by the value (s). Adapted from ref. 171.

the emitted light in function of the illumination power is not the same for different complexes. The power-dependent spectra, renormalized to the X emission intensity

are shown in figure 6.2(c). Obviously, the three satellite peaks located at lower energy increase non-linearly with the excitation power. The peak area (corresponding to the spectrally integrated intensity) of each peak is plotted as a function of the illumination power in a loglog scale in panel (d). This representation allows to retrieve the factor - s - linking the radiated intensity with the laser power and following the relationship $I_{X_i} \sim P^s$, where I is the radiated intensity, P is the laser power and x_i stands for the different excitonic complexes.

The slope for the X peak (black circles) is expected to vary linearly with the power, and can be seen to do so. The slope is close to 1 (0.95) before it reaches a plateau corresponding to the saturation of the optical transition. The two peaks attributed to trions (X^+ -red upward triangles- and X^- -cyan downward triangles-) both increase non-linearly in intensity, with intermediate slope of respectively 1.6 and 1.5. The X^+ peak is by far the most intense of the four at high excitation power but, importantly, yields to the X at lower excitation power. Finally, the last peak (purple squares) can be seen to evolve with a slope close to 2 *i.e.* quadratically with respect to the laser power. This behaviour is typical of the XX, as its formation is conditional of the presence of an X, which itself follows a linear dependence.

A particular feature of the emission spectrum of strongly confined GaAs QDs can be found in figure 6.2 as well as the majority of the following spectra: the X^+ peak is particularly intense. This observation is almost systematically made in other type (droplet epitaxy (DE) or local droplet etching) of strongly confined GaAs QDs in an AlGaAs matrix.[90,172] The presence of charged excitons indicates an imbalance of carriers in the QDs, originating in its turn from either a spatial or temporal imbalance of carriers in the AlGaAs matrix. A more detailed analysis of this phenomenon will be given in chapter 8.

6.3.2 Cross-correlation and lifetimes of excitonic complexes

In order to strictly relate the observed peaks to the same QD, cross-correlation analysis is realized between the different peaks. The cross-correlation measurements $g^2_{X_i-X_j}(\tau)$ should present a dip for zero time delay similar to second-order auto-correlation signals. If the different optical transitions originate from the same single QD, the value of $g^2_{X_i-X_j}(0)$ should be below 0.5, as it is the case for the auto-correlation.

The figure 6.3(a) represents the $g^2_{X-X}(\tau)$ second-order auto-correlation histogram for a single shell-QD. The antibunching dip is well below the 0.5 threshold, but does not reach zero. The deconvoluted fit (solid blue line) is shown to fit closely the data. This is due to the use of faster SPADs for this measurement, with typical timing jitter of around 35 and 40 ps for each SPAD. Thus, the non-zero value of $g^2_{X-X}(0)$ cannot be attributed to an event-timing effect in this case. The solid black line below the dip represents the estimated contribution of the background luminescence (from the AlGaAs bulk and defect continuum and nearby shell-QDs). This estimation is based

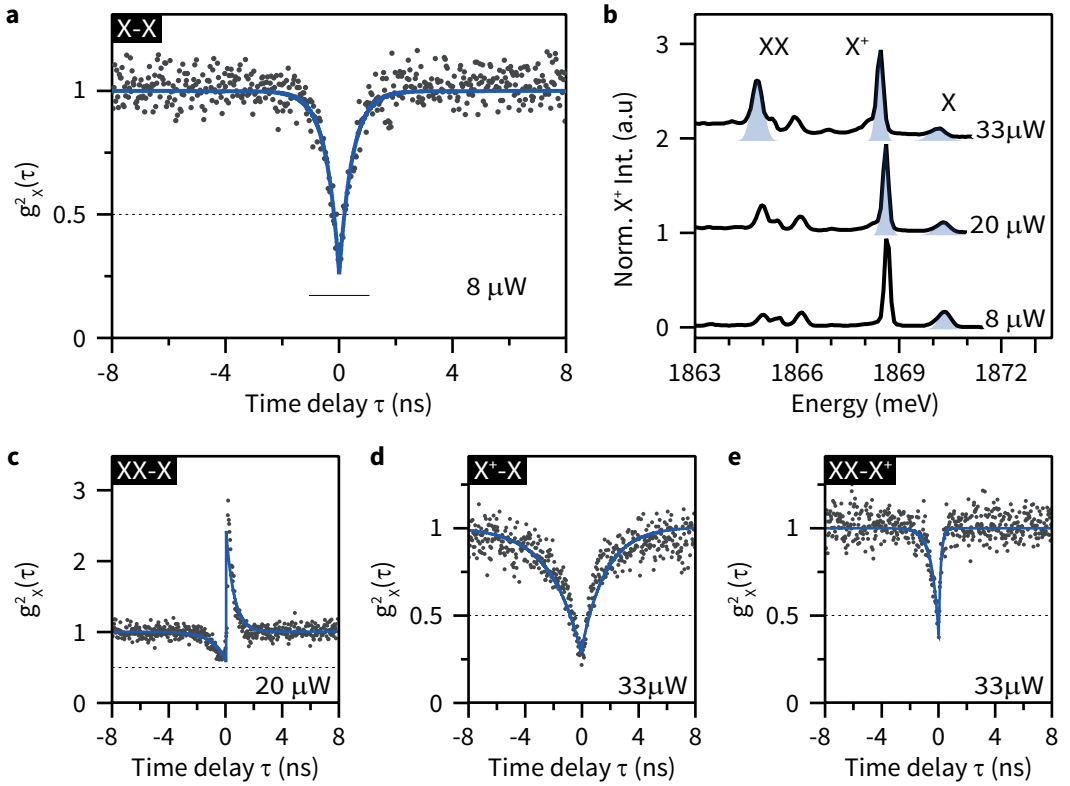

Figure 6.3 • a. Second-order autocorrelation signal of the X peak of a single shell-QD. The solid black bar represent the estimated contribution of uncorrelated background emission. **b.** Spectra of the measured QD for excitation intensities corresponding to the different measurements. The X, X^+ and XX emission peaks are indicated. **c. - e.** Second-order cross-correlation histograms $g^2_{X_i-X_j}(\tau)$ between the emission lines shown in (b). The excitation intensities are shown in inset. The blue solid lines are deconvoluted fit to the data.

on the spectra shown in (b). Indeed, the spectral window of the filter used to isolate the X emission is 1.6 meV FWHM (approximatively Gaussian). Thus if uncorrelated luminescence happens in the spectral region of the X emission line, it will contribute to the reduction of the dip. Since the correlation signal depends on the square of the total signal, the relation between the total signal (I_{tot}), the QD luminescence (I_{QD}) and the background luminescence (B) is the following:

$$\begin{aligned} I_{tot} &= I_{QD} + B \\ g^2_{tot}(t) \sim I^2_{tot} &= (I_{QD} + B)^2 = I^2_{QD} + 2I_{QD}B + B^2 \\ g^2_{QD}(t) \sim I^2_{QD} &= \frac{I^2_{tot} - B^2}{2I_{QD}B} \end{aligned} \tag{6.2}$$

It must be pointed out that this value is (i) indicative, as the real fraction of spurious light entering the optical fibers connected to the SPADs can be larger than

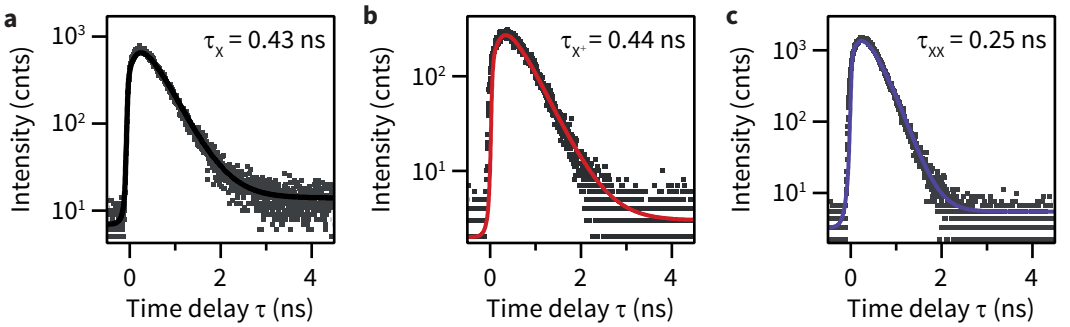

Figure 6.4 • a. - c. Radiative lifetimes for respectively the neutral (X), positively charged (X^+) and biexciton (XX). Each decay time trace is fitted with a single exponential function triggered at τ=0 and convoluted with the temporal shape of the laser pulse. The fits are represented by respectively black, red and purple lines.

the background luminescence and (ii) even if the $g^2(0)$ signal is expected to decrease without background luminescence, the latter is in this case an intrinsic property of the shell-QD/NW system. In this aspect, better results can mainly be obtained through a global optimization of the system (particularly the interfaces and defects).

The panel (b) of figure 6.3 includes the normalized spectra of the measured QD. The different powers for which the auto and cross-correlation measurements were done are represented. The peaks are labeled with the corresponding attribution (X, XX and X^+, the X^- position is not clear). The shaded areas highlight the peaks used for the correlation histograms. The histograms of the cross-correlations can be seen in the panels (c) to (e). The attribution of the XX peak is justified by the strong correlation peak at small positive delays. This peak is the results of the XX-X cascade process; since the final state after an XX decay is the X state, the probability of emission of an X photon is high, thus the correlation peak just after zero time delay. The measurement was performed at intermediate laser power in order to increase the visibility of the cascade. At higher laser power, the X optical transition is saturated (see spectrum for 33 μW) and a X photon emission is less likely to happen as the QD is quickly repumped in the XX state.[173]

The cross-correlation between the X^+ and X peaks shown in panel (d) also confirms that both transitions originates from the same QD, and not from two neighboring emitters. The antibunching dip is seen to plunge well below the 0.5 threshold. As expected, the same conclusion applies to the XX-X^+ histogram in (e). In particular, the signal for positive time delay do not show the trace of correlation. Hence the emission of an X^+ photon does not stem from a direct cascade as it is the case for the neutral exciton.

Differences between the excitonic complexes can also be seen in their decay dynamics. This is presented (for a different QD) in figure 6.4. The time-traces of the X, X^+ and XX after pulsed excitation are presented. In each case, the measurements

(black dots) are fitted with a single exponential decay model convoluted with the temporal shape of the laser pulse. The latter is approximatively 80 ps at the FWHM, but presents an important low-power tail which is much wider. Taking it into consideration, the time traces in figure 6.4(a-c) are perfectly fitted. The conclusion is that the apparent rise time observed for each measurement cannot be attributed to the carrier dynamics in the AlGaAs matrix, at least at the time scale considered here, around 70-100 ps.

The lifetime of the X in this measurement agrees remarkably well with the lifetime shown in figure 6.1(b). Additionally, it is found that the X^+ lifetime is comparable to the X one. The XX radiative decay is approximatively twice as fast as the X, which is also comparable to what is usually found for the X/XX couple in QDs. In general, the decay rates of shell-QDs agree well with measurements performed on DE GaAs QDs, but are significantly smaller (longer lifetimes) than reported in interface fluctuation QDs in QWs.[174–176] Indeed the latter are more prone to exhibit a so-called giant oscillator strength, due to the extension of the e-h wavefunction over a wider area.

6.3.3 Binding energies

A striking feature of single shell-QDs spectra is the ordering of the charged and biexciton luminescence peaks. The three complexes systematically exhibited a negative energy shift (binding energy) with respect to the X. This in contrast with typical InGaAs or InAs SK QDs were an antibinding energy is often reported for the positive trion.[177–179] The exact binding energies are usually found to be strongly dependent on the QD size and morphology.[180] For lattice mismatched materials, two important factors complicate the picture: the effect of interfacial strain between the growth substrate and the QD material, and the induced piezo-electric field, which directly acts on the charge distribution.[102] Due to the almost perfectly matched lattices of GaAs and AlGaAs, shell-QDs allow to investigate the binding energies and their dependence on the emission energy in a strain-free environment.

The values for the binding energies of a few shell-QDs are shown in figure 6.5(a). The first outcome, beside the fact that all the transition energies are redshifted, is the rather small variation of these energies with respect to the X transition energy. The shell-QD with the most energetic X emission measured (1.96 eV) is the only one to present a strong variation, but only in the X^- binding energy. The shell-QDs emitting in the 1.8-1.9 eV range present fairly constant binding energies, in particular for the XX and X^-. For the two latter complexes, the scatter is large enough so that their emission lines can exchange position in the spectra. A small yet noticeable trend seems to affect the X^+; a slow decrease in the binding energy can be seen with the increasing X emission energy.

The panel (b) of the same figure shows results obtained by Abbarchi *et al.* on GaAs DE quantum dots. Side by side, the two sets of results show very similar values for the binding energies, but the emission energy for shell-QDs is remarkably higher

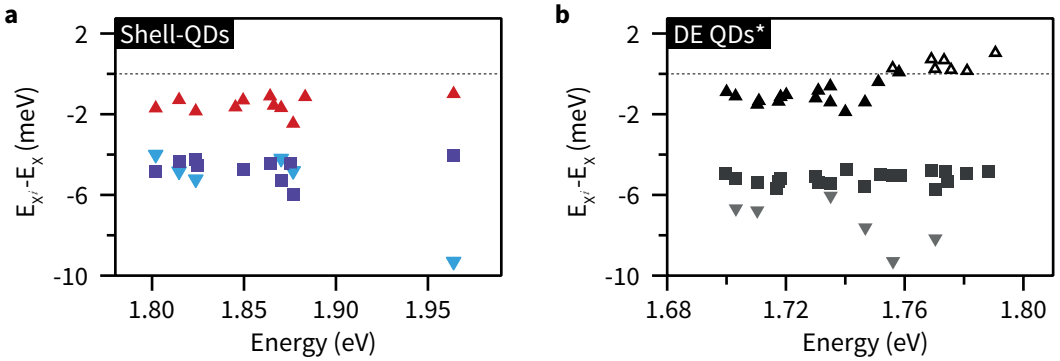

Figure 6.5 • a. Offset of measured transition energies for the X^+ (red upward triangles), X^- (cyan downward triangles) and XX (purple squares), with respect to the neutral exciton X. The data are plotted against the X emission energy. **b.** Same measurements as in (a) reported by Abbarchi *et al.* on pure GaAs droplet epitaxy QDs. The symbols stands for the the same complexes as in (a). The black dashed line marks the crossing from binding to antibinding energies. * Adapted from ref. 181.

(approximatively 100 μeV). The minute details of the evolution in function of the increase in emission energy also differs between the two systems. The X^- binding energy value seems to become more important for the most energetic shell-QDs, similarly to what is measured with DE-QDs. However, up to an emission energy of about 1.9 eV, no significant change can be detected. The most striking difference concerns the $\Delta E_{X/X^+}$ values. While the energy shift is monotonically decreasing, it always stays negative for shell-QDs. In the case of DE-QDs, the energetic shift gradually decreases until becoming positive (antibinding). It is worth noticing that the onset of the increase for the $\Delta E_{X/X^-}$ values corresponds to a simultaneous reduction of the X^+ binding energy. In the same trend, the most energetic Shell-QD, emitting at 1.96 eV, showed the largest X^- binding energy simultaneously with the smallest X^+ recorded. Thus, it is possible that the passage from binding to unbinding for the X^+ happens at larger energies, however hardly obtainable since the electron states would be unbound due to the vicinity of the continuum.

The comparison with results obtained for DE-QDs thus hints for shell-QDs containing a small yet non-null fraction of aluminum or, even more likely, for shell-QDs with confining barriers which are not well defined, but increase smoothly, thus pushing up (down) in energy the single-particle states for the electron and holes. In this picture, the shell-QDs size and aluminum fraction tends to compensate and the energy range for which the binding energy stay approximatively constant is larger than for pure GaAs DE-QDs with minimal alloy mixing at the interface, where only the confinement volume/height is varied.

6.4 Exchange splitting and spin effects

The following section presents the results pertaining to spin-related effects in shell-QDs. The fine-structure splitting (FSS) induced by the exchange interaction in the spectrum of the X and XX line is shown to contribute significantly to the linewidth broadening. The polarization of the two split X states give valuable information on the anisotropy of the shell-QDs as well as their orientation inside the NW shell. In addition, the partial conservation of the electron spin polarization for circular optical excitation is harnessed to demonstrate the positive nature of the X^+. In the first place, a short description of the effects on the emitted light polarization due to the shell-QDs off-axis configuration is made.

6.4.1 Polarization anisotropy and effects of the off-axis geometry

The interaction of light with non-engineered planar substrates and NWs differ significantly. This is true in terms of light propagation in general, and particularly relevant for polarization. NWs generally support different optical modes which can affect the light polarization. For NWs observed from the side, it is commonly accepted that a certain degree of anisotropy characterizes the in- and out-coupling efficiency of fields with different polarization, usually decomposed in the intensity components parallel ($I_{//}$) and perpendicular ($I_{\perp}$) to the NWs long axis, so that the (normalized) polarization ratio is commonly defined as:

$$R_P = \frac{I_{//} - I_{\perp}}{I_{//} + I_{\perp}} \tag{6.3}$$

The general assumption is that NWs strongly reduce the coupling of transverse fields. This is often a good description, but depending on the exact wire geometry the strength of this effect can be modulated or even reversed (see section 2.1.2). In particular, for processes involving the emission of light from an emitter embedded in the NW, the problem is usually treated as if the emitter was perfectly centered. This is not always the case, in particular for shell-QDs.

The figure 6.6 presents measurements realized with single shell-QDs embedded in core-multishell NWs similar to the one shown in figure 4.1(b). Due to the shell stacking (each shell is approximatively 50 nm thick), the diameter of these NWs is particularly large (between 500 and 600 nm). This important thickness places them far away from the quasi-static regime for which the parallel component of the polarization is systematically and strongly favored. A major difference is also that the emitters can be located in any of the shells, so that their position relative to the axis of the NWs can take important values.

The panel (a) of figure 6.6 illustrates these differences, particularly when compared to axial QDs in thinner NWs.[182] The intensity in function of the polarization angle shows that a certain degree of anisotropy is present, but the main axis of the polar

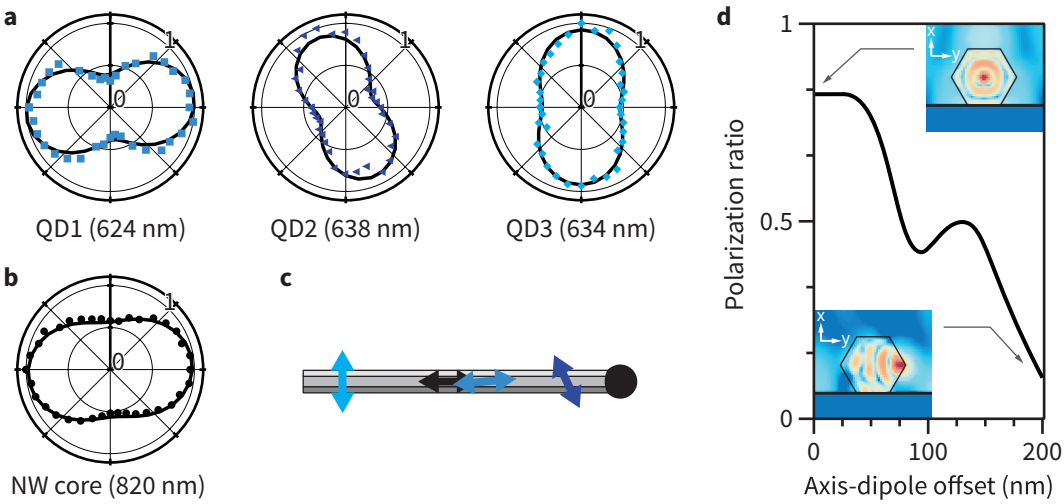

Figure 6.6 • a. Normalized intensity in function of the polarization for three different shell-QDs embedded in a NW. **b.** Normalized intensity of the polarization-dependent emission of the same NW's core. The black lines are fits with a damped Malus' law. **c.** Orientation with respect to the NW of the principal axis of polarization for the data shown in (a-b). **d.** 2D FDTD calculation of the far-field polarization ratio for two orthogonal dipoles μ_x and μ_z (z being out-of-plane, along the NW axis). The emission wavelength is set at 650 nm. The ratio is plotted as a function of the dipoles offset along x with respect to the NW axis. The insets are logarithmic-scale representation of the field energy distribution close to the NW if the dipoles are at the center (top right) or seven nanometers from the surface (bottom left). The black lines outline the cross-section of the NW and the interface with the silicon substrate. Adapted from ref. 170

plots are not necessarily aligned with the long axis of the NWs. The panel (b) shows the polarization anisotropy affecting the emission from the bulk GaAs core. In this case, the orientation is along the NW axis, but the anisotropy ratio is moderate, and certainly weaker compared to thinner NWs. The figure 6.6(c) presents the effect on the polarization ratio of the offset between a point emitter (emission at 650 nm) and the NW axis. The finite-difference time-domain (FDTD) simulation considers an infinite GaAs NWs laying on a Si substrate (as it is the case in the experiment shown in the panels (a) and (b)). The polarization ratio is the ratio (as defined in equ. 6.3) between the out-coupled power for orthogonal dipoles emitting at , oriented along the NW axis, and in the y-plane. The ratio decreases with an increasing axis-emitter distance. The two insets are representations of the field energy distribution, plotted in logarithmic scale. For an offset of 0 nm, *i.e.* a perfectly centered emitter, the dipoles are exciting a high-order mode resonance, as can be seen by the well-defined, concentric energy maxima. The polarization of the mode is principally along the NW. This translates into a rather important anisotropy ratio. On the contrary, if the emitter is located at the vicinity of the NW surface, the emitter does not hit a particular resonance of the structure, and for this wire diameter, the polarization ratio plummets. Interestingly, the

decrease in polarization ratio is not monotonic, and a rebound can be seen for an offset roughly equal to 0.5 the axis-surface distance. If the upper inset is examined again, one can realize that aside from the main central anti-node, another ring-like anti-node is visible. The latter is located at the offset for which the local maximum in polarization ratio appears. It is then likely that the local increase in polarization ratio is due to the excitation of the same mode as in the case of a centered emitter. The weaker effect is due to the energy distribution within the given mode.

Indeed, this simulation is only valid at the defined wavelength and for a given geometry, but provides an insight on the photonic effects happening for a thick NW-shell-QD system. The decrease in polarization anisotropy allows for the observation of QDs with an intrinsic polarization oriented across the NW (as seen in figure 6.6(a)). The orientation of the QDs inside the shell, and their own degree of anisotropy then define the orientation of the dipole(s) for the various electronic states (and in particular the X).

6.4.2 Fine-structure splitting

A consequence of non-null electron-hole exchange terms in QDs is the lifting of the degeneracy of certain states. The states concerned by this effect are the ones for which an electron and a hole spin are unpaired, *i.e.* there is no other particle on the same level with anti-parallel spin. This is the case for the X, as seen in section 2.2.2. On the other hand, the XX is not affected by the exchange terms as it is composed of two electrons and 2 holes on the same electronic levels. However, the final state after the decay of an XX is X. Hence, the emission spectrum of the XX will mirror the emission spectrum of the X. This section presents FSS measurements on shell-QDs. In particular, two different excitation/collection schemes are shown, one where the shell-QD is addressed from the top of the NW (upright), so that the optical axis is in-line with the growth direction, the second where the NW is deposited on a substrate after mechanical deposition and for which the optical axis is perpendicular to the axis of the NW (lying).

For both sets of results, the FSS was extracted by running an iterative fit on the polarization-resolved spectra, with the peak intensities left free for each different spectrum, but with a common FWMH and splitting energy. For the X/XX pair (figure 6.7), the fit was first realized on the X, then on the XX spectra, in order to provide an estimate of the expected accuracy of the fitting.

The results for the upright configuration are shown in figure 6.7. The spectral map as a function of the angle of the analyzed polarization is displayed in (a). The X and XX transitions are labeled accordingly, and the value extracted from the two fits are reported on the graph. The extracted value for δ_1, the FSS, is 170 ± 10 μeV. No difference is expected between the two values (as its origin is a common state). The rather large offset between the FSS extracted for the X and the one of the XX is mostly connected to the accuracy of the fit. Indeed, the XX doublet can be seen

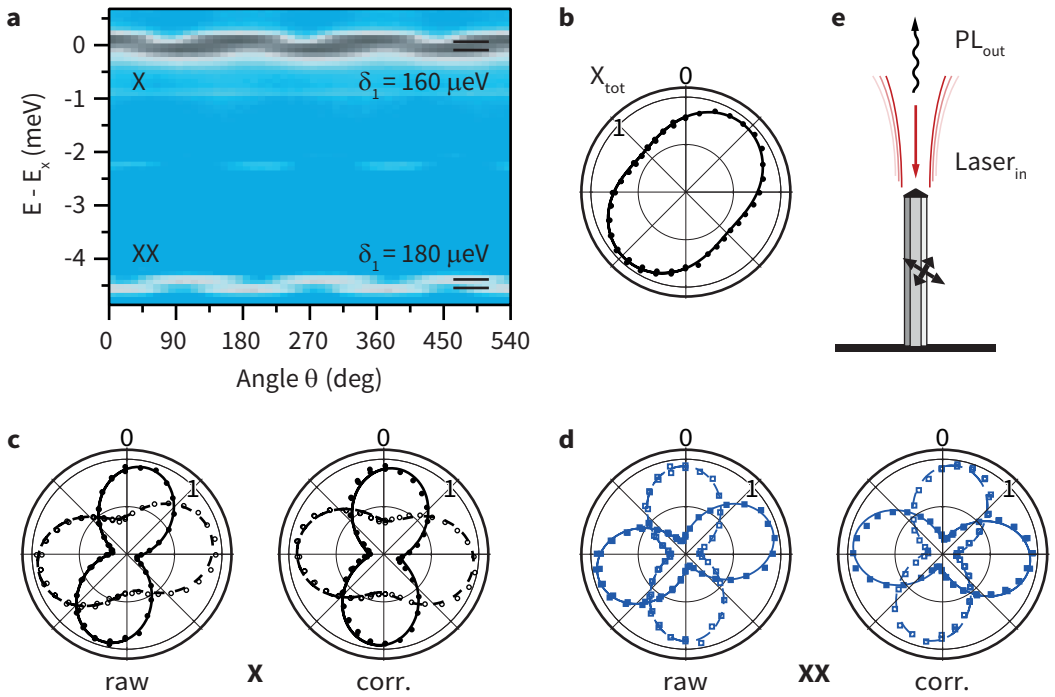

Figure 6.7 • **a.** polarization-resolved spectral map showing the X and XX peak positions in function of the polarizer angle. The (fitted) value of the FSS is indicated for both transitions. **b.** Total normalized intensity of the X doublet in function of the polarizer orientation. **c. - d.** Normalized fitted intensities of the two components of the X (c) and XX (d) doublets in function of the polarization angle. The left plots show the results for the values extracted from raw spectra. The right plots show the normalized fitted intensities after the renormalization of the spectra by the total X intensity in function of the angle. **e.** Schematic of the excitation scheme, showing a tilted orthogonal dipole pair.

to be well separated, with a lower counts number but with better defined peaks and no background. Oppositely, the visibility of the X doublet is hindered by the peak broadening, and the fit accuracy lowered by the presence of a shoulder red-shifted with respect to the X emission. Potential reasons for this difference in broadening and the red-shifted shoulder are given in section 6.6.

The panel (b) of figure 6.7 shows the intensity of the full X emission (*i.e.* the two peaks of the doublet) as a function of the analysis angle. The striking feature in this plot is the important polarization anisotropy, still present in upright configuration. The reason for this remaining polarization is not clear, and can have different origin, discussed further below.

The panel (c) and (d) present the polar plots of the normalized intensity of the two components of each transition doublet (respectively for the X and XX emission). The left-hand plots show the data obtained directly after the fitting procedure, while the right-hand represents the data after a renormalization by the X intensity as a function

of the polarization angle. The left-hand plots show a significant deviation from the expected orientations of each state forming the doublets. Indeed, the orientation of the states is such that they are far from being orthogonal to each other. In addition, the intensities before normalization are also dissimilar. Again, several phenomena could explain the non-orthogonality and the difference in intensity between the peaks of a same doublet.

The first is the coupling between the heavy and light hole valence bands (HLC). It is usually promoted by the elongation of the QD in one direction.[183] As indicated by the rather large FSS (around 170 μeV), the shell-QD depicted must indeed be significantly elongated, and it cannot be excluded that HLC plays a role in the particular pattern of this QD. HLC has been observed to happen in GaAs QDs, either weakly or strongly confined, but if the intensity of each state was different, and the total intensity polarization orientation was modified, no description of a non-orthogonality has been made.[22,184] On the other hand, non-orthogonal states were measured for InAs SKQDs and strained GaAs QDs for which the HLC arise from the strong in-plane strain field.[100,185] Since the GaAs-AlGaAs system is basically strain-free at rest, this mechanism should not play a role in the present case. Also, a strong HLC should activate the radiative decay for initially dipole-forbidden transition (X dark states). As pointed out before, a red-shifted tail can be seen in the spectrum of the X transition. However, because the XX decay paths mirrors the ones of X, a blue shifted analog should be visible in the XX spectrum, which is not the case.

Another effect which could account for the observations would be that the strong confinement axis of the QD is not oriented in a particular direction, and *a priori* not along the NW axis. This configuration (schematically described in figure 6.7(e) by the orientation of the two arrows) could easily lead to the measurement of distorted polarization direction as well as different intensities. This would be particularly enhanced if the emitter couples to a particular guided mode of the NW.

The latter explanation is reinforced by the measurements performed on lying NWs, with an example shown in figure 6.8. The figure 6.8(a) shows the polarization-dependent spectra of a couple X/X^+ acquired on a NW in lying configuration. The X and X^+ are readily identified by the presence (absence) of FSS. Again, the FSS for the X can be extracted from the dataset, and the value is found to be slightly above 90 μeV. It should be noted that the difference between this measurement value and the one presented in figure 6.7 is not particularly explained by different growth conditions or measurement conditions; within one NW, the spread in FSS for different QDs can be as high as several hundreds of μeV (from barely detectable to 200 μeV). The fit of the total X peak with the two split-states (described as H and V in the figure) is shown in panel (b). This time, the X^+ peak is visible and its polarization anisotropy plot is presented in panel (c). The measured anisotropy of X^+ allows to renormalize the X intensity and extract the intensities of each peak of the X doublet in function of the polarization angle. The results are shown in figure

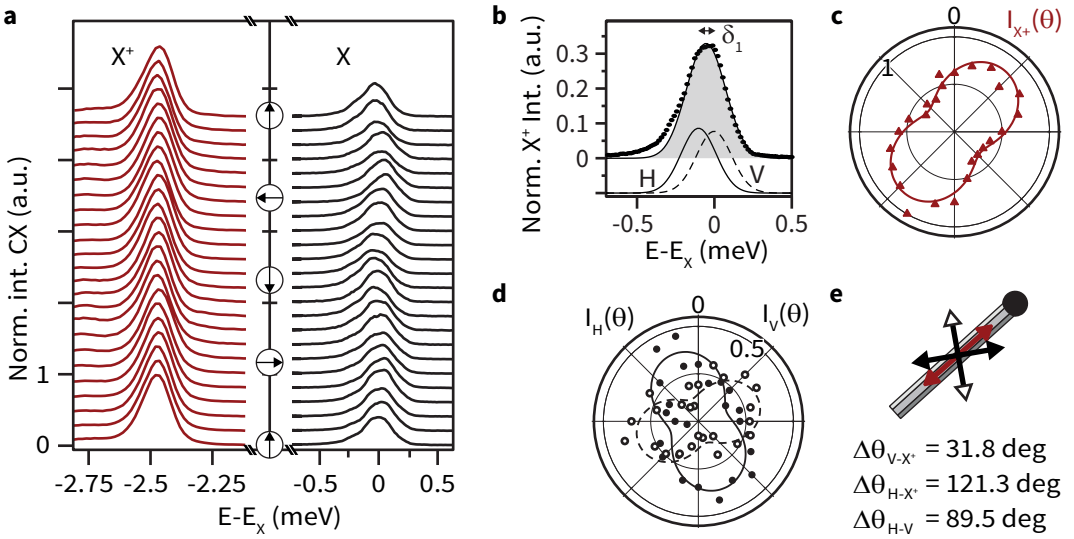

Figure 6.8 • FSS measurement in the case of a NW lying on a substrate. **a.** Spectra of the X^+ (red lines) and X emission (black lines) in function of the polarization analysis angle θ (normalized to the X^+ intensity). **b.** Example of a fitted X doublet with two underlying gaussian functions . **c.** Polar plot of the X^+ anisotropy. **d.** Polar plots of the extracted intensities for the X doublet. **e.** Schematic representation of the X doublet and X^+ polar orientation with respect to the NW. Adapted from ref 171

6.8(d). In this case, the states appear to be perfectly orthogonal. In addition, their orientation do not match the X^+ anisotropy axis, which is oriented along the NW. In this case, the picture is then not coherent with a (strong) HLC effect, as the most intense peak of the X and the charged excitons anisotropy axis should be aligned.[100] Yet the anisotropy of the X^+ emission is important, but can be explained by the effect of the NW, in particular in this geometry. Finally the panel (e) summarizes graphically the anisotropy axis of the different transitions: in black for the X doublet and in red for the X^+. From the drawing, it is clear that the QD orientation is certainly not in axis with the wire. Thus, if this particular shell-QD would be observed from the top, the PL intensity would also present a strong degree of anisotropy, without having to invoke HLC to explain it.

As a bottom line, the measured FSS energies on shell-QDs indicated a considerable anisotropy, but also revealed that the shell-QDs orientation is not necessarily aligned with the long axis of the NW. The emission anisotropy of the shell-QDs is well explained by this randomized orientation, but due to the elongation and alloy broadening, heavy-hole light-hole coupling cannot be fully excluded.

6.4.3 Determination of the positive trion *via* polarized excitation

Up to know, no justification have been brought forward for the attribution of the X^+ and X^- optical transitions seen in the different spectra. The discrimination

between the charged states of a QD is not a straightforward task, and several approaches can be taken to determine if the extra carrier(s) is an electron or a hole. Undoubtedly, the most common is the inclusion of a QD layer in a Schottky diode structure, and the deterministic injection of electrons or holes in the QDs for different bias voltage. The diode is built is a way that depending on the bias voltage, extra electrons or holes can tunnel in the QDs and is primarily used to set the QDs in a defined state. However, the making of these samples necessitates a good control of the processing, including of the doped layers during the growth, and an excellent processing not always straightforward with NWs since ready-made recipes for planar materials are often not adapted. A different method consist in the introduction of dopants in the structure, p and n in different samples. The doping concentration has to be estimated so that it matches in average the QD density, and statistically each QD contains $\sim$ 1 electron or 1 hole without optical excitation. The spectral lines belonging to the X^+ or X^- should then dominate the spectrum at low excitation power, and should be mutually exclusive.

Here, the goal is not to set the charge state of the QDs but to define the nature (extra hole or electron) of the trion peak in the spectra. Thus the method used here to validate the attribution of the intense peak to the X^+ state is different from the ones previously described. It relies on the partial conservation of the electron spin polarization when the bulk matrix material is pumped with a circularly polarized laser beam. During carrier cooling, the orientation of the hole spin is lost, so that the population of holes in the QD is a statistical mixture of $|\Uparrow\rangle$ and $|\Downarrow\rangle$. The loss of polarization of the holes in the bulk is due to the strong spin-orbit interaction. The depolarization time being in the same order of magnitude compared to the carrier thermalization time, the polarization of holes is generally considered as lost within few ps, and pump-probe measurements in bulk GaAs actually measured an even shorter relaxation time of around 110 fs.[186,187] Because of the different band configuration, the situation is different for the electrons. A significant part of the electron population will see their spin randomized, but a remnant part will keep their original orientation. Thus, the probability to find an electron in the $|\uparrow\rangle$ and $|\downarrow\rangle$ is not 50:50. Instead, the population ratio is very dependent on the polarization of the incoming excitation light.

Since the X^+ is composed of two holes and a single electron, radiative recombination is possible regardless of the electron spin polarization. Yet if one spin orientation is favored during the excitation, one recombination branch will be more probable and the photons measured from the decay will in average show a small yet measurable net circular polarization. On the opposite, the X^- is composed of two electrons (on the same s-shell level) and a hole. Because the electrons cannot share the same electronic state if their spins are parallel, the spin orientation of at least one of two electrons with parallel spins will undergo a flipping process. In conjunction, since the hole spins are lost during the carrier cooling process, there will be no net

polarization when the emitted light is analyzed. The method has been seen to work well, including when off-resonant excitation is used, and is schematized in figure 6.9(a).[188]

The application of this method to shell-QDs is complicated by the outcomes of the previous measurements: the charged exciton present a certain degree of linear polarization anisotropy, including when the NWs are examined in the upright position. For the ideal case when the charged exciton luminescence is isotropic, the read-out of the circular polarization is usually done on two channels after the transformation of circularly polarized (left and right) photons to linear, cross-polarized ones. The linearly polarized photons are then split on a polarization beamsplitter and the intensities at each output of the beamsplitter are compared, yielding the circular polarization ratio (CPR). The CPR is directly related to the population of left/right photons. In turn, the ratio of left/right photon allows for a one-to-one relation with the percentage of polarized excitons in the material.

For shell-QDs in NWs the linear polarization ratio ($LPR = \frac{I_\theta - I_{(\theta \pm \frac{\pi}{2})}}{I_\theta - I_{(\theta \pm \frac{\pi}{2})}}$) is not zero, as it can be seen in figure 6.9(b). The graph shows the unpolarized spectrum of a shell-QD (upper row), and the differential spectrum for two orthogonal polarizations. Even though the effect of the polarization can be seen (in particular on the X emission line), it is strongly hindered by the global polarization anisotropy. In particular, the X^+ peak is not canceled out despite the fact that $X^{+/-}$ intensities are expected to be isotropic with respect to linear polarization.

The reasons for this anisotropy can again be manifold: (i) the X^+ photons are strongly linearly polarized, *e.g.* due to valence band mixing or another interaction (ii) the photons are initially circularly polarized, but a birefringence phenomenon in the NW transforms them in elliptically polarized photons with a certain phase-shift. (iii) The photons are circularly polarized, the $\frac{\pi}{2}$ phase-shift is maintained (phase quadrature), but the amplitude of one of the two orthogonal components is reduced. This can happen if, as suspected, the QD orientation does not correspond to the NW axis, and the coupling to preferential photonic modes propagating in the NW is hindered for a certain polarization direction.

All three reasons prevent to use directly the CPR to measure the net spin polarization in the QD. However, for the case (i), a proper orientation of the quarter-wave plate (QWP) in the detection line, with the fast axis along the polarization axis, would not affect the polarization state of the PL (linear to linear polarization). The case (ii) should yield results comparable to regular circular polarization analysis, plus a certain broadening (uncertainty) depending on the degree of the ellipticity. For the case (iii), the ratio of left vs. right photon can be estimated with the following procedure:

1. One of the principal axis of the QWP (either fast or slow) is aligned with the main axis of linear polarization.

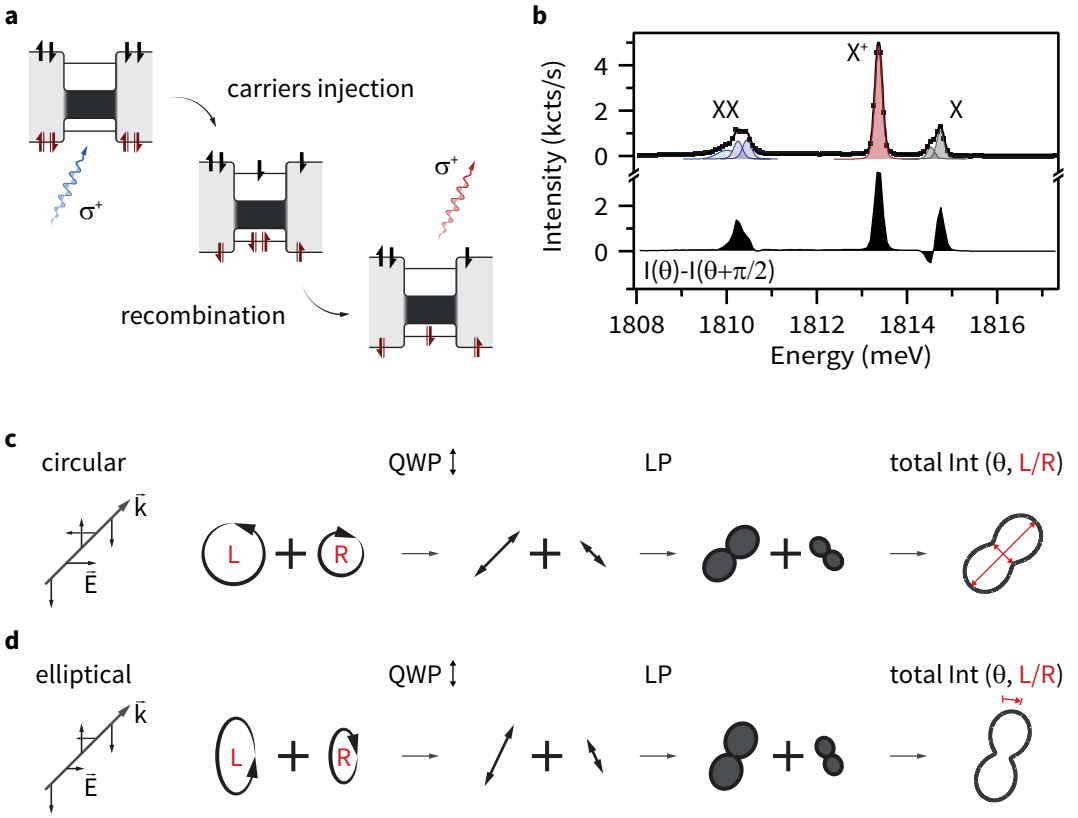

Figure 6.9 • a. Mechanism of the spin-polarization to photon polarization transfer. For the X^+, the electron spin orientation is partially conserved after excitation and thermalization. A preferential photon polarization is then expected and allows to discriminate between the X^+ and X^- **b.** Same as (a), but if the signal is renormalized. **c.** Schematic of the spin-polarization read-out method for a perfectly isotropic system, *i.e.* emitting circular photons. The arrows in the rightmost drawing indicate what is measured,*i.e.* the polarized intensities at angles ($\pm\frac{\pi}{2}$) to the QWP fast axis. **d.** Same as (c), but if one component of the electric field is reduced (elliptical polarization in phase quadrature). In this case, the rotation (phase-shift) of the polarization pattern is measured. The arrow near the QWP label indicates the slow axis.

2. The shell-QD is excited with circularly polarized light.

3. The polarization of the signal after the QWP is *fully* analyzed (on a large range of angles, typically 0 to 360 degrees).

The ellipticity of the polarization of left/right photons entering the QWP will result in linearly polarized beams, but the transformed linear polarization axis will not be orthogonal to each other. Instead, their angles with respect to the QWP fast axis will be reduced. Depending on the balance of left/right photons, the total intensity in function of the linear polarization angle will deviate from the fixed angle of ± 45 degrees. For elliptical photons with a certain phase shift, the outcome is similar, but

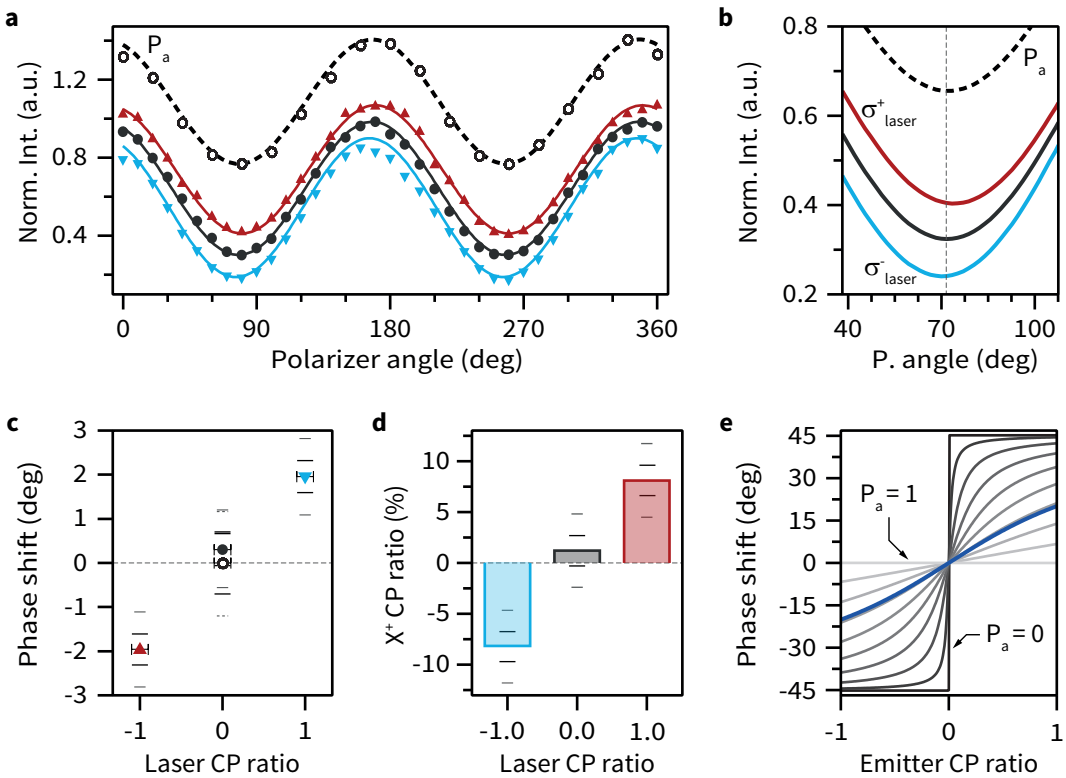

Figure 6.10 • **a.** Measured intensity as a function of the angle of polarization analysis after the QWP. Red (blue) relates to right (left) circularly polarized laser excitation. The solid black curves correspond to a linearly polarized excitation. The dashed curve/ hollow symbols show the results if the laser is linearly polarized, and no QWP is present. The data are shifted vertically for clarity. **b.** Close-up of the shift between the three measurements and the control (dashed). Only the fits are represented. **c.** Extracted phase-shifts in function of the laser polarization. The two sets of error bars correspond to the uncertainty on the fit (wide, thin) or on the extreme bounds considering a systematic error of 0.5 degrees on each datapoint . **d.** Calculated CPR, directly representing the spin polarization ratio in the shell-QD. **e.** Expected phase-shifts for a system with a 100% spin-polarization efficiency, the different lines correspond to different degree of LPR, the polarization anisotropy (marked as P_a). The line with LPR corresponding to the presented measurement is highlighted in blue.

the photons after the QWP will remain slightly elliptically polarized (leading to a broadening of the angular signal). If the total (left plus right) intensity in function of the polarization analysis changes in orientation, it also depends on the balance between left and right elliptically polarized photons, which in turns reflects the spin state of the shell-QDs. Comparing the phase-shift of the PL for left/right excitation polarization, one can then see if any spin polarization is maintained. The schematic and the schemes' main difference for perfectly circularly polarized photon and elliptical photons are shown in figure 6.9(c) and (d) respectively. The revolving arrows show the superposition of left/right light states, their transformation through a QWP (middle) and subsequent read-out with a polarizer, and the expected dependence of

the intensity on the polarization analysis angle (right).

The results are summarized in figure 6.10. The panel (a) shows the dependence of the measured X^+ emission intensity as a function of the polarization analysis angle after the QWP. The red (blue) curves and symbols are measurements with right (left) circularly polarized laser excitation. The solid black curve and symbols stand for the measurement with linearly polarized excitation. The dashed black curve and symbol is a control measurement done without HWP and with linearly polarized excitation. A small but noticeable shift can be seen and a close-up is provided in figure 6.10(b). Only the fits are reproduced for clarity. In both (a) and (b), the traces are vertically offset to facilitate the visualization.

The figure 6.10(c) shows the extracted phase-shift in function of the laser CPR. The horizontal error bars correspond to the uncertainty on the laser CPR. The wide, thin error bars are the error on the fit. The narrow thick bars represent the error if both the fit and a systematic error of $\pm$ 0.5 degrees is admitted on the measurement of the polarization after the QWP. The figure 6.10(d) shows the extracted "CPR" for the X^+ which directly corresponds to the amount of spin-polarization in the shell-QDs. The average value of around 8% (but with large uncertainty) is found, which corresponds relatively well to what was already measured in GaAs QDs. The depreciation by a few percents can be explained by a less efficient excitation mechanism. Importantly, the PL polarization was found to depend clearly on the laser polarization state, even if large and systematic error margins are considered. This allows us to conclude that the peak located few meVs on the red side of the X in our spectra is indeed corresponding to the X^+, while the other one is the X^+, by exclusion.

In panel (e), the calculation of the expected phase-shift in function of the LPR for a spin-polarization ratio of 100% is represented. The value corresponding to the measurement shown in figure 6.10 is highlighted in blue. For a perfect emitter (perfect orientation, perfect out-coupling) the LPR is 0 (indicated as P_a in panel (e)). As a results, the phase flips from -45 to 45 degrees when the laser CPR passes from negative to positive. For a structure acting as a perfect polarizer, the phase-shift is inexistent and the measurement impossible.

The measurements presented in this section thus validate the attribution of the X^+ peak, and show that a certain degree of spin-polarization can be obtained in shell-QDs. However, the measurement method is more complicated than the direct measurement of the CPR and cannot be used *e.g.* for fast read-out of the average spin states, thus limiting the outlooks.

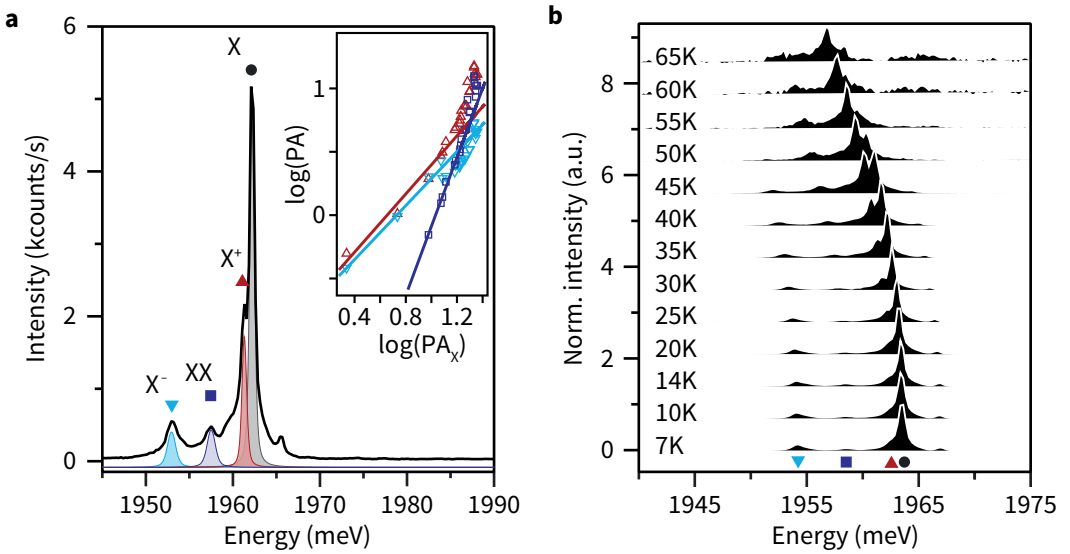

Figure 6.11 • a. PL spectrum of a high-energy shell-QD at 35K. Different peaks correspond to different charge states of the QDs. Black circles (purple squares) stand for the neutral exciton X (biexciton XX). The red (downward cyan) triangles represent the positively (negatively) charged exciton X^+ (X^-). The X^+ for this excitation power and temperature is merely a shoulder to the X peak. The extracted peak area of X^+, XX and X^- in function of the power are plotted (in logarithmic units) in the inset against the peak area of X. The slopes allow to identify the peaks in the spectrum. **b.** Normalized spectra of the shell-QD in (a) in function of the temperature. The peaks redshift as the temperature is increased, together with a slight linewidths broadening. The inversion in relative intensities between X and X^+ is clearly seen starting from 45K.

6.5 Temperature dependence and ionization in shell quantum dots

Another characteristic of strongly confined GaAs QDs in an AlGaAs matrix is the dramatic increase in the ionization energy compared to shallow, weakly confined excitons in QW fluctuation QDs. The ionization energies found for GaAs DE-QDs emitting slightly above 700 nm are often in the 100 meV range, compared to few meV for QW fluctuation. In the following section, the ionization energy of the different states belonging to a high-energy shell-QD are described. The ionization energy is found to be dependent on the carrier configuration. For this type of QD, emitting at almost 2 eV, the ionization barrier is also severely lowered, as expected, and the ionization process takes place through the escape of the electron.

The figure 6.11(a) presents the spectrum of such a high-energy QD, at 25 K. The familiar pattern of peaks, namely X, XX, X^+ and in this particular case X^- can be distinguished, and the attribution is validated by their power dependency (in inset, plotted against the intensity of the X peak at different excitation powers). It is important to notice the specially low (high) binding energy of the X^+ (X^-) peak,

which is a token of strong confinement in this QD. The panel (b) shows the normalized spectra of the QDs at different temperatures. As it is expected, a global red-shift can be measured. In addition, the main "body" of the peaks maintain a fairly constant FWHM (global increase in the order of 10%), but the bases get wider, due to an increase in the interaction between the excitons and acoustic phonons . The most striking observation is that if the total intensity decreases (see the signal to noise ratio), the rate is not similar for the different carrier configurations: the X^+ and XX intensities relative to the X peak actually increase.

These results are better seen in the panel (a) of figure 6.12. The peak area (total intensity) is plotted against the temperature for the four different states according to the labels, and the datapoints are fitted with a simple Arrhenius-type model, in order to retrieve the ionization energies E_i. The extracted values of E_i are seen to pass from the simple to the double between the X^- and X^+ transitions. The upper part of panel (b) represents the value of the peak area ratio (peak area ratio -PAR -) between the exciton complexes and the bare exciton. The PAR for the XX and X^+ are shown to increase strongly when the thermal energy reaches the ionization energy of the X. On the opposite, the PAR of the X^- can be seen to steadily decrease with the temperature. The dashed curves are simple guides for the eye.

The lower part of panel (b) shows the PAR of the XX over X^+. The tendency is much lower, as the ionization energies are closer. The proposed explanation is schematically described in the panel (c), and represents the situation for the two extreme cases (X^- and X^+) for a thermal energy between the X^- and X^+ ionization energies. Because of the strong confinement, the (SP) electron state is pushed far up, close to the continuum. The hole level on the other hand is still well separated from the valence continuum. When two electrons and one hole populate the QD, the ionization is prevented solely by the (weak) offset between the conduction band continuum and the electron state plus the binding energy of an electron-hole pair. The later is also weakened by the extension of the electrons wavefunction in the AlGaAs barrier. On the opposite, the X^+ possesses two holes protected from ionization by the energy separation between the hole state and the valence continuum. These two holes bind strongly the electron. In this simple picture, the energy barrier between the SP electron state and the conduction continuum is the same in the two cases, but the energy barrier due to direct Coulomb interactions in the QD is twice as large for the X^+ than for the X^-.

The discussion can be extended to the X and XX ionization energies. The X E_i is slightly higher than the one of the X^- due to the non-existent electron-electron repulsion term (antibinding). The difference between the XX and X^+ E_i is explained with the same argument.

Considering the small difference in E_i between the X/X^- and X_+/XX, it can be concluded that the electron-electron Coulomb term must be small, in particular in comparison with the electron-hole term. This is a consequence of the spreading of

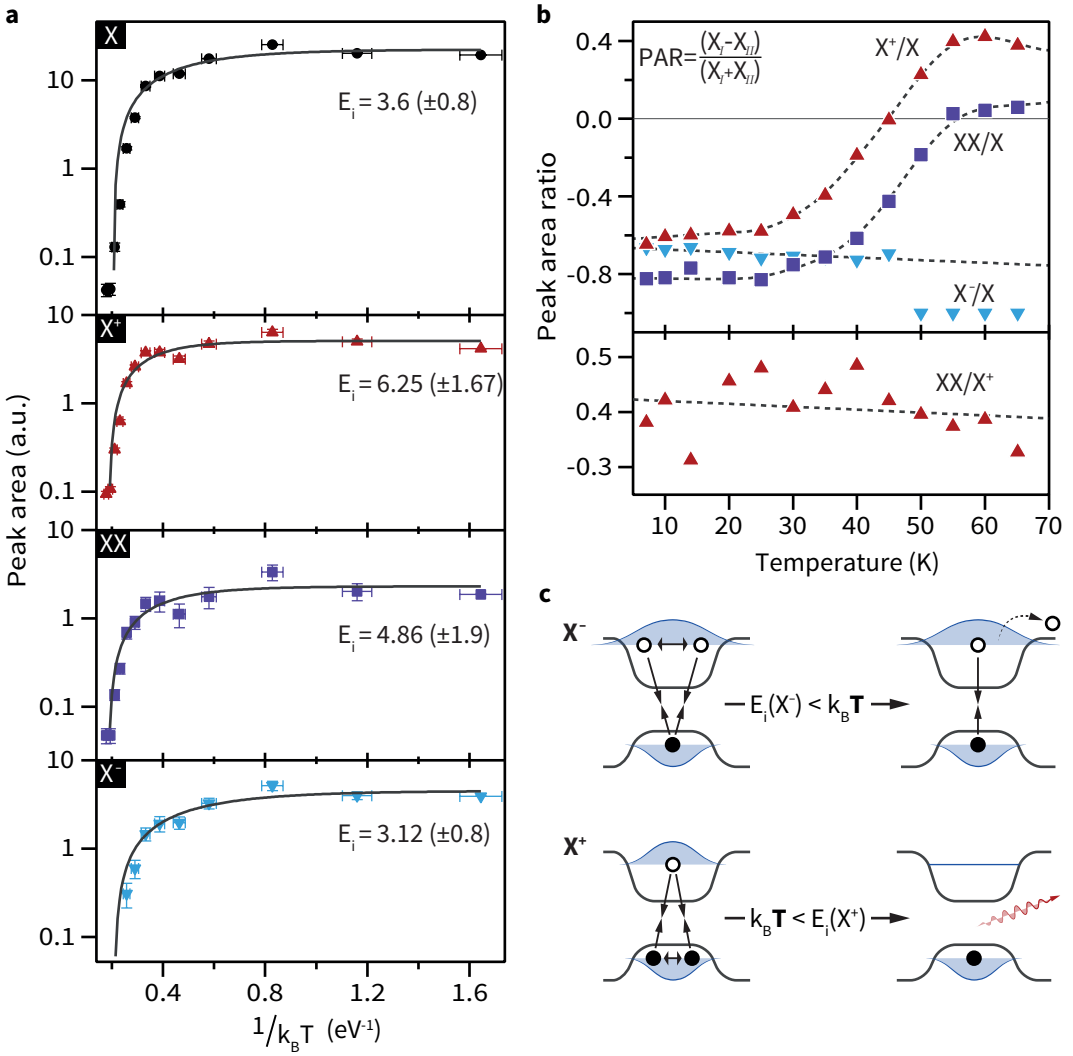

Figure 6.12 • **a.** Peak area (total emission intensity) in function of the inverse of the thermal energy for the four transitions of the shell-QD shown in figure 6.11 (see labels in topleft corners). The solid lines are fits to the data. The ionization energy E_i of the transition is extracted and displayed in the graph for each transition. **b.** Peak area ratio $\frac{X_I - X - II}{X_I + X_I I}$ as function of the temperature between the different excitonic states and X (top) and between X^+ and XX (bottom). The relative increase of the X^+ and XX decay intensity with respect to the X intensity becomes significant after 30 K. On the other hand, the X^-/X and X^+/XX couples maintain a similar level of relative intensity. **c.** Schematic of the X^- (top) and X^+ decay mechanism for an intermediate temperature **T** (*e.g.* 45K). The inward (outward) solid arrows represent binding (antibinding) interactions between carriers. At temperature **T** the X^- is preferentially ionized through the loss of an electron, while the thermal energy is not yet sufficient to overcome the binding energy of a single electron to two holes, allowing for the X^+ to decay through photon emission (red wavy arrow).

the electron wavefunction in the barrier: two electrons populating the same state will be able to minimize their interaction relatively efficiently. The results are fully coherent with the observation of an increase of the electron binding energy in function of the QD emission energy. It also supports the decrease seen in the X^+ binding energy for blue-shifted QDs.

Finally, it also shows that the high emission energy is not only due to the Al fraction in the dot, but can also be attributed to a small size, creating a significant difference between the energy offset of the hole-state/valence and electron/conduction continuums.

6.6 Spectral and temporal stability

The last section of this chapter is dedicated to a discussion on the temporal stability and the linewidths of the shell-QD emission. If linewidths below the commonly used single-stage spectrometer resolution have been observed (<100 μeV), some transitions show a relatively high level of broadening. Broad linewidth is a limiting factor (as FSS) for the implementation of QDs in many practical quantum optics schemes. A broadening due to the radiative recombination is expected (Fourier-transform limit), and represents the ultimate reachable limit. However, in the case of shell-QDs, this limit is several orders of magnitude lower than the observed linewidths (a glimpse at the difference is provided in figure 6.14).

The phenomena leading to spectral broadening can assume various origins, but the main one is the successive spectral jumps induced by the trapping and detrapping of charges nearby the QDs. The shift of the lines are then a direct consequence of a time-varying local electric field (through the quantum confined Stark effect). These effects have been shown to occur at various time scale, and with different magnitudes. Similarly, the QDs emission can be turned "off", a phenomenon referred to as blinking, and arising from the trapping of the QD in long-lived dark states (different from the X dipole-forbidden dark states). Here, the slow variations in peak energy and intensity were probed. Series of spectra are acquired at a certain rate, chosen in such a way that the time-lapse between two frame is the shortest, while maintaining a detection signal good enough to be able to fit the peaks with a good accuracy.

Figure 6.13 displays the results on the spectral and intensity stability for two different shell-QDs (left and right). For the dot 1, the whole exciton complexes multiplet can be observed, while a single emission line appear for the dot 2 (likely the X^+). The two shell-QDs are measured at different rate, respectively at 42 and 248 frame per seconds (fps). The top row shows the time-averaged spectra, while the main part of the panel (a) and (b) show the spectra in function of the acquisition real-time.

In both cases, no obvious blinking could be observed. Similarly, no important spectral jumps could be resolved, as it is the case in certain wide-gap semiconductor

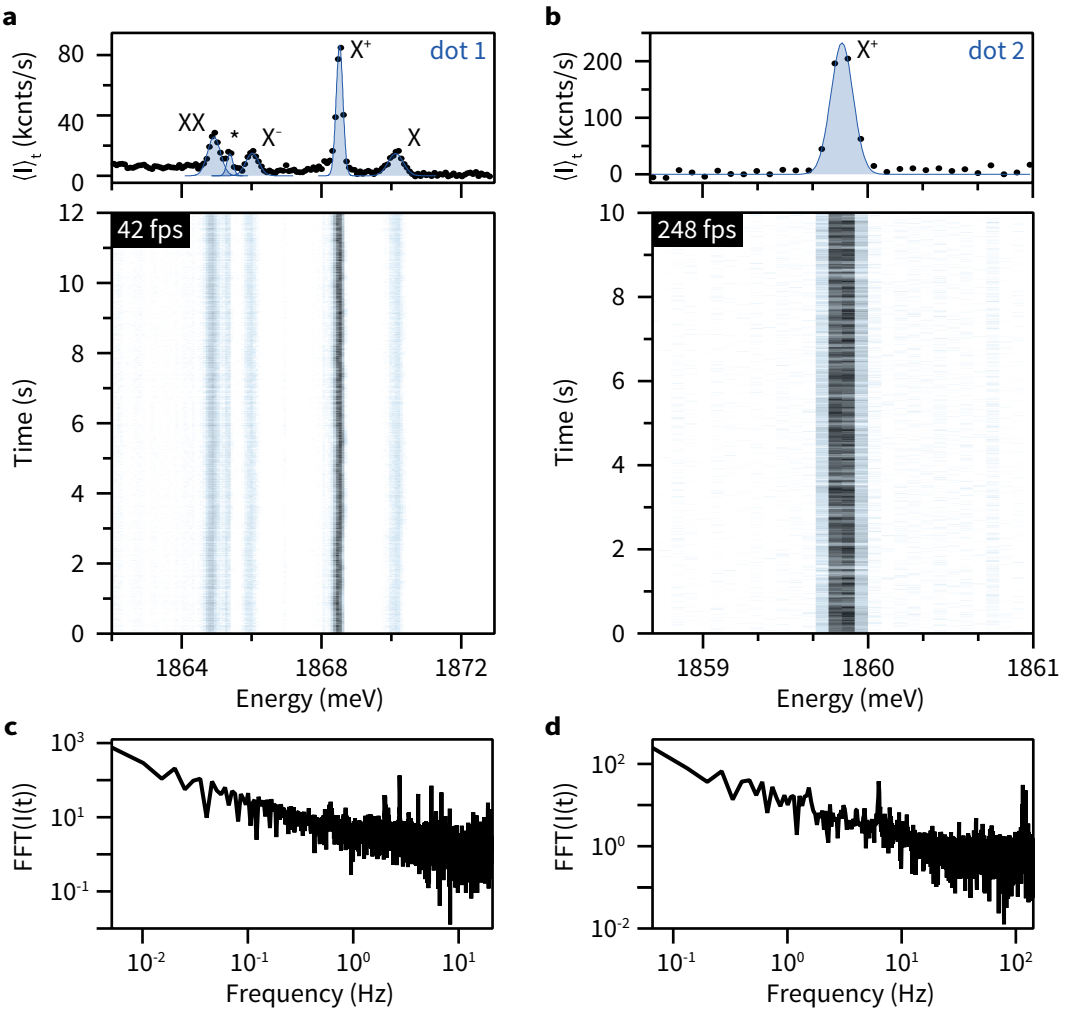

Figure 6.13 • a. Top inset: time-averaged normalized spectrum of a shell-QDs showing the complete excitonic multiplet, with the four transitions fitted with gaussian functions. The spectra acquired at each timestep is shown below. The map is shot at 42 fps, with an integration time of 20 ms. **b.** Same as (a), but monitoring the single peak of a different QD (dot2). The map is shot at 248 fps with 2 ms integration time. **c.** and (d) Fourier transform of the total intensity of the signals in (a) and (b).

systems or in early "stressor" GaAs QDs.[189–191] The insets (c) and (d) show the Fourier transform of the two signals (total intensities). Even in the Fourier transformed spectra, no particular features can be distinguished aside for weak peaks in the Hz range. These fluctuations are explained by the measurement technique: the closed-loop cryostat induces periodic vibration at around 1.5 Hz, which in turn excite the transverse vibrational modes of the optical table and of some relay components. Thus, if temporal blinking happens, it must be at shorter timescale, with a fast reactivation of the QDs from the "off" to the "on" state.

Turning toward the optical transition broadening, the peak energies extracted from the time series showed previously are represented in figure 6.14. The panel (a)-(d) focus on the four transitions of dot1 while the panel (e) is dedicated to the single line from dot2. The data are plotted in the form of histograms. The counts for each bin represents the number of spectra for which the peak energy was found to correspond to the bin energy, and the histogram are centered on the median bin. The blue curves are gaussian fits to the data (same for dot2, but without the histogram for clarity). For the graphs pertaining to dot1, the vertical solid bars represent the fifth of the time-averaged peak FWHM, in order to set the comparison, and the black arrow shows the mean of the data. For the dot2, the fit of the time-averaged peak is fully shown with a solid black line. In addition, the Lorentzian spectrum expected in case of perfect, Fourier-transformed emission is shown in dark gray.

The first outcome is that the broadening at this time scales is much weaker than the total, time-averaged broadening. Again, the broadening phenomena must happen at shorter timescale and cannot be resolved for such slow acquisition rates. Values between the nano and micro-second have been measured for spectral diffusion in DE-QDs.[192] However, the contribution is not zero, and can be seen to be smaller for the X^+ and XX compared to the other transitions, in particular compared to the X^-. This is reflected in the time-averaged FWHM and has already been observed in DE-QDs.[193] The reason can be found in the tighter confinement provided by the joint action of the two holes on the electron. If the electron wavefunction spread is made smaller, the instantaneous dipole momentum will also decrease, making the interaction between the excitonic complexes and the surrounding fields less efficient.

As a side note: the variation of the energy position of the peaks were shown to be gaussian, stochastically distributed. If it is admitted that the slow and fast components of the broadening arise from the same phenomenon (charge trappings and movements), but at different timescale, it is likely that the broadening phenomenon by time-varying electric fields cannot account for the red-shifted tail often observed in the peaks of the exciton complexes. Instead, an asymmetric broadening by acoustic phonon is more likely to be responsible for the skewing of the lineshape. Such an exciton-phonon interaction has already been noticed for QW fluctuation QDs, large GaAs DE-QDs and SKQDs, and is the best explanation to the red tail seen in the exciton spectra.[175,194–196] Since the exciton-phonon coupling is dependent on the size of the confined wavefunction, the presence of a red-shifted phonon sideband would also confirm the idea that the shell-QDs are not mere fluctuation of the Al concentration, but relatively deep yet small Al-depleted regions.

6.7 Conclusions and outlooks

This chapter presented several different optical measurements, all performed on isolated shell-QDs at cryogenic temperature. Single-photon emission has been

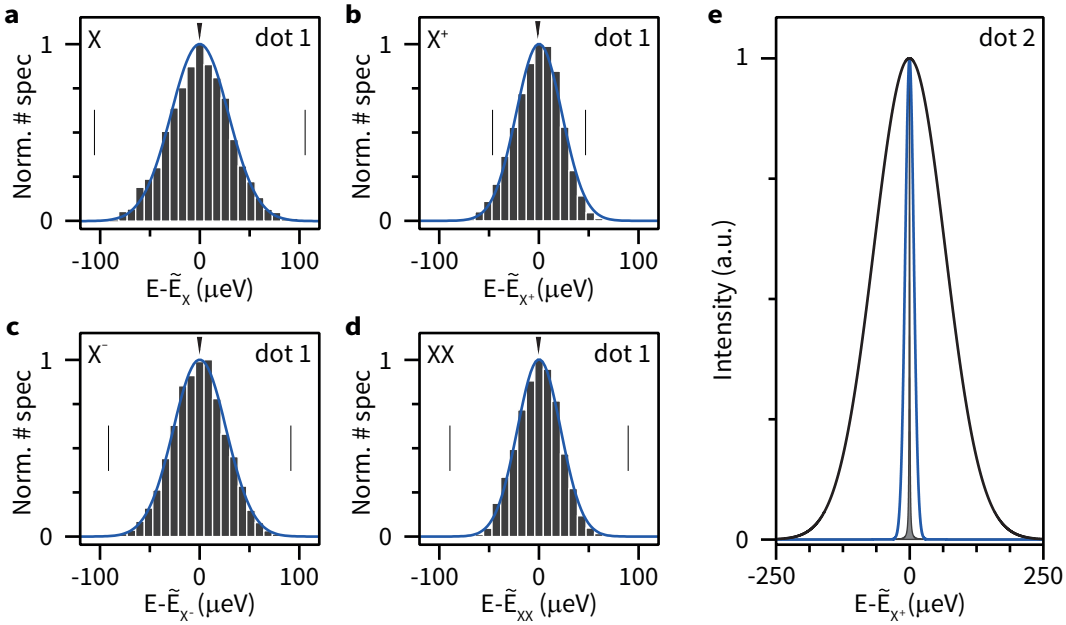

Figure 6.14 • a.-d. Histogram of the peaks energies extracted from the fit of the time serie for respectively the X, X^+, X^- and XX transitions. Each histogram is centered on the median of the distribution. The solid blue curves are gaussian fits, the black arrow shows the position of the mean energy. The pair of solid bars represent one-fifth of the time-averaged FWHM. **e.** The fit to the histogram of dot2 is represented by the solid blue line. The fitted curve to the time-averaged spectrum is fully shown as the solid black line. For comparison, the expected Fourier-transformed linewidth for this transition is shown in filled dark grey.

demonstrated in CW and in pulsed mode. The latter measurement showed that the production of triggered single photons (on demand) was possible. The optical spectra revealed the presence of satellite lines with respect to the X when the power is increased. The evolution of the intensity of these lines as a function of power hinted for s-shell excitonic complexes $X^{+/-}$ and XX. The measured radiative decay lifetimes are fast, around 500 ps for the X and 250 ps for the XX. The X^+ decay rate was usually found to be closer to the X value (slightly above in the example presented).

A cross-correlation analysis confirmed that the peaks were indeed stemming from the same QD, and that the attribution was justified. Beside the clear cascade between the XX and X states, both show complementary (mirror) FSS, as expected. Oppositely, the other peaks and in particular the peak attributed to the X^+ are not split by exchange terms. The FSS splitting energies were found to be relatively high (around the 100s of μeV), but (i) no complete statistical measurement serie has been realized, (ii) the identification of X with large FSS is easier, due to the competing intensity of the X^+ at average power and to the linewidth broadening. The reduction of the FSS for small QDs was thus not investigated, but this study would also be complicated by the uncertainty on the Al content. For small DE-QDs, the FSS is

supposed to drop due to a reduced anisotropy, however, the very different formation mechanism of shell-QDs may lead to different results.[197] The FSS measurements also revealed that the QD orientation is not locked by the NW axis. This, in turn, is believed to contribute to the measurement of optical linear polarization anisotropy even with standing wires. As it hinders the measurement of remnant spin polarization with a classical scheme, a different approach relying on the shift of the polarization anisotropy has been devised and applied on the supposed X^+ peak. The results show that the emission of this transition depends on the pumping laser polarization state. Assuming that the hole loses completely its spin orientation during the cooling and the capture process by the QD while the electron maintains a certain degree of polarization, the prominent peak of the charged exciton red-shifted by a few meV with respect to the X has been attributed to the X^+.

The attribution of the $X^{+/-}$ was found to match perfectly with the measurements acquired in function of the temperature on a high-energy QD. The measurements clearly revealed different ionization energies for the different complexes, with a particularly small energy for the X^-. The weak X^- ionization energy was attributed to the small height of the AlGaAs barrier compared to the first (and last) confined electron level. The reduction of the barrier height also promotes the spreading of the electron wavefunction out of the QD region, explaining the weak electron-electron repulsion energy.

Finally, the linewidth broadening has been investigated in the long timescale regime, down to the millisecond, to reveal that no slow blinking or spectral jumps happens. The linewidth broadening at these timescales was shown to have a very moderate influence on the time-averaged linewidth (10-15% maximum). If the issue of the FSS is harder to tackle, an enhancement of the radiative linewidth might be possible, first by removal of the crystalline faults along the NWs. As for now, the exact role or type of electronic defects created by stacking faults is not completely understood, but significant improvement in the linewidth of axial NWQDs has been measured in defect-free NWs.[133,134] The second option is to use, if the growth window allows it, a lower pressure of arsenic. This would prevent the incorporation of non-stoichiometric or substitutional As atoms, and reduce the number of carrier trapping sites. Finally, *in-situ* mid-growth annealing or a general increase of the growth temperature might prove useful. High temperature annealing was used successfully in the case of DE-QDs, with the major difference that the annealing step intervenes during an extremely low temperature process (200°C).[174]

Publications • The results on single-photon emission and fine-structure splitting presented in this chapter can be partially found in the following peer-reviewed publications:

> "Exciton footprint of self-assembled AlGaAs quantum dots in core-shell nanowires", Y. Fontana, P. Corfdir, B. Van Hattem, E. Russo-Averchi, M. Heiss, S. Sonderegger, C. Magen, J. Arbiol, R.T. Phillips and A. Fontcuberta i Morral, *Phys. Rev. B*, **90**, 075307, 2014
>
> "Self-assembled quantum dots in a nanowire system for quantum photonics", M. Heiss, Y. Fontana, A. Gustafsson, G. Wüst, C. Magen, D.D. O'Regan, J.W. Luo, B. Ketterer, S. Conesa-Boj, A.V. Kuhlmann, J. Houel, E. Russo-Averchi, J.R. Morante, M. Cantoni, N. Marzari, J. Arbiol, A. Zunger, R.J. Warburton and A. Fontcuberta i Morral, *Nature Mater.*, **12**, 439-444, 2013

Contributions • E. Russo-Averchi, M. Heiss, G. Tütünçuoglu, F. Matteini and A. Fontcuberta i Morral grew the different sample sets used in ths chapter, G. Wüst, A.V. Kuhlmann, J. Houel, supervised by R. J. Warburton measured the data shown in figure 6.1. M. Heiss produced the 2D FDTD calculations shown in Figure 6.6. P. Corfdir and YF acquired together the data in figures 6.2 and 6.8, using the infrastructures of R. T. Phillips. YF, Anna Fontcuberta i Morral and each third-party collaborators commented on the results.

Acknowledgements • G. Wüst, A.V. Kuhlmann, J. Houel and R. J. Warburton are greatly acknowledged for sharing their experience. P. Corfdir, B. Van Hattem and R. T. Phillips are warmly thanked for putting their laboratory at disposal and for the fruitful discussions.

Magneto-photoluminescence on shell quantum dots

7

Any magnetic fields will perturb the electronic states of a quantum system, regardless of its origin. Weak magnetic fields (compared to the magnetic length) add a term to the unperturbed Hamiltonian of the system : $\mathcal{H} = \mathcal{H}_0 + \mathcal{H}_M$. One example is the Overhauser effect, for which the combined magnetic field of polarized nuclear spins affects the energy of an electron (or hole). A magnetic field will essentially have a dual effect on the states of a QDs: (i) the field will split the levels with different spin configurations and (ii) it will increase the energy of all the spin-split levels (diamagnetic shift). In general, the magnetic properties of nanostructures, and in particular QDs, are interesting because the confinement has a strong influence on the response of the system. In addition, the behavior of the electronic states depending on the field can carry valuable informations on the confinement potential of the QD under observation. In this chapter, the effect of an external magnetic field on single shell-QDs emission spectrum will be presented. Magneto-photoluminescence (MPL) experiments allow to extract the Landé coefficients (g-factors) and diamagnetic coefficients of the X and X^+, and thus map the wavefunctions extension and the orientation of a shell-QD in a NW. The discussion will be first limited to the case where the magnetic field is parallel to the NW axis. In a second step, the case for which the magnetic field is rotated until being perpendicular to the NW (transverse geometry), and the effects on the QD emission spectrum will be discussed.

7.1 Diamagnetic and Zeeman effects

The energy levels of an electronic system are usually influenced if an external perturbation is applied. This is also the case if the perturbation is an external magnetic field. In this section, the effect of a moderate magnetic field is shown to affect the

emission spectrum of shell-QDs and at these field magnitudes can be described by a combination of the diamagnetic and Zeeman effects. This holds considering that the Larmor frequency $\omega_L = \frac{|e|B}{m^*}$ of the carriers is small and the associated magnetic length $l_m = \sqrt{\frac{\hbar}{m^*\omega_L}}$ is larger than the exciton radius. The magnetic length is independent of the mass and for the maximum magnetic field used in the following experiments (10 Tesla) is around 8.1 nm.

7.1.1 Diamagnetic shift

The energy variation of an exciton in a magnetic field $\Delta E_X(B)$ can be expanded for a given orientation of the field:

$$\Delta E_X(B) = \gamma_{\perp 1} B + \gamma_{\perp 2} B^2 + R(B) \tag{7.1}$$

In the weak field limit, the quadratic term dominates, and both the linear and residual terms can be dropped. The notation is also simplified: $\gamma \equiv \gamma_{\perp 2}$ is used to describe the diamagnetic coefficient. The $\perp$ sign indicate the plane perpendicular to the magnetic field. The $\perp$ sign is dropped in the discussion below, but all the relevant values used are considered to be the ones transverse to the field orientation (effective masses and correlation length).

Following the proposition of Walck anf Reinecke,[198] for a simplified geometry with cylindrical symmetry, γ takes the form:

$$\gamma = \frac{e^2}{8}\left[\left(\frac{\lambda}{\mu}\right)\langle\rho^2\rangle + \left(\frac{1}{m_e} + \frac{\lambda}{m_h} - \frac{\lambda}{\mu}\right)\langle\rho_e^2\rangle + \left(\frac{1}{m_h} + \frac{\lambda}{m_e} - \frac{\lambda}{\mu}\right)\langle\rho_h^2\rangle\right] \tag{7.2}$$

With $m_{e(h)}$, $m_{e(h)}$ and $\langle\rho^2_{e(h)}\rangle$ the electron (hole) mass and expectation values of the positions for uncorrelated charges. The reduced electron-hole mass is desinged with μ and $\langle\rho^2\rangle$ represents the correlation in the motion of the electron and hole and λ, defined as

$$\lambda = \frac{\langle\rho_e^2\rangle + \langle\rho_h^2\rangle - \langle\rho^2\rangle}{2\frac{\mu}{m_h}\langle\rho_e^2\rangle + 2\frac{\mu}{m_e}\langle\rho_h^2\rangle} \tag{7.3}$$

Equ. 7.3 points out how λ describes the effect of lateral confinement. For weak confinement, the single electron and hole are delocalized and $\lambda \to 1$. In case of strong confinement, the direct Coulomb term is merely a correction to the states energy, and the position of the electron and hole depends mainly on the geometry and $\lambda \to 0$.

In turn, the equation for γ (equ. 7.2) can be simplified to correspond to the weak and strong confinement regimes:

$$\gamma_{weak} = \frac{e^2}{8\mu}\langle\rho^2\rangle \tag{7.4}$$

and

$$\gamma_{strong} = \frac{e^2}{8}\left[\frac{1}{m_e}\langle\rho_e^2\rangle + \frac{1}{m_h}\langle\rho_h^2\rangle\right] \approx \frac{e^2}{8m_e}\langle\rho_e^2\rangle \tag{7.5}$$

The last simplication in equ. 7.5 is justified in the situation where the electron-hole mass ratio is large, like in GaAs. As a corollary, the hole wavefunction is also more localized, and the diamagnetic coefficient is dominated by the electron. It is worth noticing that the dependence of the diamagnetic coefficient on the QD size is not monotonic. For large QDs, the value converges toward the one dictated by the exciton binding energy in the bulk. As the QD size become smaller, the diamagnetic coefficient decreases. For very high confinement energies, the wafefunctions of the carriers and in particular of the electron will have the tendency to spread in the barrier material. Thus, γ is expected to increase again.[198]

This result can be used as an approximation for different QD morphology. This allows to map the confinement potential of a QD in function of the angle of the magnetic field, as shown below.

7.1.2 Zeeman splitting

The Zeeman effect manifests itself as a splitting of the spin sublevels of the observed QD. The effect strongly depends on the orientation of the magnetic field with respect to the strong confinement axis of the QD. For QDs with a well known strong confinement axis, in general co-linear with the symmetry axis of the QD, two particular cases can be readily differentiated:

Faraday configuration In this geometry, the wavevector of the observed luminescence ($\vec{k_\lambda}$) and the magnetic field ($\vec{B}$) are co-linear (z-direction). Often, the strong confinement axis of the QD (S_{axis}) is also aligned with the field and optical axis. For finite fields, the symmetry axis is defined by the magnetic field. If the symmetry of the QD is lowered (*e.g.* because of elongation), the field tends to re-establish the symmetry of the field-QD system, eventually overcoming the effect of FSS.

Voigt configuration This configuration corresponds to the case where $\vec{k_\lambda}$ and $\vec{B}$ are perpendicular (xy-plane). Again, classically the S_{axis} of the QD and $\vec{k_\lambda}$ are aligned to be co-linear. In this case, the magnetic field will break the symmetry (if any) of the QD for any finite value. It will also hybridize the dipole-allowed and -forbidden states, opening two new radiating channels (dark states). This configuration is extremely attractive to set-up so called "spin-Λ systems" used for optical spin-pumping. It allows the realization of *e.g.* coherent population trapping (CPT) or to use stimulated Raman adiabatic passage (STIRAP) to manipulate spins coherently.[199–203]

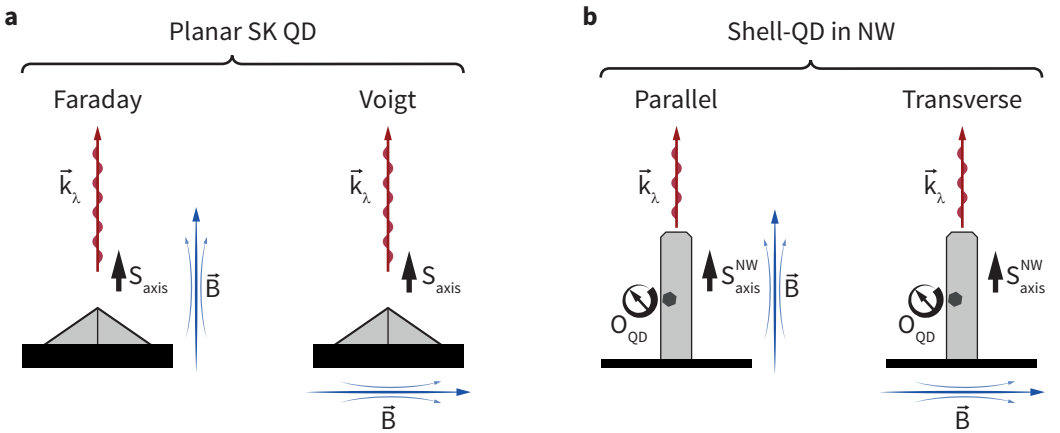

Figure 7.1 • Different magnetic field configuration ($\vec{B}$, triple blue arrows). **a.** For QDs with well-known quantum confinement and strong confinement axis (S_{axis}, black arrow), Faraday configuration refers to co-linear $\vec{B}$, S_{axis} and $\vec{k}_\lambda$, the wavevector of the observed light emission. Voigt configuration refers to co-linear S_{axis} and $\vec{k}_\lambda$, with $\vec{B}$ perpendicular to S_{axis}. **b.** For shell-QDs, the orientation of an hypothetical strong confinement axis is unknown (O_{QD}, revolving arrow). The host NW serves as a reference, and the configurations are described as parallel (transverse) to the NW long axis.

These "typical" configurations are illustrated in figure 7.1(a) with a planar SK QD (in grey), where the observed emission is pictured by a red arrow, and the magnetic field by a triple blue arrow. The strong confinement axis is represented with a black arrow. For axial QDs grown in NWs, these configurations are also valid as the axis of the NW is co-linear with the strong confinement axis of the QD.

The Hamiltonian describing the X energy for these two boundary cases can be expressed in a matrix form, with as a basis-set the pure states $\{ |\downarrow\Uparrow\rangle ; |\uparrow\Downarrow\rangle ; |\uparrow\Uparrow\rangle ; |\downarrow\Downarrow\rangle \}$:

$$\mathcal{H}_B^F = \frac{1}{2}\mu_B B_z \begin{pmatrix} (g_{ez}+g_{hz}) & 0 & 0 & 0 \\ 0 & -(g_{ez}+g_{hz}) & 0 & 0 \\ 0 & 0 & -(g_{ez}-g_{hz}) & 0 \\ 0 & 0 & 0 & (g_{ez}-g_{hz}) \end{pmatrix} \tag{7.6}$$

The F superscript denotes the Faraday configuration, μ_B is the Bohr magneton, g are the Landé factors for a given particle and orientation: the e (h) and z (x) subscripts stands for electron (holes) and the z (x, in-plane) direction. From the Hamiltonian in equ. 7.6, it is clear that the eigenvector in Faraday configuration relates directly to the basis-set given above. The eigenstates are then pure spin-states, and the two dipole-allowed transitions emit circularly polarized photons. For low fields, this is mitigated because of non-trivial exchange terms (see section 2.2.2).

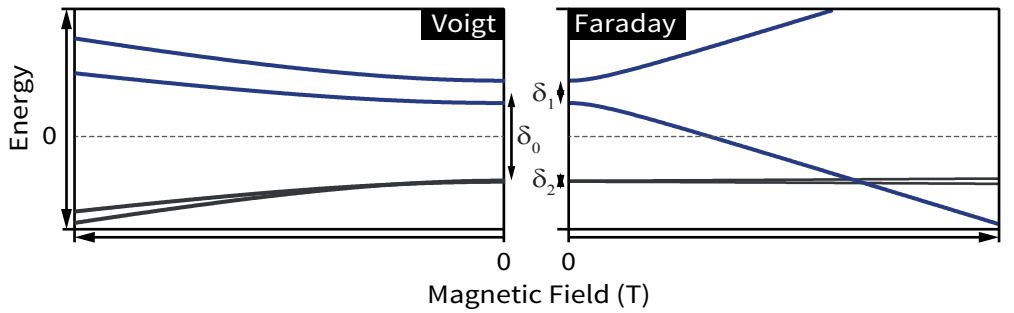

Figure 7.2 • Energy of the spin sub-levels of an arbitrary X as a function of the magnetic field for the Voigt and Faraday configurations (see figure 7.1(a)). The dark blue (anthracite) lines are the states which, at zero field, correspond to dipole-allowed, radiative (dipole-forbidden, non-radiative) states. The thick lines represent radiative states for different fields. The inset in the right panel shows a magnification of the anti-crossings between states tending toward the same energy. The exchange terms are shown in-between the two graphs.

$$\mathcal{H}_B^{V(x)} = \frac{1}{2}\mu_B B_x \begin{pmatrix} 0 & 0 & g_{ex} & g_{hx} \\ 0 & 0 & g_{hx} & g_{ex} \\ g_{ex} & g_{hx} & 0 & 0 \\ g_{hx} & g_{ex} & 0 & 0 \end{pmatrix} \tag{7.7}$$

The $V(x)$ superscript on the left-hand of equ. 7.7 stands for the Voigt configuration where $vecB$ lies in the x-direction of the xy plane. Because of the anti-diagonal form of $\mathcal{H}_B^{V(x)}$, the $\{ |\downarrow\Uparrow\rangle ; |\uparrow\Downarrow\rangle ; |\uparrow\Uparrow\rangle ; |\downarrow\Downarrow\rangle \}$ states are not eigenvectors of the Hamiltonian anymore. Instead, the new eigenstates are linear combinations of the basis vectors. A typical example of Zeeman splitting as a function of the magnetic field is shown for an X in figure 7.2. The case of Voigt (left) and Faraday (right) configurations are represented, with the thick lines marking the radiative states. In perfect Voigt geometry, all four states can emit photons with the same probability. In the Faraday configuration, only two states are optically active, provided that the holes have an almost pure heavy hole character. In general, for low fields, there is a clear competition between the exchange (marked with the exchange parameters (δ_0, δ_0, δ_0) and the Zeeman terms. As the field becomes stronger, the eigenstates recover pure spin characters.

As shown in the following section, this description is not always sufficient for shell-QDs. Because the strong confinement axis (the orientation) of an observed shell-QD is not necessarily in the axis of the NW, the configuration with $vecB$ along the z-direction is not automatically in Faraday geometry. The same holds for the field transverse to the NW axis. This is illustrated in figure 7.1(b). In the schematic, the indeterminacy of the strong confinement axis of the shell-QD (O_{QD}) is represented with a revolving arrow.

Instead, the configuration should only be described as either "parallel" or "transverse" (to the NW axis). The outcome is that the Hamiltonian of the system for

these two configuration is likely to be a generalized expression of the Zeeman hamiltonian instead of the particular form given in equ. 7.6 and 7.7.

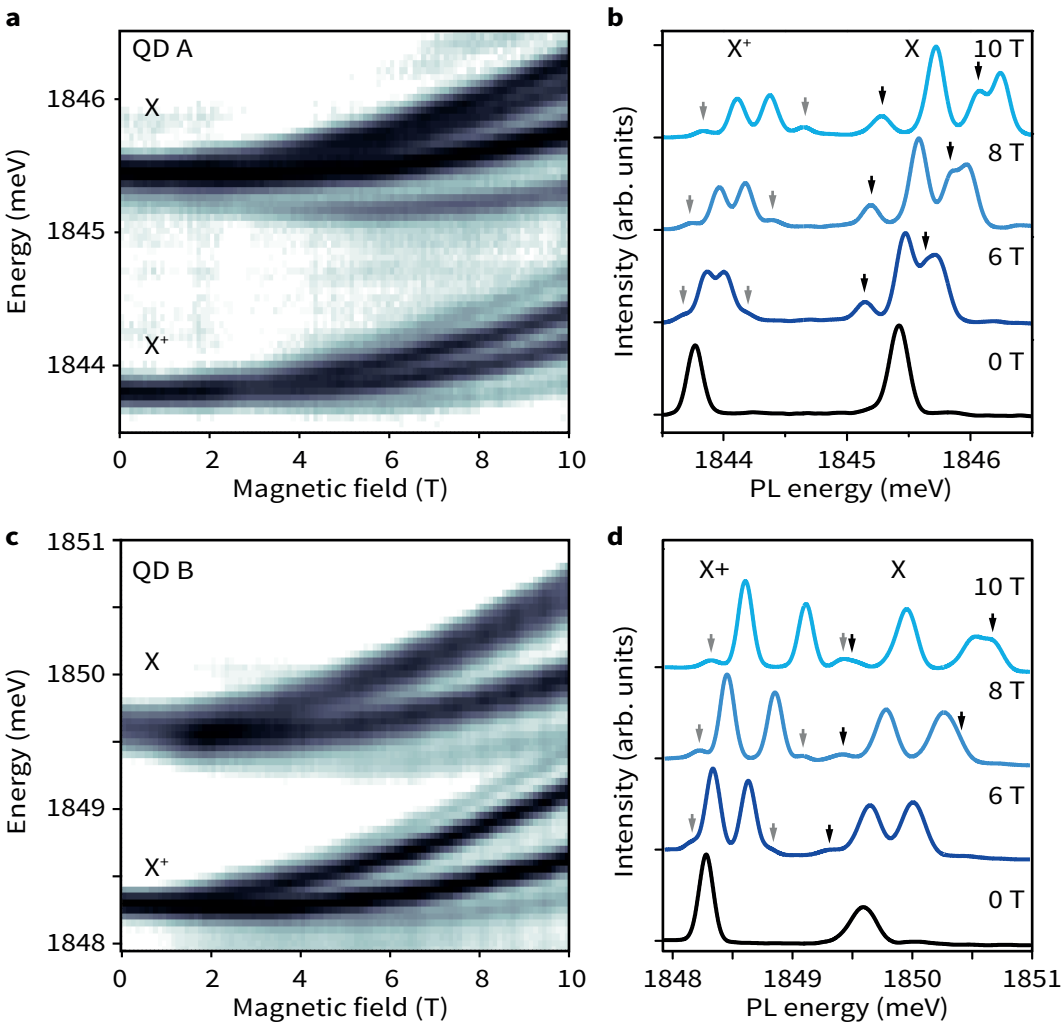

Figure 7.3 • **a.** MPL spectral map of a shell-QD (A) in the parallel configuration. **c.** Same as (a) for a second QD (B). For both shell-QDs, the X and X^+ emission peaks are visible. Each spectrum has its maximal emission intensity renormalized to 1. **b.**and **d.** Luminescence spectra of the two shell-QDs for different magnetic fields. The black (gray) arrows point at the bright and dark transitions. Adapted from ref. 171

7.2 MPL: Parallel configuration

7.2.1 Experimental details

For parallel configuration, the NWs were mounted in the cryostat described in the figure 3.4 on their silicon growth substrate and cooled to 4.7 K. The high yield in vertical NWs combined with the large tilt angle of remnant non-vertical NWs give a high-confidence bound to measure NWs in-axis with the field and optical axis (*i.e.* parallel configuration).[38,204] QDs were excited in non-resonant conditions with the 632 nm line of an HeNe laser. The signal was analyzed with a 500 mm spectrometer (1200 l/mm grating) with a resolution of around 100 μeV. The signal was recorded on a LN_2-cooled CCD camera. The magnetic field was ramped in 0.1 T increments, and a spectrum was acquired at each step.

7.2.2 Results

The MPL spectra for magnetic fields between 0 and 10 T are presented in figure 7.3 for two different QDs. In both case, the emission line of the X and X^+ (redshifted by few meV) is recorded. For both electronic configurations, similarities can be seen: the initial peak splits in a quadruplet. Out of each quadruplet, a differentiation can be made between intense peaks (bright transitions) and weak peaks (dark transitions). In figure 7.3(b) and (d), the dark transitions are tagged with arrows. The splitting between the peaks is increasing as expected from the Zeeman effect, and the diamagnetic response rigidly blue-shifts the spectra for each magnetic field step. The evolution of the X^+ is noticeably clearer for both case of QD A and B. This is due to a very different situation compared to X. Indeed, the presence of a second hole in the shell-QD leads to a hole spin-pairing, effectively canceling the exchange interactions. Thus, at zero field the optical transitions between spin sublevels for X^+ are degenerate in energy.

In order to clarify the picture, the energy position of the peaks for QD A are reproduced in the left panel of figure 7.4. In this case, the peaks corresponding to upper bright (X_2) and lower dark (X_I) states are plotted on the right side and the peaks corresponding to lower bright (X_1) and upper dark (X_{II}) on the left. The different peaks are labeled accordingly in the right panel of figure 7.4, which reproduces the spectrum at 10 T.

This representation shows that in a first approach, the evolution of the different bright and dark transition energies can be represented with a heuristic, quadratic model of the following form:

$$E_b^X = E_b^0 \pm \frac{1}{2}\mu_B g_b^* B + \gamma B^2 \tag{7.8}$$

and

$$E_d^X = E_d^0 \pm \frac{1}{2}\mu_B g_d^* B + \gamma B^2 \tag{7.9}$$

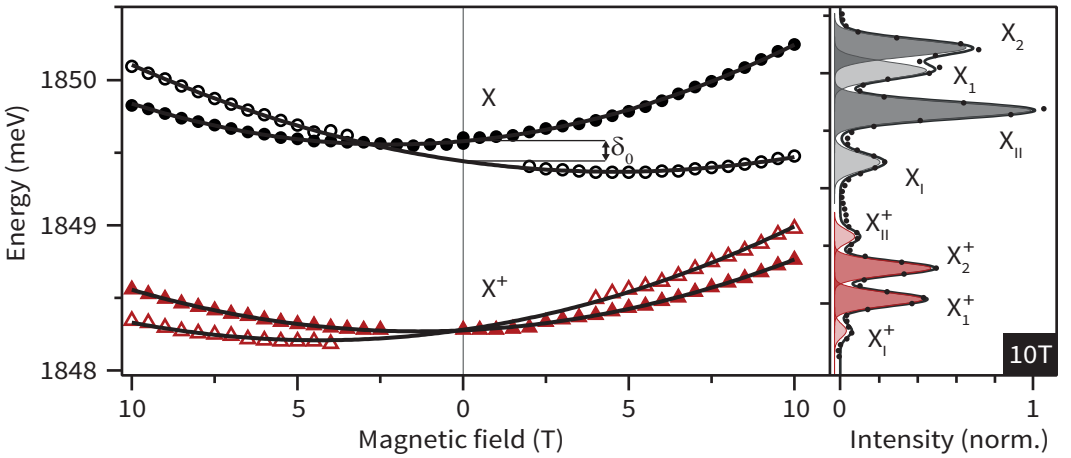

Figure 7.4 • Extracted energies of the X and X^+ sub-levels peaks for QD A (see figure 7.3(a)). The lower branches of the dark (open symbols) and bright (closed symbols) states are reflected against $B = 0$ and the energies are fitted with equ. 7.8 and 7.9 (solid lines). The spectrum at 10T is shown in the right-hand panel with the label for the states. The exchange splitting between the dipole-allowed and forbidden states δ_0 can be extrapolated at 0T.

Here for the bright (b) and dark (d) transitions of X. The constant term E^0 represents the energy at zero fields. The linear term stands for the effect of the magnetic field on the spin sublevels (Zeeman), and is characterized by effective Landé coefficients ($*$ superscripts) related to the particular orientation of the magnetic field (along the NW long axis). Finally, the quadratic term is due to the effect of the magnetic field on the total exciton energy (diamagnetic shift). The fits with this heuristic model are represented as black lines in the left panel of figure 7.4.

The diamagnetic coefficient directly relates to the wavefunction extension in the plane perpendicular to the applied field. Different coefficients were measured for shell-QD in neutral and charged configuration and yield wavefunction spatial extensions in the order of 6 to 12 nm, in excellent agreement with the measurements of segregated Ga-rich islands imaged with TEM or more recently APT (see chapter 4). The γ found for neutral and charged excitons are represented by respectively blue circles and red stars symbols in figure 7.5a. In addition, it is worth mentioning that for the shell-QDs were the X-X^+ couple could be clearly identified, γ_{X^+} was always significantly lower than γ_X. This is consistent with the presence of an additional (heavy) hole in the QD. In our case, the high emission energies and overall low γ indicates that the shell-QDs can be described as being in the strong confinement regime. In turn, this implies low λ values for the equation 7.3. The diamagnetic coefficient is then well described by the equation 7.5 and stems mainly from the electron contribution. For strong confinement energies and finite potential barriers, the electron wavefunction will have the tendency to extend slightly in the barriers. For an X, this extension is mitigated by the presence of a heavy hole which tends to bind the electron on the hole site (by Coulomb interactions). In

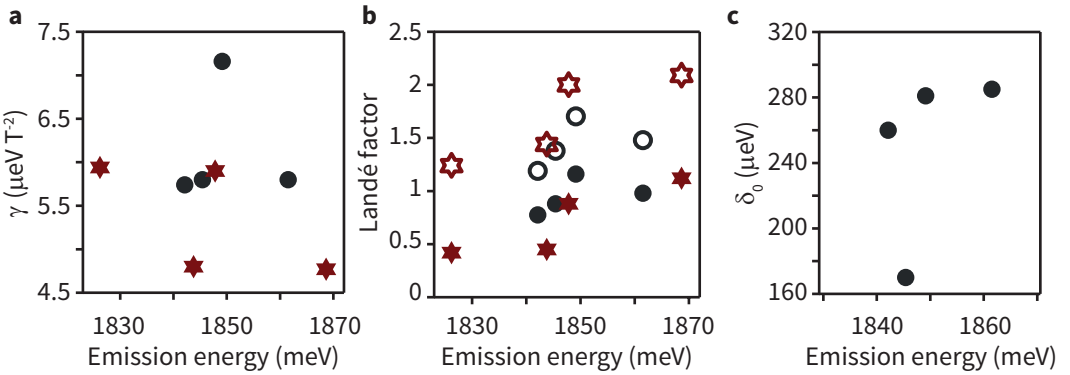

Figure 7.5 • QDs parameters measured in the parallel configuration in function of the emission energy. **a.** Diamagnetic coefficients for Xs (circles) and trions ($X^{+/-}$, stars). **b.** Effective Landé factors for bright (closed symbols) and dark (open symbols) transitions of Xs and $X^{+/-}$s. **c.** Dipole-allowed /-forbidden exchange splitting energy δ_0 for the Xs in (a) and (b).

the case of an X^+, this effect is increased as there is now two positive charges acting on a single electron.

Responsible for the linear terms, the bright and dark effective Landé coefficients are composites of the electron and hole g-factors and thus can be written as $g_b^* = (g_e^* + g_h^*)$ and $g_d^* = (g_e^* - g_h^*)$. Every shell-QD measured so far (in neutral and charged electronic configurations) presented a larger Zeeman splitting for the dark emission peaks compared to the bright ones. The measurements are shown in figure 7.5b (blue circles (red stars) stand for X (X^+) and closed (open) symbols for brigth (dark) transitions). Hence, the sign of g_e and g_h must be opposite. Given the consistency of this observation for all the shell-QD measured, the opposite sign of the electron and hole g-factors is likely to arise from the material properties combined with strong confinement energies. The exact determination of the signs was unfortunately not possible in this case due to setup limitations (as a polarization analysis is made impossible due to faraday rotation in the optical fiber). A positive sign is arbitrarily attributed to the electron g-factor.

In addition, the extrapolation at zero field allows to retrieve the bright-dark splitting stemming from the exchange interaction (δ_0). For the shell-QD A, δ_0 is found to be around 170 μeV. As mentioned before, the splitting is zero for charged excitons. A compilation of the values for $\delta 0$ of X in different shell-QDs is shown in figure 7.5c. The values are comprised between 170 and 290 μeV. The enhancement of the splitting compared to bulk and quantum well values again illustrates the effect of the strong 0D confinement in shell-QDs.

Finally, the splitting of each excitonic complex into four optically active transition peaks when the magnetic field is applied perfectly parallel to the NW axis is a major difference with what is usually measured with axial NW QDs (or planar QDs). A similar four-fold splitting has been noticed for crystal-phase QDs in InP NWs.[12] In

a tentative to explain this phenomenon, the authors pointed out the possibility of a mixing between light holes and heavy holes, which can arise *e.g.* from strain. A similar observation has been made in the case of InAs QDs and has been clearly attributed to strain.[100] LH-HH mixing can also happens in the case of a very elongated QD (tending to a quantum wire) or if the QD symmetry is strongly broken. In the latter case, the nominally dark states can even radiate at zero field (see ref. 105) Finally, four emission lines can also be measured for specific cases of highly symmetric QDs (C_{3v} symmetry), as in the case described in ref.[205–208]

In the present case, the measurement in a single direction, *i.e.* along the NW axis does not allow to differentiate between these different cases. A simpler explanation is hinted at the beginning of the chapter. Due to the formation process, the strong confinement axis of the shell-QD is not necessarily collinear with the long axis of the NW. This is described in the schematic in figure 7.1b. In that case, the measurement of four optically active states is expected, as the magnetic field hybridizes the dipole-allowed (100% bright) with the dipole-forbiden (100% dark) states.

7.3 Angle-resolved magneto-photoluminescence

7.3.1 Experimental and analysis details

In order to obtain a better understanding of the electronic and spin sublevels of shell-QDs, measurements for magnetic fields titled with respect to the NW axis where realized. The results can be modeled with using simultaneously two generalized hamiltonian. One for the exciton and one for the positive trion, as these two cases are indeed different. Nevertheless, the X and X^+ share characteristics. If the weak optical transitions in figure 7.3 are not due to heavy-light hole mixing, they could be explained for a tilt between the shell-QD strong confinement axis and the NW axis. In this case, it is reasonable to assume that this tilt should be taken in account for both X and X^+. Two hamiltonians encompassing exchange (for X), Zeeman (angle-dependant, a generalization of equ. 7.6 and 7.7) and diamagnetic contributions (in addition to a X-X^+ binding energy) can be simultaneously fitted to the QD optical transitions. Spectral maps are acquired for NW axis-magnetic field angles between 0 and 90 degrees (in seven steps). The shell-QD examined is the same as the one previously labeled QD A (shown above).

The fitting parameters are limited to the exchange δ_0 parameter, and the Zeeman and diamagnetic parameters. For both X and X^+, the electron g-factor is taken to be isotropic (an approximation justified by the moderate electrons g-factor anisotropy compared to the holes). The holes are described with an out-of-plane (colinear to the shell-QD strong axis -z-) and in-plane g-factor. The diamagnetic coefficients are fitted for each angle. The tilt angle between the shell-QD and the NW axis is a global fitting parameter.

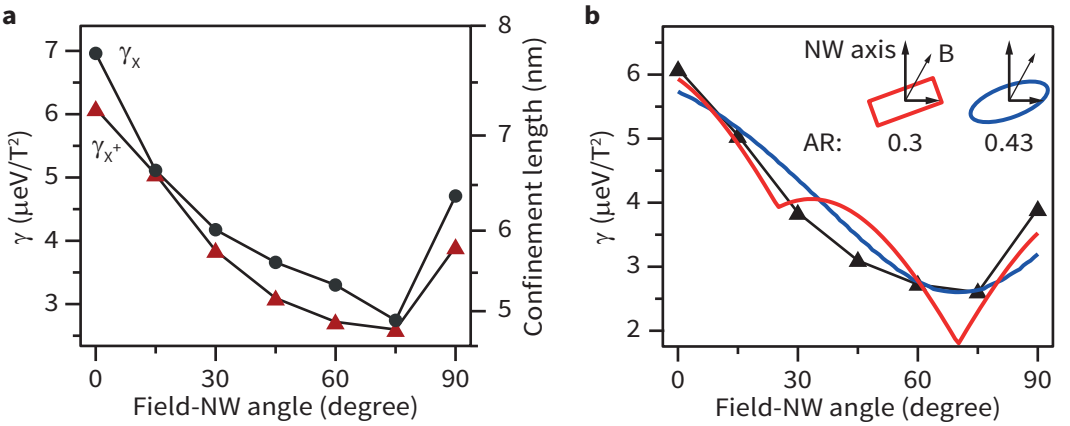

Figure 7.6 • a. Diamagnetic coefficient as a function of the NW axis-magnetic field angle for the X (blue circles) and X^+ (red triangles). Black lines are simple connections between data points. The corresponding scale for the calculated confinement size appears has the right vertical axis. **b.** Diamagnetic coefficient for X^+ compared to two different ideal cases of cross-section: a cuboid (red) and an ellypsoid (blue). The solids have been rotated (-20 degrees) in order to have their minimum coinciding with the measurements. $AR = \frac{F_s}{F_l}$ the ratio between the short and long Ferret's diameters. Adapted from ref. 209

The optical path and experimental components are mainly the same as in the previous section.

7.3.2 Angular dependence of the diamagnetic coefficient

The first quantities that can be extracted from the fit are the diamagnetic coefficients for the X and X^+ as a function of the field angle. The results for both excitons are shown in figure 7.6(a). The blue circles represent the diamagnetic coefficient γ_X at each angular step for the X. The red triangle stand for γ_{X^+}, the coefficient of the positive trion. It can be readily seen that both coefficient have very similar values. Nevertheless, the diamagnetic coefficient of the X^+ is systematically slightly smaller for the measured angular range. This confirms what was already remarked in the previous section for neutral and charged excitons in different QDs (see figure 7.5(a)). The smaller diamagnetic coefficients for charged species correspond to an overall smaller spread of the electron wavefunction, as it is the dominant term for the diamagnetic coefficient (see equ. 7.5). As expected, this reduced extension is taking place in 3D as seen in figure 7.6(a). Aside from its extension, the general shape of the positive trion wavefunction is not majorly modified compared to the neutral exciton. The right-hand scale in figure 7.6(a) shows the calculated wavefunction extension considering an electron effective mass corresponding to the alloy $Al_{0.1}Ga_{0.9}As$. The calculated extension is in excellent agreement with the size of segregated islands presented in chapter 4. The small extension is a clear evidence for strong confinement. It explains (i) the large emission

energy which can be recorded from shell-QDs (ii) the absence of a p-shell emission, as the second quantized levels for the electrons is likely to be in the continuum and (iii) the moderate exciton ionization energy.

Another important information is found in the minimum measured for a field angle of 70 degrees. The confinement length is minimum at this point, and shows that the shell-QD possess a clearly defined axis of strong quantization. Interestingly, this axis is neither along the NW growth axis, nor perpendicular to it. This offset between the NW axis and the QD strong confinement axis is important to interpret the observation of more than two Zeeman sublevels when the magnetic field is applied.

The global shape of the curve of the diamagnetic coefficient (for X^+) is further compared with the cross-sections associated to idealized, simple trial geometries. The comparison in shown in figure 7.6(b). The black curve with triangle markers represents γ_{X^+}. The cross-section for an ellipsoid (cuboid) is shown in blue (red). The cross-section are calculated analytically by projection the solids on a plane, at various angles. The orientation of the solid is modified in order to reproduce the minimum at 70 degrees. Further, a certain elongation ratio (AR), defined as $AR = \frac{F_s}{F_l}$ the ratio between the short (F_s) and long (F_l) Ferret's diameters, is adjusted to the experimental curve.

Because of the simplicity of their shape, it is not expected that the trial cross-sections would be in close agreement with the measured curve of the diamagnetic coefficient. Yet, it is worth noting that for angles up to 70 degrees, the ellipsoid model seems to represent better the smooth shape of the measurement. The situation is very different for the very last point of the measurement, *i.e.* right after the minimum. The measurement shows a steep increase in the diamagnetic coefficient. This behavior cannot be reproduced with a smooth model like the ellipsoid but can appear for shape with sharper transition between different facet like in the cuboid case. Based on this observation, one can conclude that in this particular case, the QD shape is likely to present at least one disruption despite an overall smooth shape. The lack of sharp features can be expected if the diffusion character of the formation process is taken into account. It should be noted that the uncertainty on the data point is smaller than the marker, and a measurement or fitting inaccuracy can be ruled out.

7.3.3 Angle-dependent Zeeman effect

The figure 7.7 represents the energy of Zeeman-split sublevels for X (blue circles) and X^+ (red circles). The diamagnetic contribution to the energy has been removed. The first seven panels correspond to measurements for different NW axis-field angle (indicated in a black inset), while the last panel (bottom right) shows the energy of the sublevels in function of the field angle, for a fixed magnetic field value of 10T.

The first outcome of the fit shows that it is not necessary to include a contribution from the light-holes in order to reproduce accurately the measurements. The main

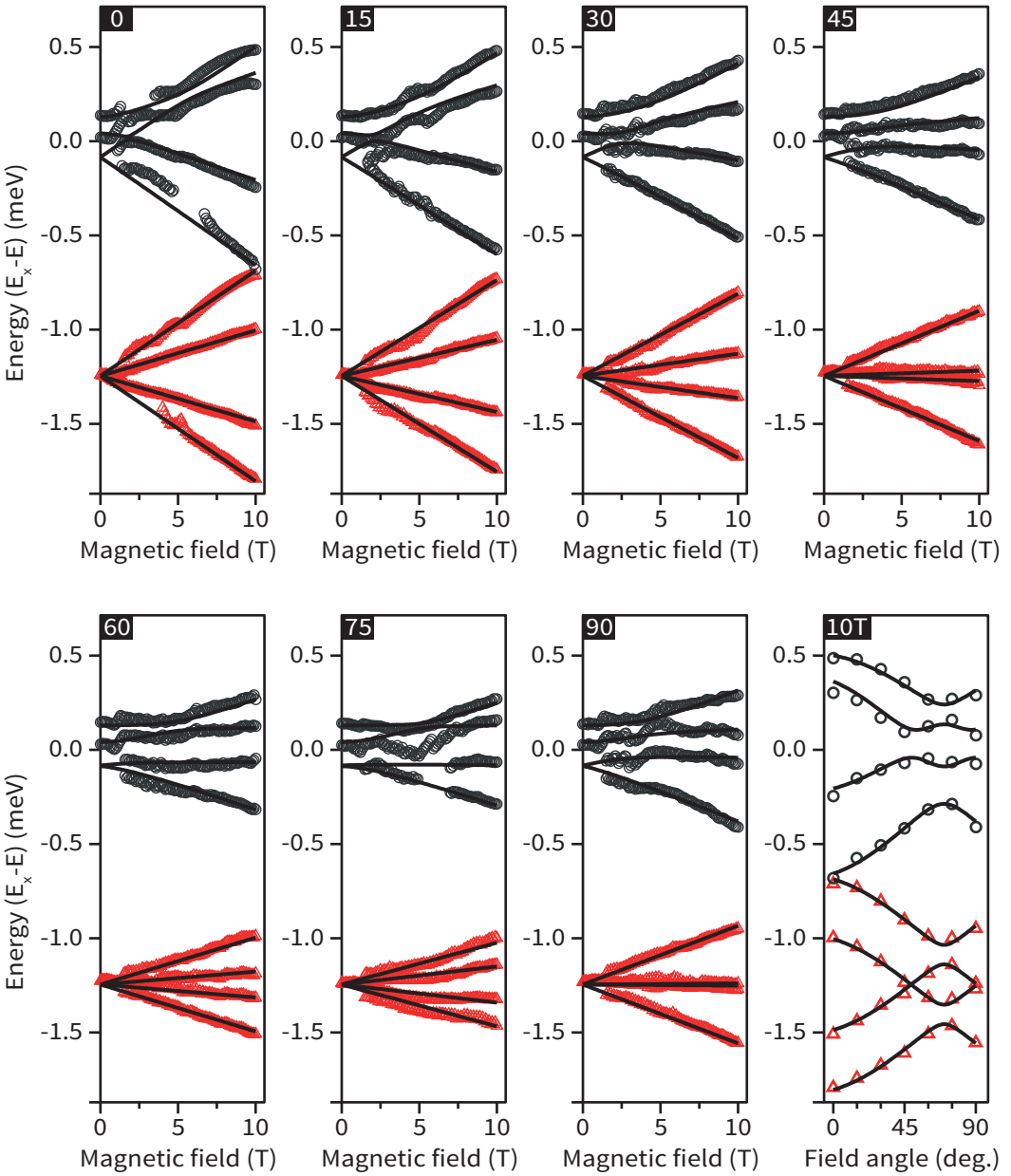

Figure 7.7 • Fitting of the emission energies of QD A: X (grey circles) and X^+ (red triangles) Zeeman-split sub-levels for different field angles (0 to 90) with respect to the NW axis. Lower right: Energy levels at 10T for all the angles. The diamagnetic shift has been subtracted and the energy shifted so that $E_X^0 = 0$.The black lines represent the results of the fit with the relevant angle-dependent (total) Hamiltonian (see main text).

reason for that is the offset in angle between the shell-QD strong confinement axis and the NW axis. The angles in figure 7.7 and following are systematically referring to the

	FWHM*	δ_0^*	δ_1^*	g_e	g_{hz}	$g_{h\perp}$
X	*200 ± 1*	170 ± 5	*91 ± 3*	0.5 ± 0.01	-1.57 ± 0.01	-0.38 ± 0.04
X^+	*140 ± 1*	x	x	0.55 ± 0.01	-1.47 ± 0.02	-0.18 ± 0.02

Table 7.1 • Main values for the QD emission shown in figure 7.7. The diamagnetic coefficients are left out and can be seen graphically represented in figure 7.6. The values in italic are determined prior to the fit, with independent procedures. δ_2, the exchange splitting between dark states, was set arbitrarily to 2 μeV. * *in μeV*

angle of the field with respect to the NW axis.

All the data can be well represented for an offset angle of 19.9 degrees. This agrees remarkably well with the diamagnetic coefficient minima of 70 degrees (and thus its complementary angle of 20 degrees) found in the previous section. The values of the fit for both X and X^+ are displayed in the table 7.1

Effect on the exciton

For the X, because of this initial angle offset, the dipole-forbidden and -allowed states of the primary basis $\{ |\downarrow\Uparrow\rangle ; |\uparrow\Downarrow\rangle ; |\uparrow\Uparrow\rangle ; |\downarrow\Downarrow\rangle \}$ hybridize for any measured angles. Even in the case of the minimal 0 degree measurement. In general, for low angles, the model predicts first an anti-crossings between the second (X_{II}) and third (X_1) sublevels. This has the effect to deflect the third state X_1 to higher energy and makes it meet the most energetic sublevel (X_2), leading to another avoided crossing. For larger angles, the evolution of the sublevels eigenenergies as a function of the field tends to resemble the typical Voigt geometry. A particular specificities can nevertheless be pointed out. Instead of seeing the two higher states X_I and X_{II} diverging from each other, the opposite happens, and is particularly visible for the field angle of 75 degrees. The two states slowly converge and ultimately avoid crossing each other.

In addition to the eigenenergies, the model also yield the eigenvectors for each states. These eigenvectors are indeed expressed in the basis formed by the pure states already described beforehand. Considering that only $|\downarrow\Uparrow\rangle$ *and* $|\uparrow\Downarrow\rangle$ are dipole-allowed, the radiative intensity of a given sublevel for a certain set of field strength and angle will be directly linked to the projection of this sublevel on the $\{ |\downarrow\Uparrow\rangle ; |\uparrow\Downarrow\rangle \}$ subspace. With that in mind, it is possible to reconstruct the expected MPL spectral scans with the parameters obtained from the fit of the energies. The comparison between the measured MPL scans and the calculated spectral maps can be seen in figure 7.8(a), respectively 7.8(b). In this case diamagnetic effects were also included. The figure 7.8 shows a comparison for a subset of measured angles, chosen for their particular features. Taking into account in the calculation the broadening of both X (200 μeV) and X^+ (140 μeV) and a slightly higher emission rate of the X^+, the intensities of the calculated maps agree well with the measured data.

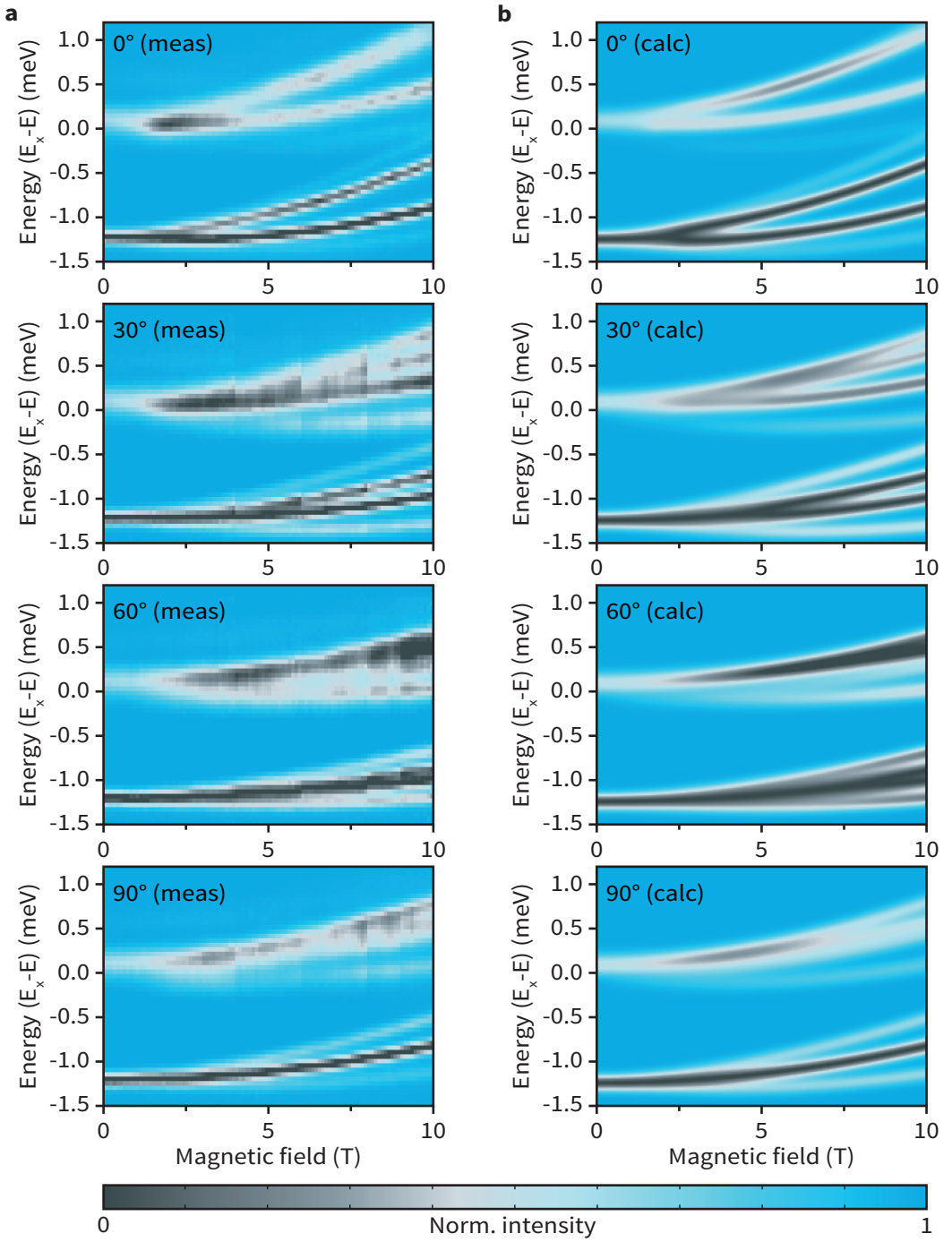

Figure 7.8 • Side-by-side comparison of the measured and calculated MPL maps. **a.** Measured spectral maps. **b.** Calculated spectral maps generated with the fitted parameters (calc) for 0, 30, 60 and 90 degrees. The intensities have been renormalized to the maximal intensity of the X^+. The computed intensity ratio of the X and X^+ was scaled according the emission ratio at zero field. The computed intensities reflect fairly accurately the measured intensities. The broadness of the linewidths hinders the clear observation of any anti-crossings.

In particular, it can be remarked that the significant line broadening hinders the observation of the predicted anti-crossings. Their effect can be however seen, as nominally dark states such as X_{II} gain significant visibility due to an exchange of character with X_1 at low fields.

A detail of the "composition" of the different Zeeman split sublevels is given here in different cases. The figure 7.9 shows the case for the field parallel to the NW axis (0 degrees). The panel 7.9(a) reproduces on the right the fitted energy levels for the X (same as figure 7.7 up left), and on the left a close-up of the anti-crossing between the sublevels X_1 and X_{II} (marked in dashed red on the full spectrum). The low field at which this anti-crossing takes place is a direct consequence of a large, sign-reversed, hole g-factor with respect to the electron.

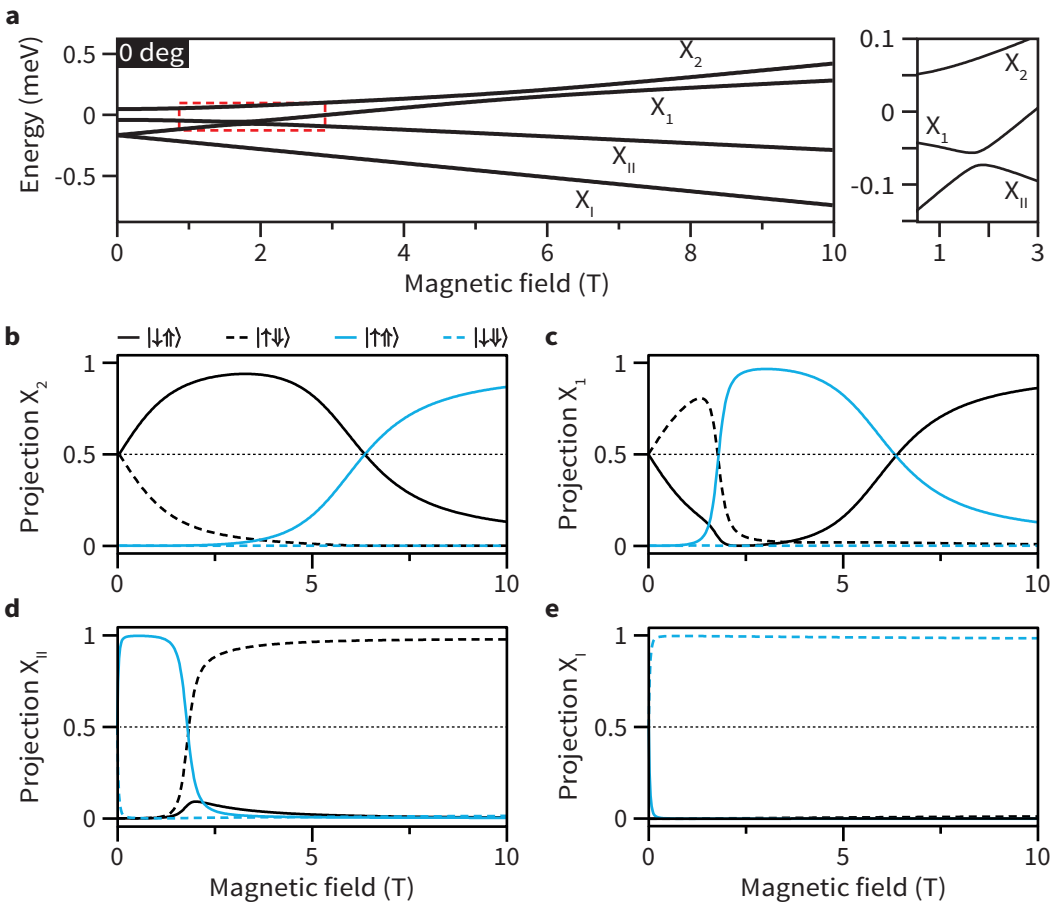

Figure 7.9 • a. Exciton sublevels energies for a magnetic field parallel to the NW (0 deg). The right panel shows a close-up of the anti-crossing between the states X_1 and X_{II}. **b. - e.** Decomposition of each sublevel eigenstate (X_2, X_1, X_{II} and X_I) into its projection on the pure states ($|\downarrow\Uparrow\rangle$, $|\uparrow\Downarrow\rangle$, $|\uparrow\Uparrow\rangle$, $|\downarrow\Downarrow\rangle)_z$. Changes in the states character are particularly marked at the two anti-crossing (ar. 2 and 6 T), where superpositions of a dark and a bright pure states can be created.

The panels 7.9(b), (c), (d) and (e) represent respectively the projection of the states X_2, X_2, X_{II} and X_I on the four basis states. For example the solid black curve in 7.9(b) is given by $\| \langle X_2 \mid \downarrow\Uparrow \rangle \|^2$. For both panels (b) and (c), it can be readily seen that the each states correspond first to exchange interaction-mixed dipole-allowed states. For an increasing magnetic field, X_1 and X_2 tend toward the two dipole-allowed pure states first. However, the avoided crossing between X_1 and X_{II} leads to an rapid exchange of character. Witek *et al.* (see ref. 210) proposed to use this phenomenon to create a superposition of a bright and dark state, in which case the electron (in their case the hole) could be factored out (physically removed) without destroying the electron state superposition. This is less realistic here because both X_1 and X_{II} contain a non-negligible $|\downarrow\Uparrow\rangle$ character. This is due to a combination of the important anisotropic exchange splitting value and the low magnetic field for which the anti-crossing takes place. Instead, a similar idea could be applied at higher magnetic field, between the states X_1 and X_2. Indeed, for a field around 6.5 T, X_1 and X_2 are described by a 50:50 superposition of the states $|\downarrow\Uparrow\rangle$ and $|\uparrow\Uparrow\rangle$, while X_{II} and X_I are purely composed of respectively $|\uparrow\Downarrow\rangle$ and $|\downarrow\Downarrow\rangle$. The superposition would also be much more resistant to noise in the magnetic field due to the smoother evolution of the states characters in function of the field.

As for X_1, for vanishing QD-NW angles its character is mainly constant. The minimal amount of mixing is due to (i) the small (20 degrees) angle between the shell-QD strong confinement axis and the field and (ii) the moderate value of the hole in-plane g-factor mediating the mixing.

The situation is very different in the case shown in figure 7.10. In this case, the QD-magnetic field configuration is actually close to the Voigt configuration (the magnetic field is in-plane with respect to the QD strong confinement axis). The states energy spectrum in 7.10(a) shows nevertheless a peculiar characteristic, as the X_1 and X_2 states slowly converge and ultimately anti-cross for a field close to 5.5 T (see the close-up on the right). As it was previously hinted, this can be seen as the signature of (i) $sign(g_e) = -sign(g_h)$, the difference in sign of the electron and hole g-factors, for all the angle and (ii) $|g_{hz}| > |g_{ez}| \approx |g_{e\perp}| > |g_{h\perp}|$. As it can be seen in figure 7.10(b) and (c), the anti-crossing correspond to a narrow window in magnetic field strength for which the two states X_2 and X_1 respectively gain strong $|\uparrow\Downarrow\rangle$ and $|\downarrow\Uparrow\rangle$ pure state character. Panels (d) and (e) also show that the states X_{II} and X_I progressively gain a dipole-allowed character as the magnetic field increases.

This evolution of the states character is also depicted in figure 7.11 as a function of the field angle for the critical field of 5.5 T. Panel (a) shows the energy of the states, and the anti-crossing seen in 7.10(a) is visible at 70 degrees. The panels (b), (c), (d) and (e) pictures the evolution of the character of each states in function of the angle, and the exchange of character at the anti-crossing between X_2 and X_1 can be seen to be extremely sensitive on the angle as well. Finally, the panel (f) in figure 7.11 represents a contour plot of the projection of X_1 on the pure state $|\uparrow\Downarrow\rangle$, with dark

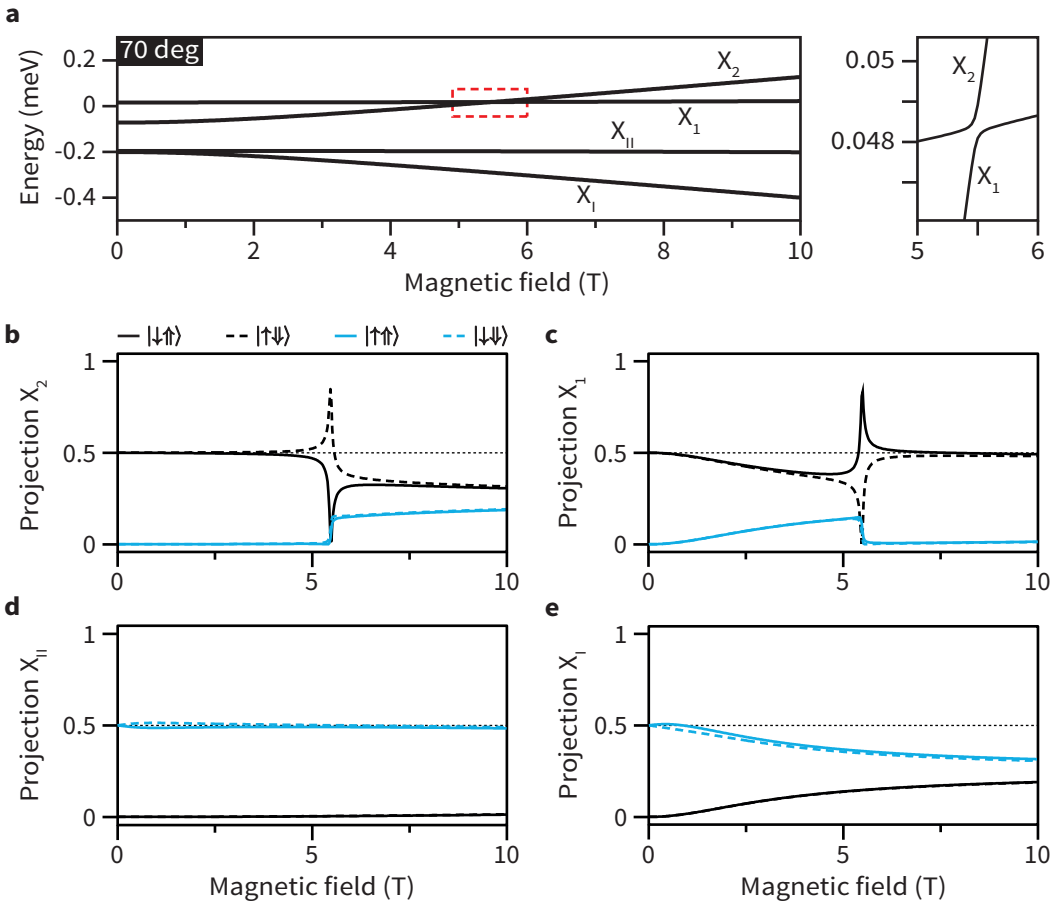

Figure 7.10 • a. Exciton sublevels energies for a magnetic field in plane with the shell-QD (*i.e.* an NW axis-field angle of ar. 70 degrees). This correspond to the particular case of Voigt configuration. Right panel: close-up of the sharp anti-crossing between the states X_2 and X_1, with a particularly narrow splitting ($< 0.5\ \mu$eV). **b. - e.** As in figure 7.9, each panel shows eigenstates projection on the primary basis. Interestingly, the X_2 and X_1 states acquire quasi-pure dipole-allowed character for a field corresponding to their anti-crossing. This behavior is strongly resonant and quickly decays for higher or lower fields.

grey shades corresponding the unitary value. Two regions are outlined with dashed white boundaries. The one at low field strength and low angle corresponds to the case where the field first starts to reestablish the pure state character of X_1, before an avoided crossing with X_{II} swaps the character of these two states. The second, at intermediate fields and high angles, encompass the particular point where X_2 and X_1 rapidly exchange their characters. From this plot, it is clear that this particular point is actually a narrow singularity. For angles in between these two regions and starting at 2 T, X_1 more or less keeps its character, as it does not come close in energy with another state.

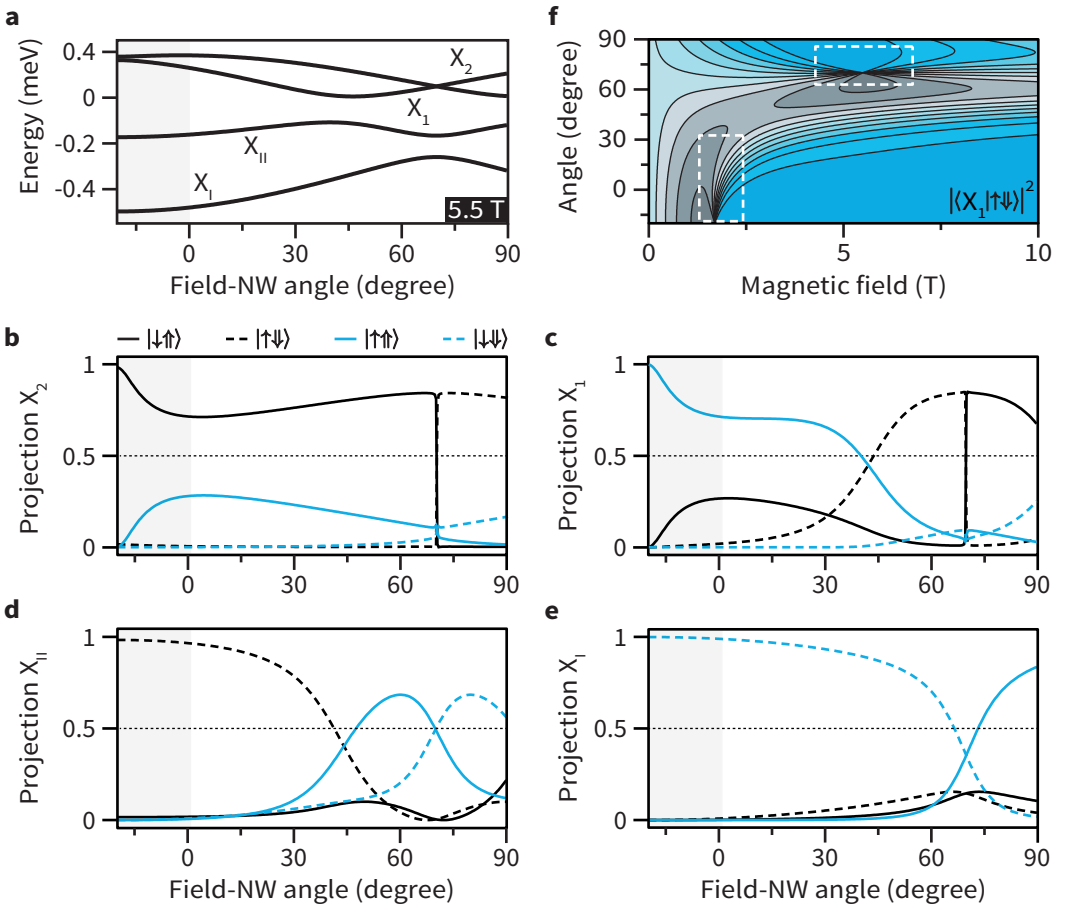

Figure 7.11 • a. Exciton sublevels as a function of the NW axis-field angle for a fixed magnetic field of ar. 5.5 T, corresponding to the field at anti-crossing in figure 7.10. The avoided crossing splitting can be seen for angles close to 70 degrees. The shades areas (negative angles) correspond to angles not measured in the experiments. **b. - e.** Projections of each states on the pure states. For all four states, a clear exchange of character can be seen as the NW axis-field angle passes 70 degrees. However, the modest hole in-plane g-factor combined with the opposite signs of the electron-hole g-factors makes the change particularly steep for the states X_2 and X_1, with predominantly bright characters. **f.** Contour plot of the projection of state X_1 on $|\uparrow\Downarrow\rangle$ as a function of both B and the angle (blue: 0, dark grey: 1). The region corresponding to exchange of character with mainly X_{II} is outlined in dashed white for both low-fields and low-angles. Similarly, the outlined region at medium-fields and high-angles corresponds to an exchange of character with X_2.

Effect on the positive trion

The situation for the positive trion is, at first sight, less intricate (see the figure 7.7). The absence of exchange interaction simplifies the picture and the main particularity arise from a vanishing splitting of the dominantly bright states slightly after 45 degrees and at 90 degrees. As it will be discussed after, at these angles no avoided crossing is taking place: despite a degeneracy of the emitted photons, the actual excited and

ground electronic states are not crossing.

It is tempting to describe the trion emission (the case of negatively of positively charged trions is basically the same) as an exciton, leaving out the exchange terms. This approach however relies on incorrect assumptions as the pure state basis does not correspond to anything for three-particle states. Similarly, if the ground state is common ($|0\rangle$) for all the optical transitions involving the X sublevels, this is not the case for the positive trions, for which the extra hole forms the ground states.

The problem must then be divided in two parts: one for the actual trion, for which the orthogonal basis is $|\uparrow\Downarrow\Uparrow\rangle$; $|\downarrow\Uparrow\Downarrow\rangle$ and one for the ground state with basis $|\Uparrow\rangle$; $|\Downarrow\rangle$. In this case the projection for the spins is along the shell-QD strong confinement axis. The magnetic field will split and hybridized the two states of the trion and the ground states. For the trion, this splitting is directly proportional to the electron g-factor, has the two anti-parallel hole spins cancel each other. For the ground states, the g-factor of the remaining hole is the sole determinant of their splitting.

Based on our measurements (in figure 7.7), the energy of the two excited and ground states can be calculated and is shown for a magnetic field of 10 T in figure 7.12(a) for angles between -20 to 90 degrees. the negative part (shaded) corresponds to angles that where not measured. The energy levels are indicated with blue (solid and dashed) lines. Because the electron g-factor is mainly isotropic, the splitting of the trion states (indicated as E^+ and E^-) is constant and does not depend on the angle for a given value of the field strength. On the opposite, the ground states (indicated as G^+ and G^-) energy is strongly influenced by the angle between the field and the NW axis. As expected, the splitting is maximal for an angle of -20 degrees (not measured, corresponding to a magnetic field parallel to the shell-QD strong confinement axis), and minimal for an angle of 70 degrees corresponding to a field in the plane of the QD.

Similarly to the X case, when the magnetic field is at a finite angle with respect to the shell-QD strong confinement axis, the pure states for both excited and ground states are not eigenstates of the system anymore. Instead, the eigenstates E^+, E^-, G^+ and G^- are linear combination of these pure states forming the basis. This has consequences on the number of optical transitions observed, and on their intensities. In a pure Faraday geometry, only two transitions (counter circularly polarized) are expected. This is illustrated in figure 7.12(b). For magnetic field not aligned with the QD axis, the hybridization of the states leads to the activation of "diagonal" optical transitions, as shown in figure 7.12(c). For panel (c), the situation corresponds to the Voigt geometry and, in this case, the states (*e.g.* trion states) are composed equivalently of $|\uparrow\Downarrow\Uparrow\rangle$ and $|\downarrow\Uparrow\Downarrow\rangle$. This yields that all optical transitions are active and should show the same intensity.

The degree of mixing between the trion (respectively ground) states is variable as a function of the field angle (but invariant on the field strength). This is also represented in the figure 7.12(a), where the projection value of the excited states (ground states) onto

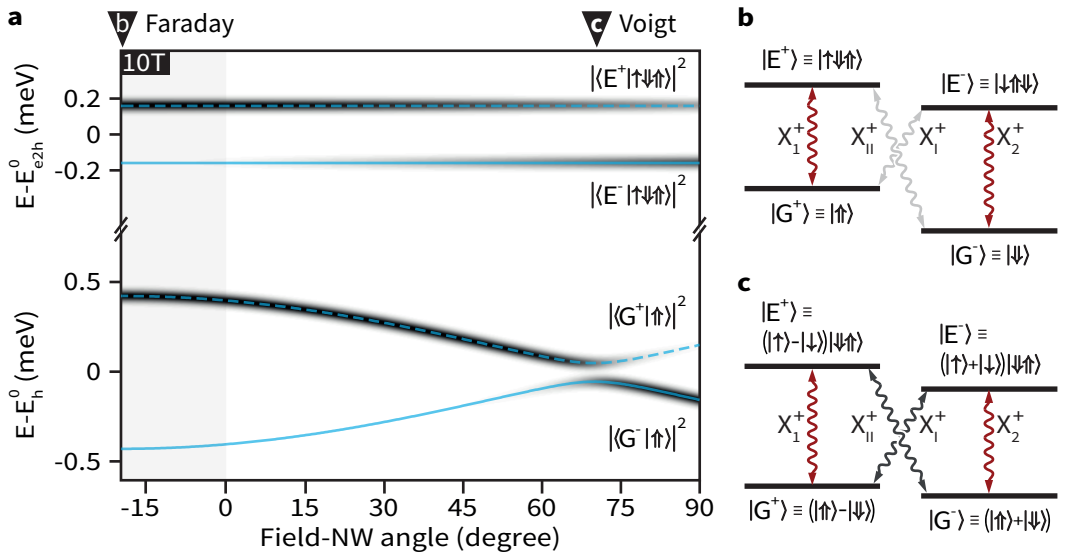

Figure 7.12 • a. Energies of the relevant levels for the X^+ trion (blue lines). The calculation relies on measured parameters. The states projections on $|\uparrow\Downarrow\Uparrow\rangle$ ($|\Uparrow\rangle$) for excited (ground) states are represented by the colour map. As the field is tilted, the pure states acquire mixed characters. For NW axis-field angles around 50 and 70 degrees, the energies of the two vertical transitions (red arrows in (b) and (c)) coincide, without any of the actual trion or hole states being degenerate. **b.** For -20 degrees tilt between the field and NW (not measured) the field would be close to be colinear with the shell-QD strong confinement axis (Faraday configuration). The energy states correspond to the pure states of the system, and the diagonal transitions are fully dipole-forbidden. **c.** For finite angles, state-mixing allows diagonal transitions. Particularly, at 70 degrees tilt between the field and NW, the energy states are admixed with equal contribution from each states forming the bases and thus are all optically active, with equal intensities. The energy states are written without the $\frac{1}{\sqrt{2}}$ renormalization factor for sake of simplicity.

$|\uparrow\Downarrow\Uparrow\rangle$ ($|\Uparrow\rangle$) is encoded in the black contrast. Because of the g_e isotropy, the projection $|\langle E^+|\uparrow\Downarrow\Uparrow\rangle|^2$ smoothly varies from 1 (-20 degrees) to 0.5 (70 degrees). Differently, because $g_{h_\perp} < g_{h_z}$, the ground states maintain a strong pure state character for a wide range of angles. A significant hybridization only takes place for angles above 60 degrees.

From this diagrams, we can further infer that between the measurements at 45 and 90 degrees, the two "bright" states, which seems to cross (see figure 7.7), indeed do so. No anti-crossing is expected because only the photon energy, and not the electronic states themselves, have the same energy.

Another noticeable specificity of our system, linked to the signs and values of the g-factors, is that the two pairs of trions and ground states connected by vertical transitions are arranged in a clear "type-II", staggered fashion. This is seen in the spectrum, as the diagonal transition emit photon with the highest and lowest energy. This is particularly different that most of the (SK, InAs based) QDs, for which the arrangement of the level is of "type-I", with the vertical transitions having the respectively higher and lower

transition energies.

7.4 Discussion

This chapter showed how applying a magnetic field allowed to unambiguously differentiate between neutral and charged excitons. For the shell-QD investigated, the analysis of their diamagnetic coefficient reveals that the wavefunctions are tightly confined in space, justifying the assumption of strong confinement regime.[211] It can be noted as well that the diamagnetic coefficients linked with the emission from charged species were always smaller than the neutral one. This emphasize the role of the extra carrier as a "binder". In particular, an extra hole would strongly act on the wavefunction extension of a lone electron.

For all the QDs emission investigated so far, the electron and hole g-factors were of opposite signs. This translates into larger Zeeman splitting for dark transitions compared to the bright ones, and is verified for both neutral and charged species. Opposite g-factors in GaAs QWs are reported either for wide wells, above 10nm, or narrow ones, below 5 nm.[212] The main difference between the two cases is the sign of the electron g-factor. In our experiments, it was impossible to measure signs directly (analyzing the polarization), but a brief look at the $|g_{hz}|$ value (above 1) and a comparison with literature on QWs (see ref. 212) indicates that in the case of tight confinement and high absolute value for g_{hz}, the electron g-factor is positive while the hole's is negative, and both increase in absolute value with the confinement.

Further, the data agree with the model of an isotropic electron g-factor, while the hole g-factor is found to be highly anisotropic, the in-plane value being 4 to 8 times smaller than the out-of-plane. Despite of the strong reduction of $g_{h\perp}$ compared to g_{hz}, its value is still relatively high compared to in-plane hole g-factor measured in either SK InAs QDs or monolayer fluctuations GaAs QDs. The differences can be attributed to the stronger lateral confinement, in particular when compared to GaAs monolayer fluctuation QDs.

The differences between the values found for the neutral and positively charged species can also be clearly understood as a slight change in confinement:

- The electron g-factor is 10% larger for X^+: the second hole provide an enhanced confinement compared to the single electron-hole pair case.

- The hole g-factor is smaller for X^+: the lack of electron in the ground state allows the resident hole to spread slightly more than in the X case. This is particularly marked in the case of the in-plane g-factor.

Finally, the tilt angle between the shell-QDs strong confinement axis and the NWs axis as it was measured in this case is not expected to be representative of all shell-QDs. First because the QDs shape is a result of diffusion mechanism and might vary

from dot to dot, but also because the potential landscape is influenced by factors such as surface-induced electric fields, which vary depending on the exact location of the shell-QD in the shell.

7.5 Conclusion and outlooks

The particular values of the electron and hole g-factors makes shell GaAs QDs acutely different compared to other III-Vs QDs or monolayer fluctuation GaAs QDs. The type-II spin-sublevel arrangement of the X^+ can be particularly relevant for the preparation of so-called Λ-schemes, as spin-flip processes between the ground states can be efficiently prevented by a large energy offset. At the same time, an interesting scenario can arise when the magnetic field angle is tuned in such a way that the two vertical transitions are degenerate in energy. In this configuration, a single (non-polarized) resonant laser would at the same time act as a pump and re-pump beam between the two ground states, much like in a double CPT experiment.

As for the exciton: the change in the hole g-factor amplitude leads to a decreased splitting between states X_2 and X_1 for angles above 50 degrees and appropriate fields. Ultimately, it was shown in figure 7.10 that the anti-crossing energy between these two states can be strongly reduced. The value extracted from the right panel of 7.10(a) shows that the energy splitting of the states can be brought down to the same magnitude of the expected lifetime-broadened linewidth. This can be used to erase the spurious which-path information due to exchange splitting in a XX-X polarization entanglement experiment.

In the same spirit, it can be seen in panel (f) of figure 7.11 that the character of (in this case) the X_1 sublevel can be extremely sensitive to both the field orientation and its magnitude. The character of the state could be probed via its polarization and its sensitivity used to detect changes in field amplitude or orientation.

Publications • The results presented in this chapter are based on the following peer-reviewed publications:

> "Exciton footprint of self-assembled AlGaAs quantum dots in core-shell nanowires", Y. Fontana, P. Corfdir, B. Van Hattem, E. Russo-Averchi, M. Heiss, S. Sonderegger, C. Magen, J. Arbiol, R.T. Phillips and A. Fontcuberta i Morral, *Phys. Rev. B*, **90**, 075307, 2014
>
> "Tuning the g-factor of neutral and charged excitons confined to self-assembled (Al,Ga)As shell quantum dots", P. Corfdir, Y. Fontana, B. Van Hattem, E. Russo-Averchi, M. Heiss, A. Fontcuberta i Morral and R.T. Phillips, *Appl. Phys Lett.*, **105**, 223111, 2014

Contributions • P. Corfdir and YF acquired together the data in figures 6.2 and 6.8, with the help of B. Van Hattem for the set-up and using the infrastructures of R. T. Phillips. PC and YF treated the data for the fixed parallel magnetic field, an alternative description for the rotation experiment is given in ref. 209. YF, Anna Fontcuberta i Morral and each third-party collaborators commented on the results of the measurements.

Acknowledgements • P. Corfdir, B. Van Hattem and R.T. Phillips are greatly acknowledged for providing time and expertise with the 10T rotation setup as well as for the discussions. P. Plochocka and R. J. Warburton are warmly thanked for the insightful discussions.

Shell quantum dots: Nanolab-in-a-wire to probe carrier dynamics

8

The last chapter of this thesis investigates the potential of shell-QDs acting as localized nanoscopic probes able to yield informations on their surrounding. Epitaxial QDs have already been used successfully as *in-situ* sensors, in particular for internal electric and magnetic (micro) fields.[213–217] The measurement techniques rely almost always on at least one of the two major characteristics of quantum emitters, *i.e.* the very specific photon statistics, and particularly the ability to emit single photons and/or the well-defined and isolated energy levels. In the following pages, the counting statistics (the second-order auto- and cross-correlation signals) will be leveraged in order to shed light on the processes leading to the simultaneous appearance of the X, $X^{+/-}$ and XX optical transitions. The question is valid for shell-QDs, but also for other type of strongly confined GaAs quantum dots, such as DE-QDs or locally etched QDs. In particular, the explanation of the prominence of the X^{+} emission is discussed, as its origin is not yet clearly established. The measurements are performed using non-resonant excitation. As a consequence, the QD, but also and at the first place its environment, are interrogated.

8.1 Experimental Details

The measurements presented in this chapter were realized on GaAs/$Al_{0.33}Ga_{0.67}As$ core-shell NWs. The NWs had a shell thickness of nominally 50 nm. The samples were deposited mechanically on a silicon substrate, and cooled in a close-loop cold-finger cryostat down to a temperature of 3.85K. The NWs were excited using a power-stabilized HeNe laser. The spectra were acquired on a LN2-cooled Si-CCD camera after being dispersed by the 1200 l/mm grating of a 500 mm spectrometer.

The photon counting experiments were realized using the arrangement described in

section 3.2.2. The detection was done with a pair of SPADs with a temporal resolution in the order of 40 ps.

The auto- and cross-correlation curves shown below are systematically fitted using the time response of the diode to deconvolve the signal, and the plotted fits are the deconvoluted fits.

8.2 Slow timescale statistics and autocorrelations

The question of the observation of the X^+ transition and in particular the reason of its dominant character have been generally eluded in the literature related to GaAs QDs. The reason commonly advanced for the presence of the X^+ is the residual "background" doping, usually by carbon acting as an acceptor. However, the activation energy of carbon in AlGaAs is much higher than the thermal energy at which most of the PL experiments are done.[218] An acceptor-QD charge transfer could still happen if the impurity is located close to a QD, but the probability that almost all the QDs are coupled to an acceptor at tunneling distance is rather small if the background doping is in the order of $10^{15/16}$ cm^{-3}. The doping could also be the result of a contamination by other impurities, including Si, a common dopant with a smaller ionization energy. In any of these cases, the expected behavior would be that in the absence of optically generated carriers, the QDs are loaded with an extra hole. Upon non-resonant optical excitation, "hot" electrons and holes are created, cool down and, if the lattice temperature and carrier density are moderate, bind to form excitons. If the excitons are taken to represent the major population of excited carriers, the QD is expected to spend a relatively long time with a resident hole before a lone electron is also captured and restore the charge neutrality in the QD *via* the emission of a X or XX photon.

In figure 8.1, the time arrival of photons from X and X^+ transitions are recorded in parallel during 30 s. The excitation power was adjusted in order to balance the two signals. The events are summed in time-bins of 2 ms to produce the well-known "telegraph" plots. The panel (a) focuses on the binned counts for the X, while (b) represents the X^+. Directly from the time traces, no differences or complementary behavior can be seen. Complementary signals would indicate the passage from charged to neutral and back to charged. On the right side of the graphs, the distribution of the signals are plotted in the form of histograms in order to reveal potential on/off states. At these timescale, the results clearly indicate that the emission intensities (the photon arrival rate) do not follow a telegraph distribution, but are simply gaussian-distributed. A last check is made in figure 8.1(c) in order to reveal a potential distribution of two complementary states (X on / X^+ off and X off / X^+ on). Indeed if these two states are broad enough , they might also produce a gaussian distribution with two "hidden " maxima. The normalized ratio $\frac{N^i_{X^+} - N^i_X}{N^i_{X^+} + N^i_X}$,

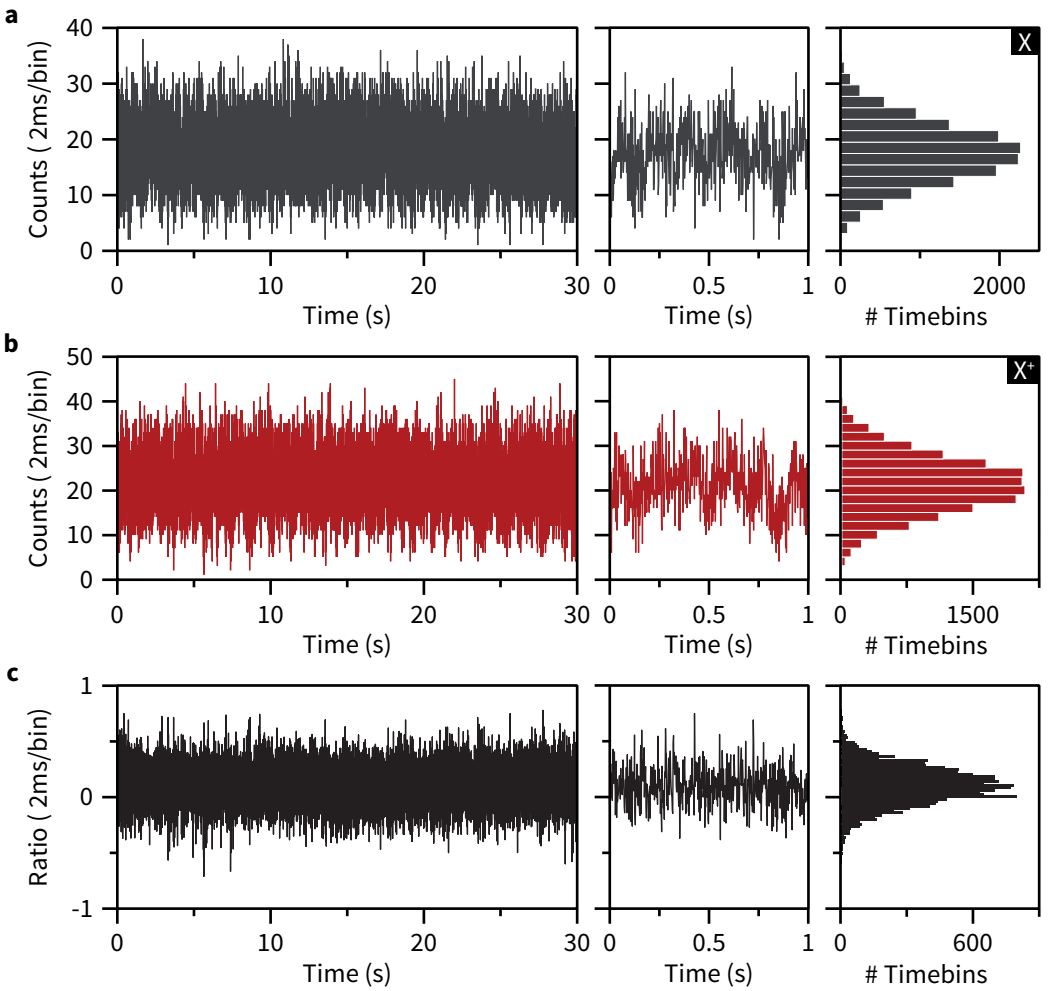

Figure 8.1 • **a.** Telegraph plot of the X emission (2ms timebins), on the full 30s timescale (left), and between 0 and 1 second (middle). The right panel shows the histogram of the number of counts per timebin. **b.** Same as (a), for the X^+ emission. The two signals were acquired in parallel. **c.** Normalized ratio of the X/X^+ counts per bin. The increased number of bins in the right histogram is possible thanks to the passage from integers to rational numbers.

where N represents the number of counts per time-bin of 2 ms and i is the bin number, is plotted. The mean of the distribution is pushed a bit above zero, as the emission from the X^+ is slightly dominant. Compared to the original time-traces, no differences can be spotted. The histogram of the telegraph plot can be constructed again, with the benefits of a higher density of bins since the signal consists now of rational numbers instead of integers. However, the distribution still retains the quasi-perfect gaussian shape.

From the results in figure 8.1, it is obvious that if any passage from a QD with a resident hole to a charge neutral QD exists, the timescales must be smaller than the

millisecond. Considering the fast radiative lifetimes of the QDs, faster timescale is not surprising. At saturation, a residence time for a hole of around 1 μs would allow the X^+ to cycle in average 2000 times before being neutralized and passing to the X emission cycle. These passages could happen several time during a ms, thus erasing any correlation at this timescale. If the loading/unloading of an extra hole is the result of a tunneling process between a QD and an adjacent impurity, the tunneling rate would also be representative of the time difference between loading and/or unloading events and should be relatively high (considering the peak intensities).

The examination of auto-correlation signals should allow to validate the idea of a medium to long term extra resident hole in the QDs, eventually neutralized by a free electron (rare event). The second order auto-correlation analysis is first presented for the X transition, at two different powers, below and above the X saturation threshold.

The results are visible in figure 8.2. The panel (a) show the two spectra, one taken for an excitation intensity corresponding to roughly half the saturation intensity of the X transition, the other for an excitation intensity 20% above the saturation of the same transition. The panel (b) show the power at which the spectra and auto-correlation histograms were taken on the power/intensity curve of the X (cyan dots).

The figure 8.2(c) and (d) shows the CW $g^2_X(\tau)$ histograms for the two different excitation powers. Aside from the increased contribution of the uncorrelated background at higher power, a striking observation is the clear decrease in dip width. The meaning of this decrease can be understood as follow: The QD X emission cycle is not perfectly represented by a two level system. If the capture of free carriers is considered as a rare event, the XX/X/0 (0 standing for an empty dot) levels form a cascaded three-level system. At low excitation rate, the width of the dip is dominated by the capture of excitons. At intermediate excitation rate, the width relates to the intrinsic radiative lifetime of the X state. However at higher excitation rate, *i.e.* when the population of the XX state becomes significant, the width of the dip narrows further. This narrowing goes beyond the limit of the X intrinsic radiative lifetime because the capture of excitons by the QD leads to the (re)pumping in the XX state. For these excitation rates above the saturation threshold, the time during which the X state can decay to the ground state 0 is shortened. As a consequence, the numbers of $X \leftrightarrow 0$ cycles are strongly limited in time and likely to happen in successive short bursts. This usually leads to the observation of bunching peaks or wings right before and after the antibunching dip. The absence of wings in the case presented can be explained by the relatively small value of the excitation rate with respect to the saturation power (in a first approach).

As for now, the picture is then consistent with a QD loaded mostly by excitons and spending long (10s of ns) periods in a neutral state after the neutralization of the resident hole.

The attention is now brought on a second set of auto-correlation measurements, again for different excitation powers but this time focused on the X^+ signal. The spectra

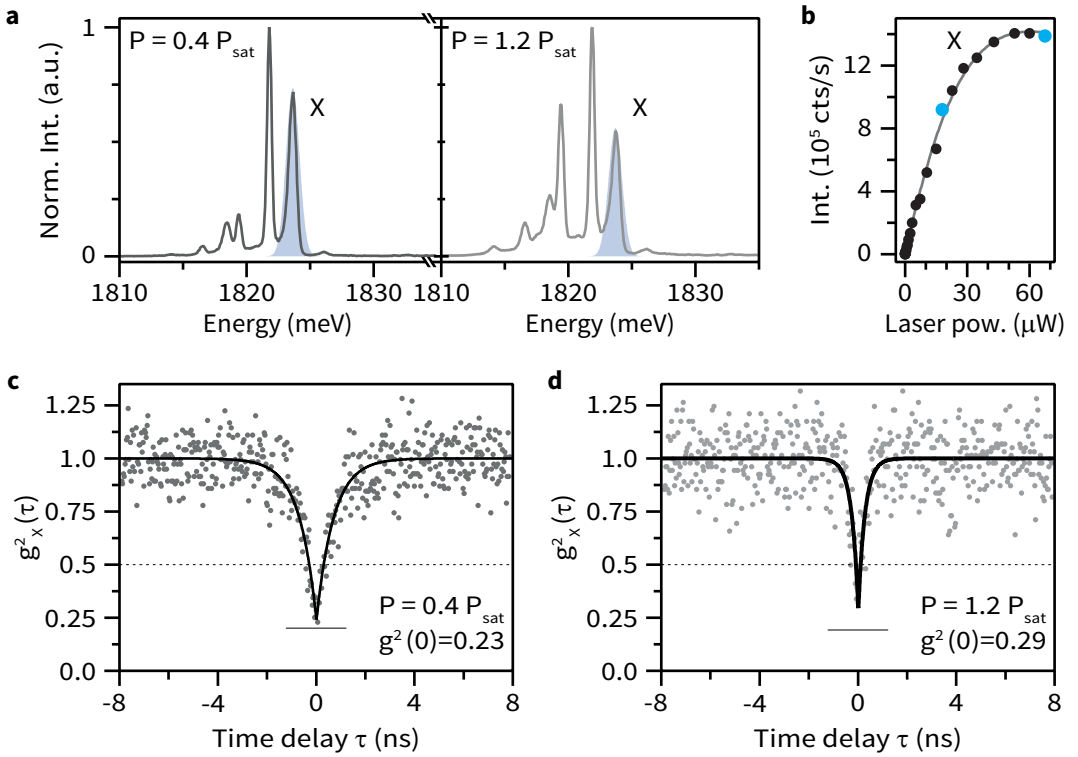

Figure 8.2 • a. Normalized spectra of a shell-QD for two different laser powers: (left) around 20 μW, corresponding to 0.4 P_{sat}, the X saturation power, (right) around 70 μW, corresponding to 1.2 P_{sat}. The X peak is labeled and the shaded area represents the signal sent to the HBT setup. **b.** Total intensity in counts per second of the X peak. The cyan dots show the powers at which the measurements in (c-d) were done. **c.**and **d.** CW second-order autocorrelation on the X peak pumped at 0.4 P_{sat} and 1.2 P_{sat} respectively. The black lines are exponential fits to the data. The fitted values of $g^2(0)$ are visible on the graphs. The dashed grey lines indicate the classical threshold. The solid levels show the estimated contribution of the background PL to the $g^2(0)$ signal.

corresponding to the different powers are shown in figure 8.3(a)-(c). Clearly, the X^+ transition is dominant at all power as it can be seen in the spectra. In the picture of a hole residing in a QD fed by excitons, this would translates in long cycling time between the X^+ and 1-hole states, eventually interrupted by the capture of a lone electron. The three auto-correlation signals for the different powers are shown in figure 8.3(d)-(f).

Interestingly, the X^+ auto-correlation signal presents the very same characteristic as the X auto-correlations. Upon an increase of excitation power, the width of the antibunching dip decreases. Yet the microscopic situation is now quite different. If the capture of free-carriers is considered a rare event and for a QD presenting only s-shell bound states (the p-shell emission was never observed for shell-QDs emitting at this energy, but p-shell levels for the holes are very likely), the X^+ transition should be well described by a 2-level system. Thus for intermediate and high excitation rates,

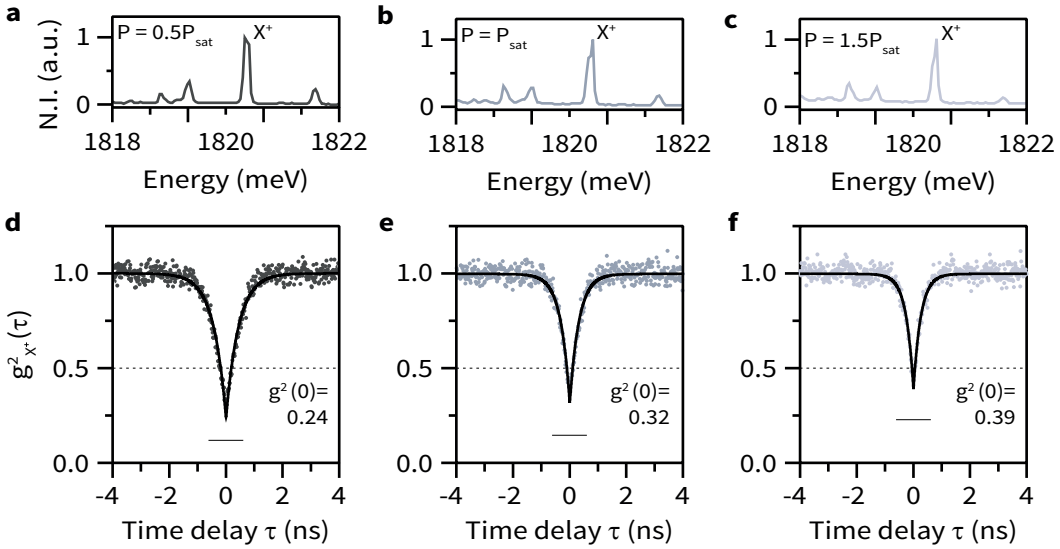

Figure 8.3 • a. - c. Normalized spectra of the shell-QD emission at different excitation levels (P_{sat} is the saturation of the X transition). The X^+ peak is labeled, the X peak is its direct blue-shifted neighbor. **d.** -(f) CW Second-order auto-correlation histograms of the X^+ corresponding to the spectra on the upper row. The black lines are exponential fits to the data. The fitted values of $g^2(0)$ are visible on the graphs. The dashed grey lines indicate the classical threshold. The solid levels show the estimated contribution of the background PL to the $g^2(0)$ signal.

the dip width should saturate and get locked to the value corresponding to the intrinsic lifetime of the X^+ state. This is obviously not seen in the correlation histograms of figure 8.3, and hints for a different mechanism to explain the dominant character of the X^+ emission.

8.3 Random population model

In order to gain at least qualitative knowledge on the charge dynamics in and around the QDs, a population model can be used. The model is limited to QDs with only one shell (s-shell), represented as nine microstates, each with a population of n-holes and m-electrons (n,m={0, 1, 2}). The so-called random population model (RPM) has first been used to model ensemble of QDs, and later to describe the temporal dynamics of single QDs, under various optical excitation pattern (CW, pulsed, resonant...)[219–224] The complete model is fully and well described in the work of Gomis-Bresco *et al.* (see ref. 223) and thus will simply be outlined here. The focus will be set on two variations introduced with respect to the original RPM.

The general idea is outlined in figure 8.4. The panel (a) shows the bulk of the model: a quantum dot (s-shell only -circled, lower row-) is connected and fed by external reservoirs (the matrix -upper row-). Upon laser excitation carriers are excited

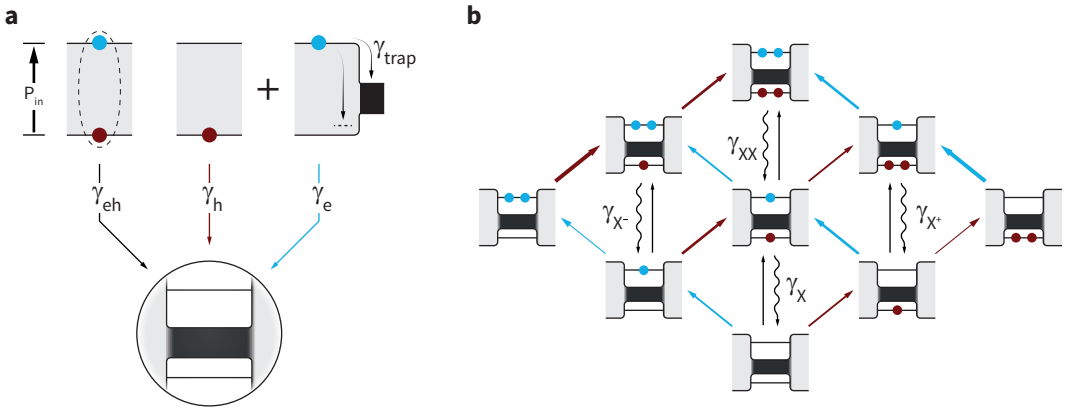

Figure 8.4 • Main components of the RPM toy model: **a.** Representation of the feeding reservoirs and their interaction with the QD. Optical excitation (upward thick arrow) populates the exciton reservoir (left) with a fraction f, and populates with a fraction $(1-f)$ the two free carriers reservoirs (equally). The population balance between the free hole (red dots) and free electrons (cyan dots) can be broken if electrons diffuse to the NW core or get trapped (*e.g.* eA transitions). Each reservoir feed the QD at a different rate (thin black, red and cyan arrows). **b.** The nine microstates and the possible paths for population transfer. Black solid lines: exciton capture, red solid lines: free holes capture, cyan solid lines: free electron captures. Depopulation through photon emission (wavy black arrows) transfers the population to the lower-rung state. The thickness of the lines indicates the increased (decreased) probability of capture due to Coulomb attraction (repulsion).

and populate these reservoirs at a total rate P directly proportional to the power. The reservoirs are of three different kinds: (i) the excitons (electron-hole pairs), (ii) free holes and (iii) free electrons. The pumping of the free electrons and holes reservoir is always equal, as photons create equally an electron and a hole for each absorption event. A certain fraction f of the excited electrons and holes populates the exciton reservoir, while the complementary fraction populates equally the free carriers reservoirs. However, and this marks the first difference with the model in ref. 223, the electron reservoir can be depopulated at a certain rate γ_{trap} either because the electrons diffuses to a lower bandgap material (typically the nearby GaAs core) or because they get trapped and/or recombine without eliminating one of the optically created hole (*e.g.* through the important electron-acceptor eA transition in AlGaAs). The three reservoirs are coupled to the QD via three independent capture rates γ_{eh}, γ_h and γ_e.

The panel (b) of figure 8.4 shows the "internal" dynamics of the model, *i.e.* the organization and population transfer between the microstates. The sum of the population of the microstates is of course equal to one, and the population of a single microstate can take any value between 0 and 1. The internal rules directing the population transfer between the microstates are outlined with arrows. The capture of an exciton allows to transfer population vertically to the upper state (solid straight black arrows). Conversely, emission of a photon transfers the population vertically

downward (wavy black arrows). The capture of a free hole lead to diagonal upward transitions (red arrows) similarly as the capture of a free electron (cyan arrows). The carriers are not allowed to escape the QD (no escape rates). Nominally, the capture rates correspond to γ_{eh}, γ_h and γ_e if the electron/ hole level is fully unoccupied and to $\frac{1}{2}\gamma_{eh}$, $\frac{1}{2}\gamma_h$ and $\frac{1}{2}\gamma_e$ if the electron/hole level is already occupied by a carrier.

In addition, Coulomb repulsion effects for free carriers are added (second modification) and simply modeled as a linear decrease in capture probability if the QD is not charge neutral. Thus the capture rate becomes for the electrons: $\gamma_e \rightarrow (1 + \Delta N_{e,h}\xi)\gamma_e$, where $\Delta N_{e,h}$ is the difference between the number of holes and electrons, and ξ is a factor between 0 and 1 regulating the strength of the effect.

Due to the number of parameters of such a model, it is hard to obtain more than qualitative results, but some reasonable assumptions can be made: (i) the intrinsic recombination rates can be measured in a time-resolved experiments (generally set at 2.32, 4, 2.27 and 2.27 ns^{-1} for the X, XX, X^+ and X^- respectively, according to previous measurements). (ii) Given the fast rise times seen in the time-resolved measurements, the capture rates are likely to be high, at least an order of magnitude higher than the recombination rates.

Once the parameters set, the system can be solved iteratively for a given excitation rate by starting with an empty QD. When the steady-state solution is found, the population of the reservoirs are kept. Subsequently, the model QD can be initialized in an arbitrary state, say the single hole state to simulate a X^+ transition, with the reservoirs set to their steady-state values. The system is then left to evolve again. The time-evolutions of the different radiative states directly yield the probability in function of time to emit a X, XX, X^+ or X^- photon, *i.e.* the $g^2(\tau)$ signal.

The RPM model is first used to confront the assumptions that the important X^+ contribution to the spectra arise from resident holes and that the QDs mainly capture excitons. The results for two different calculations are shown in figure 8.5.

The panel (a) show the calculated $g^2_{X^+}$ on a long timescale (negative time values) and on a short timescale (positive time values). In this calculation, the microstates were initialized at probability 0 apart for the 1-hole state, set at unity (the X^+ just decayed to the 1-hole state). The QD can only capture excitons (f=1), at a rate γ_{eh}=100 (10 ps). The parameters are summed-up in table 8.1 The different curves represent different excitation rates, from black to light grey 0.25, 1, 1.5 and 2 ns^{-1}. The inset shows the expected intensities of the four excitonic complexes.

Obviously, since no free charges are created, the system cannot escape from the $X^+ \leftrightarrow h$ cycle and the emission of the other complexes is zero. In addition, as discussed previously, the correlation trace is the same or almost for all the excitation rate, and is locked at the radiative lifetime.

The figure 8.5(b) shows the results of a similar calculation, but allowing this time for the creation of free electrons and holes, with a f ratio of 0.8 (80% of excitons, 20% of free electrons and holes). In order to simulate slow electron/hole captures,

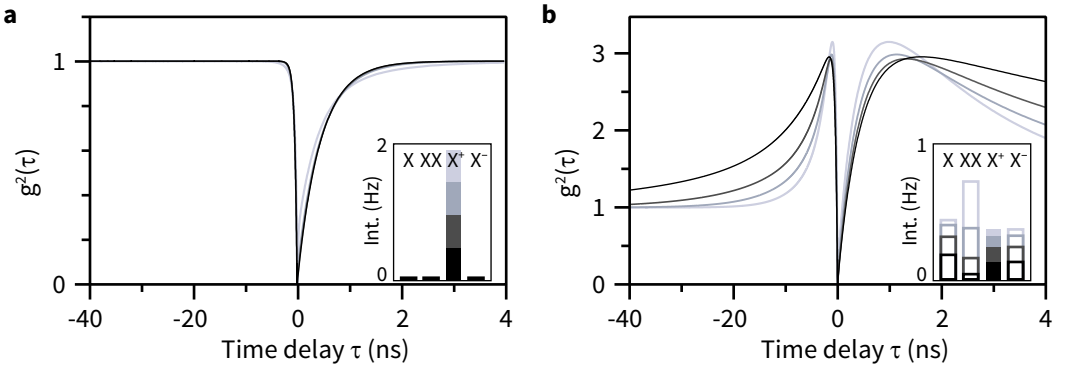

Figure 8.5 • a. Calculated $g^2_{X^+}$ for a QD initialized in a single hole state and perfect excitonic capture. The negative axis shows the evolution on an extended time scale. The four traces correspond to excitation rates of 0.25,1,1.5 and 2 ns^{-1} from black to light grey. The inset indicates the calculated intensities of the different transitions for the different excitation rates, with the X^+ intensity as solid rectangles. **b.** same as (a) but with a free electron-hole generation ratio f=0.8, and $\gamma_{e/h}$=0.1 (10 ns).

the capture rates for both electrons and holes are set to 0.1 ns^{-1} (10 ns). The RPM parameters can be seen in table 8.1. This time, the system is not forced to stay in the $X^+ \leftrightarrow h$ cycle. The QD actually evolves to a mixture of different states, as it can be seen in the intensities inset. Indeed, the intensities of the other transitions are not zero anymore. In particular, the steady-state $X^{+/-}$ intensities are equal for all the power since no imbalance for the capture of carriers was introduced in the calculation, aside from its starting point.

There are two main effects which follow the inclusion of free carriers in the system. The first one is the reduction of the dip width for increasing excitation rates. This corresponds to what is observed in figure 8.5 and is linked with the fact that the X^+ (or the 1-hole) state can now be depopulated by non-radiative population transfer toward a different state. The second is the appearance of important bunching side-wings denoting a strong probability to emit a second (or several) X^+ photon right after an emission event took place. The time window of this reemission probability shrinks for increased excitation rates, but the correlation (the height of the bunching peak) becomes higher. This can be understood intuitively given the calculation parameters: because of the high exciton ratio f and the fast capture rate, the QD will rapidly be repumped into the X^+ state after an emission event. It will then have a limited time to recombine before the capture of an electron transfer the population into the XX state. As the power is increased, the population of the electron reservoir is also leveled-up, so that the probability for the QD to capture a free electron after a short time increases as well, and the bunching wings narrow down.

The second phenomenon is not observed in the auto-correlation measurements in figure 8.5. Further, the wings magnitudes and spans can be seen to increase with

Ref.	f	γ_{eh} [ns^{-1}]	γ_h [ns^{-1}]	γ_e [ns^{-1}]	γ_{trap} [ns^{-1}]	ξ
Figure 8.5(a)	0	100	-	-	-	0
Figure 8.5(b)	0.8	100	0.1	0.1	0	0

Table 8.1 • Parameters used for the RPM calculations shown in figure 8.5. The excitation rates were 0.25, 1, 1.5 and 2 ns^{-1}.

a decreasing hole capture rate and free carrier fraction. In this view, the importance of the X^+ transition intensity cannot be explained by the occupation of the QD by a long-lived hole. This argument adds up with the observation of the X/X^+ relative intensities in function of the power. If a long-lived hole was present in the QD, the X^+ transition would not appear at higher, but at lower excitation power compared to the X. Apart if a phenomenon of photo-depletion is invoked, in which case the X would then be systematically the most intense peak at higher power.[225] Thus, in the case of shell-QDs at least, and most likely for other GaAs QDs, resident holes do not account for the observation of the X^+ peaks. In addition, it seems that slow capture times of free-carrier are also unlikely, and that the QDs are able to rapidly gain both electrons and holes.

8.4 Cross-correlations and dynamics

As seen in the previous sections, the vision of a QDs capturing mainly excitons and only a few electrons and holes at slow pace does not account for the observations in the auto-correlation signals nor for the power dependence spectra. In the following pages, the results of cross-correlations and in particular the X^+-X and XX-X^+ cross-correlations are examined to illustrate the intricate sub-nanosecond dynamics taking place during the non-resonant excitation of shell-QDs.

The results of a complete cross-correlation between the X and the other complexes at the X saturation is shown in figure 8.6. The panels (a) to (c) show the cross-correlations between the different excitonic complexes and the neutral exciton. Panel (d) shows the XX-X^+ cross-correlation. The spectrum of the shell-QD can be seen in panel (e) for the excitation power for which the correlations have been measured. The excitation power corresponds to the saturation power of the X transition. The first observation concerns the strong asymmetries for each of the signals. An asymmetric profile is expected for all the signals, as the negative time delay $\tau < 0$ corresponds to a repumping of the QD to a higher level. In order to disentangle the cross-correlation signals, the interest is first set on the positive-time parts of the cross-correlations.

The XX-X cascade peak decay is well fitted by an inverse exponential with lifetime of 0.2 ns. This value cannot be compared to the intrinsic 0.43 ns lifetime of the X

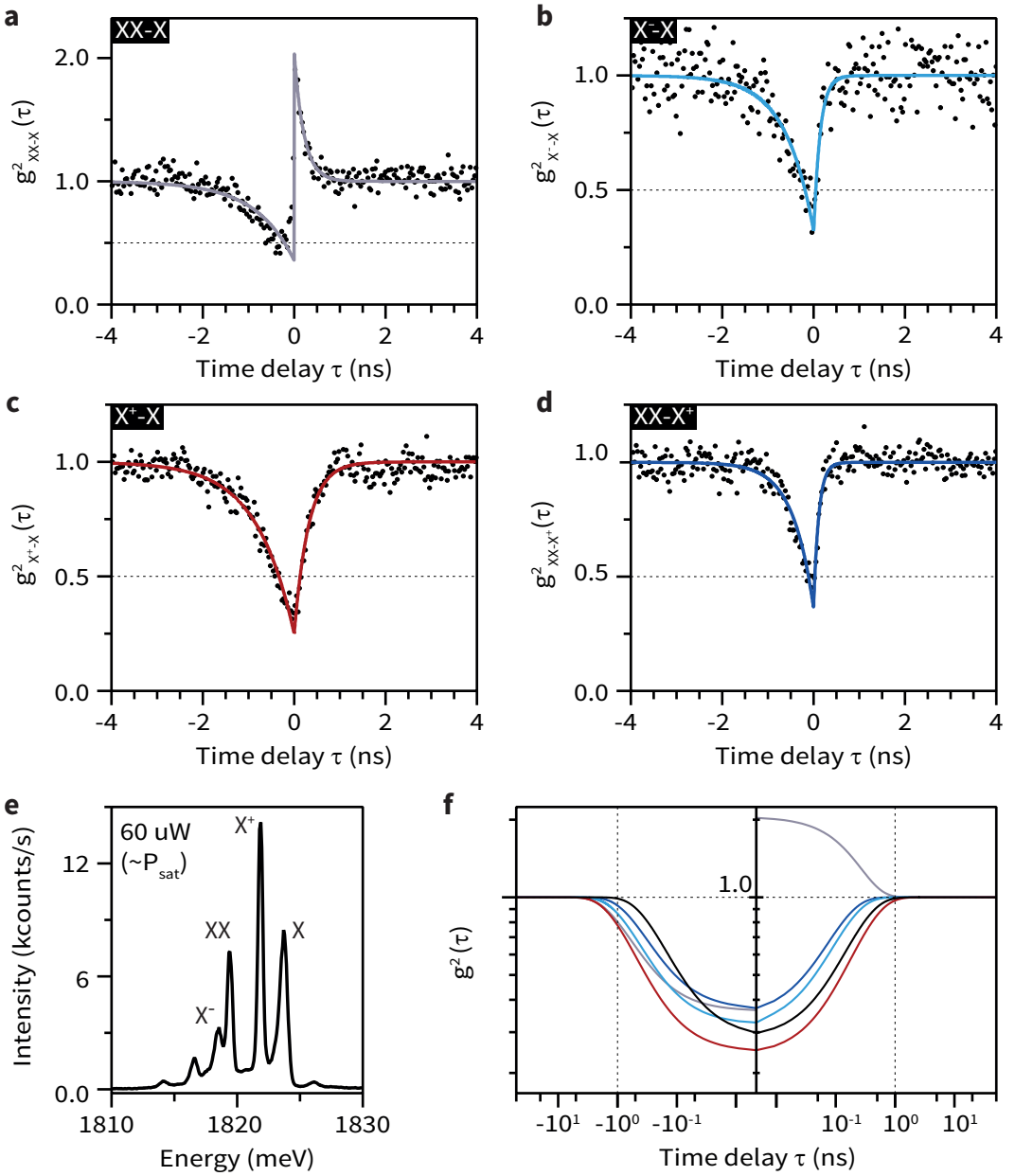

Figure 8.6 • a. XX-X cross-correlation showing the XX-X cascade. **b.** X^{-}-X cross-correlation. **c.** X^{+}-X cross-correlation. **d.** XX-X^{+} cross-correlation. All the histograms are fitted with a deconvoluted function. The fits consist in piece-wise exponential functions with dedicated lifetimes for negative and positive times. **e.** Spectrum of the shell-QD at the excitation power for which the cross-correlation have been measured. **f.** Representation of the fits in (a)-(d) plus the fit to the X-X autocorrelation (solid black line) in a loglog plot.

(measured by pulsed time-resolved PL). Thus, in CW operation close to the X saturation, the effective lifetime of the X state is strongly reduced. This reduction is in

agreement with the auto-correlation measurements and tells about a significant repumping effect to higher levels (XX, X^+ or X^-). Passing directly to the XX-X^+ signal, it can also be seen that the emission of a X^+ photon after a XX decay is extremely quick (0.11 ns). After the XX decay, the QD is in the X states, and needs an additional hole to climb up to the X^+ state. This seems to happen fast, as the probability to monitor a X^+ decay event increases steeply. However, the intrinsic lifetime of the X^+ (0.44 ns) is too slow to explain the rapid increase in the X^+ event probability. Again, the intrinsic lifetime is not dominating the statistic and only the fast x^+ decay events are recorded. If photon emission does not happen fast enough, the X^+ is repumped to a higher level. In the limit of a s-shell QD, the only level higher than the X^+ is the XX state. Thus, the QD should capture rapidly (within 0.11 ns) a free electron.

Back to the X^--X signal, similar mechanisms can be glimpsed at. The time between a X^- decay and a subsequent X decay is found to be fast, around 0.17 ns. This again is explained by the reduced X lifetime due to continuous capture of carriers. Interestingly, when the X^+-X cross-correlation is considered, the dynamics slows down significantly. Indeed, the time measured in figure 8.6(c) between a X^+ and an X decay is 0.31 ns. If it is still quicker than the intrinsic X lifetime, the escape rate from the X state is slower when it is reached from the 1-hole state compared to the 1-electron state.

Likewise, the electron capture from the X^+ to the XX is seen to be fast and the limiting factor for the observation of long XX-X^+ decay chains. The same rate or faster can be expected for the passage $h \rightarrow X$ since the 1-hole and the positive trion possess the same net charge (and thus attracts electrons), while the occupation of the electron level is already $\frac{1}{2}$ for the X^+ (against 0 for the 1-hole state). However the electron capture rate apparently drops significantly after the $h \rightarrow X$ passage, otherwise the X state would depopulate fast and the positive side of the X^+-X cross-correlation signal would be as steep as the one for XX-X^+.

This counterintuitive observation, in particular between the XX-X^+ and X^+-X cross-correlations, is also perceptible in the signals at negative time *i.e.* the X^+-XX and X-X^+ chain of events. After a X decay the QD is necessarily empty. Due to the higher probability to populate empty states than half-full ones, it could be expected that the climbs from the empty state 0 to X^+ followed by an emission from the later state would happen faster than the complete filling of the QD from the 1-hole state. This is clearly not the case, as it can be seen in figure 8.6(c) and (d).

The same tendency can be seen in other QDs, at different degrees. Two additional examples are shown in figure 8.7. The upper panel (a) focuses on the X^+-X signals while the panel (b) is dedicated to the XX-X^+ cross-correlations. The first column (dot1) correspond to the measures already presented in figure 8.6. Systematically, the timescales for the X^+-X processes are longer compared to the XX-X^+ decay chains (both the $\tau > 0$, "forward" and $\tau < 0$ "backward" processes).

The figure 8.7(c)-(d) represent the most direct path between the QD charge

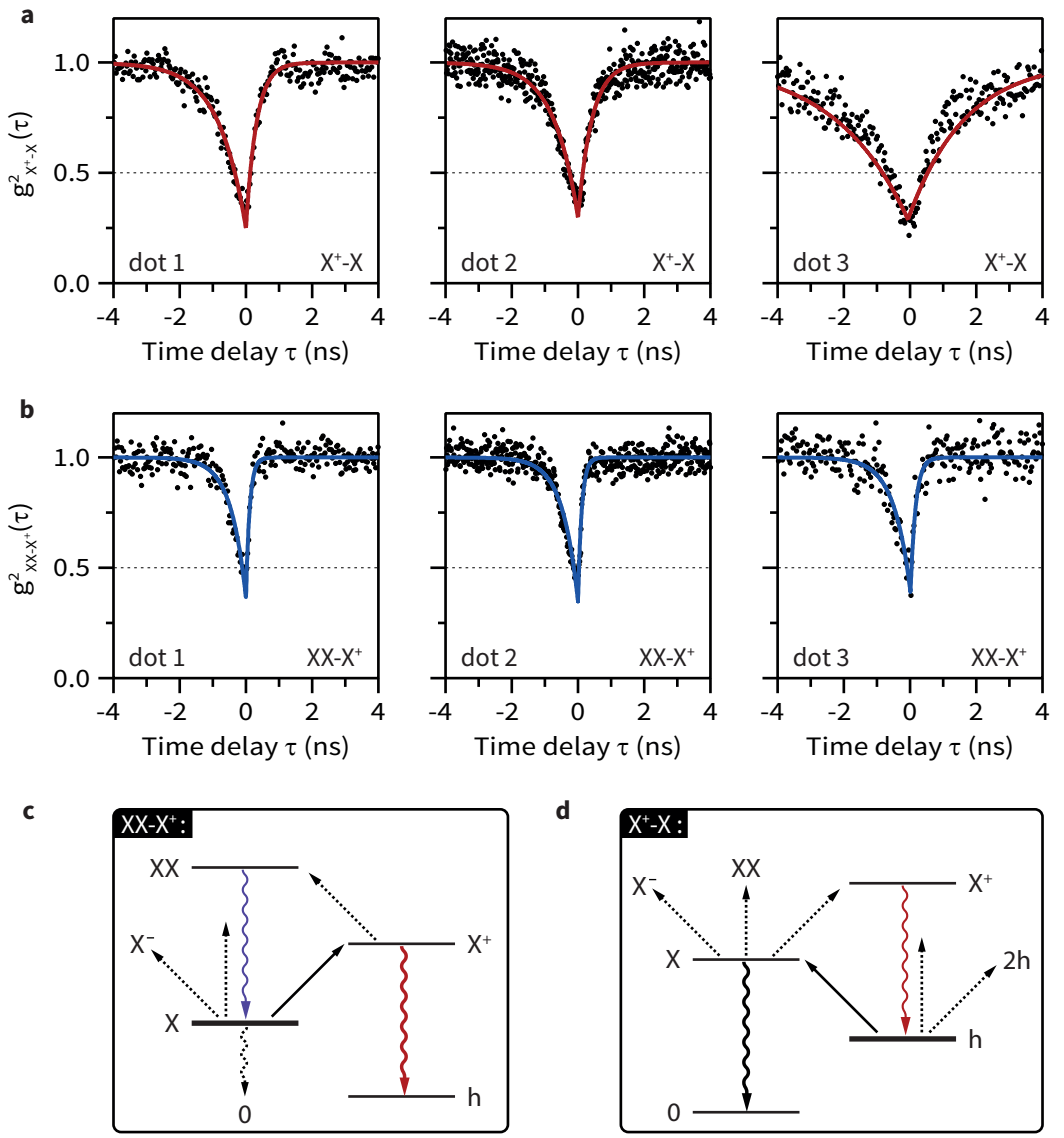

Figure 8.7 • **a.** X^+-X cross-correlation signals for three different QDs. The dot1 signals are the same as shown in figure 8.6. **b.** Same as (a) but for the XX-X^+ signals. **c.**and **d.** schematics of the XX-X^+ and X^+-X chain of events. The wavy arrows are photon emission events starting and stopping the measurements. The thick level indicates the starting point of the forward process and thick black arrows show the step toward the emission of the ``stop'' photon. Dashed arrows indicate the escape capture/recombination events.

configurations for the forward processes. The thin wavy arrows represent the emission of the photon starting a time-difference measurement. The event signals with certainty in which state the QD is (the thick level). The thick black arrows show the intermediate step required for each case: the capture of a free hole ($X \rightarrow X^+$) or

a free electron ($h \rightarrow X$). The dashed arrows show for each step the potential concurrent depopulating paths, either radiative (dashed wavy) or through the capture of a carrier (dashed straight).

This particular dynamics is not easily reproduced without the existence of a significant fraction of free (or split) electrons and holes in the matrix, *i.e.* the free carrier reservoir in the RPM model.

Similarly, a certain degree of imbalance must exist between the holes and electrons capture times. The rapid depletion of the X^+ state toward (most probably) the XX state points at rapid electron captures. Nevertheless, the time-integrated PL signals show that the QDs should spend a considerable amount of time in the X^+ state, so that hole capture events should be frequent as well.

In addition, the rather long time between the emission of X^+ and X photons indicates that the capture of an extra hole in the 1-hole state is a rare event, otherwise, the 1-hole state would quickly be depleted while the 2-holes state's population increases. Yet the $e \rightarrow X$ and $X \rightarrow X^+$ passages also necessitate the capture of a hole and this capture is apparently not a limiting factor in the overall X^-m-X and XX-X^+ dynamics. This observation pushes forward the role of the QD charge in the capture of free carriers. Indeed, positively charged QDs (*e.g.* in the 1-hole state) are likely to attract free electrons while free holes are repelled (and vice-versa for a negatively charged QD). In this picture, the Coulomb attractions/repulsions provide a restoring force toward a neutral QD.

If the consideration of Coulomb-assisted capture of electrons and holes helps understanding certain parts of the QDs dynamics, other aspects are still clarified: if the electron capture time is supposed to be fast and in particular if this argument is used to explain the steep increase of the signal after τ_0 in the X^--X correlation, why a similar effect is not seen in the X^+-X? The X state, reached from the 1-hole state after a first electron capture event, should be also rapidly depleted by the capture of a second electron (thus passing to the X^- state). One reason why this passage could be prevented or at least delayed is if the first electron capture could deplete significantly the number of free electrons around the QD. In this case, the second electron capture process would be delayed until new free electrons are optically generated. In order for this depletion to happen, the influence of the removal of one electron from the reservoir population should be large, meaning that the reservoir population should be in the order of few electrons. The only option left to justify a strong imbalance in the population of the electron and hole reservoirs is to admit sink terms for the electrons since a "doping" generation term for the holes is not compatible with the observations.

These sink terms are actually likely to happen. For a QD in pure bulk AlGaAs, the aforementioned carbon doping create acceptor states, not ionized at cryogenic temperatures, to which the electrons can decay (eA peaks). Furthermore, in the case of shell-QDs (and for other GaAs-based QDs without wetting layer), the growth of

Ref.	P_{in} [ns^{-1}]	f	γ_{eh} [ns^{-1}]	γ_h [ns^{-1}]	γ_e [ns^{-1}]	γ_{trap} [ns^{-1}]	ξ
Sink	2.5	0.1	50	50	100	200	0
Coulomb	1.5	0.1	50	200	50	0	0.8
Sink + C.	4	0.1	50	50	100	800	0.8

Table 8.2 • RPM parameters for the calculations in figure 8.8. The parameters were minimally adjusted in each case to globally represents the emission intensities seen in the spectra of shell-QD.

the QDs starts at a moderate distance from bulk GaAs. The strong chemical potential gradients combined with the 10-fold higher diffusion coefficient of electrons compared to holes would allow the trapping of a significant fraction of the electrons before the induced field sets the equilibrium.

Figure 8.8 represents the results of the RPM model used to calculate the XX-X^+ and X^+-X cross-correlations. The parameters were first adjusted to yield realistic values of the excitonic complexes intensities (shown in inset, normalized to the X intensity) in the case of the calculation including a sink and a Coulomb term. The parameters for the two other calculations were adjusted so that the intensities are again approximatively representative of the spectra. The exact parameters can be seen in table 8.2. The panel (a) shows the results of the calculation with a sink term, but without Coulomb forces. Panel (b) corresponds to the calculation without sink term, but with Coulomb forces. Finally, the calculation in panel (c) include both sink term and Coulomb forces. Only the combination of a sink term, fast intrinsic electron captures and Coulomb attraction/repulsion terms is able to reproduce the slower dynamics of the X^+-X cross-correlation. In addition, the ratio exciton/free carriers f has to be considered low (0.1 for all the calculations) in order to avoid strong "cycling" behavior which produce the important bunching wings at times $\tau > 0$.

Figure 8.8(d) and (e) present flow charts which illustrate respectively the $XX \rightarrow X^+$ and $X^+ \rightarrow X$ event chains. For both, the upper row (Q) shows the net charge of the QD. The second-to-top line sketch the level of the hole (red) and electron (cyan) reservoirs $N_{e/h}$ for each step (not accounting for the CW excitation). The bottom row shows the evolution of the QD population. The sink is represented by the permanently trapped electron at the right of the dot.

In (d) the QD is seen to undergo a radiative decay from the XX level, leaving the QD in the X state. If the QD gains a hole (solid arrow) before the depopulation of the X state by electron/exciton capture or radiative recombination (dashed arrows), it can transit to the X^+ states. From there, a radiative recombination event will "stop" the XX-X^+ event chain. If the recombination is not fast enough, another electron is captured due to the combination of a fast electron capture rate, sufficient population of free electrons and a positive net charge, preventing the slow recombination events to take place.

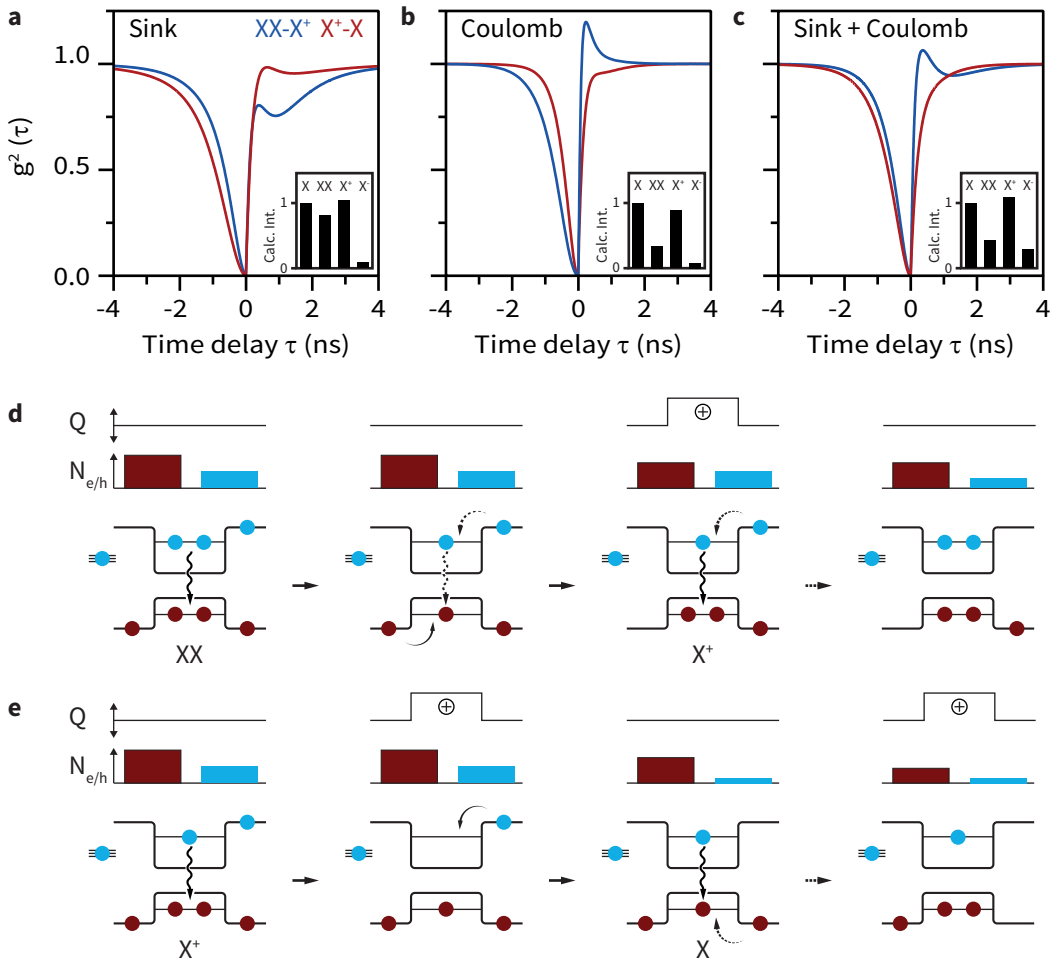

Figure 8.8 • a. Results of the RPM calculations for the XX-X^+ (blue) and X^+-X (red) cross-correlations when a sink term is activated, but the Coulomb term is neglected. **b.** Same as (a) but for a sink term set to zero and a non-null Coulomb term. **c.** Signals if both sink and Coulomb coefficients are set to a finite value. The insets show the calculated intensities of the different optical transitions. The excitation rate and electron/hole capture rates were adjusted for each calculation in order to represent realistic values of the various intensities. The parameters for each calculations can be found in table 8.2. **d.** Schematic of the time evolution for the XX-X^+ event chain considering a sink term and Coulomb forces. The sink is represented by the trapped state on the left of the QD. The top line (Q) shows the net charge of the QD, while the second-to-top ligne shows the population of free electrons (in cyan) and holes (in red) available for capture ($N_{e,h}$). **e.** Same as (d), but for the X^+-X event chain. The slowdown is taking place due to an electron depletion in the third phase.

In (e), the QD in the X^+ state decays to the 1-hole state. The positively charged QD is quickly neutralized by the capture of an electron from the reservoir, and doing so decrease the population of available electrons and transit to the X state. In the X state, the QD can emit an X photon during a time limited by the hole capture time (or until the electron reservoir is sufficiently filled again to allow for an electron capture,

not shown here). The capture time of either a hole or an electron is also lengthened since the QD is globally charge neutral. If no emission occur during this "rest" time, the QD transits to the X^+ state again (or to the X^-).

8.5 Conclusion and outlooks

This chapter showed that the quasi-systematic observation of the X^+ peak and in particular its high intensity is unlikely to be the result of a background doping by carbon atoms. The dynamics of the electron and hole configurations in the QDs were probed with ps-resolved auto- and cross-correlations and were found to evolve rapidly. In particular, diagonal transitions involving the gain and loss of single carriers happen at sub-nanosecond timescale. Based on these observations and with the help of a toy model, it can be concluded that the QDs capture mainly single carriers. In addition, the rates associated with the XX-X^+ and X^+-X cross-correlation histograms indicate that the effective capture rate of free carriers depend on the charge state of the QD at a given time. The intrinsic capture rate of electrons is most probably the highest, but the free electron population in the matrix is depleted by nearby sinks, potentially the GaAs core or carbon atoms acting as acceptors and mediating the electron-acceptor transition.

The low amount of free excitons in the matrix could be related to their trapping at defect states, and their subsequent recombination there, cutting short the possibility of capture by a QD (The bound exciton peak usually dominates the AlGaAs spectrum). The absence of a wetting layer is also likely to play a role in the free-carrier/exciton capture ratio. Its absence makes the binding of electron and holes into exciton less likely to happen, while the capture of carriers by the QD is not mediated by an intermediate confined structure.

The particular dynamics of the shell-QDs combined with their location in the NWs could open alternative routes to control the charge state of quantum emitter. Layered structures with AlAs or AlSb barriers could be selectively excited to enhance either the population of holes or electron, in an all-optical way. Mechanism similar to photo-depletion could then be used to tune the number of charges in the QDs on the fly.

Acknowledgements • Many thanks to Esther Alarcon-Llado, Francesca Amaduzzi and L. Francaviglia for the fruitful discussions.

Summary and concluding remarks

9

This thesis focused on quantum dots (QDs) embedded in the shell of nanowires, with an emphasis on the characterization of those QDs with optical spectroscopy. The first results presented showed the occurrence of strong segregation effects in the AlGaAs shell of GaAs/AlGaAs core/shell nanowires. The main effect is seen in the formation of Al-rich planes separating the {110} facets. In addition, dark-field aberration-corrected high-resolution scanning transmission microscopy and complementary EELS and EDX studies allowed for the location of regions were the *inverse* phenomenon happens. In these regions, the gallium concentration increases at the detriment of aluminum, leading to the formation of nanoscopic Ga-rich islands embedded in the bulk of the AlGaAs shell. In parallel, low-temperature micro-photoluminescence studies revealed the emission of light in the form of narrow, very intense peaks, delivering single-photon stream up to the MHz range. The light is emitted in a spectral region corresponding to the visible (red) and is seemingly linked to point emitters in the nanowire shell. The latter assumption was proved to be correct thanks to the increase in spatial resolution brought by cathodoluminescence and the possibility to directly observe the off-centered localization of the emitters. The link between the Ga-rich regions and the emitters observed in cathodo- and photoluminescence was tightened by large-scale computations with two different methods showing the ability of the Ga-rich islands to capture and bind electron and holes.

The possibility to tune the occurrence, distribution and emission energy of the so-called shell-QDs was demonstrated in various series of growths run at different temperatures and for different shell thicknesses and stacking sequences. In particular, the growth window of optically active shell-QDs has been seen to be considerably extended. This allows wide margins to find the best conditions for which key characteristics such as the emission linewidth and the QDs elongation can be optimized. The possibility to grow active layers of QDs in complex radial heterostructures is particularly appealing.

The confirmation that the shell-QDs are indeed quantum light emitters was brought by single QD spectroscopy and time-correlated photon counting. Due to the ability to single-out the emitting shell-QDs, the observation of excitonic complexes was made. The latter were directly related to a single QD leveraging cross-correlation measurements, validating fully the picture of isolated Ga-rich islands. In particular, the few-particle interactions between the different carriers present in the QDs led to the identification of the neutral-, charged- and bi-excitons. Interestingly, the positively charged exciton was shown to dominate the spectrum for intermediate excitation power. The different binding energies of the excitonic complexes were comparable to the values found for other type of GaAs QDs, but for higher emission energies. This difference led to the conclusion that a certain fraction of aluminum was still present in the QDs, as already seen in transmission electron microscopy and atom-probe tomography measurements. The different deactivation temperatures of the various excitonic complexes provided complementary informations on the single-particle states. The ionization process was seen to affect first the negatively charged exciton due to the proximity of the electron state with the continuum. This proximity leads to a certain extension of the electron wavefunction in the barrier material, while the holes are still tightly confined in the QD.

This effect is also seen in the measurements performed in a magnetic field. The comparison of the positive trion and neutral exciton diamagnetic coefficients clearly showed the binding character of the second hole on the electron wavefunction. The measurement in a magnetic field also brought forward the particular energetic arrangement of the hybridized states due to the opposite signs of the electron and hole g-factors. The difference in signs was attributed to the strong confinement of the carriers, as it has also been seen in extra-narrow quantum wells. Angle-dependent measurements were used to demonstrate the tunability of the exciton composite g-factors, mainly through the modulation of the hole g-factor. This could lead to the generation of interesting superposition of states, in particular when the energies of the two bright transitions are degenerate. Furthermore, angle-resolved magnetic field measurements confirmed that the strong confinement axis of the QDs is not necessarily aligned parallel or perpendicular to the nanowires, as it was suggested by previous measurements on the fine-structure splitting of exciton peaks.

Finally, the observation of peculiar dynamics of shell-QDs and the fast transitions between different charge states hinted for an alternative understanding on the origin and prominence of the positive trion in the time-integrated spectra. The proposition that the QDs are mainly populated through free-carrier trapping, occurring at different rates was made. This hypothesis is supported by the measurements and by comparison with a random population model going beyond the standard three-level rate equations. The model allows to take into account the local depletion of electrons, possibly because of preferential diffusion and trapping in the core of the nanowire. The QDs respond to these changes in their environment and their response is translated to a modification of

the internal dynamics. Thus the shell-QDs could be helpful to probe the local density of carriers, *e.g.* close to transport dedicated structures such as remotely doped 2DEG.

Many aspects of the shell-QDs are still not understood. The exact formation mechanism is shadowed by the difficulty to observe the nanowire morphology and its relationship to QDs nucleation in three dimensions and at at large scale. The exact role of the core morphology and in particular of the stacking defects happening during the nanowire growth is still subject to debates. Regarding their optical properties, the shell-QDs are promising as fast, intense sources of single photons. Yet the linewidth of the optical transitions and the fact that the broadening do not happen at slow timescale is detrimental regarding their properties as quantum emitters. Several routes are possible to counter the broadening, amongst which an increased control over the crystalline integrity. This subject is a main challenge concerning the growth of self-catalyzed NWs in general. The possibility to grow optically active QDs at high temperature is also promising, as it would allow to either directly grow above 480°C or proceed to annealing steps in order to reduce the amount of point defects. Finally, the important fine-structure splitting is also detrimental to many quantum optics experiment. Here again, a better understanding of the growth process could lead to significant progress. Post-growth tuning of the exchange splitting is also possible *e.g.* using strain or an external magnetic/electric field.

Altogether, shell-QDs have already demonstrated highly interesting characteristics. Their location in nanowires and their robustness allowed for the fabrication of size-controlled nanodisks embedded in a polymeric substrate. The delicate control on the size could open the way for the fabrication of highly reconfigurable nano-photonic hybrids using single-photon sources.[226] Shell-QDs were also the first fully bottom-up nanostructures approaching the ultra-strong coupling regime between the motional degree of freedom of a microscopic object (the nanowire) and a quantum emitter.[129] In general, GaAs/AlGaAs QDs are regaining interest at fast pace in the last years, with important successive milestones such as the polarization entanglement of exciton and biexciton photons without temporal or spectral filtering, the optical polarization of nuclear spins at zero magnetic field or the transition from heavy-hole to light-hole exciton, allowing to potentially use light-holes as spin qubits.[93,101,227] In this context, the exploration of new quantum light sources embedded in nanowires is both a stimulating goal and the promise of new discoveries, even in a well-known system such as the GaAs/AlGaAs couple.

Author Contribution

A minute description of the work realized by people other than the author (YF) is included at the end of every relevant chapter after the **Contributions** • marker. The reader can refer to those paragraphs to know the origins of the data. All data which are not described in those paragraphs have been obtained by the author directly. Direct

collaborative work is mentioned.

A brief thank-you paragraph is also added after the **Acknowledgements** • marker, for participations (mainly through discussion) not necessarily crucial with regards to the chapters' results, but which provoked reflections.

In addition to the data acquisition and analysis, the author also entirely built the optical setup around the closed-loop cryostat and modified significantly the setup around the open-loop cryostat. The author has been deeply involved in the analysis of all the data presented, including the one coming from collaborators. He wrote the manuscript and certifies that it is original. All the images are originals, or original adaptations from papers if mentioned. The entire thesis work has been directly supervised by Anna Fontcuberta i Morral.

Bibliography

[1] R. Dingle, W. Wiegmann, and C. H. Henry, "Quantum states of confined carriers in very thin algaas-gaas-algaas heterostructures," *Physical Review Letters*, vol. 33, pp. 827–830, Sep 1974.

[2] A. I. Ekimov and A. A. Onushchenko, "Size Quantization of the Electron Energy Spectrum in a Microscopic Semiconductor Crystal," *Journal of Experimental and Theoretical Physics Letters*, vol. 34, p. 345, 1984.

[3] M. Grundmann, "The physics of semiconductors," *Springer-Verlag, Heidelberg*, 2010.

[4] P. Harrison, *Quantum wells, wires and dots: theoretical and computational physics of semiconductor nanostructures*. John Wiley & Sons, 2005.

[5] C. Kittel, *Introduction to solid state physics*. Wiley, 2005.

[6] R. S. Wagner and W. C. Ellis, "Vapor-Liquid-Solid Mechanism of Single Crystal Growth," *Applied Physics Latters*, vol. 4, no. 5, pp. 89–&, 1964.

[7] S. Iijima, "Helical Microtubules of Graphitic Carbon," *Nature*, vol. 364, pp. 56–58, 1991.

[8] F. Glas, J.-C. Harmand, and G. Patriarche, "Why does wurtzite form in nanowires of iii-v zinc blende semiconductors?," *Physical Review Letters*, vol. 99, no. 14, p. 146101, 2007.

[9] D. Spirkoska, J. Arbiol, A. Gustafsson, S. Conesa-Boj, F. Glas, I. Zardo, M. Heigoldt, M. H. Gass, A. L. Bleloch, and S. Estrade, "Structural and Optical Properties of High Quality Zinc-Blende/Wurtzite GaAs Nanowire Heterostructures," *Physical Review B*, vol. 80, no. 24, p. 245325, 2009.

[10] K. A. Dick, C. Thelander, L. Samuelson, and P. Caroff, "Crystal phase engineering in single inas nanowires," *Nano Letters*, vol. 10, no. 9, pp. 3494–3499, 2010.

[11] M. Heiss, S. Conesa-Boj, J. Ren, H. H. Tseng, A. Gali, A. Rudolph, E. Uccelli, F. Peiró, J. R. Morante, D. Schuh, J. Arbiol, A. Fontcuberta i Morral, and E. Kaxiras, "Direct Correlation of Crystal Structure and Optical Properties in Wurtzite/Zinc-Blende GaAs Nanowire Heterostructures," *Physical Review B*, vol. 83, no. 4, p. 045303, 2011.

[12] N. Akopian, G. Patriarche, L. Liu, J. C. Harmand, and V. Zwiller, "Crystal Phase Quantum Dots," *Nano Letters*, vol. 10, no. 4, pp. 1198–1201, 2010.

[13] A. De and C. E. Pryor, "Predicted Band Structures of III-V Semiconductors in the Wurtzite Phase," *Physical Review B*, vol. 81, no. 15, p. 155210, 2010.

[14] M. T. Borgström, V. Zwiller, E. Müller, and A. Imamoglu, "Optically Bright Quantum Dots in Single Nanowires," *Nano Letters*, vol. 5, pp. 1439–1443, July 2005.

[15] P. Caroff, K. A. Dick, J. Johansson, M. E. Messing, K. Deppert, and L. Samuelson, "Controlled Polytypic and Twin-Plane Superlattices in III-V Nanowires," *Nature Nanotechnology*, vol. 4, no. 1, pp. 50–55, 2009.

[16] R. E. Algra, M. A. Verheijen, M. T. Borgström, L.-F. Feiner, G. Immink, W. J. P. van Enckevort, E. Vlieg, and E. P. A. M. Bakkers, "Twinning Superlattices in Indium Phosphide Nanowires," *Nature*, vol. 456, pp. 369–372, Nov. 2008.

[17] M. D. Kelzenberg, S. W. Boettcher, J. A. Petykiewicz, D. B. Turner-Evans, M. C. Putnam, E. L. Warren, J. M. Spurgeon, R. M. Briggs, N. S. Lewis, and H. A. Atwater, "Enhanced absorption and carrier collection in si wire arrays for photovoltaic applications," *Nature Materials*, vol. 9, no. 3, pp. 239–244, 2010.

[18] C. Colombo, P. Krogstrup, J. Nygård, M. L. Brongersma, and A. Fontcuberta i Morral, "Engineering Light Absorption in Single-Nanowire Solar Cells with Metal Nanoparticles," *New Journal Of Physics*, vol. 13, p. 123026, Dec. 2011.

[19] H. Drexler, D. Leonard, W. Hansen, J. P. Kotthaus, and P. M. Petroff, "Spectroscopy of Quantum Levels in Charge-Tunable InGaAs Quantum Dots," *Physical Review Letters*, vol. 73, no. 16, pp. 2252–2255, 1994.

[20] K. Brunner, G. Abstreiter, G. Böhm, G. Tränkle, and G. Weimann, "Sharp-Line Photoluminescence and Two-Photon Absorption of Zero-Dimensional Biexcitons in a GaAs/AlGaAs Structure," *Physical Review Letters*, vol. 73, pp. 1138–1141, Aug. 1994.

[21] D. J. Norris, A. L. Efros, M. Rosen, and M. G. Bawendi, "Size Dependence of Exciton Fine Structure in CdSe Quantum Dots," *Physical Review B*, vol. 53, no. 24, p. 16347, 1996.

[22] D. Gammon, E. S. Snow, B. V. Shanabrook, D. S. Katzer, and D. Park, "Fine Structure Splitting in the Optical Spectra of Single GaAs Quantum Dots," *Physical Review Letters*, vol. 76, no. 16, pp. 3005–3008, 1996.

[23] P. Ramvall, P. Riblet, S. Nomura, Y. Aoyagi, and S. Tanaka, "Optical Properties of GaN Quantum Dots," *Journal Of Applied Physics*, vol. 87, no. 8, p. 3883, 2000.

[24] V. Zwiller, L. Jarlskog, M. E. Pistol, C. Pryor, P. Castrillo, W. Seifert, and L. Samuelson, "Photoluminescence Polarization of Single InP Quantum Dots," *Physical Review B*, vol. 63, no. 23, pp. 233301–233301, 2001.

[25] N. Akopian, N. Lindner, E. Poem, Y. Berlatzky, J. Avron, D. Gershoni, B. Gerardot, and P. M. Petroff, "Entangled Photon Pairs from Semiconductor Quantum Dots," *Physical Review Letters*, vol. 96, p. 130501, Apr. 2006.

[26] O. Benson, C. Santori, M. Pelton, and Y. Yamamoto, "Regulated and entangled photons from a single quantum dot," *Physical Review Letters*, vol. 84, pp. 2513–2516, Mar 2000.

[27] S. Hoffmann, I. Utke, B. Moser, J. Michler, S. H. Christiansen, V. Schmidt, S. Senz, P. Werner, U. Gösell, and C. Ballif, "Measurement of the bending strength of vapor-liquid-solid grown silicon nanowires," *Nano Letters*, vol. 6, no. 4, pp. 622–625, 2006.

[28] Y. Cui, X. Duan, J. Hu, and C. M. Lieber, "Doping and electrical transport in silicon nanowires," *The Journal of Physical Chemistry B*, vol. 104, no. 22, pp. 5213–5216, 2000.

[29] J. A. Del Alamo, "Nanometre-scale electronics with iii-v compound semiconductors," *Nature*, vol. 479, no. 7373, pp. 317–323, 2011.

[30] R. Yan, D. Gargas, and P. Yang, "Nanowire Photonics," *Nature Photonics*, vol. 3, no. 10, pp. 569–576, 2009.

[31] R. A. Laudise, *The growth of single crystals*. Prentice Hall, 1970.

[32] A. Y. Cho and J. R. Arthur, "Molecular beam epitaxy," *Progress in solid state chemistry*, vol. 10, pp. 157–191, 1975.

[33] F. Martelli, M. Piccin, G. Bais, F. Jabeen, S. Ambrosini, S. Rubini, and A. Franciosi, "Photoluminescence of mn-catalyzed gaas nanowires grown by molecular beam epitaxy," *Nanotechnology*, vol. 18, no. 12, p. 125603, 2007.

[34] M. Heiss, A. Gustafsson, S. Conesa-Boj, F. Peiro, G. Morante, J. R.and Abstreiter, J. Arbiol, L. Samuelson, and A. Fontcuberta i Morral, "Catalyst-free nanowires with axial inxga1- xas/gaas heterostructures," *Nanotechnology*, vol. 20, no. 7, p. 075603, 2009.

[35] R. Perumal, Z. Cui, G. Patniarche, J.-C. Harmand, and K. Yoh, "Palladium assisted hetroepitaxial growth of an inas nanowire by molecular beam epitaxy," *Semiconductor Science and Technology*, vol. 29, no. 11, p. 115005, 2014.

[36] C. Colombo, D. Spirkoska, M. Frimmer, G. Abstreiter, and A. Fontcuberta i Morral, "Ga-Assisted Catalyst-Free Growth Mechanism of GaAs Nanowires by Molecular Beam Epitaxy," *Physical Review B*, vol. 77, no. 15, p. 155326, 2008.

[37] T. Mårtensson, C. P. T. Svensson, B. A. Wacaser, M. W. Larsson, W. Seifert, K. Deppert, A. Gustafsson, L. R. Wallenberg, and L. Samuelson, "Epitaxial III-V Nanowires on Silicon," *Nano Letters*, vol. 4, no. 10, pp. 1987–1990, 2004.

[38] E. Russo, M. Heiss, L. Michelet, P. Krogstrup, J. Nygård, C. Magen, J. R. Morante, E. Uccelli, J. Arbiol, and A. Fontcuberta i Morral, "Suppression of Three Dimensional Twinning for a 100% yield of Vertical GaAs Nanowires on Silicon," *Nanoscale*, vol. 4, no. 5, pp. 1486–1490, 2012.

[39] A. Fontcuberta i Morral, D. Spirkoska, J. Arbiol, M. Heigoldt, J. R. Morante, and G. Abstreiter, "Prismatic Quantum Heterostructures Synthesized on Molecular Beam Epitaxy GaAs Nanowires," *Small*, vol. 4, pp. 899–903, July 2008.

[40] P. Mohan, J. Motohisa, and T. Fukui, "Realization of conductive inas nanotubes based on lattice-mismatched inp/ inas core-shell nanowires," *Applied Physics Letters*, vol. 88, no. 1, p. 013110, 2006.

[41] F. Qian, Y. Li, S. Grade□ ak, H.-G. Park, Y. Dong, Y. Ding, Z. L. Wang, and C. M. Lieber, "Multi-quantum-well nanowire heterostructures for wavelength-controlled lasers," *Nature Materials*, vol. 7, no. 9, pp. 701–706, 2008.

[42] R. E. Algra, M. Hocevar, M. A. Verheijen, I. Zardo, G. G. W. Immink, W. J. P. van Enckevort, G. Abstreiter, L. P. Kouwenhoven, E. Vlieg, and E. P. A. M. Bakkers, "Crystal structure transfer in core/shell nanowires," *Nano Letters*, vol. 11, no. 4, pp. 1690–1694, 2011.

[43] J. Wang, M. S. Gudiksen, X. Duan, Y. Cui, and C. M. Lieber, "Highly polarized photoluminescence and photodetection from single indium phosphide nanowires," *Science*, vol. 293, no. 5534, pp. 1455–1457, 2001.

[44] L. Cao, J. S. White, J.-S. Park, J. A. Schuller, A. Clemens, and M. L. Brongersma, "Engineering Light Absorption in Semiconductor Nanowire Devices," *Nature Materials*, vol. 8, no. 8, pp. 643–647, 2009.

[45] L. Cao, J.-S. Park, P. Fan, A. Clemens, and M. L. Brongersma, "Resonant Germanium Nanoantenna Photodetectors," *Nano Letters*, vol. 10, no. 4, pp. 1229–1233, 2010.

[46] L. Cao, P. Fan, and M. L. Brongersma, "Optical Coupling of Deep-Subwavelength Semiconductor Nanowires," *Nano Letters*, 2011.

[47] R. Paniagua-Dominguez, G. Grzela, J. GómezRivas, and J. A. Sanchez-Gil, "Enhanced and directional emission of semiconductor nanowires tailored through leaky/guided modes," *Nanoscale*, vol. 5, no. 21, pp. 10582–10590, 2013.

[48] G. Grzela, R. Paniagua-Domínguez, T. Barten, D. van Dam, J. A. Sánchez-Gil, and J. Goómez Rivas, "Nanowire antenna absorption probed with time-reversed fourier microscopy," *Nano Letters*, vol. 14, no. 6, pp. 3227–3234, 2014.

[49] G. Grzela, R. Paniagua-Domínguez, T. Barten, Y. Fontana, J. A. Sánchez-Gil, and J. Gómez-Rivas, "Nanowire antenna emission," *Nano Letters*, vol. 12, no. 11, pp. 5481–5486, 2012.

[50] K. Seo, M. Wober, P. Steinvurzel, and E. Schonbrun, "Multicolored Vertical Silicon Nanowires," *Nano Letters*, 2011.

[51] M. H. Huang, S. Mao, H. Feick, H. Yan, Y. Wu, H. Kind, E. Weber, R. Russo, and P. Yang, "Room-Temperature Ultraviolet Nanowire Nanolasers," *Science*, vol. 292, no. 5523, p. 1897, 2001.

[52] B. Hua, J. Motohisa, Y. Kobayashi, S. Hara, and T. Fukui, "Single gaas/gaasp coaxial core- shell nanowire lasers," *Nano Letters*, vol. 9, no. 1, pp. 112–116, 2008.

[53] J. Bleuse, J. Claudon, M. Creasey, N. S. Malik, J.-M. Gérard, I. Maksymov, J.-P. Hugonin, and P. Lalanne, "Inhibition, enhancement, and control of spontaneous emission in photonic nanowires," *Physical Review Letters*, vol. 106, no. 10, p. 103601, 2011.

[54] I. Friedler, C. Sauvan, J.-P. Hugonin, P. Lalanne, J. Claudon, and J.-M. Gérard, "Solid-state single photon sources: the nanowire antenna," *Optics Express*, vol. 17, no. 4, pp. 2095–2110, 2009.

[55] M. E. Reimer, G. Bulgarini, N. Akopian, M. Hocevar, M. Bouwes Bavinck, M. A. Verheijen, E. P. A. M. Bakkers, L. P. Kouwenhoven, and V. Zwiller, "Bright single-photon sources in bottom-up tailored nanowires," *Nature Communications*, vol. 3, p. 737, 2012.

[56] J. Claudon, J. Bleuse, N. S. Malik, M. Bazin, P. Jaffrennou, N. Gregersen, C. Sauvan, P. Lalanne, and J.-M. Gérare, "A highly efficient single-photon source based on a quantum dot in a photonic nanowire," *Nature Photonics*, vol. 4, no. 3, pp. 174–177, 2010.

[57] M. Munsch, N. S. Malik, E. Dupuy, A. Delga, J. Bleuse, J.-M. Gérard, J. Claudon, N. Gregersen, and J. Mø rk, "Dielectric GaAs Antenna Ensuring an Efficient Broadband Coupling between an InAs Quantum Dot and a Gaussian Optical Beam," *Physical Review Letters*, vol. 110, p. 177402, 2013.

[58] M. Munsch, J. Claudon, J. Bleuse, N. S. Malik, E. Dupuy, J.-M. Gérard, Y. Chen, N. Gregersen, and J. Mørk, "Linearly polarized, single-mode spontaneous emission in a photonic nanowire," *Physical Review Letters*, vol. 108, p. 077405, Feb 2012.

[59] A. P. Foster, J. P. Bradley, K. Gardner, A. B. Krysa, B. Royall, M. S. Skolnick, and L. R. Wilson, "Linearly polarized emission from an embedded quantum dot using nanowire morphology control," *Nano Letters*, vol. 15, no. 3, pp. 1559–1563, 2015.

[60] E. Moreau, I. Robert, J.-M. Gérare, I. Abram, L. Manin, and V. Thierry-Mieg, "Single-mode solid-state single photon source based on isolated quantum dots in pillar microcavities," *Applied Physics Letters*, vol. 79, no. 18, pp. 2865–2867, 2001.

[61] M. Pelton, C. Santori, J. Vu kovi , B. Zhang, G. S. Solomon, J. Plant, and Y. Yamamoto, "Efficient source of single photons: A single quantum dot in a micropost microcavity," *Physical Review Letters*, vol. 89, p. 233602, Nov 2002.

[62] A. Badolato, K. Hennessy, M. Atatüre, J. Dreiser, E. Hu, P. M. Petroff, and A. Imamo lu, "Deterministic Coupling of Single Quantum Dots to Single Nanocavity Modes," *Science*, vol. 308, no. 5725, pp. 1158–1161, 2005.

[63] D. Englund, D. Fattal, E. Waks, G. Solomon, B. Zhang, T. Nakaoka, Y. Arakawa, Y. Yamamoto, and J. Vu kovi , "Controlling the spontaneous emission rate of single quantum dots in a two-dimensional photonic crystal," *Physical Review Letters*, vol. 95, no. 1, p. 013904, 2005.

[64] A. Dousse, J. Suffczy ski, A. Beveratos, O. Krebs, A. Lemaître, I. Sagnes, J. Bloch, P. Voisin, and P. Senellart, "Ultrabright source of entangled photon pairs," *Nature*, vol. 466, no. 7303, pp. 217–220, 2010.

[65] O. Gazzano, S. M. de Vasconcellos, C. Arnold, A. Nowak, E. Galopin, I. Sagnes, L. Lanco, A. Lemaître, and P. Senellart, "Bright solid-state sources of indistinguishable single photons," *Nature Communications*, vol. 4, p. 1425, 2013.

[66] S. Varoutsis, S. Laurent, P. Kramper, A. Lemaître, I. Sagnes, I. Robert-Philip, and I. Abram, "Restoration of photon indistinguishability in the emission of a semiconductor quantum dot," *Physical Review B*, vol. 72, no. 4, p. 041303, 2005.

[67] G. Khitrova, H. M. Gibbs, M. Kira, S. W. Koch, and A. Scherer, "Vacuum rabi splitting in semiconductors," *Nature Physics*, vol. 2, no. 2, pp. 81–90, 2006.

[68] M. Minkov and V. Savona, "Automated optimization of photonic crystal slab cavities," *Scientific reports*, vol. 4, 2014.

[69] U. P. Dharanipathy, M. Minkov, M. Tonin, V. Savona, and R. Houdré, "Evolutionarily optimized ultrahigh-q photonic crystal nanocavity," *Applied Physics Letters*, vol. 105, p. 101101, 2013.

[70] K. Hennessy, A. Badolato, M. Winger, D. Gerace, M. Atatüre, S. Gulde, S. Fält, E. L. Hu, and A. Imamo□lu, "Quantum nature of a strongly coupled single quantum dot–cavity system," *Nature*, vol. 445, no. 7130, pp. 896–899, 2007.

[71] A. Dousse, L. Lanco, J. Suffczy□ski, E. Semenova, A. Miard, A. Lemaître, I. Sagnes, C. Roblin, J. Bloch, and P. Senellart, "Controlled Light-Matter Coupling for a Single Quantum Dot Embedded in a Pillar Microcavity Using Far-Field Optical Lithography," *Physical Review Letters*, vol. 101, Dec. 2008.

[72] G. Bulgarini, M. E. Reimer, T. Zehender, M. Hocevar, E. P. A. M. Bakkers, L. P. Kouwenhoven, and V. Zwiller, "Spontaneous emission control of single quantum dots in bottom-up nanowire waveguides," *Applied Physics Letters*, vol. 100, no. 12, p. 121106, 2012.

[73] A. C. Scofield, S.-H. Kim, J. N. Shapiro, A. Lin, B. Liang, A. Scherer, and D. L. Huffaker, "Bottom-up Photonic Crystal Lasers," *Nano Letters*, p. 111118112841007, Nov. 2011.

[74] Y. Fontana, E. P. A. M. Grzela, G.and Bakkers, and J. Gómez Rivas, "Mapping the directional emission of quasi-two-dimensional photonic crystals of semiconductor nanowires using fourier microscopy," *Physical Review B*, vol. 86, no. 24, p. 245303, 2012.

[75] S. Diedenhofen, O. Janssen, M. Hocevar, A. Pierret, E. Bakkers, H. Urbach, and J. Gómez Rivas, "Controlling the Directional Emission of Light by Periodic Arrays of Heterostructured Semiconductor Nanowires," *ACS Nano*, 2011.

[76] T. B. Hoang, A. F. Moses, H. L. Zhou, D. L. Dheeraj, B. O. Fimland, and H. Weman, "Observation of free exciton photoluminescence emission from single wurtzite gaas nanowires," *Applied Physics Letters*, vol. 94, no. 13, p. 133105, 2009.

[77] L. Ahtapodov, J. Todorovic, P. Olk, T. Mjåland, P. Slåttnes, D. L. Dheeraj, A. T. J. van Helvoort, B.-O. Fimland, and H. Weman, "A story told by a single nanowire: optical properties of wurtzite gaas," *Nano Letters*, vol. 12, no. 12, pp. 6090–6095, 2012.

[78] L. C. Chuang, M. Moewe, K. W. Ng, T.-T. D. Tran, S. Crankshaw, R. Chen, W. S. Ko, and C. Chang-Hasnain, "Gaas nanoneedles grown on sapphire," *Applied Physics Letters*, vol. 98, no. 12, p. 123101, 2011.

[79] B. Ketterer, M. Heiss, E. Uccelli, J. Arbiol, and A. Fontcuberta i Morral, "Untangling the electronic band structure of wurtzite gaas nanowires by resonant raman spectroscopy," *ACS Nano*, vol. 5, no. 9, pp. 7585–7592, 2011.

[80] P. Corfdir, B. Van Hattem, E. Uccelli, A. Fontcuberta i Morral, and R. T. Phillips, "Charge carrier generation, relaxation, and recombination in polytypic gaas nanowires studied by photoluminescence excitation spectroscopy," *Applied Physics Letters*, vol. 103, no. 13, p. 133109, 2013.

[81] A. M. Graham, P. Corfdir, M. Heiss, S. Conesa-Boj, E. Uccelli, A. Fontcuberta i Morral, and R. T. Phillips, "Exciton localization mechanisms in wurtzite/zinc-blende gaas nanowires," *Physical Review B*, vol. 87, no. 12, p. 125304, 2013.

[82] S. Buckley, K. Rivoire, and J. Vu□kovi□, "Engineered quantum dot single-photon sources," *Reports on Progress in Physics*, vol. 75, no. 12, p. 126503, 2012.

[83] D. Hommel, K. Leonardi, H. Heinke, H. Selke, K. Ohkawa, F. Gindele, and U. Woggon, "Cdse/znse quantum dot structures: structural and optical investigations," *Physica Status Solidi (b)*, vol. 202, no. 2, pp. 835–843, 1997.

[84] J. R. Guest, T. H. Stievater, X. Li, J. Cheng, D. G. Steel, D. Gammon, D. S. Katzer, D. Park, C. Ell, A. Thränhardt, G. Khitrova, and H. M. Gibbs, "Measurement of optical absorption by a single quantum dot exciton," *Physical Review B*, vol. 65, no. 24, p. 241310, 2002.

[85] K. Yamaguchi, K. Yujobo, and T. Kaizu, "Stranski-krastanov growth of inas quantum dots with narrow size distribution," *Japanese journal of applied physics*, vol. 39, no. 12A, p. L1245, 2000.

[86] A. F. Tsatsulnikov, A. R. Kovsh, A. E. Zhukov, Y. M. Shernyakov, Y. G. Musikhin, V. M. Ustinov, N. A. Bert, P. S. Kopev, Z. I. Alferov, A. M. Mintairov, J. L. Mertz, N. N. Ledentsov, and D. Bimberg, "Volmer–weber and stranski–krastanov inas-(al, ga) as quantum dots emitting at 1.3 μm," *Journal of Applied Physics*, vol. 88, no. 11, pp. 6272–6275, 2000.

[87] K. Watanabe, N. Koguchi, and Y. Gotoh, "Fabrication of gaas quantum dots by modified droplet epitaxy," *Japanese Journal of Applied Physics*, vol. 39, no. 2A, p. L79, 2000.

[88] S. Sanguinetti, K. Watanabe, T. Tateno, M. Gurioli, P. Werner, M. Wakaki, and N. Koguchi, "Modified droplet epitaxy gaas/algaas quantum dots grown

on a variable thickness wetting layer," *Journal of Crystal Growth*, vol. 253, no. 1, pp. 71–76, 2003.

[89] C. Heyn, A. Stemmann, A. Schramm, H. Welsch, W. Hansen, and A. Nemcsics, "Regimes of gaas quantum dot self-assembly by droplet epitaxy," *Physical Review B*, vol. 76, no. 7, p. 075317, 2007.

[90] L. Wang, V. K□ ápek, F. Ding, F. Horton, A. Schliwa, D. Bimberg, A. Rastelli, and O. G. Schmidt, "Self-assembled quantum dots with tunable thickness of the wetting layer: role of vertical confinement on interlevel spacing," *Physical Review B*, vol. 80, no. 8, p. 085309, 2009.

[91] P. A. Dalgarno, J. McFarlane, D. Brunner, R. W. Lambert, B. D. Gerardot, R. J. Warburton, K. Karrai, A. Badolato, and P. M. Petroff, "Hole recapture limited single photon generation from a single n-type charge-tunable quantum dot," *Applied Physics Letters*, vol. 92, no. 19, pp. 193103–193103, 2008.

[92] G. S. Solomon, J. A. Trezza, A. F. Marshall, and J. S. Harris, "Vertically aligned and electronically coupled growth induced inas islands in gaas," *Physical Review Letters*, vol. 76, no. 6, p. 952, 1996.

[93] T. Kuroda, T. Mano, N. Ha, H. Nakajima, H. Kumano, B. Urbaszek, M. Jo, M. Abbarchi, Y. Sakuma, K. Sakoda, I. Suemune, X. Marie, and T. Amand, "Symmetric quantum dots as efficient sources of highly entangled photons: Violation of bell's inequality without spectral and temporal filtering," *Physical Review B*, vol. 88, p. 041306, Jul 2013.

[94] Q. Zhu, E. Pelucchi, S. Dalessi, K. Leifer, M. A. Dupertuis, and E. Kapon, "Alloy Segregation, Quantum Confinement, and Carrier Capture in Self-Ordered Pyramidal Quantum Wires," *Nano Letters*, vol. 6, pp. 1036–1041, May 2006.

[95] A. E. Romanov, P. M. Petroff, and J. S. Speck, "Lateral ordering of quantum dots by periodic subsurface stressors," *Applied Physics Letters*, vol. 74, no. 16, pp. 2280–2282, 1999.

[96] A. Stemmann, C. Heyn, T. Köppen, T. Kipp, and W. Hansen, "Local droplet etching of nanoholes and rings on gaas and algaas surfaces," *Applied Physics Letters*, vol. 93, no. 12, p. 123108, 2008.

[97] M. H. Baier, E. Pelucchi, E. Kapon, S. Varoutsis, M. Gallart, I. Robert-Philip, and I. Abram, "Single photon emission from site-controlled pyramidal quantum dots," *Applied Physics Letters*, vol. 84, no. 5, pp. 648–650, 2004.

[98] L. O. Mereni, V. Dimastrodonato, R. J. Young, and E. Pelucchi, "A site-controlled quantum dot system offering both high uniformity and spectral purity," *Applied Physics Letters*, vol. 94, no. 22, p. 223121, 2009.

[99] G. Juska, V. Dimastrodonato, L. O. Mereni, A. Gocalinska, and E. Pelucchi, "Towards quantum-dot arrays of entangled photon emitters," *Nature Photonics*, vol. 7, no. 7, pp. 527–531, 2013.

[100] Y. Léger, L. Besombes, L. Maingault, and H. Mariette, "Valence-band mixing in neutral, charged, and mn-doped self-assembled quantum dots," *Physical Review B*, vol. 76, p. 045331, July 2007.

[101] Y. H. Huo, B. J. Witek, S. Kumar, J. R. Cardenas, J. X. Zhang, N. Akopian, R. Singh, E. Zallo, R. Grifone, D. Kriegner, R. Trotta, F. Ding, J. Stangl, V. Zwiller, G. Bester, A. Rastelli, and O. G. Schmidt, "A light-hole exciton in a quantum dot," *Nature Physics*, vol. 10, no. 1, pp. 46–51, 2014.

[102] C. Jarlov, P. Gallo, M. Calic, B. Dwir, A. Rudra, and E. Kapon, "Bound and anti-bound biexciton in site-controlled pyramidal gainas/gaas quantum dots," *Applied Physics Letters*, vol. 101, no. 19, p. 191101, 2012.

[103] M. E. Reimer, M. P. van Kouwen, A. W. Hidma, M. H. M. van Weert, E. P. A. M. Bakkers, L. P. Kouwenhoven, and V. Zwiller, "Electric field induced removal of the biexciton binding energy in a single quantum dot," *Nano Letters*, vol. 11, no. 2, pp. 645–650, 2011.

[104] H. W. Van Kesteren, E. C. Cosman, W. A. J. A. Van der Poel, and C. T. B. Foxon, "Fine structure of excitons in type-ii gaas/alas quantum wells," *Physical Review B*, vol. 41, no. 8, p. 5283, 1990.

[105] M. Bayer, G. Ortner, O. Stern, a. Kuther, A. Gorbunov, A. Forchel, P. Hawrylak, S. Fafard, K. Hinzer, T. Reinecke, S. Walck, J. Reithmaier, F. Klopf, and F. Schäfer, "Fine structure of neutral and charged excitons in self-assembled In(Ga)As/(Al)GaAs quantum dots," *Physical Review B*, vol. 65, p. 195315, May 2002.

[106] K. Kowalik, O. Krebs, A. Lemaitre, S. Laurent, P. Senellart, P. Voisin, and J. A. Gaj, "Influence of an in-plane electric field on exciton fine structure in inas-gaas self-assembled quantum dots," *Applied Physics Letters*, vol. 86, no. 4, p. 1907, 2005.

[107] R. M. Stevenson, R. J. Young, P. See, D. G. Gevaux, K. Cooper, P. Atkinson, I. Farrer, D. A. Ritchie, and A. J. Shields, "Magnetic-field-induced reduction of the exciton polarization splitting in inas quantum dots," *Physical Review B*, vol. 73, no. 3, p. 033306, 2006.

[108] R. Trotta, E. Zallo, C. Ortix, P. Atkinson, J. D. Plumhof, J. Van den Brink, A. Rastelli, and O. G. Schmidt, "Universal recovery of the energy-level degeneracy of bright excitons in ingaas quantum dots without a structure symmetry," *Physical Review Letters*, vol. 109, no. 14, p. 147401, 2012.

[109] B. D. Gerardot, S. Seidl, P. A. Dalgarno, R. J. Warburton, D. Granados, J. M. Garcia, K. Kowalik, O. Krebs, K. Karrai, A. Badolato, and P. Petroff, "Manipulating exciton fine-structure in quantum dots with a lateral electric field," *arXiv preprint cond-mat/0608711*, 2006.

[110] S. Marcet, K. Ohtani, and H. Ohno, "Vertical electric field tuning of the exciton fine structure splitting and photon correlation measurements of gaas quantum dot," *Applied Physics Letters*, vol. 96, no. 10, p. 101117, 2010.

[111] A. I. Tartakovskii, M. N. Makhonin, I. R. Sellers, J. Cahill, A. D. Andreev, D. M. Whittaker, J. P. R. Wells, A. M. Fox, D. J. Mowbray, M. S. Skolnick, K. M. Groom, M. J. Steer, H. Y. Liu, and M. Hopkinson, "Effect of thermal annealing and strain engineering on the fine structure of quantum dot excitons," *Physical Review B*, vol. 70, no. 19, p. 193303, 2004.

[112] W. Langbein, P. Borri, U. Woggon, V. Stavarache, D. Reuter, and A. D. Wieck, "Control of fine-structure splitting and biexciton binding in in x ga 1- x as quantum dots by annealing," *Physical Review B*, vol. 69, no. 16, p. 161301, 2004.

[113] H. J. Kimble, M. Dagenais, and L. Mandel, "Photon antibunching in resonance fluorescence," *Physical Review Letters*, vol. 39, pp. 691–695, Sep 1977.

[114] E. D. Minot, F. Kelkensberg, M. Van Kouwen, J. A. van Dam, L. P. Kouwenhoven, V. Zwiller, M. T. Borgström, O. Wunnicke, M. A. Verheijen, and E. P. A. M. Bakkers, "Single quantum dot nanowire LEDs.," *Nano Letters*, vol. 7, pp. 367–371, 2007.

[115] M. P. Van Kouwen, M. H. M. Van Weert, M. E. Reimer, N. Akopian, U. Perinetti, R. E. Algra, E. P. A. M. Bakkers, L. P. Kouwenhoven, and V. Zwiller, "Single quantum dot nanowire photodetectors," *Applied Physics Letters*, vol. 97, p. 113108, 2010.

[116] M. D. Birowosuto, A. Yokoo, G. Zhang, K. Tateno, E. Kuramochi, H. Taniyama, M. Takiguchi, and M. Notomi, "Movable high-q nanoresonators realized by semiconductor nanowires on a si photonic crystal platform," *Nature Materials*, vol. 13, no. 3, pp. 279–285, 2014.

[117] R. Singh and G. Bester, "Nanowire Quantum Dots as an Ideal Source of Entangled Photon Pairs," *Physical Review Letters*, vol. 103, no. 6, pp. –, 2009.

[118] S. Bounouar, M. Elouneg-Jamroz, M. den Hertog, C. Morchutt, E. Bellet-Amalric, R. André, C. Bougerol, Y. Genuist, J.-P. Poizat, S. Tatarenko, and K. Kheng, "Ultrafast room temperature single-photon source from nanowire-quantum dots," *Nano Letters*, vol. 12, no. 6, pp. 2977–2981, 2012.

[119] S. Deshpande, J. Heo, A. Das, and P. Bhattacharya, "Electrically driven polarized single-photon emission from an InGaN quantum dot in a GaN nanowire," *Nature Communications*, vol. 4, p. 1675, 2013.

[120] M. J. Holmes, K. Choi, S. Kako, M. Arita, and Y. Arakawa, "Room-temperature triggered single photon emission from a iii-nitride site-controlled nanowire quantum dot," *Nano Letters*, vol. 14, no. 2, pp. 982–986, 2014.

[121] A. Tribu, G. Sallen, T. Aichele, R. Andre, J.-P. Poizat, C. Bougerol, S. Tatarenko, and K. Kheng, "A high-temperature single-photon source from nanowire quantum dots," *Nano Letters*, vol. 8, no. 12, pp. 4326–4329, 2008.

[122] P. Corfdir, B. Van Hattem, E. Uccelli, S. Conesa-Boj, P. Lefebvre, A. Fontcuberta i Morral, and R. T. Phillips, "Three-dimensional magneto-photoluminescence as a probe of the electronic properties of crystal-phase quantumdisks in gaas nanowires," *Nano Letters*, vol. 13, no. 11, pp. 5303–5310, 2013.

[123] N. Vainorius, S. Lehmann, D. Jacobsson, L. Samuelson, K. A. Dick, and M.-E. Pistol, "Confinement in thickness-controlled gaas polytype nanodots," *Nano Letters*, vol. 15, no. 4, pp. 2652–2656, 2015.

[124] E. Uccelli, J. Arbiol, J. R. Morante, and A. Fontcuberta i Morral, "Inas quantum dot arrays decorating the facets of gaas nanowires," *ACS Nano*, vol. 4, no. 10, pp. 5985–5993, 2010.

[125] J. Kwoen, K. Watanabe, Y. Ota, S. Iwamoto, and Y. Arakawa, "Growth of high-quality inas quantum dots embedded in gaas nanowire structures on si substrates," *Physica Status Solidi (c)*, vol. 10, no. 11, pp. 1496–1499, 2013.

[126] I. Yeo, N. S. Malik, M. Munsch, E. Dupuy, J. Bleuse, Y.-M. Niquet, J.-M. Gérard, J. Claudon, E. Wagner, S. Seidelin, A. Auffèves, J.-P. Poizat, and G. Nogues, "Surface effects in a semiconductor photonic nanowire and spectral stability of an embedded single quantum dot," *Applied Physics Letters*, vol. 99, no. 23, pp. –, 2011.

[127] C.-H. Cho, C. O. Aspetti, M. E. Turk, J. M. Kikkawa, and R. Nam, S.-W.and Agarwal, "Tailoring Hot-Exciton Emission and Lifetimes in Semiconducting Nanowires via Whispering-Gallery Nanocavity Plasmons," *Nature Materials*, vol. 10, pp. 669–675, July 2011.

[128] I. Yeo, P.-L. De Assis, A. Gloppe, P. Verlot, N. S. Malik, E. Dupuy, J. Claudon, A. Auffeves, G. Nogues, S. Seidelin, J.-P. Poizat, O. Arcizet, M. Richard, and J.-M. Gérard, "Strain-mediated coupling in a quantum dot – mechanical oscillator hybrid system," *Nature Nanotechnology*, vol. 9, no. February, pp. 106–110, 2014.

[129] M. Montinaro, G. Wüst, M. Munsch, Y. Fontana, E. Russo-Averchi, M. Heiss, A. Fontcuberta i Morral, and M. Warburton, R.J. Poggio, "Quantum dot opto-mechanics in a fully self-assembled nanowire," *Nano Letters*, 2014.

[130] I. Wilson-Rae, P. Zoller, and A. Imamo□ lu, "Laser Cooling of a Nanomechanical Resonator Mode to its Quantum Ground State," *Physical Review Letters*, 2004.

[131] B. J. M. Hausmann, T. M. Babinec, J. T. Choy, J. S. Hodges, S. Hong, I. Bulu, A. Yacoby, M. D. Lukin, and M. Lon□ ar, "Single-color centers implanted in diamond nanostructures," *New Journal of Physics*, vol. 13, no. 4, p. 045004, 2011.

[132] M. A. M. Versteegh, M. E. Reimer, K. D. Jöns, D. Dalacu, P. J. Poole, A. Gulinatti, A. Giudice, and V. Zwiller, "Observation of strongly entangled photon pairs from a nanowire quantum dot," *Nature Communications*, vol. 5, 2014.

[133] D. Dalacu, K. Mnaymneh, J. Lapointe, X. Wu, P. J. Poole, G. Bulgarini, Z. V., and M. Reimer, "Ultraclean emission from InAsP quantum dots in defect-free wurtzite InP nanowires," *Nano Letters*, vol. 12, pp. 5919–5923, 2012.

[134] M. E. Reimer, G. Bulgarini, R. W. Heeres, B. J. Witek, M. A. M. Versteegh, D. Dalacu, J. Lapointe, P. J. Poole, and V. Zwiller, "Overcoming power broadening of the quantum dot emission in a pure wurtzite nanowire," *arXiv preprint arXiv:1407.2833*, 2014.

[135] V. N. Kats, V. P. Kochereshko, A. V. Platonov, T. V. Chizhova, G. E. Cirlin, A. D. Bouravleuv, Y. B. Samsonenko, I. P. Soshnikov, E. V. Ubyivovk, J. Bleuse, and H. Mariette, "Optical study of gaas quantum dots embedded into algaas nanowires," *Semiconductor Science and Technology*, vol. 27, no. 1, p. 015009, 2012.

[136] J. Heinrich, A. Huggenberger, T. Heindel, S. Reitzenstein, S. Höfling, L. Worschech, and A. Forchel, "Single photon emission from positioned gaas/algaas photonic nanowires," *Applied Physics Letters*, vol. 96, no. 21, p. 211117, 2010.

[137] T. Huber, A. Predojevic, M. Khoshnegar, D. Dalacu, P. J. Poole, H. Majedi, and G. Weihs, "Polarization entangled photons from quantum dots embedded in nanowires," *Nano Letters*, vol. 14, no. 12, pp. 7107–7114, 2014.

[138] C. Matthiesen, A. N. Vamivakas, and M. Atatüre, "Subnatural linewidth single photons from a quantum dot," *Physical Review Letters*, vol. 108, no. 9, p. 093602, 2012.

[139] C. Matthiesen, M. Geller, C. H. H. Schulte, C. Le Gall, J. Hansom, Z. Li, M. Hugues, E. Clarke, and M. Atatüre, "Phase-locked indistinguishable photons with synthesized waveforms from a solid-state source," *Nature Communications*, vol. 4, p. 1600, 2013.

[140] H. Kamada, H. Gotoh, J. Temmyo, T. Takagahara, and H. Ando, "Exciton rabi oscillation in a single quantum dot," *Physical Review Letters*, vol. 87, no. 24, p. 246401, 2001.

[141] A. Zrenner, E. Beham, S. Stufler, F. Findeis, M. Bichler, and G. Abstreiter, "Coherent properties of a two-level system based on a quantum-dot photodiode," *Nature*, vol. 418, no. 6898, pp. 612–614, 2002.

[142] E. B. Flagg, A. Muller, J. W. Robertson, S. Founta, D. G. Deppe, M. Xiao, W. Ma, G. J. Salamo, and C.-K. Shih, "Resonantly driven coherent oscillations in a solid-state quantum emitter," *Nature Physics*, vol. 5, no. 3, pp. 203–207, 2009.

[143] X. Xu, B. Sun, P. R. Berman, D. G. Steel, A. S. Bracker, D. Gammon, and L. J. Sham, "Coherent optical spectroscopy of a strongly driven quantum dot," *Science*, vol. 317, no. 5840, pp. 929–932, 2007.

[144] T. Kehoe, M. Ediger, R. T. Phillips, and M. Hopkinson, "Cryogenic confocal microscopy with rotation in a magnetic field," *Review of Scientific Instruments*, vol. 81, no. 1, p. 013906, 2010.

[145] B. S. Robinson, A. J. Kerman, E. A. Dauler, R. J. Barron, D. O. Caplan, M. L. Stevens, J. J. Carney, S. A. Hamilton, J. K. Yang, and K. K. Berggren, "781 mbit/s photon-counting optical communications using a superconducting nanowire detector," *Optics letters*, vol. 31, no. 4, pp. 444–446, 2006.

[146] S. N. Dorenbos, E. M. Reiger, U. Perinetti, T. Zwiller, V .and Zijlstra, and T. M. Klapwijk, "Low noise superconducting single photon detectors on silicon," *Applied Physics Letters*, vol. 93, no. 13, p. 131101, 2008.

[147] C. M. Natarajan, M. G. Tanner, and R. H. Hadfield, "Superconducting nanowire single-photon detectors: physics and applications," *Superconductor science and technology*, vol. 25, no. 6, p. 063001, 2012.

[148] R. Hanbury Brown and R. Q. Twiss, "A test of a new type of stellar interferometer on sirius," *Nature*, vol. 178, no. 4541, pp. 1046–1048, 1956.

[149] J. Christen, M. Grundmann, and D. Bimberg, "Scanning cathodoluminescence microscopy: A unique approach to atomic-scale characterization of heterointerfaces and imaging of semiconductor inhomogeneities," *Journal of Vacuum Science & Technology B*, vol. 9, no. 4, pp. 2358–2368, 1991.

[150] G. Biasiol and E. Kapon, "Mechanisms of Self-Ordering of Quantum Nanostructures Grown on Nonplanar Surfaces," *Physical Review Letters*, vol. 81, no. 14, pp. 2962–2965, 1998.

[151] G. Biasiol, A. Gustafsson, K. Leifer, and E. Kapon, "Mechanisms of Self-Ordering in Nonplanar Epitaxy of Semiconductor Nanostructures," *Physical Review B*, vol. 65, Apr. 2002.

[152] N. Sköld, J. B. Wagner, G. Karlsson, T. Hernán, W. Seifert, M.-E. Pistol, and L. Samuelson, "Phase segregation in alinp shells on gaas nanowires," *Nano Letters*, vol. 6, no. 12, pp. 2743–2747, 2006.

[153] J. B. Wagner, N. Sköld, R. L. Wallenberg, and L. Samuelson, "Growth and Segregation of GaAs-AlxIn1-xP Core-Shell Nanowires," *Journal of Crystal Growth*, vol. 312, no. 10, pp. 1755–1760, 2010.

[154] M. Keplinger, T. Martensson, J. Stangl, E. Wintersberger, B. Mandl, D. Kriegner, V. Holý, G. Bauer, K. Deppert, and L. Samuelson, "Structural Investigations of Core - shell Nanowires Using Grazing Incidence X-ray Diffraction," *Nano Letters*, vol. 9, pp. 1877–1882, May 2009.

[155] S. Adachi, "Gaas, alas, and al$_x$ga$_{1-x}$as: Material parameters for use in research and device applications," *Journal of Applied Physics*, vol. 58, no. 3, pp. R1–R29, 1985.

[156] C. Zheng, J. Wong-Leung, Q. Gao, H. H. Tan, C. Jagadish, and J. Etheridge, "Polarity-Driven 3-Fold Symmetry of GaAs/AlGaAs Core Multishell Nanowires," *Nano Letters*, vol. 13, pp. 3742–3748, 2013.

[157] T. S. Kuan, T. F. Kuech, W. I. Wang, and E. L. Wilkie, "Long-Range Order in AlxGa(1-x)As," *Physical Review Letters*, vol. 54, no. 3, p. 201, 1985.

[158] W. I. Wang, "On the long-range order in algaas," *Journal of applied physics*, vol. 58, no. 8, pp. 3244–3245, 1985.

[159]

[160] V. Dhaka, J. Oksanen, H. Jiang, T. Haggren, A. Nykänen, R. Sanatinia, J.-P. Kakko, T. Huhtio, M. Mattila, J. Ruokolainen, S. Anand, E. Kauppinen, and H. Lipsanen, "Aluminum-induced photoluminescence red shifts in core–shell gaas/al x ga1–x as nanowires," *Nano Letters*, vol. 13, no. 8, pp. 3581–3588, 2013.

[161] D. Rudolph, S. Funk, M. Doeblinger, S. Morkoetter, S. Hertenberger, L. Schweickert, J. Becker, S. Matich, M. Bichler, D. Spirkoska, I. Zardo, J. J. Finley, and G. Abstreiter, "Spontaneous alloy composition ordering in gaas-algaas core–shell nanowires," *Nano Letters*, vol. 13, no. 4, pp. 1522–1527, 2013.

[162] L. Mancini, Y. Fontana, S. Conesa-Boj, I. Blum, F. Vurpillot, L. Francaviglia, E. Averchi, M. Heiss, J. Arbiol, A. Fontcuberta i Morral, and L. Rigutti, "Three-dimensional nanoscale study of al segregation and quantum dot formation

in gaas/algaas core-shell nanowires," *Applied Physics Letters*, vol. 105, no. 24, p. 243106, 2014.

[163] B. Gault, F. Vurpillot, A. Vella, M. Gilbert, A. Menand, D. Blavette, and B. Deconihout, "Design of a femtosecond laser assisted tomographic atom probe," *Review of Scientific Instruments*, vol. 77, no. 4, p. 043705, 2006.

[164] P. J. Price, "Tunneling in algaas by γ-x scattering," *Surface Science*, vol. 196, no. 1, pp. 394–398, 1988.

[165] Y. Masumoto, T. Mishina, F. Sasaki, and M. Adachi, "Interlayer γ-x scattering in staggered-alignment al 0.34 ga 0.66 as-alas ternary alloy multiple-quantum-well structures," *Physical Review B*, vol. 40, no. 12, p. 8581, 1989.

[166] J. Feldmann, J. Nunnenkamp, G. Peter, E. Göbel, J. Kuhl, K. Ploog, P. Dawson, and C. T. Foxon, "Experimental study of the γ-x electron transfer in type-ii (al, ga) as/alas superlattices and multiple-quantum-well structures," *Physical Review B*, vol. 42, no. 9, p. 5809, 1990.

[167] S. W. Da Silva, Y. A. Pusep, J. C. Galzerani, M. A. Pimenta, D. I. Lubyshev, P. P. G. Borrero, and P. Basmaji, "Raman study of interface roughness in (gaas) n (alas) n superlattices grown on tilted surfaces: Evidence of corrugation of the (113) interface," *Physical Review B*, vol. 53, no. 4, p. 1927, 1996.

[168] S. Minari, L. Cavigli, F. Sarti, M. Abbarchi, N. Accanto, G. Munoz Matutano, S. Bietti, S. Sanguinetti, A. Vinattieri, and M. Gurioli, "Single photon emission from impurity centers in algaas epilayers on ge and si substrates," *Applied Physics Letters*, vol. 101, no. 17, p. 172105, 2012.

[169] F. Sarti, G. Munoz Matutano, D. Bauer, N. Dotti, S. Bietti, G. Isella, A. Vinattieri, S. Sanguinetti, and M. Gurioli, "Multiexciton complex from extrinsic centers in algaas epilayers on ge and si substrates," *Journal of Applied Physics*, vol. 114, no. 22, p. 224314, 2013.

[170] M. Heiss, Y. Fontana, A. Gustafsson, G. Wüst, C. Magen, D. O'Regan, J. W. Luo, B. Ketterer, S. Conesa-Boj, A. Kuhlmann, J. Houel, E. Russo-Averchi, J. R. Morrante, M. Cantoni, N. Marzari, J. Arbiol, A. Zunger, R. Warburton, and A. Fontcuberta i Morral, "Self-assembled quantum dots in a nanowire system for quantum photonics," *Nature Materials*, vol. 12, pp. 439–44, 2013.

[171] Y. Fontana, P. Corfdir, B. Van Hattem, E. Russo-Averchi, M. Heiss, S. Sonderegger, C. Magen, J. Arbiol, R. T. Phillips, and A. Fontcuberta i Morral, "Exciton footprint of self-assembled algaas quantum dots in core-shell nanowires," *Physical Review B*, vol. 90, no. 7, p. 075307, 2014.

[172] M. Abbarchi, T. Kuroda, T. Mano, K. Sakoda, C. Mastrandrea, A. Vinattieri, M. Gurioli, T. Tsuchiya, J. Ihm, and H. Cheong, "Binding Energy of Exciton Complexes in Self-Assembled GaAs Quantum Dots," *AIP Conference Proceedings*, vol. 1399, no. 1, p. 465, 2011.

[173] T. Kuroda, M. Abbarchi, T. Mano, K. Watanabe, M. Yamagiwa, K. Kuroda, K. Sakoda, G. Kido, C. Koguchi, N.and Mastrandrea, L. Cavigli, M. Gurioli, M. Ogawa, and F. Minami, "Photon correlation in gaas self-assembled quantum dots," *Applied Physics Express*, vol. 1, no. 4, p. 042001, 2008.

[174] T. Mano, M. Abbarchi, T. Kuroda, C. Mastrandrea, A. Vinattieri, S. Sanguinetti, K. Sakoda, and M. Gurioli, "Ultra-narrow emission from single gaas self-assembled quantum dots grown by droplet epitaxy," *Nanotechnology*, vol. 20, no. 39, p. 395601, 2009.

[175] P. Tighineanu, R. Daveau, E. H. Lee, J. D. Song, S. Stobbe, and P. Lodahl, "Decay dynamics and exciton localization in large gaas quantum dots grown by droplet epitaxy," *Physical Review B*, vol. 88, p. 155320, Oct 2013.

[176] J. Hours, P. Senellart, E. Peter, A. Cavanna, and J. Bloch, "Exciton radiative lifetime controlled by the lateral confinement energy in a single quantum dot," *Physical Review B*, vol. 71, no. 16, p. 161306, 2005.

[177] M. E. Ware, A. S. Bracker, E. Stinaff, D. Gammon, D. Gershoni, and V. L. Korenev, "Polarization spectroscopy of positive and negative trions in an inas quantum dot," *Physica E: Low-dimensional Systems and Nanostructures*, vol. 26, no. 1, pp. 55–58, 2005.

[178] S. Rodt, A. Schliwa, K. Pötschke, F. Guffarth, and D. Bimberg, "Correlation of structural and few-particle properties of self-organized in as/ ga as quantum dots," *Physical Review B*, vol. 71, no. 15, p. 155325, 2005.

[179] M. Ediger, G. Bester, A. Badolato, P. M. Petroff, K. Karrai, A. Zunger, and R. J. Warburton, "Peculiar many-body effects revealed in the spectroscopy of highly charged quantum dots," *Nature Physics*, vol. 3, no. 11, pp. 774–779, 2007.

[180] G. Moody, R. Singh, H. Li, I. A. Akimov, M. Bayer, D. Reuter, A. D. Wieck, A. S. Bracker, D. Gammon, and S. T. Cundiff, "Influence of confinement on biexciton binding in semiconductor quantum dot ensembles measured with two-dimensional spectroscopy," *Physical Review B*, vol. 87, p. 041304, Jan 2013.

[181] M. Abbarchi, T. Kuroda, T. Mano, K. Sakod, C. Mastrandrea, A. Vinattieri, M. Gurioli, and T. Tsuchiya, "Binding Energy of Exciton Complexes in Self□ Assembled GaAs Quantum Dots," *AIP Conference Proceedings*, vol. 465, no. 2011, pp. 465–466, 2011.

[182] M. H. M. van Weert, N. Akopian, F. Kelkensberg, U. Perinetti, M. P. van Kouwen, J. Gómez-Rivas, M. T. Borgström, R. E. Algra, M. A. Verheijen, E. P. A. M. Bakkers, L. P. Kouwenhoven, and V. Zwiller, "Orientation-dependent optical-polarization properties of single quantum dots in nanowires.," *Small*, vol. 5, pp. 2134–2138, Oct. 2009.

[183] L. Besombes, K. Kheng, and D. Martrou *Physical Review Letters*, vol. 85, pp. 425–428, July 2000.

[184] T. Belhadj, T. Amand, A. Kunold, C.-M. Simon, T. Kuroda, M. Abbarchi, T. Mano, K. Sakoda, S. Kunz, and U. B. Marie, X., "Impact of heavy hole-light hole coupling on optical selection rules in gaas quantum dots," *Applied Physics Letters*, vol. 97, no. 5, p. 051111, 2010.

[185] S. Kumar, E. Zallo, Y. H. Liao, P. Y. Lin, R. Trotta, P. Atkinson, J. D. Plumhof, F. Ding, B. D. Gerardot, S. J. Cheng, A. Rastelli, and O. Schmidt, "Anomalous anticrossing of neutral exciton states in gaas/algaas quantum dots," *Physical Review B*, vol. 89, no. 11, p. 115309, 2014.

[186] F. Meier and B. P. Zakharchenya, *Optical orientation*. Elsevier, 2012.

[187] D. J. Hilton and C. L. Tang, "Optical orientation and femtosecond relaxation of spin-polarized holes in gaas," *Physical review letters*, vol. 89, no. 14, p. 146601, 2002.

[188] T. Belhadj, T. Kuroda, C.-M. Simon, T. Amand, T. Mano, K. Sakoda, and v. n. p. y. p. Koguchi, Nobuyuki. journal=Physical Review B, "Optically monitored nuclear spin dynamics in individual gaas quantum dots grown by droplet epitaxy,"

[189] L. Besombes, K. Kheng, L. Marsal, and H. Mariette, "Few-particle effects in single cdte quantum dots," *Physical Review B*, vol. 65, p. 121314, Mar 2002.

[190] R. Seguin, S. Rodt, A. Strittmatter, L. Reißmann, T. Bartel, A. Hoffmann, D. Bimberg, E. Hahn, and D. Gerthsen, "Multi-excitonic complexes in single ingan quantum dots," *Applied Physics Letters*, vol. 84, no. 20, pp. 4023–4025, 2004.

[191] D. Bertram, M. C. Hanna, and A. J. Nozik, "Two color blinking of single strain-induced gaas quantum dots," *Applied Physics Letters*, vol. 74, no. 18, pp. 2666–2668, 1999.

[192] M. Abbarchi, T. Kuroda, T. Mano, M. Gurioli, and K. Sakoda, "Bunched photon statistics of the spectrally diffusive photoluminescence of single self-assembled gaas quantum dots," *Physical Review B*, vol. 86, no. 11, p. 115330, 2012.

[193] M. Abbarchi, F. Troiani, C. Mastrandrea, G. Goldoni, T. Kuroda, T. Mano, K. Sakoda, N. Koguchi, S. Sanguinetti, A. Vinattieri, and M. Gurioli, "Spectral

diffusion and line broadening in single self-assembled gaas/ algaas quantum dot photoluminescence," *Applied Physics Letters*, vol. 93, no. 16, p. 162101, 2008.

[194] L. Besombes, K. Kheng, L. Marsal, and H. Mariette, "Acoustic phonon broadening mechanism in single quantum dot emission," *Physical Review B*, vol. 63, no. 15, p. 155307, 2001.

[195] I. Favero, G. Cassabois, R. Ferreira, D. Darson, C. Voisin, J. Tignon, C. Delalande, G. Bastard, P. Roussignol, and J. M. Gérard, "Acoustic phonon sidebands in the emission line of single inas/gaas quantum dots," *Physical Review B*, vol. 68, no. 23, p. 233301, 2003.

[196] E. Peter, J. Hours, P. Senellart, A. Vasanelli, A. Cavanna, J. Bloch, and J. M. Gérard, "Phonon sidebands in exciton and biexciton emission from single gaas quantum dots," *Physical Review B*, vol. 69, no. 4, p. 041307, 2004.

[197] M. Abbarchi, C. A. Mastrandrea, T. Kuroda, T. Mano, K. Sakoda, N. Koguchi, S. Sanguinetti, A. Vinattieri, and M. Gurioli, "Exciton fine structure in strain-free gaas/al 0.3 ga 0.7 as quantum dots: extrinsic effects," *Physical Review B*, vol. 78, no. 12, p. 125321, 2008.

[198] S. N. Walck and T. L. Reinecke, "Exciton diamagnetic shift in semiconductor nanostructures," *Physical Review B*, vol. 57, no. 15, p. 9088, 1998.

[199] B. D. Gerardot, D. Brunner, P. A. Dalgarno, P. Öhberg, S. Seidl, M. Kroner, K. Karrai, N. G. Stolz, P. M. Petroff, and R. J. Warburton, "Optical pumping of a single hole spin in a quantum dot," *Nature*, vol. 451, pp. 441–444, 2008.

[200] X. Xu, B. Sun, P. R. Berman, D. G. Steel, A. Bracker, D. Gammon, and L. J. Sham, "Coherent population trapping of an electron spin in a single negatively charged quantum dot," *Nature Physics*, vol. 4, no. 9, pp. 692–695, 2008.

[201] J. Houel, J. H. Prechtel, A. V. Kuhlmann, D. Brunner, C. E. Kuklewicz, B. D. Gerardot, N. G. Stoltz, P. M. Petroff, and R. J. Warburton, "High resolution coherent population trapping on a single hole spin in a semiconductor quantum dot," *Physical Review Letters*, vol. 112, no. 10, p. 107401, 2014.

[202] P. Chen, C. Piermarocchi, L. J. Sham, D. Gammon, and D. G. Steel, "Theory of quantum optical control of a single spin in a quantum dot," *Physical Review B*, vol. 69, no. 7, p. 075320, 2004.

[203] K. Bergmann, H. Theuer, and B. W. Shore, "Coherent population transfer among quantum states of atoms and molecules," *Reviews of Modern Physics*, vol. 70, no. 3, p. 1003, 1998.

[204] E. Uccelli, J. Arbiol, C. Magen, P. Krogstrup, E. Russo-Averchi, M. Heiss, G. Mugny, F. Morier-Genoud, J. Nygard, J. R. Morante, and A. Fontcuberta i Morral, "Three-dimensional multiple-order twinning of self-catalyzed gaas nanowires on si substrates," *Nano Letters*, vol. 11, no. 9, pp. 3827–3832, 2011.

[205] G. Sallen, B. Urbaszek, M. M. Glazov, E. L. Ivchenko, T. Kuroda, T. Mano, S. Kunz, M. Abbarchi, K. Sakoda, D. Lagarde, A. Balocchi, X. Marie, and T. Amand *Physical Review Letters*, vol. 107, p. 166604, Oct 2011.

[206] K. F. Karlsson, M. a. Dupertuis, D. Y. Oberli, E. Pelucchi, a. Rudra, P. O. Holtz, and E. Kapon, "Fine structure of exciton complexes in high-symmetry quantum dots: Effects of symmetry breaking and symmetry elevation," *Physical Review B*, vol. 81, p. 161307, Apr. 2010.

[207] D. Y. Oberli, "Intertwining of zeeman and coulomb interactions on excitons in highly symmetric semiconductor quantum dots," *Physical Review B*, vol. 85, p. 155305, Apr 2012.

[208] M. V. Durnev, M. M. Glazov, E. L. Ivchenko, M. Jo, T. Mano, T. Kuroda, K. Sakoda, S. Kunz, G. Sallen, L. Bouet, X. Marie, D. Lagarde, T. Amand, and B. Urbaszek, "Magnetic field induced valence band mixing in [111] grown semiconductor quantum dots," *Physical Review B*, vol. 87, p. 085315, Feb. 2013.

[209] P. Corfdir, Y. Fontana, B. Van Hattem, E. Russo-Averchi, M. Heiss, A. Fontcuberta i Morral, and R. T. Phillips, "Tuning the g-factor of neutral and charged excitons confined to self-assembled (al, ga) as shell quantum dots," *Applied Physics Letters*, vol. 105, no. 22, p. 223111, 2014.

[210] B. J. Witek, R. W. Heeres, U. Perinetti, E. P. A. M. Bakkers, L. P. Kouwenhoven, and V. Zwiller, "Measurement of the g-factor tensor in a quantum dot and disentanglement of exciton spins," *Physical Review B*, vol. 84, no. 19, p. 195305, 2011.

[211] M. Erdmann, C. Ropers, M. Wenderoth, R. Ulbrich, S. Malzer, and G. Döhler, "Diamagnetic shift of disorder-localized excitons in narrow GaAs□ AlGaAs quantum wells," *Physical Review B*, vol. 74, no. 12, p. 125412, 2006.

[212] M. J. Snelling, E. Blackwood, C. J. McDonagh, R. T. Harley, and C. T. B. Foxon, "Exciton, heavy-hole, and electron g factors in type-i gaas/al x ga 1- x as quantum wells," *Physical Review B*, vol. 45, no. 7, p. 3922, 1992.

[213] A. Sallen, G.and Tribu, T. Aichele, R. André, L. Besombes, C. Bougerol, M. Richard, S. Tatarenko, K. Kheng, and J.-P. Poizat, "Subnanosecond spectral diffusion measurement using photon correlation," *Nature Photonics*, vol. 4, no. 10, pp. 696–699, 2010.

[214] G. Sallen, A. Tribu, T. Aichele, R. André, L. Besombes, C. Bougerol, M. Richard, S. Tatarenko, K. Kheng, and J.-P. Poizat, "Subnanosecond spectral diffusion of a single quantum dot in a nanowire," *Physical Review B*, vol. 84, no. 4, p. 041405, 2011.

[215] J. Houel, A. V. Kuhlmann, L. Greuter, F. Xue, M. Poggio, B. D. Gerardot, P. A. Dalgarno, A. Badolato, P. M. Petroff, A. Ludwig, D. Reuter, A. D. Wieck, and R. J. Warburton, "Probing single-charge fluctuations at a gaas/alas interface using laser spectroscopy on a nearby ingaas quantum dot," *Physical review letters*, vol. 108, no. 10, p. 107401, 2012.

[216] A. V. Kuhlmann, J. Houel, A. Ludwig, L. Greuter, D. Reuter, A. D. Wieck, M. Poggio, and R. J. Warburton, "Charge noise and spin noise in a semiconductor quantum device," *Nature Physics*, vol. 9, no. 9, pp. 570–575, 2013.

[217] C. Matthiesen, M. J. Stanley, M. Hugues, E. Clarke, and M. Atatüre, "Full counting statistics of quantum dot resonance fluorescence," *Scientific Reports*, vol. 4, 2014.

[218] R. Heilman and G. Oelgart, "Ionization energy of the carbon acceptor in $al_xga_{(1-x)}as$," *Semiconductor Science and Technology*, vol. 5, no. 10, p. 1040, 1990.

[219] M. Grundmann and D. Bimberg, "Theory of random population for quantum dots," *Physical Review B*, vol. 55, no. 15, p. 9740, 1997.

[220] G. Muñoz-Matutano, J. Gomis, B. Alén, J. Martínez-Pastor, L. Seravalli, P. Frigeri, and S. Franchi, "Exciton, biexciton and trion recombination dynamics in a single quantum dot under selective optical pumping," *Physica E: Low-dimensional Systems and Nanostructures*, vol. 40, no. 6, pp. 2100–2103, 2008.

[221] M. Abbarchi, C. Mastrandrea, T. Kuroda, T. Mano, A. Vinattieri, K. Sakoda, and M. Gurioli, "Poissonian statistics of excitonic complexes in quantum dots," *Journal of Applied Physics*, vol. 106, no. 5, p. 3504, 2009.

[222] T. Kazimierczuk, M. Goryca, A. Koperski, M.and Golnik, J. A. Gaj, M. Nawrocki, P. Wojnar, and P. Kossacki, "Picosecond charge variation of quantum dots under pulsed excitation," *Physical Review B*, vol. 81, no. 15, p. 155313, 2010.

[223] J. Gomis-Bresco, G. Muñoz-Matutano, J. Martínez-Pastor, B. Alén, L. Seravalli, P. Frigeri, G. Trevisi, and S. Franchi, "Random population model to explain the recombination dynamics in single inas/gaas quantum dots under selective optical pumping," *New Journal of Physics*, vol. 13, no. 2, p. 023022, 2011.

[224] H. S. Nguyen, G. Sallen, M. Abbarchi, R. Ferreira, C. Voisin, P. Roussignol, G. Cassabois, and C. Diederichs, "Photoneutralization and slow capture of carriers in quantum dots probed by resonant excitation spectroscopy," *Physical Review B*, vol. 87, no. 11, p. 115305, 2013.

[225] A. Hartmann, Y. Ducommun, E. Kapon, U. Hohenester, and E. Molinari, "Few-particle effects in semiconductor quantum dots: Observation of multicharged excitons," *Physical Review Letters*, vol. 84, no. 24, p. 5648, 2000.

[226] D. C. Watson, R. V. Martinez, Y. Fontana, E. Russo-Averchi, M. Heiss, A. Fontcuberta i Morral, G. M. Whitesides, and M. Lon□ ar, "Nanoskiving core-shell nanowires: A new fabrication method for nano-optics," *Nano Letters*, vol. 14, no. 2, pp. 524–531, 2014.

[227] G. Sallen, S. Kunz, T. Amand, L. Bouet, T. Kuroda, T. Mano, D. Paget, O. Krebs, X. Marie, K. Sakoda, and B. Urbaszek, "Nuclear magnetization in gallium arsenide quantum dots at zero magnetic field.," *Nature Communications*, vol. 5, p. 3268, 2014.

Acknowledgments

As commonly stated in the acknowledgements of most of the work of a certain amplitude, and in particular for PhD theses, the final work is far from being only the product of the sole author. One might even argue that a PhD thesis is more than the sum of each individual contributions.

First I would like to greatly thank Prof. Anna Fontcuberta i Morral who was not only my PhD advisor for the last four years, but also the teacher who introduced semiconductor physics to me back in 2009 and co-supervised my master thesis. I how her to have been able to orient my research in the directions which I found interesting. She has always been supportive with regards to my ideas and beyond that, made me benefit from her experience and network. That said, it is thus clear that this thesis would not exist (at least in its present form) without her.

In addition to its professor, a research group is of course composed of other researchers: PhD students, trainees, postdocs, students etc. When I joined LMSC, I had the pleasure to meet many colleagues who helped me, both in direct and indirect ways, and deserve thanks. Sharing the office with me where Anna Dalmau, the sportive and fierce Barcelona supporter, Olivier Demichel and Pierre Blanc, often up for evening beers. The team was completed with Eleonora Russo-Averchi, who was always there to share a coffee and discuss in the morning, and deserves big kudos for completing a PhD while having one, then two wonderful daughters. Bernt Ketterer, always up to remotivate the troops, Martin Heiss, who in addition to being a close collaborator on the first paper on shell-QDs is most likely the best person to ask to ensure your ideas are bulletproof (they will not be), Santi Novoa, always positive, Carlo Colombo, a guy gifted with the incredible ability to bind people together (in addition to discuss politics and economics at 3 a.m. out of a bar), and of course huge thanks to Daniel Rüffer, who in addition to being my english-german translator for this thesis abstract is also a great friend and helped and taught me much regarding to electronics, signal processing and computer-related stuff. Daniel later moved to our office, resulting in an unbeatable amount of cheesy and low-level jokes (best time in the office). Finally I would like to warmly thanks Yvonne Cotting, who was the LMSC administrative assistant at this time. Thanks Yvonne for your kindness (And all the

lifts you gave me while I was still living in Crissier). Thanks to all of you guys for the awesome time!

Labs change and peoples come and go. Thus new people showed up: Alberto Casadei dragged the Californian spirit straight from the Valley to Lausanne with his warm mood and chill spirit. Then I've to admit that, alas! the timeline becomes confuse... So in the (dis)continuity many many thanks to Gözde Tütünçuoglu. I'm happy you didn't disappear in piranha, I would have lack someone to laugh at my cheesy jokes and a great friend. Thanks to Ruining Wang who is a good friend, a fellow EPFL graduate, and did his master thesis at LMSC. Thanks also to Federico Matteini. In addition to being a great friend, you are also always ready to discuss about science, in particular growth despite my lack of knowledge in the field. This is great and it was an immense pleasure. Many thanks to Esther Alarcon-Llado, absolutely always present to discuss and help me with a huge variety of problems. Esther I wish you all the best and beyond for your future career (*Esther now joined AMOLF as a team leader. I'm so glad for you, good luck there with the rain*). The academic community needs more people like you. Thanks to Heidi Potts, in particular for correcting my negation present/past mistakes in english until I got it (almost) right! Another great person at LMSC is Jelena Vukajlovic-Plestina. Jelena I will miss you and your awesome family much and not only because you are certainly the only one to be able to differentiate between, and appreciate, my sarcastic remarks. Francesca Amaduzzi, *tante grazie* for the translation of the *riassunto*, for being such a nice person, and for your contribution and willingness to engage in scientific discussion. Thanks also to Monika Salas-Tesar, who replaced Yvonne as administrative assistant, for being so helpful with all the administrative hassle! Thanks also to many students and trainee for the good time: Jane Herriman, Thibaud Ruelle *(at this time we are actually working again together, the world is small!!)*, Romain Froidevaux, Jil Schwender, the awesome Ignasi Canales-Mundet who also happened to be my flatmate for a while, the amazing Hubert "Hubi" Hauptmann and Luca Del Carro, and of course Mohammad Ramezani, who in addition to being a great guy is also an impressive scientist, had the good taste to start his PhD in optics, and is always up for discussing about light-related topics. After completing their master thesis at LMSC, two other outstanding dudes kicked in for the PhD: Martin Friedl and Luca Francaviglia, who was also working with me on the QDs and has been tremendously helpful (Chapter 5 is yours). I was really glad to have you guys in the office/lab for a few months. I wish you both all the possible luck for your PhD. Carve your own paths, it is worth it. Recently (well, almost one year), Dmitry Mikulik and Eleonora Frau strengthened the group. Good luck to you guys! Even more recent is the arrival of Jean-Baptiste Leran as an engineer in the group. There again good luck JB, the group is very lucky to have such a person: always positive and helpful! I omitted one person who was part of LMSC until last year. This is on purpose and for a good reason: Sonia Conessa-Boj is so special, I cannot remember someone else like her. You have always been present

for me, kind, crazy and understanding at the same time, always ready to discuss, help, counsel, allay the sorrow in bad times and laugh in the good ones. Your help was and still is beyond description. I wish you all the best for you and your family!

Still members of the scientific community, but beyond LMSC, several persons have my gratitude. Many collaborators have already been thanked in the appropriate chapters, but definitely deserve a second round: Jordi Arbiol and his collaborators in Barcelona and Zaragoza for the TEM, EPFL-THEOS head Prof. Nicola Marzari and David O'Reagan, Alex Zunger and Jun-Wei Luo at Boulder for the theory, Anders Gustafsson for the early CL mappings, all the Attolight people for the access to the Attolight CL microscope and for the thorough explanations. Gwenolé Jacopin, Mehran Shahmohammadi, Jean-Daniel Gagnière and Benoit Deveaud at LOEQ was the CL and femto-second spectroscopy, in addition to the discussions. Great thanks again to Lorenzo Mancini and Lorenzo Rigutti for the impressive and high-value APT results.

Thanks to Ramses V. Martinez, George M. Whitesides, Douglas C. Watson and Marko Lon□ar in Harvard who collaborated on and initiated the nanoskiving methods, leading to a somewhat unexpected outcome regarding TEM sample preparation. Thanks as well to Carsten Ronning and Andreas Johannes, and Alois Lugstein and Markus Glaser for the collaboration on the "wiring quantum dots" project.

Many thanks as well the Pierre Corfdir, Barbara Van Hattem and Richard. T. Phillips for all the help and discussions. It was great to be able to come to Cambridge and work with you! Huge thanks as well to the groups of Richard J. Warburton and Martino Poggio in Basel University. In addition to helping me a lot getting my next position, their teams and in particular Gunther Wüst, Andreas V. Kuhlmann, Julien Houel, Michele Montinaro, Davide Caddedu and Nicola Rossi have been extremely helpful and both directly and indirectly contributed to this thesis. Thanks also to Floris, Andrea, Arne and the others for the good time in Arosa, Lausanne, Basel and Tel-Aviv! In general, thanks to QSIT for organizing excellent meetings and event, and participating to the funding of my research. The Swiss National Fund for Scientific Research SNF is acknowledged for funding this project through the DACH "wiring quantum dots" project.

Thanks as well to all my friends at EPFL - particularly at LMOM :) - , and special and many thanks to one of my collaborators, on an unrelated topic, Dragana Paripovic. Thanks Dragana for being such a great friend! You are amazing!

Of course life is not limited to research and related. For this reason I would like to thank all my friends and the nice persons I met these last four years and before, either on/off the ski slopes, on/off surf boards, running, relaxing, going out and even in the 18/3, *In Corde Veritas*! It was great to be able to switch off (sometime completely). I would also like to thank my flatmate, and of course particularly my girlfriend for being so supportive despite the distance.

At the very end, I owe my biggest thanks to my family, and in particular to my parents who always supported me. *Maman, Papa, Mélanie et les compagnons à pattes, merci infiniment. Peu importent les mots, ils ne seront jamais que l'ombre de ma gratitude.*

List of Publications

Quantum Dots in Nanowires

1. *Quantum dots in GaAs/AlGaAs Core-Shell Nanowires: statistical occurrence as a function of the shell thickness*
   L. Francaviglia, Y. Fontana, S. Conesa-Boj, G. Tütüncuoglu, L. Duchesne, M. B. Tanasescu, F. Matteini and A. Fontcuberta i Morral
   Appl. Phys. Lett., **107** (2015)

2. *Three-dimensional Nanoscale Study of Al Segregation and Quantum Dot Formation in GaAs / AlGaAs Core-Shell Nanowires*
   L. Mancini, Y. Fontana, S. Conesa-Boj, I. Blum, F. Vurpillot, L. Francaviglia, E. Russo-Averchi, M. Heiss, J.Arbiol, A. Fontcuberta i Morral and L. Rigutti
   Appl. Phys. Lett., **105** (2014)

3. *Tuning the g-factor of Excitons and Charged Excitons Confined to Self-assembled (Al, Ga)As Shell Quantum Dots*
   P. Corfdir*, Y. Fontana*, B. Van Hattem, E. Russo-Averchi, M. Heiss, A. Fontcuberta i Morral, and R. T. Phillips
   Appl. Phys. Lett., **105** (2014)

4. *Exciton Footprint of Self-assembled AlGaAs Quantum Dots in Core-Shell Nanowires*
   Y. Fontana*, P. Corfdir*, B. Van Hattem, E. Russo-Averchi, M. Heiss, S. Sonderegger, C. Magen, J. Arbiol, R. T. Phillips and A. Fontcuberta i Morral
   Phys. Rev. B **90** (2014)

5. *Quantum Dot Opto-Mechanics in a Fully Self-Assembled Nanowire*
   M. Montinaro, G. Wuest, M. Munsch, Y. Fontana, E. Russo-Averchi, M. Heiss, A. Fontcuberta i Morral, R.J. Warburton and M. Poggio
   Nano Lett. **14** (2014)

6. *Nanoskiving Core-Shell Nanowires: A New Fabrication Method for Nano-optics*
   D.C. Watson, R.V. Martinez, Y. Fontana, E. Russo-Averchi, M. Heiss, A. Fontcuberta

i Morral, G.M. Whitesides and M. Loncar
Nano Lett. **14** (2014)

7. *Self-Assembled Quantum Dots in a Nanowire System for Quantum Photonics*
M. Heiss*, Y. Fontana*, A. Gustafsson, G. Wuest, C. Magen, D. D. O'Regan, J. W. Luo, B. Ketterer, S. Conesa-Boj, A. V. Kuhlmann, J. Houel, E. Russo-Averchi, J. R. Morante, M. Cantoni, N. Marzari, J. Arbiol, A. Zunger, R. J. Warburton and A. Fontcuberta i Morral
Nat. Mater. **12** (2013)

* Authors contributed equally to the work

Others

1. *Tailoring the Diameter and Density of Self-Catalyzed GaAs Nanowires on Silicon*
F. Matteini, V. G. Dubrovskii, D. Rüffer, G. Tütüncuoglu, Y. Fontana and A. Fontcuberta i Morral
Nanotechnology, **26** (2015)

2. *Functional Carbon Nanosheets Prepared from Hexayne Amphiphile Monolayers at Room Temperature*
S. Schrettl, C. Stefaniu, C. Schwieger, G. Pasche, E. Oveisi, Y. Fontana, A. Fontcuberta i Morral, J. Reguera, R. Petraglia, C. Corminboeuf, G. Brezesinski and H. Frauenrath
Nat. Chem. **4** (2014)

3. *Nanowire Antenna Emission*
G. Grzela, R. Paniagua-Domínguez, T. Barten, Y. Fontana, J. A. Sánchez-Gil and J. Gómez Rivas
Nano Lett. **12** (2012)

4. *Mapping the Directional Emission of Quasi Two-dimensional Photonic Crystals of Semiconductor Nanowires Using Fourier Microscopy*
Y. Fontana, G. Grzela, E.P.A.M. Bakkers and J. Gómez Rivas
Phys. Rev. B **86** (2012)

5. *Optical Properties of $GaAs/GaAs_{(1-x)}Sb_x$ Heterostructure Nanowires Grown by MBE*
Y. Fontana, S. Conesa-Boj, P. Carroff and A. Fontcuberta i Morral
31^{st} International Conference on the Physics of Semiconductors, ICPS 2012, 2012, Zurich, Switzerland

Author's Resume

yannik.fontana(at)gmail.com

Education & Research

Aug. 2011 - Present	PhD Candidate *"Optically Active Quantum Dots in Bottom-up GaAs/AlGaAs Core-Shell Nanowires"*, Advisor : A. Fontcuberta i Morral École Polytechnique Fédérale de Lausanne *Optical & Electron spectroscopy • Quantum emitters • Experiment & Setup design*
Nov. 2010 - Jul. 2011	Master research project *"Resolving the Directional Emission of Semiconductor Nanowire Arrays with Fourier Microscopy"*, Advisor: J. Gomez-Rivas FOM-AMOLF C/o Phillips Research, the Netherlands *Nanophotonics & Plasmonics • Alternative optical microscopy • Optical setup design*
Sept. 2009 - June 2011	Master of Science (M.S.) Material Science and Engineering, École Polytechnique Fédérale de Lausanne *Materials for biotechnological and medical applications • Materials for microelectronics and microengineering*
Sept. 2006 - June 2009	Bachelor of Science (B.S.) Material Science and Engineering, École Polytechnique Fédérale de Lausanne

Competences

Techniques	Optical spectroscopy techniques (PL • Raman • SPCC).
	Advanced setup design (Spectroscopy • Imaging).
	High-resolution imaging (SEM • AFM • STED).
	High-resolution material characterization (CL • EDX).
Teaching	Teaching assistant for various classes (Bachelor • Master).
	Project mentoring (Bachelor • Master).
Informatics	Various Operating systems (OS X • Windows • Linux-based).
	Computing environment (Matlab • Octave • Mathematica).
	Various H/L level languages (C/C++ • Python • Labview).
	CAD & CGI (SolidWorks • Catia • Adobe CS • Blender).
	Sys-admin *ad-interim* (2014) (Windows network • Linux servers).

Languages

French (native speaker) • English (fluent) • German (basic)